INFORMATION TO USERS

NOTE TO USERS

The original manuscript received by UMI contains broken or light print. All efforts were made to acquire the highest quality manuscript from the author or school. Page(s) were microfilmed as received.

This reproduction is the best copy available

UMI

HEAT CONVECTION FROM AN OSCILLATING CYLINDER

BY

FATHI MOHAMED ABD AL-AZIM MAHFOUZ

A Dissertation Presented to the

FACULTY OF THE COLLEGE OF GRADUATE STUDIES

KING FAHD UNIVERSITY OF PETROLEUM & MINERALS

DHAHRAN, SAUDI ARABIA

In Partial Fulfillment of the
Requirements for the Degree of

DOCTOR OF PHILOSOPHY
In

MECHANICAL ENGINEERING

MAY, 1998

UMI Number: 9908081

UMI

300 North Zeeb Road
Ann Arbor, MI 48103
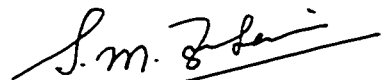
KING FAHD UNIVERSITY OF PETROLEUM AND MINERALS
DHAHRAN 31261, SAUDI ARABIA
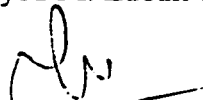
College of graduate studies

This dissertation, written by **FATHI MOHAMED ABD EL-AZIM MAHFOUZ** under the direction of his dissertation advisor and approved by his Dissertation Committee, has been presented to and accepted by the Dean of the College of Graduate Studies, in partial fulfillment of the requirement for the degree of **DOCTOR OF PHILOSOPHY IN MECHANICAL ENGINEERING**

Dissertation Committee
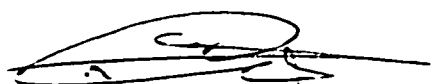
Dr. Hassan M. Badr (Chairman)

Dr. Syed M. Zubair (Member)

Dr. Syed A. Said (Member)

Dr. Mohamed A. EL- Gebeily (Member)

Department Chairman

Dean, College of Graduate Studies

5/9/9 ...
Date
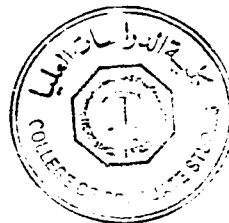
When I was on my first year in primary school she had a hard time convincing me to go to school. She was incredibly patient and made unlimited sacrifices.

I dedicate this dissertation

TO

MY MOTHER

ACKNOWLEDGMENT

CONTENTS

LIST OF TABLES

LIST OF FIGURES

ix

x

ABSTRACT

Name   : Fathi Mohamed Abd El-Azim Mahfouz
Title   : Heat Convection from an Oscillating Cylinder
Major Field : Mechanical Engineering
Date of degree: May 1998

Heat convection from a horizontal cylinder performing either rotational or rectilinear oscillations is investigated. The investigation covers forced and combined convection from a rotationally oscillating cylinder placed in either a quiescent fluid or a uniform stream as well as combined convection from cylinders performing rectilinear oscillation. For each of the cases considered the governing equations of motion and energy are solved numerically to determine the characteristics of the flow and thermal fields. In the case of a rotationally oscillating cylinder in a cross stream, the lock-on phenomenon has been predicted and its effect on the flow and thermal fields has been determined. The results show that the lock-on phenomenon occurs within a band of frequency near the natural frequency. The heat transfer coefficient as well as lift and drag coefficients show an increase within the lock-on frequency range. For a cylinder performing steady or oscillating rotary motions in a quiescent fluid, the study revealed that, for the same Rayleigh number, increasing the steady rotation of the cylinder tends to decrease the rate of heat transfer. In the case of rotational oscillation, the results showed that, for the same Rayleigh number, the heat transfer rate fluctuates around an average that lies in between two limiting values. The first, belongs to natural convection from a fixed cylinder while the second is equal to the heat rate from a cylinder rotating steadily at a speed equal to the maximum speed of rotational oscillation. For a cylinder performing vertical oscillation in a quiescent fluid, the study has shown that in the absence of buoyancy effects, the oscillation causes considerable increase in heat convection as either the amplitude or the frequency increases. However, as the buoyancy driven flow becomes dominant, the natural heat convection is almost unaffected by the cylinder oscillation.

DOCTOR OF PHILOSOPHY DEGREE

KING FAHD UNIVERSITY OF PETROLEUM AND MINERAL

DHAHRAN, SAUDI ARABIA

MAY 1998

الخلاصة

الاسم : فتحى محمد عبد العظيم محفوظ

عنوان الرسالة : الانتقال الحرارى بالحمل من اسطوانة مهتزة

التخصص : هندسة ميكانيكية

تاريخ الشهادة : مايو ١٩٩٨م

في هذه الرسالة تم بحث الانتقال الحرارى بالحمل من اسطوانه تهتز بشكل دورانى أو انتقالى. وشملت الدراسة كل من الحمل القسرى والمزدوج من اسطوانة تهتز بشكل دورانى فى انسياب مستقر او فى مائع ساكن وكذلك الحمل الحرارى من اسطوانة تهتز راسيا في مائع ساكن. ففى حالة الاهتزاز الدورانى فى انسياب مستقر تم اكتشاف ظاهرة التزامن واثبات ان هذه الظاهرة تحدث عندما يكون تردد الاهتزازات داخل نطاق يحتوى التردد الطبيعى للدوامات من اسطوانة ساكنة فى انسياب مستقر. واثبت البحث ان كل من قوة المقاومة والرفع تزداد عند حدوث هذه الظاهرة وكذلك الانتقال الحرارى بالحمل. اما حالة الدوران المنتظم او المتذبذب للاسطوانة فى مائع ساكن أثبتت الدراسة انه فى حالة الدوران المنتظم ينقص الحمل الحرارى كلما زادت سرعة الدوران بينما فى حالة الاسطوانة المتذبذبة فيتارجح الحمل الحرارى حول قيمة متوسطة تقع بين قيمة الحمل الحرارى الحر من اسطوانة ساكنة وبين الحمل الحرارى من اسطوانة تدور بانتظام بنفس السرعة المحيطية القصوى للاسطوانة المهتزة. وقد اثبتت الدراسة فى حالة الاهتزاز الراسى للاسطوانة فى مائع ساكن انه فى حالة انعدام تأثير قوى الطفو يزداد الحمل الحرارى بزيادة كل من سعة وتردد الاهتزازات. ولكن عندما يكون تأثير قوى الطفو قويا تكون الزيادة فى الحمل الحرارى نتيجة الاهتزازات غير مؤثرة.

درجة دكتوراة الفلسفة

فى الهندسة الميكانيكية

جامعة الملك فهد للبترول والمعادن

الظهران–المملكة العربية السعودية

مايو ١٩٩٨م

CHAPTER 1

INTRODUCTION

Heat transfer and fluid flow associated with a horizontal circular cylinder has been, for several decades, a subject of great attention among applied mathematicians, fluid dynamists and heat transfer analysts owing to its numerous engineering applications. These applications include heat exchangers, cooling of electronic devices, hot wire anemometers and lift enhancement as attributed to Magnus effects. It has been of great theoretical interest as being a prototypical model for studying important aspects of heat convection and hydrodynamics of unsteady flow over bluff bodies. Currently, due to various design of mechanical and electronic devices, the need arises for studying both hydrodynamics and heat transfer associated with cylinders that are performing either unsteady rotation or translation.

When a circular cylinder is placed in a cross stream, a broad wake in the rear side of the cylinder forms due to boundary-layer separation. The nature of the flow in the wake region is highly dependent on Reynolds number and exhibits several distinct flow regimes. A phenomenon of particular interest is the alternate shedding of vortices from either side of the cylinder which usually occurs at Reynolds numbers above 40. Vortex shedding introduces oscillating components to lift and drag forces as well as rate of heat transfer. The

frequency of vortex shedding is generally expressed in terms of Strouhal number, $S_o = f_o d/V$ where f_o is the frequency of vortex shedding from a rigid cylinder. If the cylinder oscillates, either in response to the oscillating lift force or due to external forces, the flow pattern in the wake region changes which may cause changes in the lift and drag forces as well as the heat transfer characteristics.

In the case of a cylinder performing transverse or in-line oscillations, when the oscillation frequency is near the natural shedding frequency (for transverse oscillation) or twice the natural shedding frequency (for in-line oscillation), vortices start shedding at the same forcing frequency. This is called the lock-on phenomenon and is found to cause significant changes in the flow and thermal fields. A graphical representation of this phenomenon is presented in the Figure 1.1 (after Tanida et al. [1]), which is a plot of S/S_v vs. S where S ($=fd/V$) and S_v ($=f_v d/V$) are the dimensionless cylinder oscillation and vortex shedding frequencies respectively. In the case of rotational oscillation in a cross stream, although the lock-on phenomenon has been reported and visualized experimentally [2], the detailed effect of this phenomenon on flow and thermal fields is not completely known.

Heat convection from a cylinder performing rotary motion in a quiescent fluid is considered in this work, for it has some applications in thermal engineering. These applications range from cooling of rotating machinery to drying in paper industry. Although the effect of steady rotation on heat transfer characteristics has been investigated, the effect of unsteady rotation has not been studied.

Heat convection from vertically oscillating cylinder in a quiescent fluid is also considered in this study, due to its numerous physical applications. The most familiar direct application

is the heat convection from overhead transmission lines. These lines when subject to air currents usually vibrate in response to the oscillating lift and drag forces. This vibration affects one way or another the heat transfer rate and, consequently, the cooling of transmission lines. In contrast to the considerable work published (see Chapter 2 for details) on the problem of heat convection from a cylinder performing rectilinear oscillations in a uniform stream, very little theoretical work was carried out on the problem of a cylinder oscillating in a quiescent fluid. The main difficulty was the determination of the boundary conditions at the moving solid boundary. One remedy which is adopted here, is the use of a non-inertial frame of reference.

This work aims to conduct a theoretical investigation of the problem of heat convection from a cylinder performing either rotational or rectilinear oscillations. In this regard, the following three problems are considered:

1. Forced convection from a rotationally oscillating cylinder in a cross stream.

2. Mixed convection from a rotationally oscillating cylinder in a quiescent fluid.

3. Heat convection from a vertically oscillating cylinder in a quiescent fluid

In chapter 2, a comprehensive review of previous studies relevant to the above mentioned problems is presented. In the subsequent chapters, the problem statement, method of solution and a discussion of the obtained results for each of the cases considered is presented.
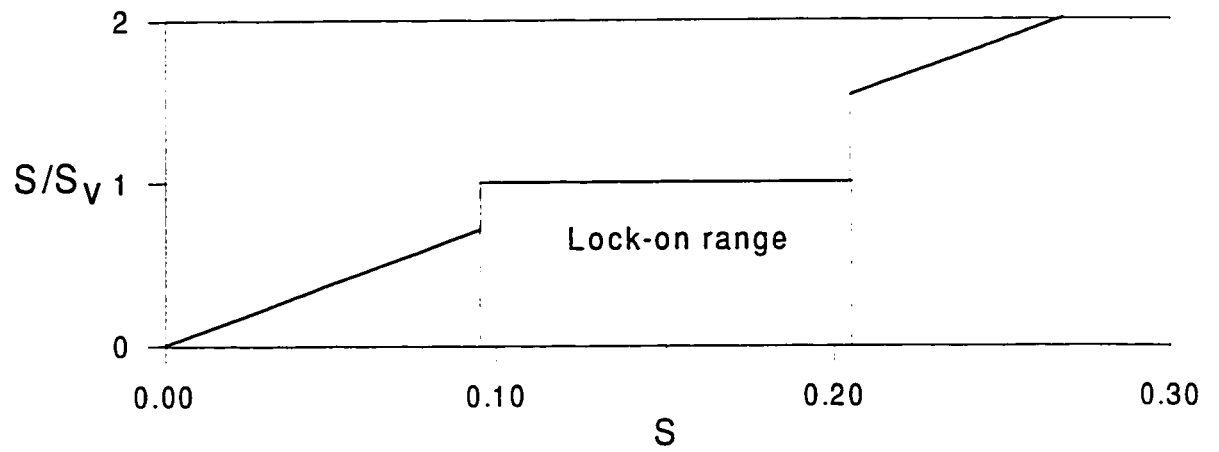
Figure 1.1 S/S_v vs. S, Re=80, after Tanida et al. [1].

CHAPTER 2

LITERATURE REVIEW

Previous research on fluid flow over and heat convection from circular cylinders performing oscillatory motions is numerous. In the following, a review of previous related theoretical and experimental studies is presented. These studies include those dealing with circular cylinders performing rotary motions (steady or oscillating) and placed horizontally in moving or quiescent Boussinesq fluids. The review also includes the work done on cylinders that are either placed in fluctuating flows or oscillate in quiescent fluids.

2.1 Heat Convection From Cylinders Rotating in Quiescent Fluids

Heat convection from a horizontal cylinder rotating in a quiescent fluid was studied by several investigators who found that the heat transfer rate from a rotating cylinder depends on Reynolds number, Re (based on the surface velocity), Grashof number, Gr, and Prandtl number, Pr.

Anderson and Saunders [3] were the first to study experimentally the heat transfer from horizontal cylinders rotating in still air. Heat transfer by convection was measured for different rotational speeds, cylinder temperatures and diameters. They found that up to a

critical value of Reynolds number, the Nusselt number slightly decreases with increasing Reynolds number and the heat transfer is dominated by free convection. Above the critical Reynolds number, they found that Nusselt number increases in proportion to $Re^{2/3}$ whereas Grashof number has a negligible effect on the rate of heat transfer. Etemad [4] studied experimentally the heat transfer and fluid flow around horizontal cylinders rotating in air. A range of Reynolds numbers from 0 to 65,000 was investigated. From interferometric observations, the laminar Couette flow was found to break down at a critical Reynolds number ranging from 800 to 1,200. The study also showed that for values of Reynolds number less than the critical value, the average Nusselt number decreases slightly with increasing Reynolds number and depends mainly on Grashof number. His results showed a good agreement with Ref. [3] in the range of Re > 6,000 where the effect of free convection is negligible. Dropkin and Carmi [5] studied experimentally the problem of natural convection from a rotating cylinder in air. Their results covered a range of Reynolds number up to 43,300. The results showed that up to Re =15,000, rotation has no effect on the heat transfer coefficient. Above this critical value, the heat transfer coefficient increases as Reynolds number increases.. For Reynolds number larger than 15,000 they recommended the correlation Nu = 0.073 $Re^{0.7}$. In the region where both rotation and natural convection influence the heat transfer, their data were correlated by: Nu = 0.095(0.5 Re +Gr)$^{0.35}$.

Kays and Bjorklund [6] measured heat transfer from a horizontal cylinder rotating in air with and without crossflow. In case of zero crossflow, their results compared very well with the investigations previously mentioned [3-5]. They also investigated the problem theoretically by means of momentum and heat transfer analogy and found that the Nusselt number could be related to friction coefficient , Prandtl number and Reynolds number. In

the case of air (Pr=0.72), the analogy solution agreed well with the experimental results. Seban and Johnson [7] studied experimentally heat transfer from a horizontal cylinder rotating in a tank of oil. Their results covered a Prandtl number range from 130 to 670 and Reynolds number up to 15,000. The results showed an increasing dependence of free convection on rotation as Prandtl number increases. At higher rotative speeds, where the flow became turbulent and the free convection effects vanished, the results were correlated by plotting $Nu/Pr^{0.356}$ versus Reynolds number. Some additional measurements were also done using water. Becker [8] measured convection heat transfer from a horizontal cylinder rotating in a tank of water. The results covered the range of Prandtl numbers from 2.2 to 6.4 and Reynolds numbers from 1,000 top 46,000. All his measurements were limited to the region where the effects of natural convection are negligible and the heat transfer rates depend only on Reynolds and Prandtl numbers. The results were correlated in terms of Re and Pr as: $Nu=0.133 \, Re^{2/3} \, Pr^{1/3}$. This correlation compared well with the experimental data reported by Anderson and Saunders [3]. Also, a good agreement was found between these results and the theoretical momentum and heat transfer analogy solution of Kays and Bjorklund [6].

Badr and Ahmed [9] investigated numerically the problem of heat convection from a horizontal cylinder rotating in a quiescent fluid for Reynolds numbers up to 200, Richardson number, Ri, being varied in the range 0 <Ri <1.4, while Pr is kept constant at 0.7. Their study was based on the solution of conservation equations of mass, momentum and energy. They showed that the transient heat transfer following a sudden temperature rise is well defined in three stages, the first one is a conduction stage followed by a transition (conduction/convection) phase and finally by a stage of steady convection. The details of

the steady velocity and temperature fields were obtained and, accordingly, the variation of vorticity and the local Nusselt number around the cylinder surface were plotted for different cases. Their results were compared with the available experimental data and a satisfactory agreement was found.

Farouk and Ball [10] studied both theoretically and experimentally the induced convective flows around a rotating isothermal cylinder stationed horizontally in air. Their numerical solutions were carried out for free convection dominated flows and covered a wide range of Grashof number (up to 1.39×10^7) and the rotational parameter, Gr/Re^2, was selected greater than one. Their computations showed a slight decrease of the mean Nusselt number with the increase of Re at the same value of Gr. The experimental studies, through Schlieren photographs, showed a two dimensional flow regime with the mean heat transfer rates remaining essentially constant at the same Gr. As the rotational speed increases above a critical value, three dimensional disturbances in the form of axial waves appear, with the mean heat transfer rates undergo a marked increase with the increase of rotational speed.

Wu-Shang et al. [11] studied numerically the enhancement of natural convection heat transfer in an enclosure by a rotating cylinder. The enclosure was two-dimenstional with adiabatic upper and lower walls. The left and right walls are maintained at high and low temperatures, respectively. They solved the governing equations using a penalty finite element method with a Newton-Raphson algorithm. Their results revealed that the contribution of rotation to natural convection depends on the direction of rotation of the cylinder. For counter-clockwise rotation, the contribution was found to be substantial when

the value of Gr/Re^2 is larger than 100, however, for the clockwise rotation, the contribution is hardly detected even when the value of Gr/Re^2 is equal to 1.

2.2 Heat Convection From a Cylinder Rotating in a Cross Stream

The problem of heat convection from a cylinder rotating in a cross stream has attracted many researchers both theoretically and experimentally. Badr and Dennis [16] solved numerically the problem of forced convection from a rotating isothermal cylinder. The solution covered the range of Reynolds number (based on free stream velocity) up to 100, and velocity ratios (ratio between tangential velocity and free stream velocity) up to 4. The obtained results showed that the local Nusselt number as well as the surface vorticity distributions, were highly influenced by the rotational motion of the cylinder. At low values of the rotational speed, the variation of local Nusselt number, Nu, deviates only slightly from the symmetrical distribution that prevails for a fixed cylinder. As the rotational speed increased, the variation of Nu tended to be more uniform. The same behavior occurred at higher values of Reynolds number. It was also found that the average Nu decreases as the rotational speed increases .

Ryohachi et al. [17] investigated experimentally mixed heat convection from a rotating cylinder with and without cross flow by Mach-Zender interferometer with visual observation of flow patterns. Their experiments covered the range of cross flow Reynolds number ($Re_d = Vd/v$) up to 3,000, rotational Reynolds number, Re_r (based on cylinder velocity) up to 3000 and Grashof number, Gr, from 4.8×10^4 to 2.6×10^5. The study showed that heat transfer is not influenced by natural convection as long as Re_d greater than 1,000.

The results showed that average heat transfer coefficients of a rotating cylinder are equal to the case of static cylinder in a uniform flow when $Re_d > 1,000$ and the velocity ratio less than one. It was also found that heat transfer from the cylinder is least at a velocity ratio of 2 and Re_d below 1000. At velocity ratios greater than 2, the heat transfer rates were found to be dominated by rotational speed and the data obtained for $\overline{Nu}$ were correlated in terms of Re_d, Re_r and Gr as : $\overline{Nu} = 0.055 \, Re_r^{0.7} \, (1+8 \, Gr/ \, Re_r^2 \,)^{0.35}$.

Chiou and Lee [18] studied the flow structure and heat transfer from a rotating cylinder cooled with an air jet. The Nusselt numbers were obtained for jet Reynolds numbers of 100, 500 and 1000 under various rotation Reynolds numbers up to $Re_r = Re_j$. For slow rotation speeds, the jet flow is separated into two branches after hitting the cylinder with a separation point for every branch. The rotating cylinder accelerates one of the jet branches such that the separation point moves downstream, while the other separation point receives no significant influence. As a result, the overall heat transfer coefficient was enhanced. For high rotational speeds, however, this trend were reversed due to the presence of a buffer layer of air round the cylinder. This condition, nevertheless, resulted in more uniform heat transfer rates.

Shehata [19] studied theoretically the problem of mixed convection from a rotating horizontal isothermal cylinder placed in a cooling cross stream. His study covered the range of Reynolds number from 20 to 500, Grashof number up to 10^6 and speed ratio up to 8.0. The study focused on the effect of the ratio of Gr/Re^2 on the local and average heat transfer coefficients for selected values of Reynolds number and speed ratio while keeping the Prandtl number unchanged. It was found that both Grashof number and speed ratio have

profound effect on the local and average Nusselt numbers. Increasing Grashof number for constant speed and Reynolds number (i.e. increasing Gr/Re^2) tended to increase the average Nusselt number, whereas increasing the speed ratio for fixed values of Gr and Re caused a significant decrease in the average Nusselt number.

Nguyen et al. [20] studied mixed heat convection from a rotating circular cylinder immersed in a spatially uniform, time-dependent convective environment including the effects due to buoyancy force and a small fluctuations in the free stream velocity. The flow equations, based on vorticity-stream function formulation, are solved along with the energy equation by a hybrid spectral scheme that combines the Fourier spectral method in the angular direction and a spectral element method in the radial direction. They investigated several cases in the range of Reynolds number up to 200, Grashof number up to 20,000 and speed ratios from -0.5 to 0.5. The results show that vortex shedding is promoted by the cylinder rotation but vanishes by the presence of buoyancy force. They found that, the direction of rotation, whether aids the buoyancy force or opposes it , greatly affects the heat flux along the cylinder surface. This implies that the heat transfer rate is strongly dependent upon Reynolds number , Grashof number, Rotational speed and gravity direction. The effect of flow pulsation is reflected in the Nusselt number history in the form of periodic oscillations.

2.3 Flow Over Rotationally Oscillating Cylinders

The first study dealt with flow over an oscillating cylinder was due to Hori [21] who solved the unsteady boundary layer on a circular cylinder performing rotational oscillations in a

uniform flow. The two-dimensional, laminar-flow equations were linearized based on the assumption that the velocity fluctuation in the boundary layer is small. The frequency of the fluctuation is also assumed low, thus retaining terms up to the first order in frequency. The solutions are expressed as linear combinations of a family of universal functions by extending the Blasius' series method to unsteady flow. A new criterion of the unsteady boundary-layer separation is proposed by observation of streamline patterns near the point of separation. This criterion is based on the asymptotic behavior of these streamlines at a large distance from the solid wall.

Okajima et al. [22] studied viscous flow around a rotationally oscillating circular cylinder both numerically and experimentally. Their numerical solution of Navier-Stokes equations is carried out at one value of velocity amplitude (surface velocity/free stream velocity), $\alpha = 0.2$, and covered a range of Reynolds number, Re=40 to 80, whereas their experimental results covered a range of Reynolds numbers, Re=40 to 6,100. Their numerical results for lift forces showed a good agreement with the experimental results at Re=40, 80. On the other hand, the phenomenon of the so called synchronization (this occur when vortex shedding frequency equal to imposed cylinder frequency) has been reported in their investigation. Finally, they concluded that there may be a close relation between time variation of flow pattern and that of the lift force on the oscillating cylinder.

Using flow visualization, Tanida [23] investigated the flow structure around a circular cylinder performing rotary oscillations about its own axis while placed in a uniform stream. The study covered a range of Reynolds numbers between 30 and 300 and Strouhal numbers between 0 and 55. The study revealed that, as the frequency of oscillation increases the dead

fluid in the wake of the cylinder reduces, and that the critical Strouhal number at which this dead region vanishes is approximately proportional to the reciprocal of the angular amplitude of oscillation , but independent of Reynolds number.

The unsteady flow over a rotationally oscillating cylinder was investigated both numerically and experimentally by Wu et al. [24]. The numerical solution was obtained by solving the full Navier-Stokes equations which were written in the form of vorticity and stream function equations. Shedding of vortices with and without external excitations were discussed. The results showed that the forces acting on the cylinder strongly depend on the oscillation frequency and amplitude. Flow visualization was conducted with laser-induced fluorescence and colored dye techniques in a water tunnel for both fixed and oscillating cylinders. The experiment showed that when the forced frequency is near the natural vortex shedding frequency, the vortex shedding in the wake becomes more organized, which was found to agree with their numerical predictions. It has been also found that both unsteady lift and drag forces reach their maximum when the resonance flow state is reached (i.e., when the forced frequency is equal to natural vortex shedding frequency).

Tokumaru and Dimotakis [2] studied experimentally the possibility of rotary oscillation control of a cylinder wake. The study was based on flow visualization and measurements of the wake profile using Laser-Doppler anemometer at moderate Reynolds number, Re=15000, Strouhal number, S_f in the range $0.17 \leq S_f \leq 3.3$ and velocity amplitude up to 16. Their results showed that, at fixed frequency, as the amplitude of oscillation increases the wake becomes wider. With the variation of amplitude and frequency of oscillation, several modes of vortex shedding were observed. At a fixed velocity amplitude, $\alpha = 8$, and

$0 \leq S_f \leq 0.9$, the wake structure was found to be synchronized with the forced cylinder oscillation. As the frequency increased to 1.1 and 1.5, the near wake was synchronized but the far wake flow became unstable and not synchronized with the cylinder oscillation. As the frequency increased further to 2.0 and 3.3 the effect of forcing was primary observed in the shear layer separating from the cylinder. Their results at lower Reynolds numbers, $Re=3.3 \times 10^3$, showed that the effect of Reynolds number on the aforementioned vortex shedding modes in the wake was not significant. They concluded that similarity of their results with other researchers such as Roberts and Roshko [25] and Williams and Amato [26], using various bluff bodies and forcing techniques, supported the proposition that the mechanisms by which the dynamics in the wake can be controlled are largely generic and have more to do with the ejection of circulation into the flow, rather than with the behavior of the flow observed in the absence of forcing.

Tokumaru and Dimotakis [27] investigated the mean lift coefficient of a circular cylinder executing rotary motions in a uniform flow. These motions include steady rotation ($\Omega_o=$const.) and rotary oscillation with a net rotation rate in the form $\Omega = \Omega_o + \Omega_1 \sin(2\pi ft)$. Their experiments were carried out through flow visualization and LDV in the range $0.5 \leq \Omega_o \leq 10$ and Ω_1 up to 2.3 at $Re=3800$. It was found that forced oscillation increased the lift coefficient in the range $0 < \Omega_o < 2.5$ and decreased it in the range $2.5 \leq \Omega_o \leq 4.5$. These were attributed to the fact that the forced oscillation helps minimize the wake in the range $\Omega_o < 2.5$ since the flow becomes closer to potential flow but with an opposite effect in the range $2.5 \leq \Omega_o \leq 4.5$.

2.4 Heat Convection From Rotationally Oscillating Cylinders

The number of studies dealing with heat convection from a steady rotating cylinder is fairly considerable and covering almost all aspects of heat transfer. However, the only study on heat convection from a cylinder performing rotary oscillations was carried out by Childs and Mayle [28] who investigated theoretically heat transfer from a rotationally oscillating cylinder placed in a cross stream. Their work was based on solving the unsteady boundary-layer and energy equations using the series method of Blasius [29] and Howarth [30] and the perturbation method of Lighthill [31]. The amplitude of oscillation was assumed small enough to neglect its square value which makes the contribution to the velocity and temperature fields as a linear perturbation of the steady fields. Two limiting values of the Strouhal number (S) were examined, the first when S approaches zero (quasi-steady case) and the second when S approaches very large values. The first solution, for the steady case, is extended to an unsteady solution for a small but finite value of S by adding a term that includes the effect of local acceleration. As S approaches very large values, local acceleration dominates near the wall, and interaction with the convective acceleration terms in the mean flow may be neglected. The solution was shown to consist of the superposition of Stokes's 2nd problem and that for steady flow around a circular cylinder. The study revealed that the unsteady skin friction reached as high as 38% of the total drag and increases with the frequency. On the other hand, the unsteady heat transfer is found to contribute only 4% near the separation point and decreases with frequency. They concluded that the steady expressions for heat transfer are adequate even when the cylinder is oscillating, regardless of the frequency as long as the amplitude is small. They attributed the

negligible effect of cylinder oscillation on the surface heat transfer to the boundary-layer assumptions adopted in their work.

2.5 Oscillating Flow Over a Circular Cylinder

The problems of flow around an oscillating cylinder, or a fixed cylinder placed in an oscillating flow field are classical problems in fluid dynamics. Extensive experiments have been carried out to study the flow patterns around the cylinder [32-34] and the hydrodynamic forces acting on it [35,36]. Apart from experimental approaches, numerical methods have been used to predict the streamlines and equi-vorticity contours. Justesen [37] solved numerically the Navier-Stokes equations using finite-differences for flow around a circular cylinder in a planer oscillating flow at small Keulegan-Carpenter number, $KC = U_m T/D$, where U_m is the maximum velocity, T is time period of oscillation and D is the diameter, in the subcritical Reynolds number range. For very small KC (≤ 1), the numerical results were found to coincide with the analytical solutions. As KC was increased, the incipient separation and instability leading to an asymmetrical flow with vortex shedding were predicted. The computed flow field at small KC values were compared with flow visualization, and a good agreement was found for moderate values of Stokes number β ($\beta = d^2/\mu T \approx 250$ where T is the cycle time period).

Badr et al. [38] integrated the unsteady Navier-Stokes equations to solve the oscillating flow over a fixed cylinder. They studied the effect of Reynolds and Strouhal numbers on the laminar symmetric wake evolution and the results were compared with the previous numerical and experimental studies. The time variation of the drag coefficient was also

presented and compared with the inviscid flow solution for the same problem. The comparison between the viscous and inviscid flow results showed a better agreement for higher values of Reynolds number.

Recently, Zhang Hui-Liu and Zhang Xin [39] investigated numerically the flow field around an oscillating cylinder by solving the governing equations in primitive variables formulation using finite-volume method with a pressure predictor-corrector scheme. Their results covered KC < 20 and Reynolds number, Re =U_m D/v < 4,000. The results showed that at low KC and/or low Re, the flow field was symmetric, with dominance of vorticity decaying effects. At higher Re, the vorticity convection became stronger leading to the inception of asymmetrical flow pattern. The forces acting on the cylinder were predicted for both symmetric and asymmetric flows. The conventional drag and inertia coefficients were deduced and compared with other numerical and experimental results, and a good agreement was found.

2.6 Heat Convection From Rectilinearly Oscillating Cylinders

The problem of heat convection from a cylinder performing rectilinear oscillations has been experimentally investigated by several researchers [40-49]. For heated cylinders performing transverse oscillations in quiescent fluids, a number of researchers [40-43] conducted their studies using water and others [44, 45] considered oscillations in air.

Lemlich and Roa [40] studied free convection from an electrically heated cylinder (0.049 inch diameter) to water and aqueous glycerine. The cylinder was vibrated vertically at frequencies ranging from 17 to 37 Hz for amplitudes up to 0.086 inch. The coefficient of

heat transfer was found to increase considerably with frequency and amplitude, reaching ten-fold in some cases. A dimensionless correlation was devised for their results together with those of other investigators [44, 47].

On the other hand, only few theoretical works were reported on the problem of heat convection from rectilinearly oscillating cylinders. Momose et al. [50] investigated numerically the influence of horizontal vibrations on heat convection from a horizontal cylinder. They solved the governing equations using Fourier-expansion method. Their study considered only the cases of very small amplitude, high frequency vibrations at low Grashof number (Gr=100). The results showed an increase in heat transfer as a result of vibration. Also, it is shown that the vortex system in the vicinity of the cylinder plays a key role in the heat convection process. Karanth et al. [51] used a finite-difference scheme to solve the forced convection heat transfer equations for an oscillating cylinder. They investigated the effect of in-line and transverse oscillations on the time-dependent average and local Nusselt numbers at a Reynolds number of 200. The study showed that the heat transfer rate from an oscillating cylinder increases with increasing the velocity amplitude. In the case of transverse oscillation, the location of maximum local Nusselt number was found to oscillate between the upper and lower surfaces of the cylinder.

Chin-Hsiang et al. [52] investigated heat convection and flow characteristics over a transversely oscillating cylinder. The range of dominated parameters considered were $0 \le Re \le 300$ and $0 \le S_f \le 0.3$, where S_f is the dimensionless reduced frequency of oscillation ($f\,d/U_\infty$). The Prandtl number considered was either 0.71 or 7.0. The study revealed that in the lock-on regime (when vortex shedding frequency is equal to cylinder

frequency), an appreciable increase in heat transfer caused by oscillation was observed, however, outside this regime the heat transfer was almost unaffected by oscillations. A correlation expressing the dependence of heat transfer on these dominant parameters in the lock-on regime was presented. Recently, Badr [53] investigated theoretically the effect of free-stream fluctuations on forced convection from a straight tube of circular cross-section. The resulting unsteady velocity and thermal fields are obtained by solving the conservation equations. The study covered a range of Reynolds number between 50 and 500, a range of Strouhal number from $\pi/4$ to π and a range of velocity amplitude from 20 to 50% of the free stream average velocity. The study revealed that the rate of heat transfer increases with the increase of the amplitude but decreases with the increase of frequency.

2.7 Closure

From the above literature review, it is clear that the problem of heat convection from a circular cylinder performing rotary oscillations in a quiescent fluid has not been investigated. The only study reported on forced convection from a rotationally oscillating cylinder in a cross stream was carried out in the limit of very small amplitude and with the assumption of boundary-layer flow. On the other hand, heat convection from a vertically oscillating cylinder in a quiescent fluid has not been theoretically investigated. The motivation to initiate this study was the lack of enough information on heat convection from a horizontal cylinder performing either vertical rectilinear oscillations in a quiescent fluid or rotary motions with and without cross stream.

CHAPTER 3

FORCED CONVECTION FROM A ROTATIONALLY OSCILLATING CYLINDER

In this chapter, the problem of forced heat convection from a circular cylinder performing rotary oscillations is considered. The physical model is shown in Figure 3.1. The cylinder is of radius c and is placed horizontally in an unbounded, cross-stream with uniform approaching velocity V. The cylinder surface is maintained at a constant temperature T_w and is rotationally oscillating about its own axis with harmonic motion of the form:

$$\Theta = -\Theta_A \cos(2\pi f\tau)$$

where, Θ is the angular displacement, τ is the time and Θ_A and f are the angular amplitude and frequency of oscillation, respectively. The cylinder surface velocity is then

$$u'_w = u'_m \sin(2\pi f\tau)$$

where u'_m is the amplitude of surface velocity.

3.1 The Governing Equations

The conservation equations which govern the laminar, two-dimensional motion of incompressible fluid are the continuity and momentum equations. The analysis of heat convection is based on the two-dimensional unsteady energy conservation principle. In cylindrical coordinates, the governing equations are expressed as :
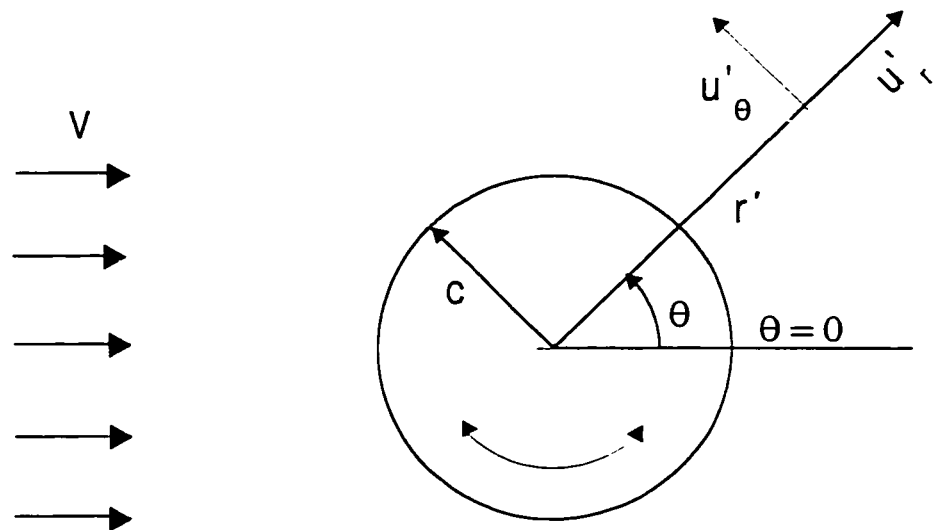
Figure 3.1 Coordinate System

Continuity equation:

$$\frac{\partial u_r'}{\partial r'} + \frac{u_r'}{r'} + \frac{1}{r'}\frac{\partial u_\theta'}{\partial \theta} = 0 \tag{3.1}$$

Radial momentum equation:

$$\frac{\partial u_r'}{\partial \tau} + u_r'\frac{\partial u_r'}{\partial r'} + \frac{u_\theta'}{r'}\frac{\partial u_r'}{\partial \theta} - \frac{u_\theta'^2}{r'} = -\frac{\partial p}{\rho \partial r'} + \nu(\nabla^2 u_r' - \frac{u_r'}{r'^2} - \frac{2}{r'^2}\frac{\partial^2 u_\theta'}{\partial \theta^2}) \tag{3.2}$$

Angular momentum equation:

$$\frac{\partial u_\theta'}{\partial \tau} + u_r'\frac{\partial u_\theta'}{\partial r'} + \frac{u_\theta'}{r'}\frac{\partial u_\theta'}{\partial \theta} - \frac{u_\theta' u_r'}{r'} = -\frac{1}{\rho r'}\frac{\partial p}{\partial \theta} + \nu(\nabla^2 u_\theta' - \frac{u_\theta'}{r'^2} + \frac{2}{r'^2}\frac{\partial^2 u_r'}{\partial \theta^2}) \tag{3.3}$$

Energy equation:

$$\frac{\partial T}{\partial \tau} + u_r'\frac{\partial T}{\partial r'} + \frac{u_\theta'}{r'}\frac{\partial T}{\partial \theta} = \frac{k}{\rho c_p}\nabla^2 T \tag{3.4}$$

In the stream function-vorticity form, the above equations read :

$$\frac{\partial \zeta'}{\partial \tau} + \frac{\partial \psi'}{r'\partial \theta}\frac{\partial \zeta'}{\partial r'} - \frac{\partial \psi'}{r'\partial r'}\frac{\partial \zeta'}{\partial \theta} = \nu\nabla^2\zeta' \tag{3.5}$$

$$\zeta' = -\nabla^2\psi' \tag{3.6}$$

$$\frac{\partial T}{\partial \tau} + \frac{\partial \psi'}{r\partial \theta}\frac{\partial T}{\partial r} - \frac{\partial \psi'}{\partial \theta}\frac{\partial T}{r'\partial \theta} = \frac{k}{\rho c_p}\nabla^2 T \tag{3.7}$$

where, ζ' is the fluid vorticity defined as

$$\zeta' = (\frac{\partial u_\theta'}{\partial r'} + \frac{u_\theta'}{r'} - \frac{\partial u_r'}{r'\partial \theta})$$

The boundary conditions are the no-slip , impermeability and isothermal conditions on the cylinder surface together with the free stream conditions very far away from it. These conditions can be expressed as

$$\psi' = \frac{\partial \psi'}{\partial \theta} = 0 \;\;,\;\; \frac{\partial \psi'}{\partial r'} = -u_w' \;\;, \; and \; T=T_w \;\;\; at \;\; r' = c,$$

$$\frac{\partial \psi'}{\partial \theta} = r'V\cos(\theta), \;\; \frac{\partial \psi'}{\partial r'} = -V\sin(\theta), \;\; \zeta' \to 0 \;\;\; and \;\; T = T_\infty \;\; as \;\; r' \to \infty \tag{3.8}$$

The governing equations (3.5-3.7) and boundary conditions (3.8) are transformed to their dimensionless form by introducing the following dimensionless quantities.

$$r = \frac{r'}{c}, \quad u_r = \frac{u'_r}{V}, \quad u_\theta = \frac{u'_\theta}{V}, \quad t = \tau\frac{V}{c}, \quad \psi = \frac{\psi'}{cV}, \quad S = f\frac{2c}{V}$$

$$\zeta = -\zeta'\frac{c}{V}, \quad \text{and} \quad \phi = (T - T_x)/(T_s - T_x)$$

Using the above quantities, equations (3.5-3.7) can now be written as

$$\frac{\partial \zeta}{\partial t} + u_r \frac{\partial \zeta}{\partial r} + \frac{u_\theta}{r}\frac{\partial \zeta}{\partial \theta} = \frac{2}{Re^2}\nabla^2\zeta \tag{3.9}$$

$$\zeta = \nabla^2\psi \tag{3.10}$$

$$\frac{\partial \phi}{\partial t} + u_r \frac{\partial \phi}{\partial r} + u_\theta \frac{\partial \phi}{r\partial \theta} = \frac{2}{Re\,Pr}\nabla^2\phi \tag{3.11}$$

where,

$$u_r = \frac{\partial \psi}{r\partial \theta}, \quad u_\theta = -\frac{\partial \psi}{\partial r}$$

$Re = \dfrac{2cV}{\nu}$ is the Reynolds number and $Pr = \dfrac{\mu c_p}{k}$ is the Prandtl number.

The dimensionless surface velocity, U_w, can be expressed as

$$U_w = \alpha \sin(\pi St)$$

where α represents the dimensionless velocity amplitude ($=u'_m/V$) and S is the dimensionless forcing frequency.

In order to have high accuracy near the cylinder surface (where steep velocity and temperature gradients exist) and at the same time cover a wide computational domain, the modified polar coordinates (ξ, θ) are used where $\xi = \ln r$. In the modified polar coordinates, the equations can be written as:

$$e^{2\xi}\frac{\partial \zeta}{\partial t} = \frac{2}{Re}\left(\frac{\partial^2 \zeta}{\partial \xi^2} + \frac{\partial^2 \zeta}{\partial \theta^2}\right) - \frac{\partial \psi}{\partial \theta}\frac{\partial \zeta}{\partial \xi} + \frac{\partial \psi}{\partial \xi}\frac{\partial \zeta}{\partial \theta} \qquad (3.12)$$

$$e^{2\xi}\zeta = \frac{\partial^2 \psi}{\partial \xi^2} + \frac{\partial^2 \psi}{\partial \theta^2} \qquad (3.13)$$

$$e^{2\xi}\frac{\partial \phi}{\partial t} = \frac{2}{Re\,Pr}\left(\frac{\partial^2 \phi}{\partial \xi^2} + \frac{\partial^2 \phi}{\partial \theta^2}\right) - \frac{\partial \psi}{\partial \theta}\frac{\partial \phi}{\partial \xi} + \frac{\partial \psi}{\partial \xi}\frac{\partial \phi}{\partial \theta} \qquad , \qquad (3.14)$$

and the boundary conditions are written as :

$$\psi = \frac{\partial \psi}{\partial \theta} = 0 \ , \quad \frac{\partial \psi}{\partial \xi} = -\alpha \sin(\pi St) \ , \quad \text{and} \quad \phi = 1 \quad \text{at} \ \xi = 0,$$

$$\frac{\partial \psi}{\partial \theta} \to e^{-\xi}\cos\theta, \quad \frac{\partial \psi}{\partial \xi} \to -e^{-\xi}\sin\theta \ , \ \zeta \to 0 \ \text{and} \ \phi \to 0 \quad \text{as} \ \xi \to \infty \qquad (3.15)$$

3.2 The Method of Solution

The method of solution is based on integrating the governing equations of motion and energy in time to obtain the velocity and temperature fields. Using the series truncation method and following the works of Collins and Dennis [54] and Badr and Dennis [16, 55], the dimensionless stream function ψ, vorticity ζ and temperature ϕ are approximated using Fourier series expansions as follows :

$$\psi(\xi,\theta,t) = \frac{1}{2}F_o(\xi,t) + \sum_{n=1}^{N}[f_n(\xi,t)\sin(n\theta) + F_n(\xi,t)\cos(n\theta)],$$

$$\zeta(\xi,\theta,t) = \frac{1}{2}G_o(\xi,t) + \sum_{n=1}^{N}[g_n(\xi,t)\sin(n\theta) + G_n(\xi,t)\cos(n\theta)] \qquad (3.16)$$

$$\phi(\xi,\theta,t) = \frac{1}{2}H_o(\xi,t) + \sum_{n=1}^{N}[h_n(\xi,t)\sin(n\theta) + H_n(\xi,t)\cos(n\theta)]$$

where F_o, f_n, F_n, G_o, g_n, G_n, H_o, h_n, and H_n are Fourier coefficients and all are functions of ξ and t. Substitution of equations (3.16) in equations (3.12)-(3.14) and using simple mathematical analysis results in the following set of differential equations:

$$\frac{\partial^2 F_o}{\partial \xi^2} = e^{2\xi} G_o \tag{3.17a}$$

$$\frac{\partial^2 f_n}{\partial \xi^2} - n^2 f_n = e^{2\xi} g_n \tag{3.17b}$$

$$\frac{\partial^2 F_n}{\partial \xi^2} - n^2 F_n = e^{2\xi} G_n \tag{3.17c}$$

$$e^{2\xi} \frac{\partial G_o}{\partial t} = \frac{2}{Re} \frac{\partial^2 G_o}{\partial \xi^2} + S_o \tag{3.18a}$$

$$e^{2\xi} \frac{\partial g_n}{\partial t} = \frac{2}{Re} \left(\frac{\partial^2 g_n}{\partial \xi^2} - n^2 g_n \right) + n F_n \frac{\partial G_o}{\partial \xi} - n G_n \frac{\partial F_o}{\partial \xi} + S_{n1} \tag{3.18b}$$

$$e^{2\xi} \frac{\partial G_n}{\partial t} = \frac{2}{Re} \left(\frac{\partial^2 G_n}{\partial \xi^2} - n^2 G_n \right) + n f_n \frac{\partial G_o}{\partial \xi} - n g_n \frac{\partial F_o}{\partial \xi} + S_{n2} \tag{3.18c}$$

$$e^{2\xi} \frac{\partial H_o}{\partial t} = \frac{2}{Re\,Pr} \frac{\partial^2 H_o}{\partial \xi^2} + Z_o \tag{3.19a}$$

$$e^{2\xi} \frac{\partial h_n}{\partial t} = \frac{2}{Re\,Pr} \left(\frac{\partial^2 h_n}{\partial \xi^2} - n^2 h_n \right) + n F_n \frac{\partial H_o}{\partial \xi} - n H_n \frac{\partial F_o}{\partial \xi} + Z_{n1} \tag{3.19b}$$

$$e^{2\xi} \frac{\partial H_n}{\partial t} = \frac{2}{Re\,Pr} \left(\frac{\partial^2 H_n}{\partial \xi^2} - n^2 H_n \right) + n f_n \frac{\partial H_o}{\partial \xi} - n h_n \frac{\partial F_o}{\partial \xi} + Z_{n2} \tag{3.19c}$$

where S_o, S_{n1}, S_{n2}, Z_o, Z_{n1} and Z_{n2} are all easily identifiable functions of ξ and t and are given in appendix A1. Equations (3.17a)-(3.17c) define a set of (2N+1) ordinary differential equations and each of equations (3.18) and (3.19) define another set of (2N+1) partial differential equations, where N is the order of truncation in the Fourier series. All these

(6N+3) equations have to be solved at every time step to get the details of the flow and thermal fields. The boundary conditions for all functions in equations (3.17)-(3.19) are obtained from equations (3.15) and can be expressed as

at $\xi=0$

$$F_0 = F_n = f_n = \partial F_n/\partial \xi = \partial f_n/\partial \xi = 0, \quad \partial F_o/\partial \xi = -2\,\alpha\,\sin(\pi St)\,, \quad H_o = 2, \quad H_n = h_n = 0$$

and as $\xi \to \infty$

$$e^{-\xi} F_0 \to 0\,, \quad e^{-\xi}\,\partial F_o/\partial \xi \to 0\,, \quad F_n \to 0\,, \quad f_n \to \delta_{1,n}$$

$$e^{-\xi}\partial F_n/\partial \xi \to 0,\ e^{-\xi}\partial f_n/\partial \xi \to \delta_{1,n}\,, \quad G_o\,, G_n\,, g_n \to 0,\ \text{and}\ H_o\,, H_n\,, h_n \to 0 \qquad (3.20)$$

Integrating both sides of equation (3.17a) with respect to ξ from $\xi=0$ to $\xi=\infty$ and using the boundary conditions in equations (3.20) gives the following integral condition:

$$\int_0^\infty e^{2\xi} G_o d\xi = 2\,\alpha\,\sin(\pi St) \qquad (3.21a)$$

Multiplying both sides of equations (3.17b) and (3.17c) by $e^{-n\xi}$ and integrating using the boundary conditions (3.20), one can obtain the following integral conditions

$$\int_0^\infty e^{(2-n)\xi} g_n d\xi = 2\delta_{1,n} \qquad (3.21b)$$

$$\int_0^\infty e^{(2-n)\xi} G_n d\xi = 0 \qquad (3.21c)$$

where
$$\delta_{1,n} = \begin{cases} 1 & \text{when } n=1 \\ 0 & \text{when } n \neq 1 \end{cases}$$

The above integral conditions (3.21a-3.21c) are used at every time step to calculate the values of the functions G_o, g_n and G_n on the cylinder surface ($\xi = 0$). These functions are then used to compute accurately the vorticity distribution on the cylinder surface. The first condition (3.21a) is essential to ensure the periodicity of the pressure around the cylinder surface. Further discussion of this point is presented in the section 3-6.

3.3 The Initial Solution

In order to advance the solution of ψ, ζ and ϕ in time, the initial condition at time t=0 must be known. In this study, it is assumed that the flow and imposed rotational oscillation start simultaneously and impulsively from rest. At the same time cylinder surface temperature is assumed to increase to T_w. The use of potential flow solution as initial solution, as was frequently adopted by many researchers, will definitely lead to inaccurate results following the start of fluid motion. However, the effect of such inaccuracy on the large time results is not known. The flow field structure at small times following the start of fluid motion is characterized by a very thin boundary-layer region close to the cylinder surface bounded by a potential flow elsewhere. As time increases, this boundary layer region grows and the proper scaling for such a case is the use of boundary-layer coordinates. Let us now introduce boundary-layer coordinates (z, t) defined as :

$$\xi = \lambda\, z, \quad \text{where } \lambda = 2\sqrt{2\, t/Re}$$

Also introduce ψ^* and ζ^* defined as :

$$\psi^* = \psi / \lambda, \quad \text{and} \quad \zeta^* = \lambda\zeta.$$

The corresponding Fourier functions become

$$F_0^* = F_0 / \lambda, \quad f_n^* = f_n / \lambda, \quad F_n^* = F_n / \lambda, \quad G_0^* = G_0\lambda, \quad g_n^* = g_n\lambda \text{ and } G_n^* = G_n\lambda \qquad (3\text{-}22)$$

The use of ψ^* and ζ^* is appropriate to the flow field structure at small time in which the viscous flow region is limited to a very thin layer. In that layer, the surface vorticity ζ reaches very high values while the stream function ψ is very small.

Using equation (3.22), the governing equations and the boundary and integral conditions (3.17a-3.21c) can be transformed to the new coordinate system and then solved to give a fairly accurate solution at small times. To start the integration in the transformed coordinates the zero time solution must be known. Closely following the methodology of Collins and Dennis [54] and Badr and Dennis [55], the initial solution at $t=0^+$ is found to be

$$\psi^*(z,\theta,0) = -2[z(1-\mathrm{erf}(z) + \pi^{-1/2}(1-e^{-z^2})]\sin(\theta) \tag{3.23}$$

$$\zeta^*(z,\theta,0) = 4\pi^{-1/2} e^{-z^2} \sin(\theta) \tag{3.24}$$

$$\phi(z,0) = -\mathrm{erf}(z\sqrt{\mathrm{Pr}}) + 1 \tag{3.25}$$

3.4 The Numerical Solution

The solution of the obtained differential equations (3.18a-3.19c) is based on numerical integration using the Crank-Nicolson finite-difference scheme. At a typical time t, the functions (F_0, F_n, f_n) related to the stream function, the functions (G_0, G_n, g_n) related to the vorticity and the functions (H_0, H_n, h_n) related to the temperature can be obtained provided that all these functions are known at (t-Δt), where Δt is the time increment. All equations (3.18a-3.19c) are of the same form and we need only to present the solution methodology for a typical equation. We now consider equation (3.18c) as an example,

$$e^{2\xi}\frac{\partial G_n}{\partial t} = \frac{2}{Re}\left(\frac{\partial^2 G_n}{\partial \xi^2} - n^2 G_n\right) + nf_n\frac{\partial G_0}{\partial \xi} - ng_n\frac{\partial F_0}{\partial \xi} + S_{n2}$$

which can be rewritten as

$$\frac{\partial G_n}{\partial t} = q_n(\xi,t) \quad (n=1,2,...,N) \tag{3.26}$$

where
$$q_n = e^{-2\xi}\left\{\frac{2}{Re}\left(\frac{\partial^2 G_n}{\partial\xi^2} - n^2 G_n\right) + nf_n\frac{\partial G_o}{\partial\xi} - ng_n\frac{\partial F_o}{\partial\xi} + S_{n2}\right\}$$

The Crank-Nicolson finite-difference approximation of Eq. (3.26) results in

$$\frac{1}{\Delta t}\left[G_n(\xi,t) - G_n(\xi,t-\Delta t)\right] = \frac{1}{2}\left[q_n(\xi,t) + q_n(\xi,t-\Delta t)\right] \qquad (3.27)$$

Using central differences for all space derivatives in (3.27) and rearranging one obtains,

$$B(\xi,t)G_n(\xi,t) = A(\xi,t)G_n(\xi+\Delta\xi,t) + C(\xi,t)G_n(\xi-\Delta\xi,t)$$

$$+ D_n(\xi,t-\Delta t) + E_n(\xi,t) \qquad (3.28)$$

where $\Delta\xi$ is the step size, A, B, C, are identifiable functions of ξ and t that can be calculated at each mesh point, $D_n(\xi,t-\Delta t)$ is a completely known function and $E_n(\xi,t)$ is a function that depends on the solution at time t. Since the problem is solved numerically, the conditions at ∞ are applied at $\xi = \xi_m$ where ξ_m defines the distance away from the cylinder surface at which ζ and ϕ approximate the free stream values. Equation (3.28) when applied at every point in the range from $\xi = 0$ to $\xi = \xi_m$ will result in a set of algebraic equations that form a tri-diagonal system of equations which can be solved by TDMA (Tri-Diagonal Matrix Algorithm) [73] for each value of n between n=1 and N. The difficulty in solving this system of equations is that the term $E_n(\xi,t)$ is not completely defined, for it depends on the solutions at time t. To overcome this problem, an iterative technique is used in which the unknown functions $E_n(\xi,t)$ are assumed initially to be the same as $E_n(\xi,t-\Delta t)$ and then corrected according to the most recent available value until a convergence criterion is achieved. For any function, the condition for convergence is reached when the difference of the values obtained in two successive iterations is within a certain limit, i.e.

$$\left| G_n^{m+1}(\xi, t) - G_n^m(\xi, t) \right| \leq 10^{-5}$$

The values of functions $G_n(0,t)$ at the cylinder surface is updated through an iterative process by writing the integral condition defined in equation (3.21c) as a numerical quadrature formula which then relates the boundary value to values of the corresponding functions at internal points of the computational domain. In a similar manner, the functions $G_0(0,t)$, $g_n(0,t)$ are updated through the same iterative process. This gives the extra conditions needed to determine the boundary values for G_0, G_n and g_n (i.e. the boundary values for vorticity). The boundary values for equations (3.19a-3.19c) are known, and accordingly, no integral condition is needed.

The solution for equations (3.17b, 3.17c) is obtained using a step-by-step integration scheme. In this scheme, equations (3.17) are factorized as follows

$$\left(\frac{\partial}{\partial \xi} - n \right) \left(\frac{\partial}{\partial \xi} + n \right) F_n = R_n(\xi, t) \tag{3.29}$$

where

$$R_n(\xi, t) = e^{2\xi} G_n(\xi, t)$$

let

$$P_n = \frac{\partial F_n}{\partial \xi} - n F_n \tag{3.30}$$

and

$$Q_n = \frac{\partial F_n}{\partial \xi} + n F_n \tag{3.31}$$

The two functions satisfy the following differential equations

$$\frac{\partial P_n}{\partial \xi} + n P_n = R_n(\xi, t) \tag{3.32}$$

$$\frac{\partial Q_n}{\partial \xi} - n Q_n = R_n(\xi, t) \tag{3.33}$$

From (3.30), (3.31), one can deduce that

$$F_n = \frac{Q_n - P_n}{2n} \tag{3.34}$$

Equation (3.32) can now be integrated in the direction of increasing ξ using the following scheme

$$P_n(\xi + \Delta\xi, t) = \chi P_n(\xi, t) + \chi e^{-n\xi} \int_{\xi}^{\xi - h} e^{nx} R_n(y, t)\, dy \tag{3.35}$$

where

$$\chi = e^{-nh}, \quad h = \Delta\xi$$

and by using the trapezoidal rule in the interval ξ to $\xi + h$ and evaluating the integral in eqn. (3.35) one gets,

$$P_n(\xi + h, t) = \chi P_n(\xi, t) + \frac{1}{n^2 h}\{R_n(\xi, t)[1 - \chi - \chi nh] + R_n(\xi + h, t)[nh + \chi - 1]\} \tag{3.36}$$

Let us introduce the variable x, such that $x = \xi_m - \xi$, one can rewrite eq. (3.33) as

$$\frac{\partial Q_n}{\partial x} + n Q_n = -R_n(x, t) = Z_n(x, t)$$

This equation is similar to eq. (3.32) and can be integrated the same way to get

$$Q_n(x + h, t) = \chi Q_n(x, t) + \frac{1}{n^2 h}\{Z_n(x, t)[1 - \chi - \chi nh] + Z_n(x + h, t)[nh + \chi - 1]\} \tag{3.37}$$

At any given time t, by knowing the function $R_n(\xi, t)$, one can obtain a solution for P_n and Q_n using the step-by-step integration given by eqns.(3.36), (3.37), respectively. The needed boundary conditions for P_n and Q_n are

$$P_n(0, t) = 0 \quad \text{and} \quad Q_n(0, t) = 2e^{2\xi} \delta_{1,n}$$

The numerical procedure can be summarized as follows:

1. The known solution at time $(t - \Delta t)$ is used as an initial solution. The tri-diagonal system of equations resulting from equation (3.28) is solved by TDMA using the most recent

available information of the function E_n to obtain solution for functions G_0, G_n, g_n, H_0, H_n and h_n, ($n=1,2,...N$) at time t.

2. The integral conditions (3.21) is used to obtain a better approximation for $G_0(0,t)$, $G_n(0,t)$ and $g_n(0,t)$.

3. Equation (3.17a) is solved using direct numerical integration to obtain $F_0(\xi,t)$.

4. Equations (3.17b) and (3.17c) are solved using step-by-step integration to obtain $F_n(\xi,t)$ and $f_n(\xi,t)$.

5. Steps 1,2,3 and 4 are repeated until convergence is reached.

6. The time is increased by Δt and steps 1,2,3,4 and 5 are repeated.

7. The solution continues until the required time is reached.

The program flow chart is shown in Figure 3.2

The number of points in the ξ direction used is 120 with a grid size taken as 0.1. This sets the outer boundary at a physical distance of approximately 20,000 times the radius of the cylinder. Such large distance is necessary to ensure that the conditions at infinity are appropriately incorporated in the numerical solution. However, the grid size is reduced to 0.05 for high Reynolds cases. This is due to steep variation of velocity and temperature within the thin boundary-layer in these cases. Following the start of fluid motion, very small time steps are used since the time variation of vorticity and temperature is quite fast. As time increases, the time step is gradually increased. For the sake of stability, smaller time steps are used for high Reynolds numbers and high forcing frequencies. Typical time steps used are $\Delta t=0.001$ for first 10 steps followed by $\Delta t=0.01$ for next 10 steps and then followed by $\Delta t=0.05$ for the rest of the solution. The number of terms in the series starts with only 2

and one more term is added when the last term exceeds 10^{-4}. The maximum number of terms increases with the increase of Reynolds number, dimensionless forcing frequency or the amplitude of oscillation. The maximum number of terms reached in all cases considered in this work is 40.

3.5 Local and Average Nusselt Numbers

The local and average Nusselt numbers are defined as

$$Nu = \frac{h\,d}{k}, \quad \overline{Nu} = \frac{\bar{h}\,d}{k} \tag{3.36}$$

where, h and $\bar{h}$ are the local and average heat transfer coefficients and are defined as

$$h = \frac{q'}{T_w - T_\infty} \quad \text{and} \quad \bar{h} = \frac{1}{2\pi}\int_0^{2\pi} h\,d\theta \tag{3.37}$$

where q' is the heat transfer rate given by:

$$q' = -k\frac{\partial T}{\partial r'}\Big|_{r'=c} \tag{3.38}$$

From the above definitions one can deduce

$$Nu = -2\left(\frac{\partial\phi}{\partial\xi}\right)_{\xi=0} = -\left[\frac{\partial H_0}{\partial\xi} + 2\sum_{n=1}^{N}\left(\frac{\partial h_n}{\partial\xi}\sin(n\theta) + \frac{\partial H_n}{\partial\xi}\cos(n\theta)\right)\right]_{\xi=0} \tag{3.39}$$

and

$$\overline{Nu} = \left(\frac{\partial H_0}{\partial\xi}\right)_{\xi=0} \tag{3.40}$$

The time-averaged Nusselt number is obtained from

$$\overline{\overline{Nu}} = \frac{1}{t_2 - t_1}\int_{t_1}^{t_2} \overline{Nu}\,dt \tag{3.41}$$

where, the time period between t_1 and t_2 is taken after reaching the quasi-steady state, covering more than one cycle.

START

$$G_n, g_n, F_n, f_n, H_n \text{ And } h_n$$

At Time t-Δt Functions
$G_n,g_n,F_n,f_n,,H_n$ And h_n
Are Known
(n=0,1,2, ,N)

$G_n,\ g_n(\xi,t)=G_n,g_n(\xi,t-\Delta t)$
$F_n,\ f_n(\xi,t)=F_n,f_n(\xi,t-\Delta t)$
$H_n,\ h_n(\xi,t)=H_n,h_n(\xi,t-\Delta t)$
for all n=0,1,2 N

Solve For All
Functions (ξ,t)
For all n=0,1,,,N

TDMA

Apply Integral Conditions
To Get $G_n,\ g_n$ (0,t)
For all n=0,1,,,N

$t=t+\Delta t$
$G_n,\ g_n(\xi,t-\Delta t)=G_n,g_n(\xi,t)$
$F_n,\ f_n(\xi,t-\Delta t)=F_n,f_n(\xi,t)$
$H_n,\ h_n(\xi,t-\Delta t)=H_n,h_n(\xi,t)$
For All n=0,1,2 N

Check Convergence of
All Functions

NO

YES

Final Time

NO

YES

Stop

Figure 3.2 The Computational Flowchart

3.6 Pressure Distribution Over the Cylinder Surface

In order to examine the pressure distribution on the cylinder surface, let us introduce the dimensionless pressure P^* defined as:

$$p_\theta^* = 2 \, (P_\theta - P_\pi) / \rho V^2,$$

Applying the angular component of momentum equation on the cylinder surface, one gets

$$\frac{\partial P_\theta^*}{\partial \theta} = -2 \frac{\partial U_w}{\partial t} - \frac{4}{Re} \left(\frac{\partial \zeta}{\partial \xi} \right)_{\xi=0} \tag{3.42}$$

Integrating the above expression w.r.t. θ starting from $\theta = \pi$ to any angle θ on the cylinder surface, the pressure distribution is found to be

$$P_\theta^* = (\pi - \theta) \left[\frac{2}{Re} \frac{\partial G_0}{\partial \xi} \Big|_{\xi=0} + 2 \frac{\partial U_w}{\partial t} \right]$$

$$- \frac{4}{Re} \left[\sum_{n=1}^{N} \frac{\sin n\theta}{n} \frac{\partial G_n}{\partial \xi} \Big|_{\xi=0} - \frac{\cos n\theta - \cos n\pi}{n} \frac{\partial g_n}{\partial \xi} \Big|_{\xi=0} \right] \tag{3.43}$$

The periodicity of surface pressure P_θ^* requires that

$$\frac{2}{Re} \frac{\partial G_0}{\partial \xi} \Big|_{\xi=0} + 2 \frac{\partial U_w}{\partial t} = 0$$

which may be written as :

$$G_0'(0,t) = -Re \frac{\partial U_w}{\partial t} \tag{3.44}$$

Closely following the line of reasoning of Badr and Dennis [55] for the problem of steady rotating cylinder in a uniform stream, it can be shown that the condition (3.44) is implicitly satisfied by the integral condition given in (3.21a). For steady rotating cylinder the needed condition for the periodicity of pressure as deduced by Badr [55] was $G_0'(0,t) = 0$. This condition comes as byproduct of Eq. (3.44) when U_w=const. Moreover, Eq. (3.44) is taken as a further check for numerical convergence.

3.7 The Lift and Drag Coefficients

The drag and lift coefficients are defined by

$$C_D = 2D / \rho V^2, \quad C_L = 2L / \rho V^2$$

where D, L are the drag and lift forces exerted on a unit length of the cylinder surface. These two forces are mainly due to pressure and viscous shear forces acting on the surface. The ones due to pressure are

$$D_P = -\int_0^{2\pi} P_\theta \cos(\theta) \, c \, d\theta, \qquad L_P = -\int_0^{2\pi} P_\theta \sin(\theta) \, c \, d\theta$$

and the others due to viscous shear are

$$D_F = -\int_0^{2\pi} \tau'_w \sin(\theta) \, c \, d\theta, \qquad L_F = \int_0^{2\pi} \tau'_w \cos(\theta) \, c \, d\theta$$

where P_θ and τ'_w are the wall pressure and wall shear stress respectively. Normalizing these forces by $\rho V^2/2$ the pressure drag/lift and viscous drag/lift coefficients are then

$$C_{DP} = -\frac{1}{2}\int_0^{2\pi} P_\theta^\bullet \cos\theta \, d\theta, \qquad C_{DF} = \frac{2}{Re}\int_0^{2\pi} (\zeta_w + 2U_w) \sin\theta \, d\theta \qquad (3.45)$$

$$C_{LP} = -\frac{1}{2}\int_0^{2\pi} P_\theta^\bullet \sin\theta \, d\theta, \qquad C_{LF} = -\frac{2}{Re}\int_0^{2\pi} (\zeta_w + 2U_w) \cos\theta \, d\theta \qquad (3.46)$$

where $P_\theta^\bullet$, ζ_w and U_w are the dimensionless wall pressure, vorticity and velocity respectively. The drag and lift coefficients are then

$$C_D = C_{DP} + C_{DF}, \quad C_L = C_{LP} + C_{LF} \qquad (3.47)$$

In terms of Fourier coefficients the drag and lift coefficients are found to be

$$C_D = \frac{2\pi}{Re}\left\{ g_1(0,t) - \left(\frac{\partial g_1}{\partial \xi}\right)_{\xi=0} \right\} \qquad (3.48)$$

$$C_L = -\frac{2\pi}{Re}\left\{ G_1(0,t) - \left(\frac{\partial G_1}{\partial \xi}\right)_{\xi=0} \right\} \qquad (3.49)$$

The time-averaged drag coefficient is obtained from

$$\overline{C_D} = \frac{1}{t_2 - t_1} \int_{t_1}^{t_2} C_D \, dt \qquad (3.50)$$

where, the time period between t_1 and t_2 is taken after reaching the quasi-steady state and covering more than one cycle.
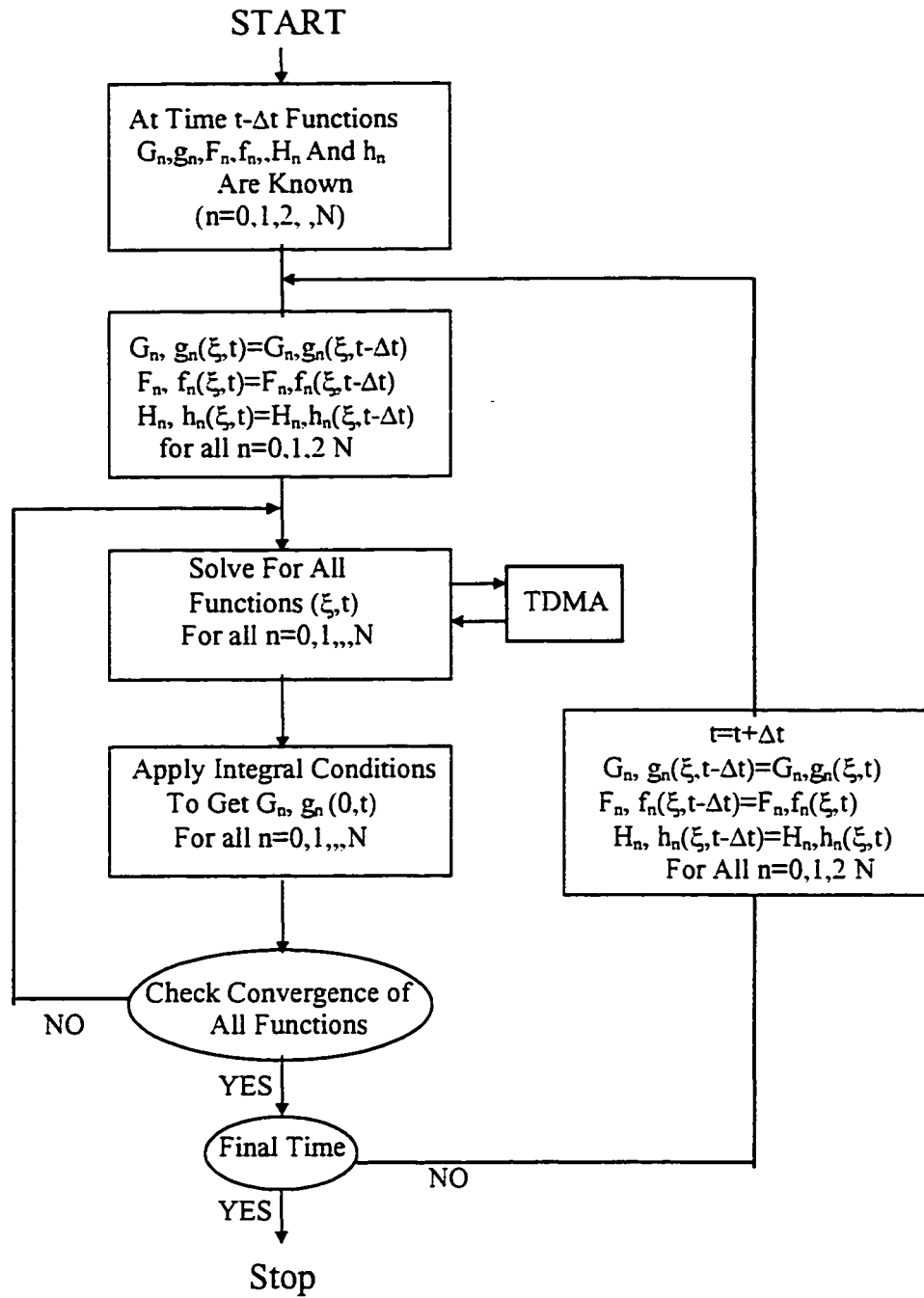
3.8 Verification of the Method of Solution

The accuracy of the mathematical model as well as computational scheme are assessed by solving a number of problems for which theoretical or experimental results are available for comparison. Although the method of solution has been tested extensively by Badr [55] and proved to be highly accurate, further checks on the consistency with the previous experimental and numerical studies are considered. The problem of initial flows over fixed and rotating cylinders starting their motion impulsively from rest are first considered. The present prediction for the initial flow over a fixed cylinder at Reynolds number (Re = 3000, t = 3), in the form of streamline pattern, is shown in Figure 3.3. The pattern compares very well with the corresponding experimental and theoretical patterns obtained by Ta Phuoc Loc and Bouard [56]. A pair of secondary vortices generated at the cylinder surface at such moderate Reynolds number is accurately predicted. Figure 3.4 shows a good agreement between the velocity distribution along line (θ=0) predicted by Ta Phuoc Loc [57] and the corresponding distribution predicted by the present method. On the other hand, the present predictions for the initial flow development over rotating cylinder are compared with that obtained from the pioneer experimental study of Coutanceau M. and Menard [58]. The comparison is carried out for two speed ratios (rotating speed/free stream velocity)

$\alpha = 1/2$, $\alpha = 1$ at Re=200. The velocity components along line (θ=0) compare quantitatively well with the experimental ones as shown in Figures 3.5 and 3.6. Based on the above comparisons one can conclude that the present predictions for the flow field are accurate. Further comparisons for both flow and thermal fields are presented in the following section.

3.9 Results and Discussion

3.9.1 Stationary Cylinder in a Cross Stream

Observation as well as numerical predictions have shown that the Reynolds number is a dominant parameter governing the flow and heat transfer characteristics. In the case of flow past a stationary cylinder, at Reynolds numbers higher than about 40, alternating vortices are shed periodically forming the well known Karman vortex street. The vortex shedding process causes unsteady flow behavior close to the cylinder surface and thus affects both flow and thermal fields. In order to investigate these effects, the vortex shedding from a stationary cylinder is examined at three Reynolds numbers (Re=80, 100, 200). In the numerical scheme, the vortex shedding process is triggered by rotationally oscillating the cylinder only for one complete cycle (at t=40) and fixing it afterwards. The Karman vortex street is developed with vortices being shed alternately from the upper and lower surfaces of the cylinder. The frequency of vortex shedding is computed from either the periodic variation of the velocity at any point in the wake or the time variation of the induced oscillating lift force [72]. The dimensionless frequency of vortex shedding is generally expressed as the natural Strouhal number, $S_o = f_o d/V$, where f_o is the vortex shedding

frequency. The Fourier analysis for the lift record or the velocity record gives almost the same value for Strouhal number as shown in Figure 3.7. The predicted values of Strouhal number as a function of Reynolds number together with the experimental values reported by Roshko [70] are displayed in Table 3.1 and a good agreement is observed.

Figures 3.8-3.10 show contour plots of streamlines, equi-vorticity lines and isotherms during one complete cycle of vortex shedding at Re=100. The streamline contour plots clearly monitor the time development of vortices and their convection in the wake. Because of vortex shedding, the equi-vorticity and isotherms contours are no longer symmetrical. It can be seen that the equi-vorticity contours and also isotherm contours are very close near the cylinder surface and far apart away from it which indicate large vorticity and temperature gradients near the surface and small gradients far away.

Figures 3.11a and b show the time variation of the average Nusselt number, $\overline{Nu}$, drag coefficient, C_D, and lift coefficient, C_L, at Re=100 and 200 respectively. While the lift coefficient is shown to oscillate with the same vortex shedding frequency, the drag coefficient and Nusselt numbers oscillate at twice that frequency. The temporary overshoot in drag and Nusselt number at Re=200 is due to the transition effect of vortex shedding triggering mechanism. The amplitude of lift, fluctuating drag and Nusselt number increase with increasing Reynolds number. The time averaged drag coefficient and Nusselt Number in cases of vortex shedding reveal appreciable increase in comparison with that of steady flow (assuming no vortex shedding). This increase in $\overline{C_D}$ reaches about 130% at Re=100 and 52% at Re=200, whereas, the increase in $\overline{\overline{Nu}}$ reaches about 20% at Re=100, 9% at

Re=200. This fact leads to suppose that the symmetrical case is not a realistic description of the flow but rather a mathematical concept especially at Reynolds numbers exceeding 40. The values of the time-averaged drag coefficient at different Reynolds number are compared with previous works displayed in Table 3.2 which shows a good agreement. The present predictions for the time-averaged Nusselt number are displayed also in Table 3.2 along with the previous studies [52, 63-68]. These previous studies give quite dispersed values for the average Nusselt number. The table shows that for any Reynolds number, the present results lie approximately in the middle of the range of the dispersed results.

Shown in Figure 3.12 is the variation of the local Nusselt number distribution over the cylinder surface during one complete cycle of vortex shedding at Re=100. At all times, the maximum heat transfer rate is found near the front stagnation point $\theta = 180^{\circ}$. However, due to vortex shedding, the local heat transfer on the rear side of the cylinder improves, showing another local peak near $\theta = 360^{\circ}$. This local improvement in heat transfer increases the average heat transfer rate in comparison with the no vortex shedding solution. It can be also seen that the local Nusselt number distributions during one complete cycle are almost unchanged over most of the cylinder surface except on the rear part where slight differences are found as a result of periodic shedding of vortices. The local Nusselt number distributions at the beginning, $t=t_o$, and at the end of the cycle, $t=t_o+T$, (T=12.5 is time period of vortex shedding at Re=100), confirms the cyclic behavior of the thermal field. This cyclic behavior comes as a result of cyclic behavior of flow field. This fact is confirmed further in the variation of surface vorticity distribution over a complete cycle of vortex shedding shown in Figure 3.13.

Table 3.1 The Predicted Strouhal number and its variation with Reynolds number together with a comparison with Roshko [70]

Re	Strouhal number, S_o	
	Present study	Roshko [70]
80	0.156	0.155
100	0.16	0.165
200	0.18	0.18-0.2

Table 3.2 The Predicted average drag coefficient and Nusselt number at different Reynolds numbers and comparison with previous studies for the case of fixed cylinder

Re	$\overline{CD}$			$\overline{\overline{Nu}}$		
	Present study	Ref.[69]	Ref.[52]	Present study	Ref. [52]	Range of Results Refs. [63-68]
80	1.56	1.4	1.33	4.80	4.8	4.59-4.95
100	1.55	1.38	1.32	5.31	5.25	4.769-5.52
200	1.21	1.32	1.31	6.99	7.8	6.67-7.63

a)

b)

c)
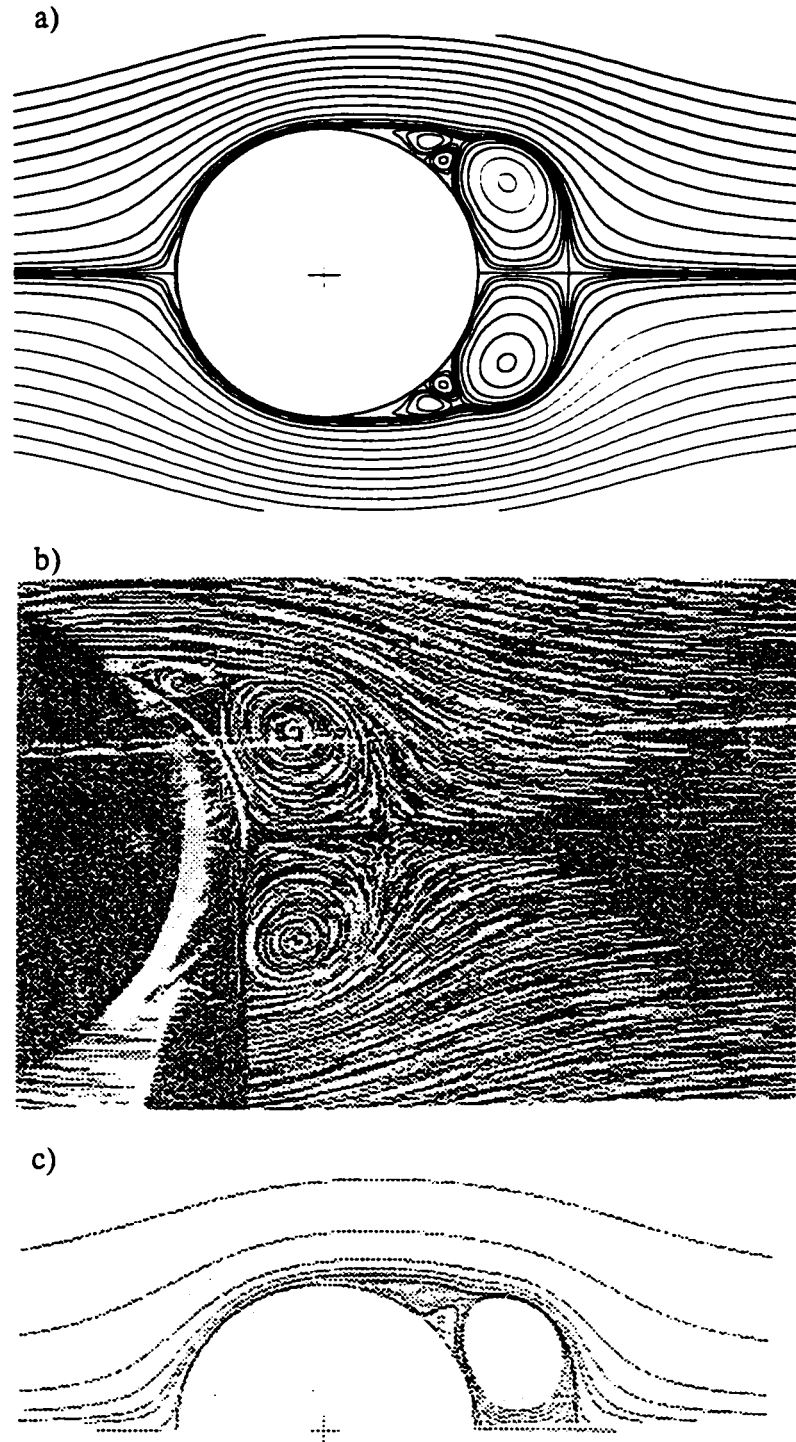
Figure 2. The streamline pattern for impulsively started flow over a fixed cylinder for the case of Re=3000 at t=3 and comparison with previous results; a) present study, b) experimental and c) theoretical results obtained by Ta phuoc Loc and Bouard [56].
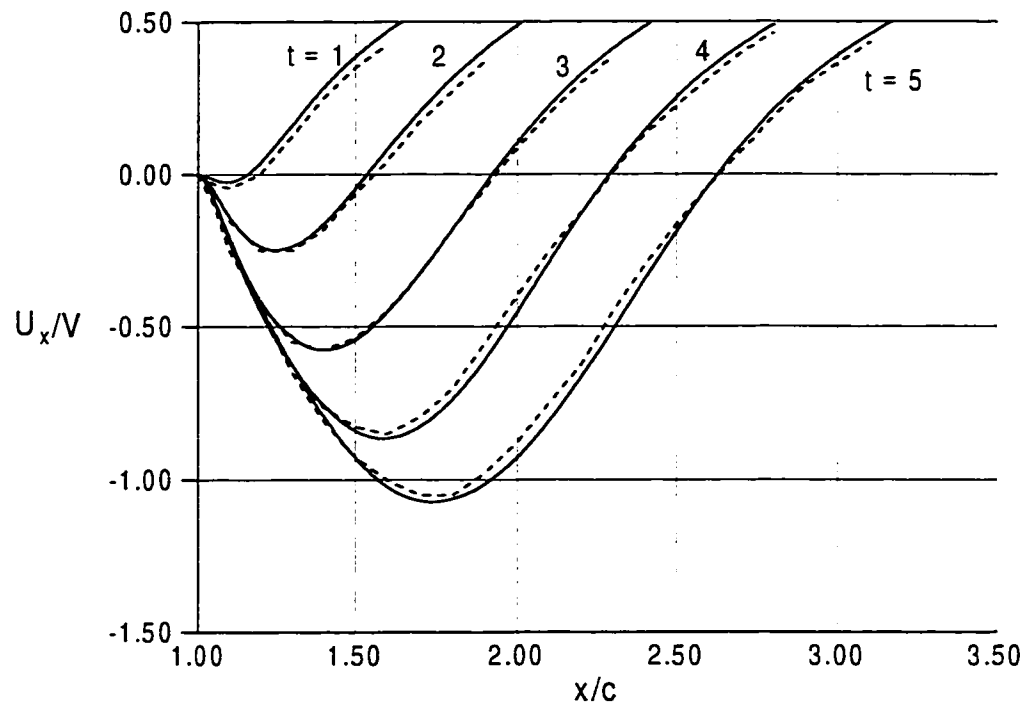
Figure 3.4. The time development of the x-component of velocity on $\theta = 0$ at Re=550 ;—— Present results; ----- numerical results of Ta Phuoc Loc [56]
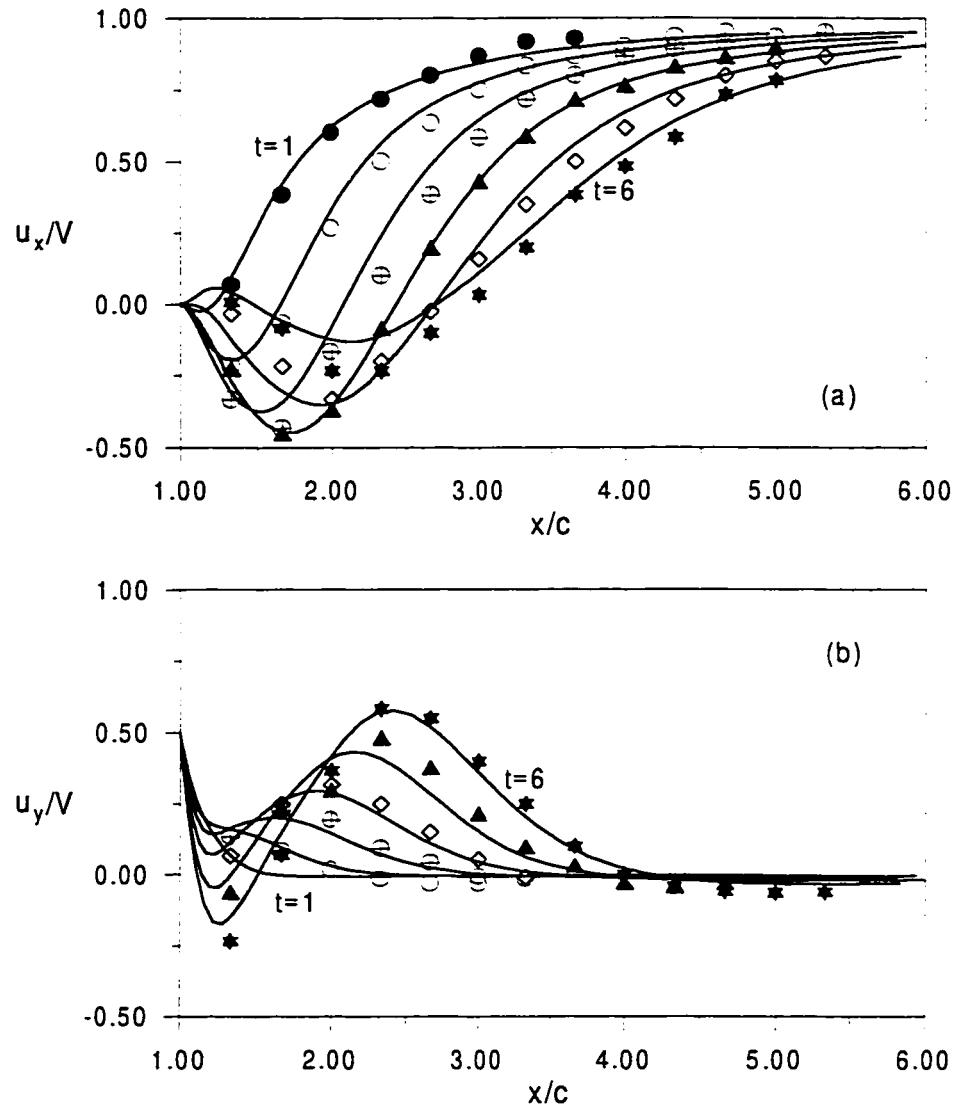
Figure 3.5 Time development of velocity components along x-axis and comparison with experimental results of [58] at Re=200 and $\alpha=1/2$.
Experimental values : • t = 1; o t = 2; ⊕ t = 3; ▲ t = 4; ◇ t = 5; ★ t = 6
———— Theoretical curves   (a) x-component   (b) y-component
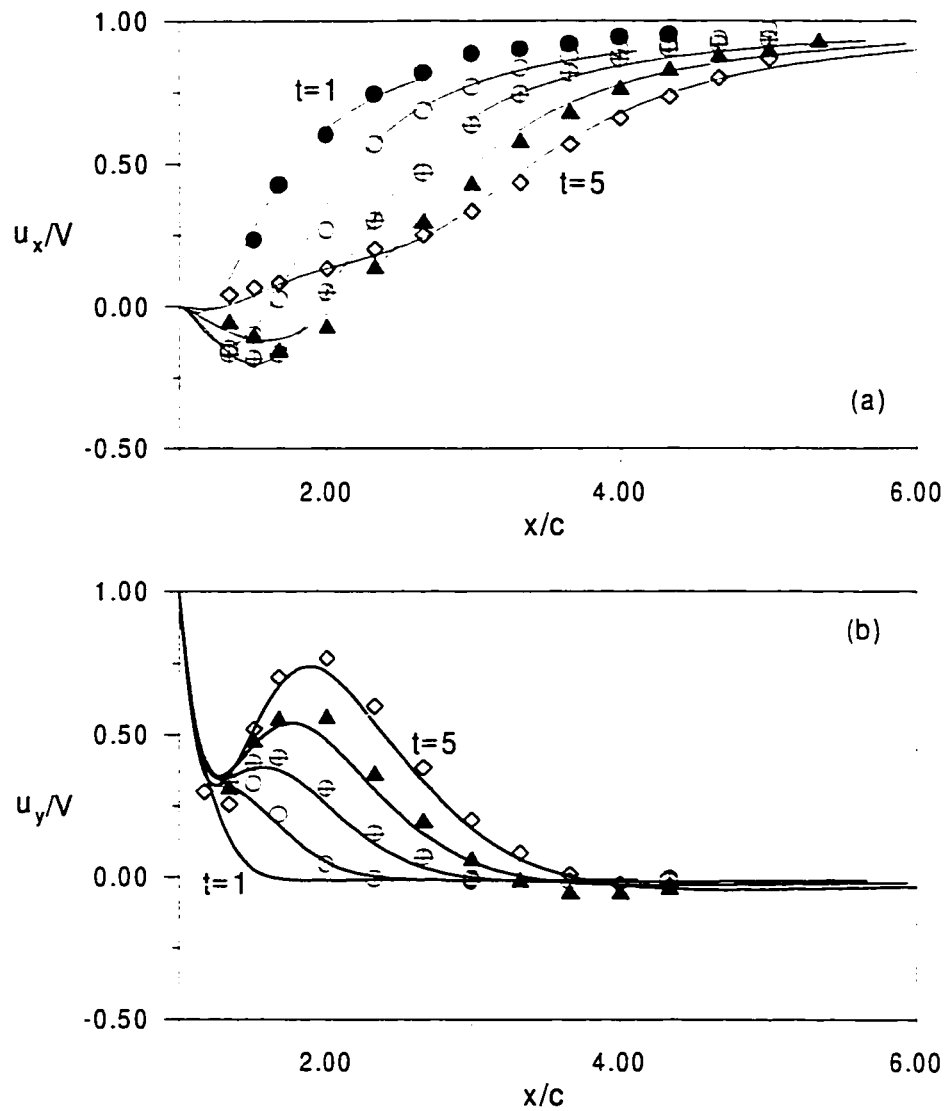
Figure 3.6 Time development of velocity components along x-axis and comparison with experimental results of [58] at Re=200 and α=1. Experimental values : • t = 1; o t = 2; ⊕ t = 3; ▲ t = 4; ◊ t = 5. ——— Theoretical curves (a) x-component (b) y-component
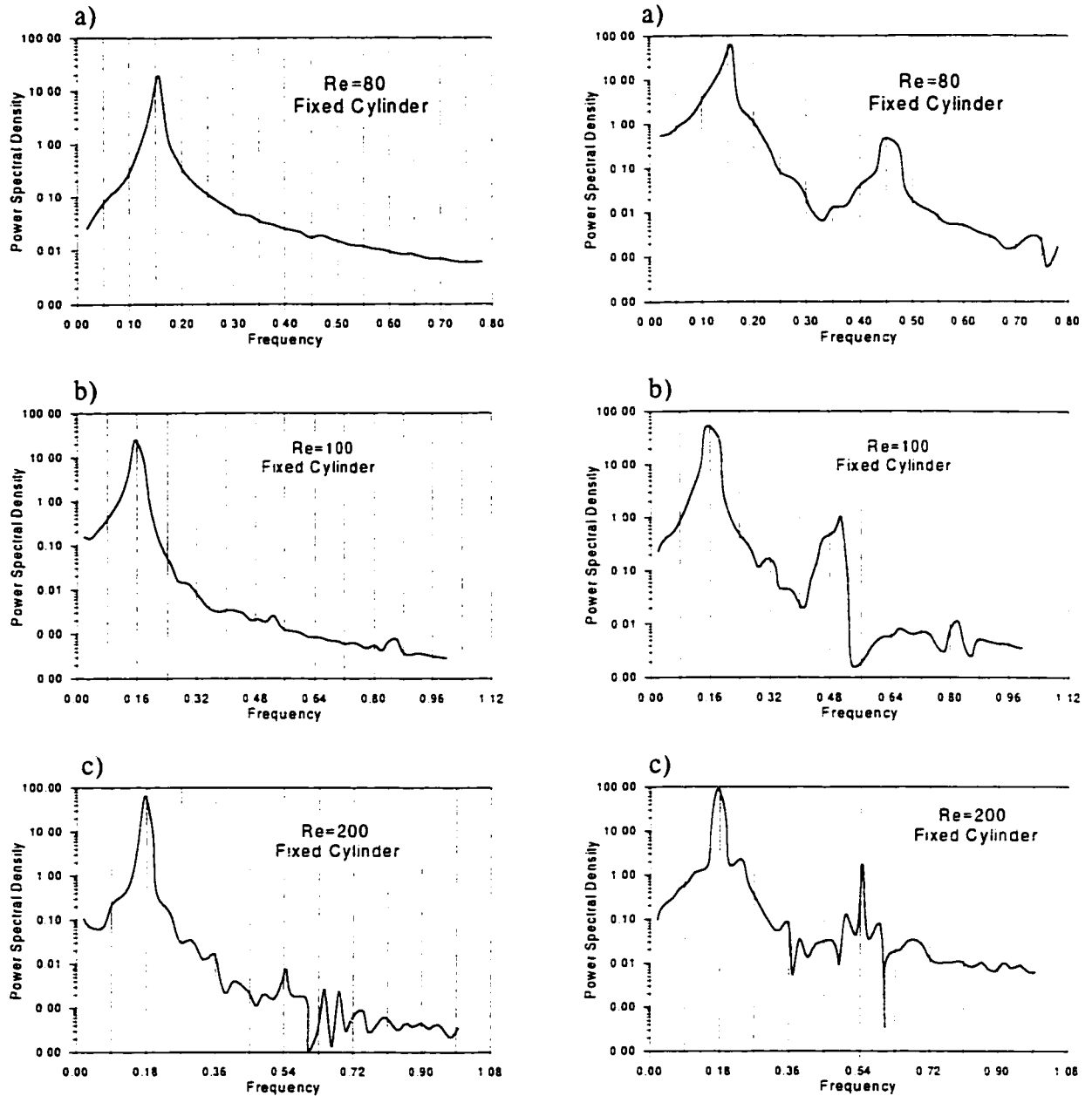
Figure 3.7 Fourier anaysis of lift records (left) and records of velocity in the wake (right) for the case of fixed cylinder. a)Re=80 b)Re=100 c)Re=200
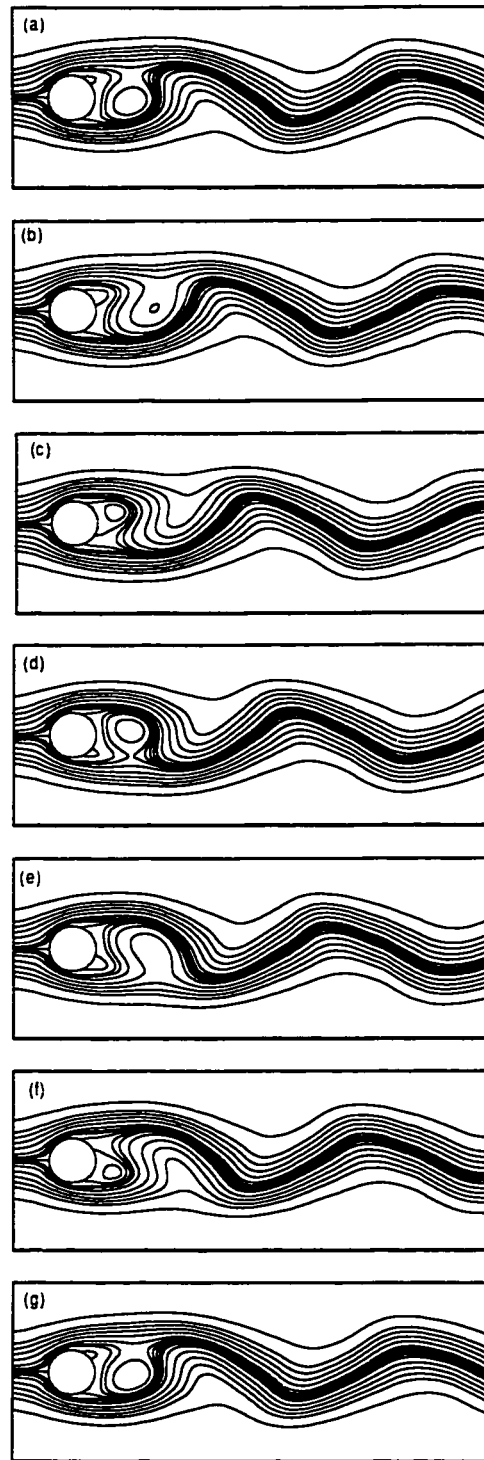
Figure 3.8 (a-g). Streamline patterns for flow over fixed cylinder at Re=100
a) t=t$_o$, b)t=t$_o$+2, c)t=t$_o$+4   d)t=t$_o$+6 e)t=t$_o$+8, f)t=t$_o$+10, and g)t =t$_o$+T
where T=12.5 is the time period of shedding cycle
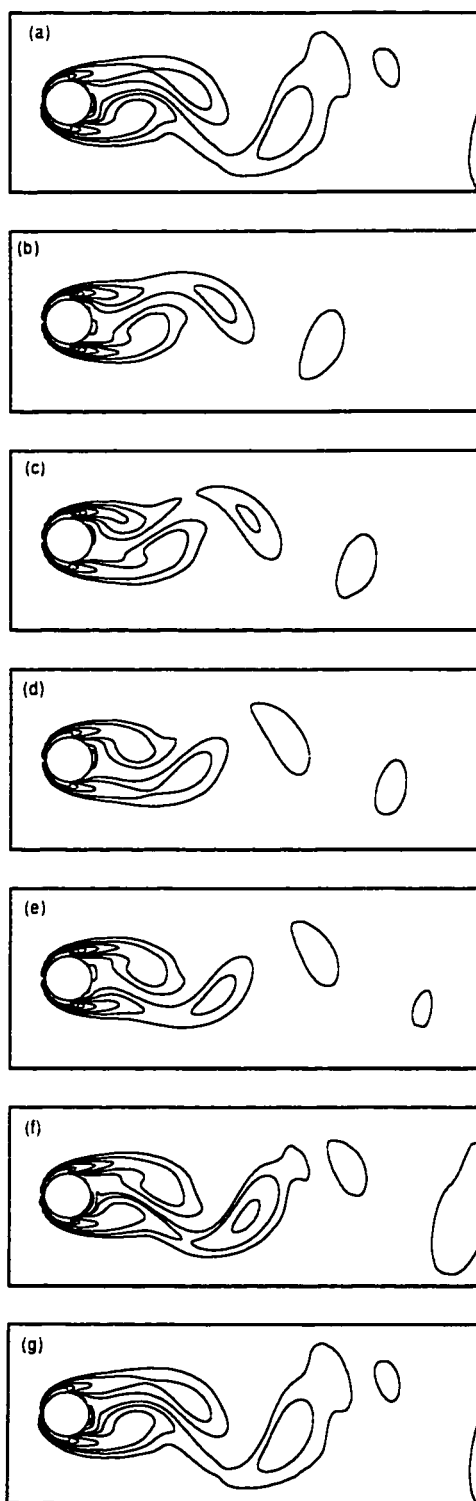
Figure 3.9 (a-g). Vortex patterns for flow over fixed cylinder at Re=100
a) t=t$_o$, b)t=t$_o$+2, c)t=t$_o$+4 d)t=t$_o$+6 e)t=t$_o$+8, f)t=t$_o$+10, and g)t =t$_o$+T
where T=12.5 is the time period of shedding cycle
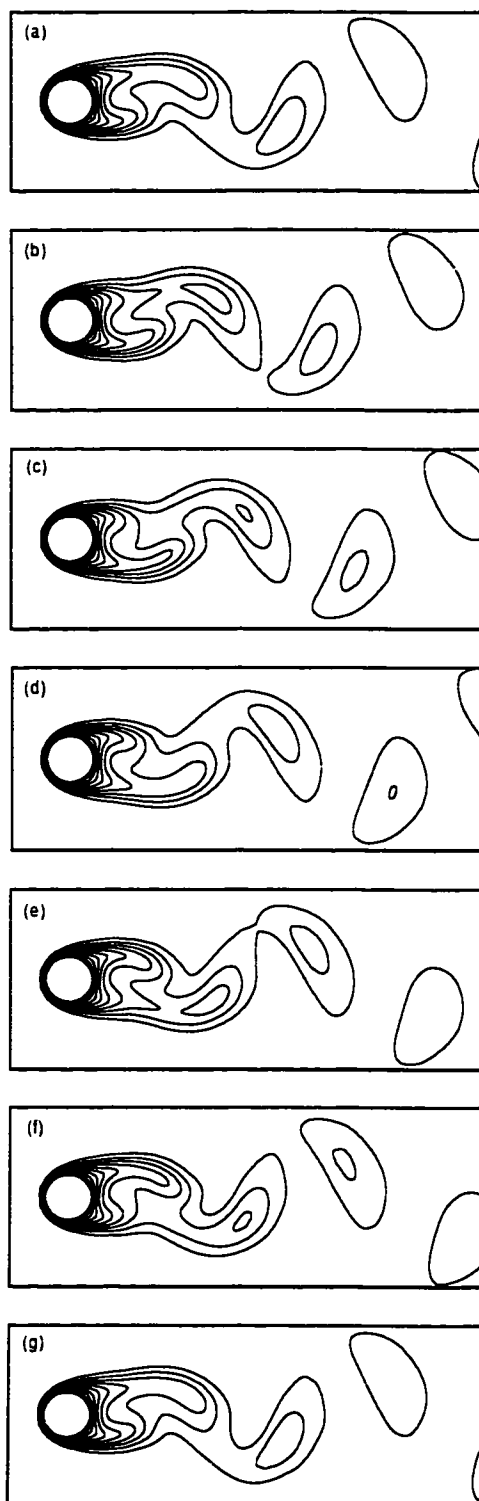
Figure 3.10 (a-g). Isotherms patterns for flow over fixed cylinder at Re=100
a) t=t_o, b)t=t_o+2, c)t=t_o+4 d)t=t_o+6 e)t=t_o+8, f)t=t_o+10, and g)t =t_o+T
where T=12.5 is the time period of shedding cycle

a)

b)
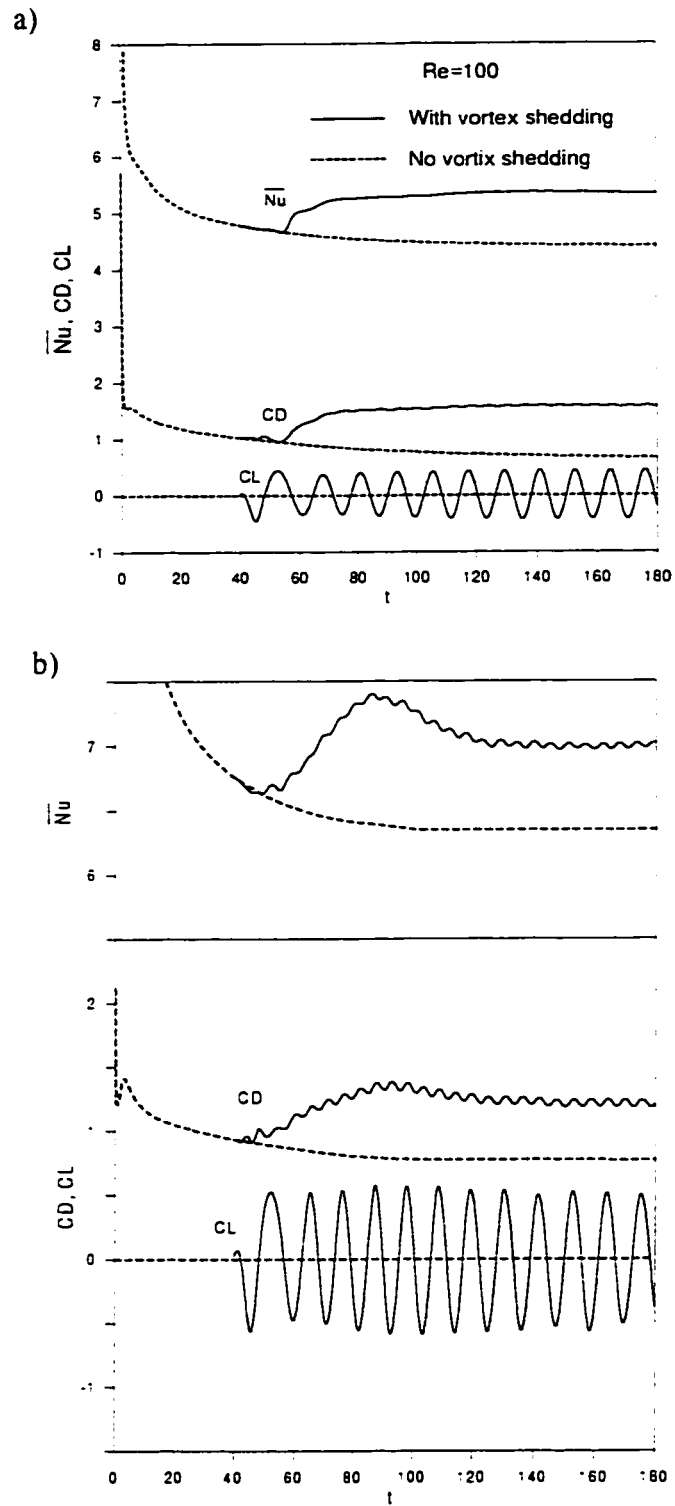
Figure 3.11 Time development of average Nusselt number, drag coefficient and lift coefficient with and without vortex shedding.
---- No vortex shedding _____ Vortex shedding
a) Re = 100   b) Re = 200
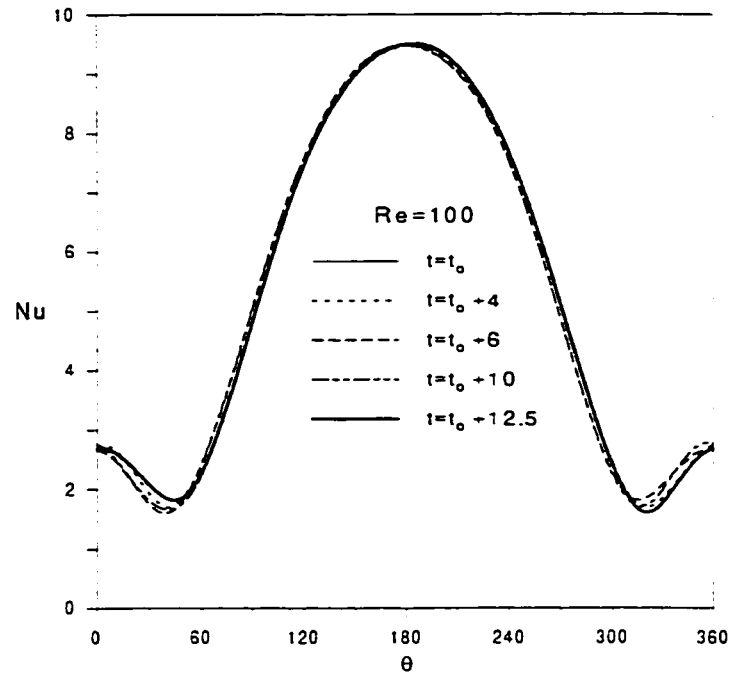
Figure 3.12 Local Nusselt number distribution during a complete cycle of vortex shedding at Re=100
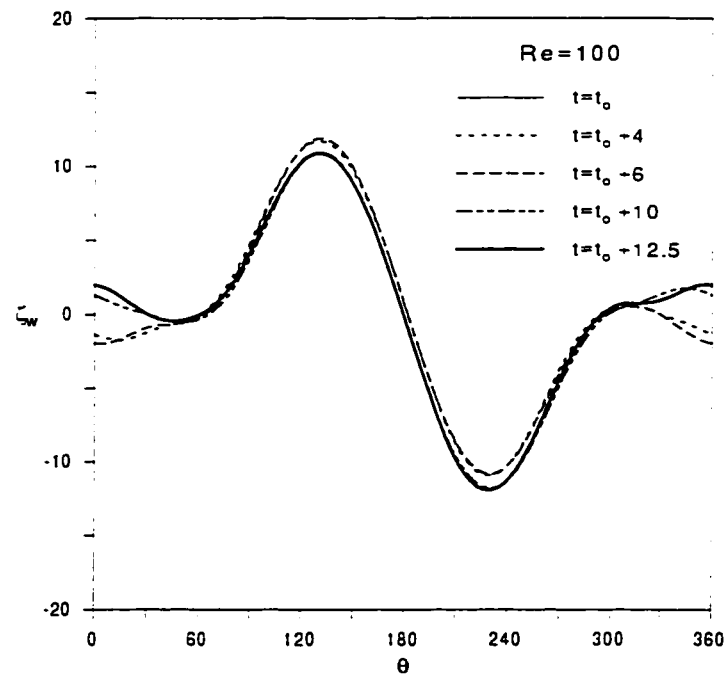
Figure 3.13 Surface vorticity distribution during a complete cycle of vortex shedding at Re=100

3.9.2 Rotationally Oscillating Cylinder in a Cross Stream

We now consider the problem of fluid flow and heat transfer in the neighborhood of a cylinder performing rotational oscillation while placed in a cross stream. Assuming negligible buoyancy forces, the velocity and thermal fields are dominated by the Reynolds number (based on the free stream velocity) and the amplitude and frequency of oscillation. In order to study the effect of rotational oscillation on flow and thermal fields, a number of cases are considered in the range of Reynolds number, Re, up to 200 , oscillation amplitude, Θ_A, up to π and dimensionless oscillation frequency S, up to $3S_o$ (i.e. up to $F_R=3$) where, S_o, is the natural Strouhal number. The Prandtl number is kept constant at 0.7.

The flow field in the wake of the oscillating cylinder is characterized by periodic shedding of vortices. Based on the frequency of vortex shedding, and similar to the previous studies [59-61] made on cylinders performing transverse oscillations in a cross stream, the present preliminary results have shown two distinct regimes. The first, called unlock-on regime, is characterized by periodic shedding of vortices at natural frequency irrespective of the oscillation frequency. Such a regime occurs when the driving cylinder frequency, f, is either smaller enough or larger enough than the natural frequency, f_o. When the oscillation frequency f approaches f_o, the second regime, called lock-on regime, occurs. In such a regime, the vortices are shed at the forced frequency, i.e the vortex shedding is synchronized with the cylinder oscillation. This synchronized or lock-on regime is found to occur within a band of frequency that brackets the natural frequency. This band of frequency is termed as the range of synchronization or the lock-on frequency range.

Since the flow field characteristics near the cylinder may differ from that far away, two new terms are being used in the discussion. These are the near wake response and far wake response. The first describes the unsteadiness in the immediate vicinity of the cylinder while the second describes it far down stream (at a distance of about r=10 and θ =0). The near wake response is depicted from lift record [72] whereas the far wake response is computed from the time variation of the tangential velocity component at a typical point (r=10, θ=0)

3.9.2.1 The Unlock-on Regime

Figures 3.14 and 3.15 show the time variations of drag and lift coefficients for the case of Re=200 when the forcing frequency is below the natural frequency (Figure 3.14) or above the natural frequency (Figure 3.15). The figures show that the amplitude of forces are not always constants, but rather change with nearly periodic beating wave forms. These beating wave forms were also found in the works of [1, 59] for the case of transverse oscillation and attributed to the combined effect of natural and forced oscillations. The beating wave form in lift forces is produced by the addition of two effects, one is due to fluctuations at natural frequency and the other is due to fluctuations at forced frequency. Figures 3.14 and 3.15 show roughly that the frequency of C_L is the same as the natural frequency of vortex shedding although the forcing frequencies in the two cases are quite different. The Fourier analysis of the far wake for the two cases is shown in Figures 3.16a and b. The figures clearly show that the far wake response is dominated by natural frequency.

Shown in Figure 3.17 is the time variation of the average Nusselt number, $\overline{Nu}$, at different frequencies below and above the range of synchronization. The figure shows that, $\overline{Nu}$ has its maximum value in the initial time stages. This is due to domination of conduction mode

of heat transfer. With the increase of time, the thermal boundary-layer thickness increases and so $\overline{Nu}$ decreases until a quasi-steady variation is reached at large time. It can be seen that $\overline{Nu}$ fluctuates with variant amplitude and in a beating wave form. Based on the obtained results, there is no appreciable enhancement in heat transfer for frequencies outside the range of synchronization. This may be attributed to the fact that the rate of vortex shedding is the same as that for a fixed cylinder. However, some enhancement, (reaching about 8.7%) occurs in some cases due to the disturbances generated by the cylinder motion especially at low amplitude, high frequency oscillation.

Typical streamline, equi-vorticity and isotherm plots for an unlock-on regime are shown in Figures 3.18-3.20 for the case of F_R=0.5, Re=200 and $\Theta_A = \pi / 4$. These are prepared at almost equal intervals through one complete cycle of oscillation. The streamline contour plots shown in Figure 3.18 provide the details of the flow field structure and its time variation during one cycle. One can see that two opposite vortices are alternately shed from the upper and lower surfaces of the cylinder per half cycle of oscillation resulting in vortex shedding frequency equal to the natural one. Unlike the case of a fixed cylinder in which the shedding vortices are all equal in size, the vortices generated in the oscillating cylinder case are of two different sizes shedding alternately from the upper and lower sides as shown in Figure 3.18. This explains the beating wave form in the lift force record for the same case (Figure 3.14). A higher peak occurs when the big vortex shed away and a smaller one occurs for the small vortex. However, one can see from Figures 3.18 and 3.19 that the far wake vortex street is similar to the familiar Karman street developed from a stationary cylinder. Figure 3.20 shows the time variation of the isotherms for the same case. The

figure shows that the thermal boundary layer is very thin near the forward stagnation point ($\Theta \sim 180°$), and extends in the wake forming an oscillating wake-shaped thermal layer. The isotherms are, in general, similar to those in the case of a fixed cylinder under vortex shedding(see Figure 3.10). Close inspection of isotherms plots and vortex patterns plots (Figure 3.19) for the same case shows the considerable resemblance between the thermal and flow fields. This resemblance illustrates the strong link between, convection and diffusion of heat and convection and diffusion of vorticity.

Figures 3.21-3.23 show the distribution of local Nusselt number, surface vorticity and surface pressure at equal time intervals in the aforementioned cycle of oscillation. Figure 3.21 shows the Nu distribution at different times during the same cycle. Although the maximum and minimum Nu values are almost the same at all times, the location clearly changes. The wake region is characterized by considerable variation of Nu as shown in the figure. The Nu distribution varies almost periodically as the cylinder oscillation. This periodic behavior is confirmed also in the distributions of surface vorticity and pressure shown in Figures 3.22 and 3.23.

Another typical streamline, equi-vorticity and isotherm contour plots at a frequency above the range of synchronization at Re=200, $\Theta_A = \pi / 8$ and $F_R = 2$, are shown in Figures 3.24-3.26. It can be seen that both flow and thermal fields at the time $t_a = 40$ are similar to those at the end of two cycles of oscillation $t_e = 51.1$, where the time period $t_e - t_a = 11.1$ covers one complete cycle of vortex shedding. Again, this makes the vortex shedding frequency equal to the natural one (with no oscillation). Two alternating non similar opposite vortices are shed from upper and lower surfaces per two cycles of oscillation. Not only the shape and

size of the two vortices are different but also the duration of their growth and detachment. Figure 3.24 shows that the vortex generated at the upper surface takes more time to develop and detach than that generated at the lower surface. One can also see that both flow and thermal fields in the near wake are affected by the cylinder oscillation. That is the longitudinal spacing of vortices is smaller than that of stationary cylinder. However, the vortices tend to form a pattern similar to that of Karman street in the far wake. The Fourier analysis of the far wake shows that oscillations occur at the natural frequency.

The distribution of local Nusselt number, surface vorticity and surface pressure at equal time intervals in the aforementioned cycle are shown in Figures 3.27-3.29. It can be seen that the Nu distributions for this case are similar on most of the cylinder surface except the rear region where remarkable deviation may be observed as a result of vortex shedding. The figure also shows that the maximum values are almost the same whereas there is a deviation in the minimum values. The interesting note in Figures 3.27-3.29 is that both flow and thermal fields attain their nearly periodic behavior at the natural shedding frequency rather than the cylinder frequency, which unlike that for the previous case at $F_R=0.5$ where the nearly periodic behavior is attained at the cylinder frequency. So, it can be concluded that in the unlock-on regimes, the vortices are shed at the natural frequency whereas, the near wake flow and thermal fields attain their nearly periodic behavior at the lowest frequency, either the imposed frequency or the natural frequency. However, the far wake oscillates only at the natural shedding frequency.
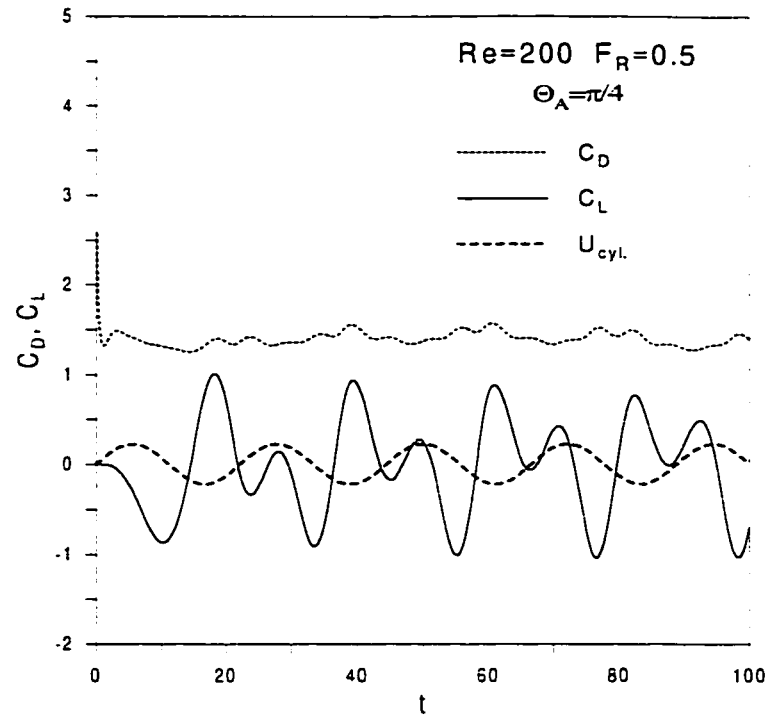
Figure 3.14 The time variation of drag and lift coeficients, unlock-on regime at Re=200, $\Theta_A=\pi/4$ and $F_R=0.5$
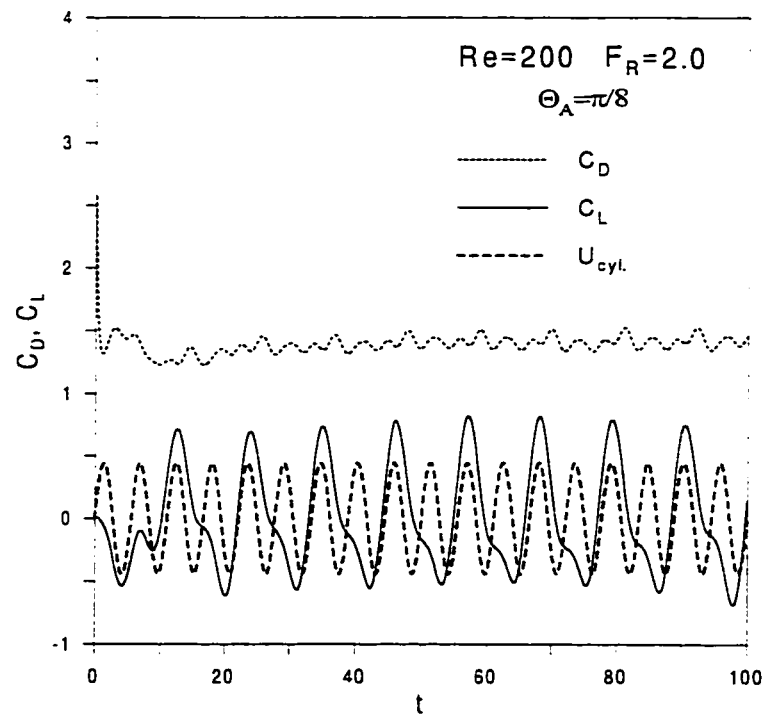
Figure 3.15 The time variation of drag and lift coeficients, unlock-on regime at Re=200, $\Theta_A=\pi/8$ and $F_R=2$
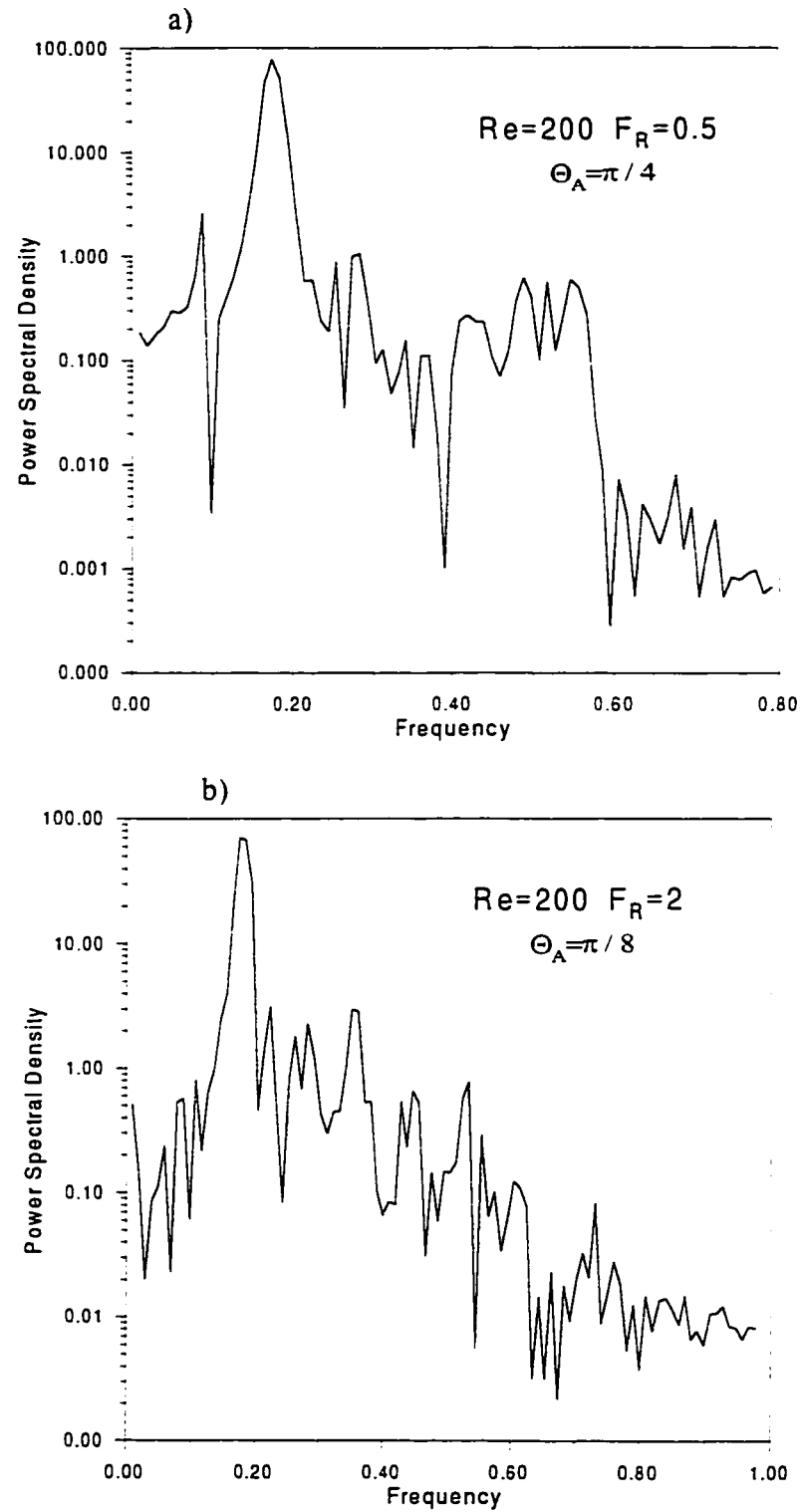
Figure 3.16 Fourier anaysis of the far wake
for unlock-on regimes at Re=200.
a) $\Theta_A=\pi/4$, $F_R=1/2$, b) $\Theta_A=\pi/8$, $F_R=2$
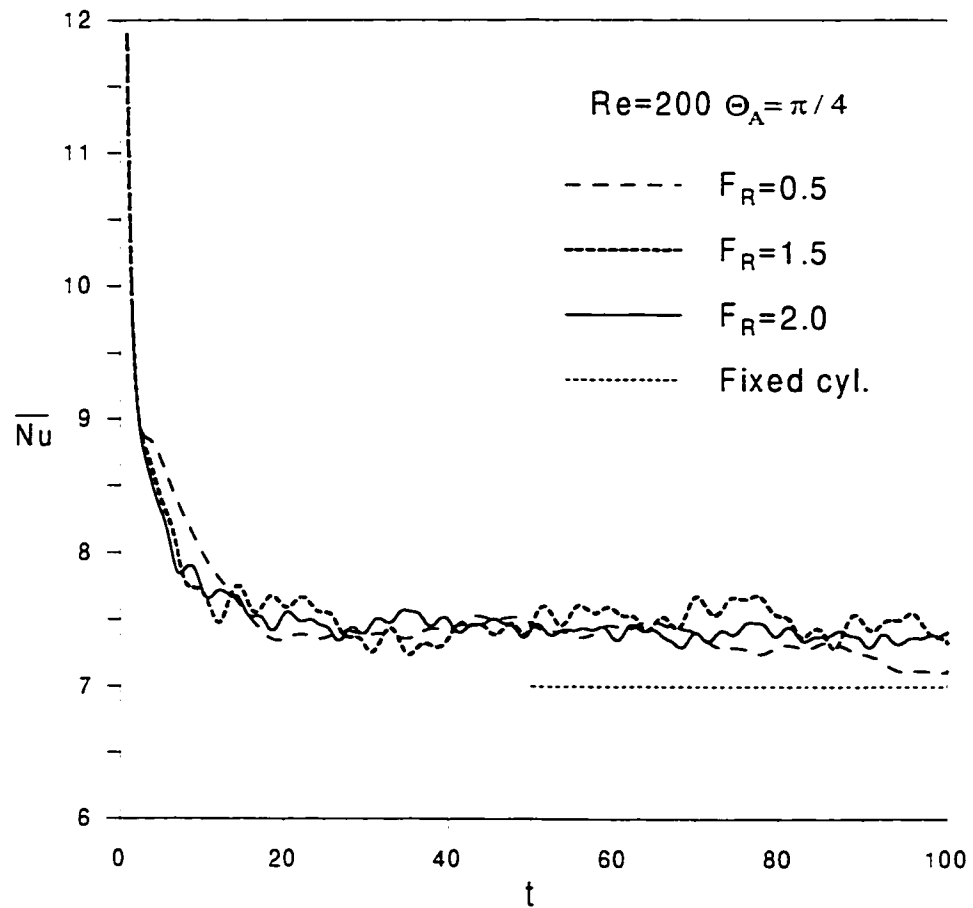
Figure 3.17 The time variation of Nusselt number (unlock-on regimes) at Re=200 and $\Theta_A = \pi / 4$

(a)

(b)

(c)

(d)

(e)
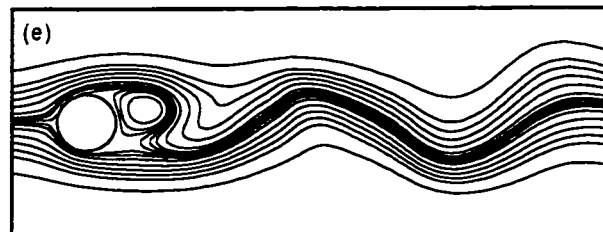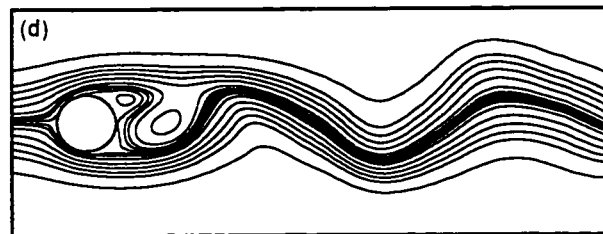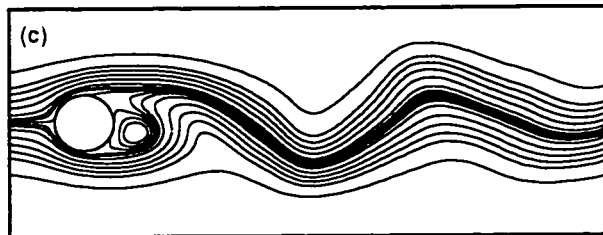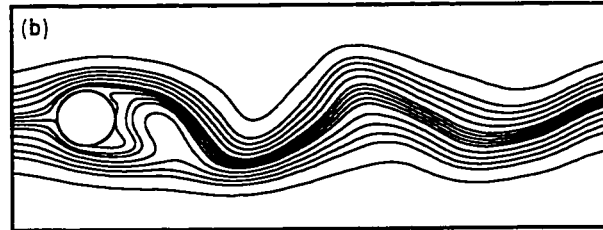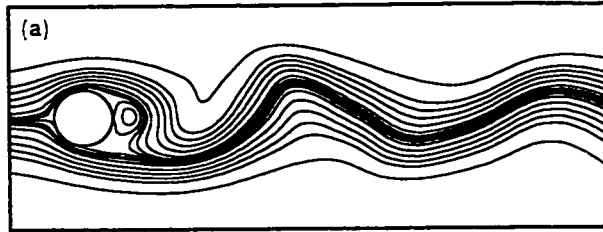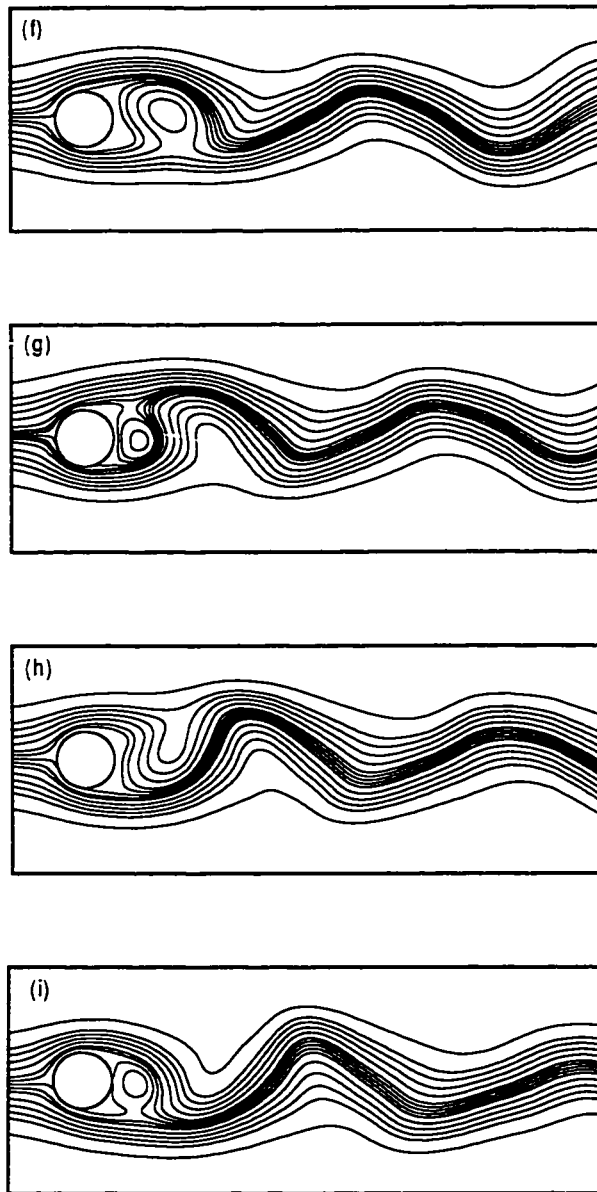
Figure 3.18 Streamlines patterns in a complete cylinder cycle
for the case of Re=200, $\Theta_A = \pi / 4$ and $F_R = 1/2$.
a) t=40, b) t=42.75, c) t=45.5, d) t=48.25, e) t=51, f) t=53.75,
g) t=56.5, h) t= 59.25, i) t=62
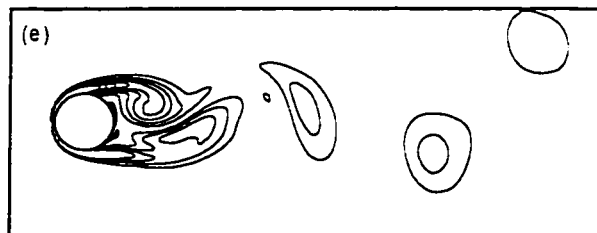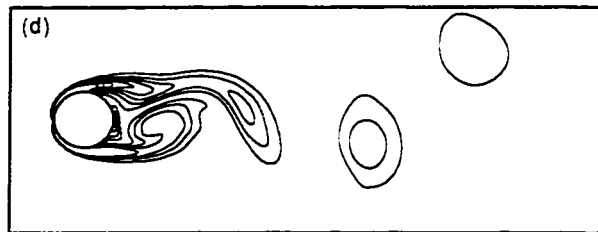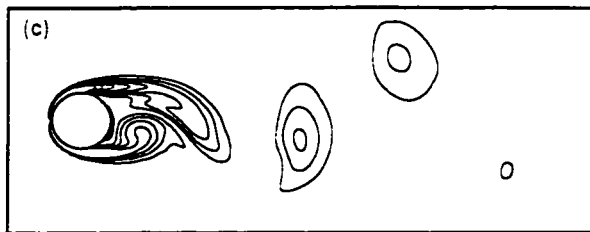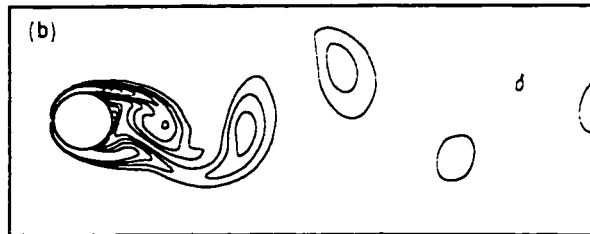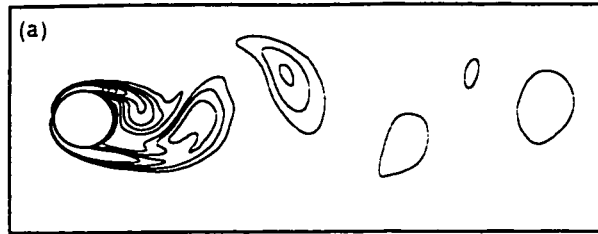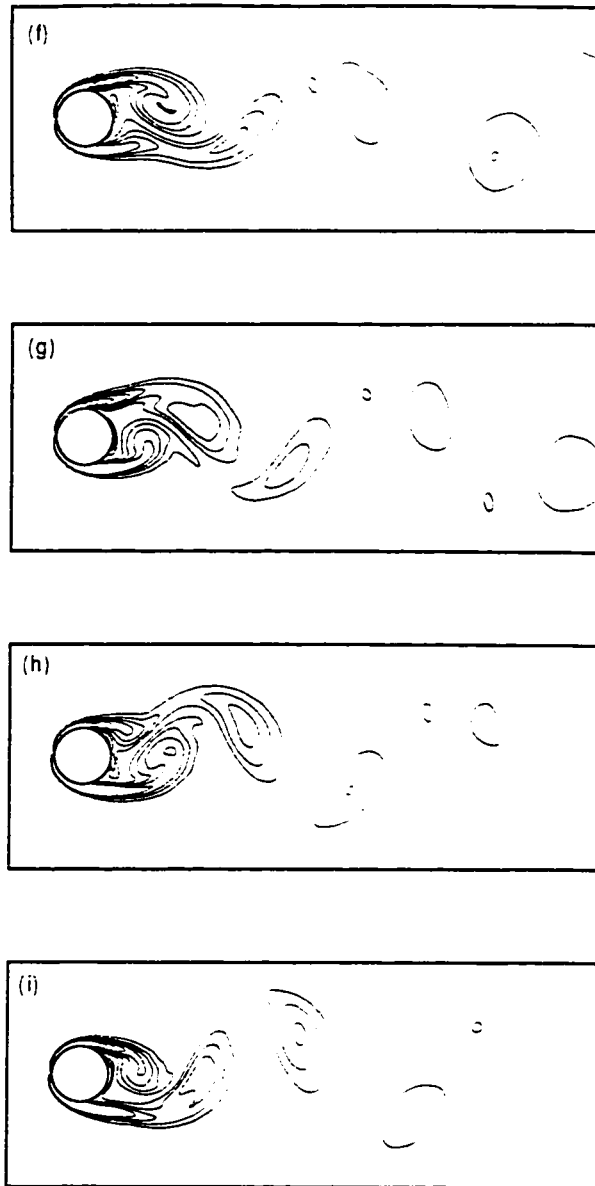
Figure 3.19 Equivorticity patterns in a complete cylinder cycle
for the case of Re=200, $\Theta_A = \pi / 4$ and $F_R = 1/2$.
a) t=40, b) t=42.75, c) t=45.5, d) t=48.25, e) t=51, f) t=53.75,
g) t=56.5, h) t= 59.25, i) t=62

(a)

(b)

(c)

(d)

(e)
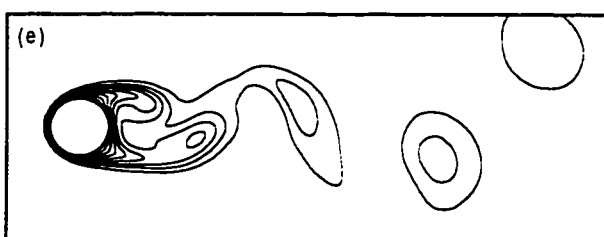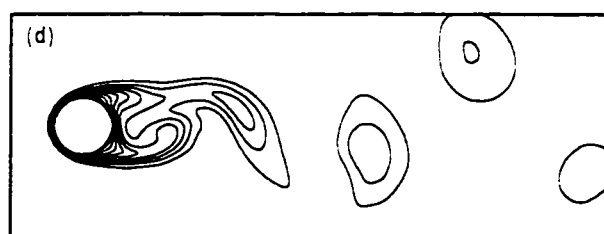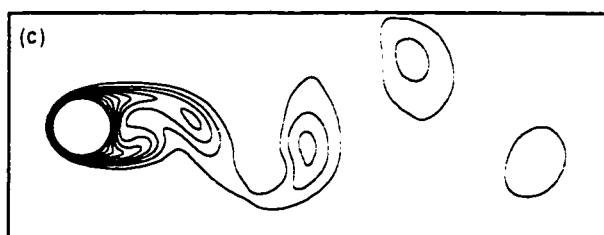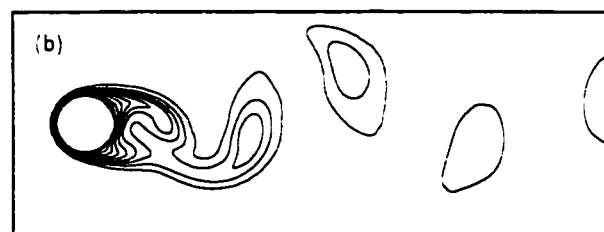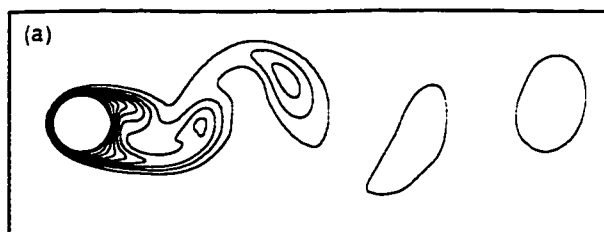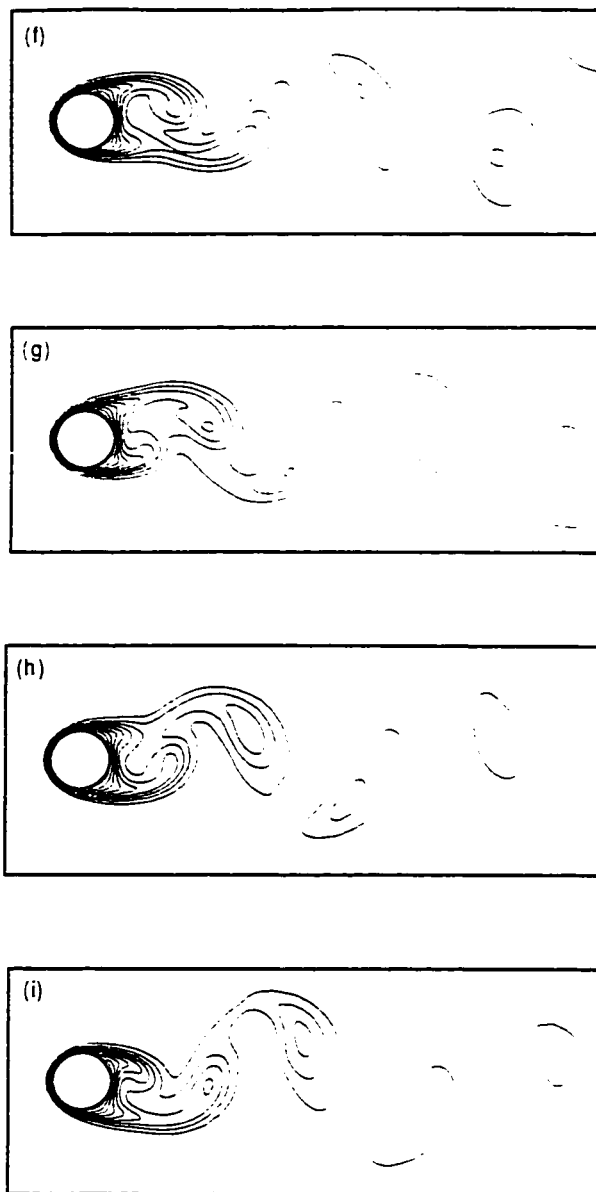
Figure 3.20 Isotherms patterns in a complete cylinder cycle
for the case of Re=200, $\Theta_A = \pi / 4$ and $F_R = 1/2$.
a) t=40, b) t=42.75, c) t=45.5, d) t=48.25, e) t=51, f) t=53.75,
g) t=56.5, h) t= 59.25, i) t=62
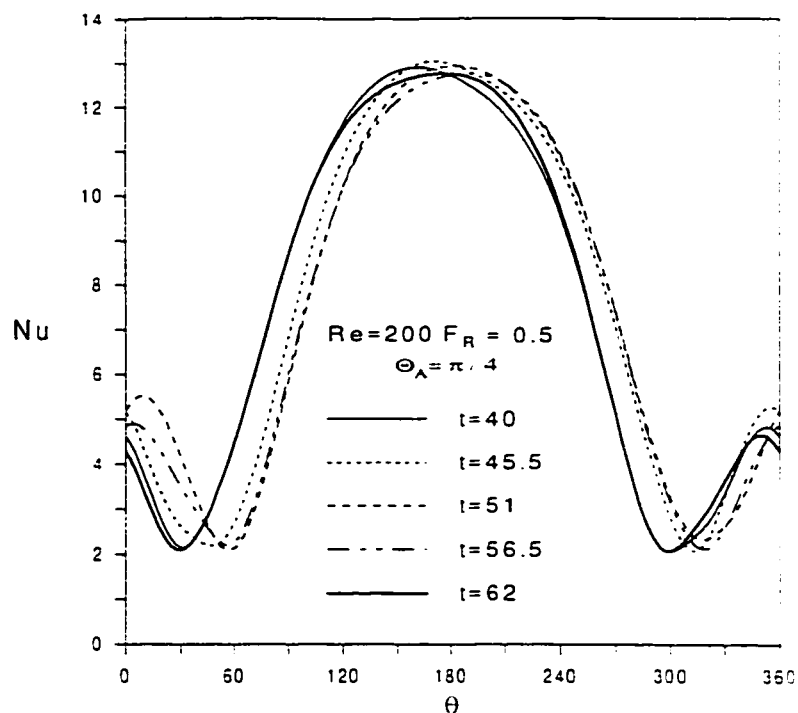
Figure 3.21 Local Nusselt number distribution in a complete cycle of oscillation (unlock-on regime).
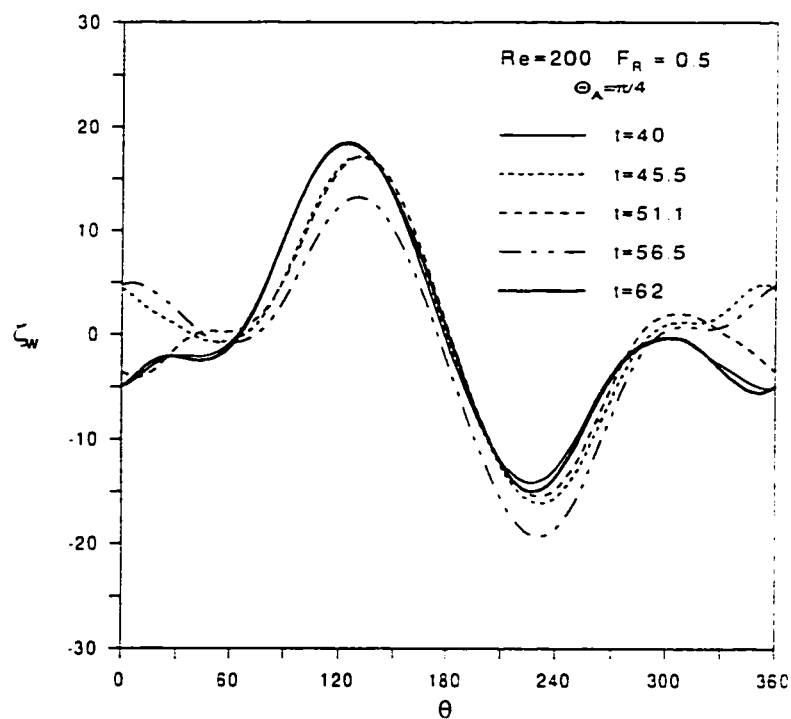
Figure 3.22 Surface vorticity distribution in a complete cycle of oscillation (unlock-on regime).
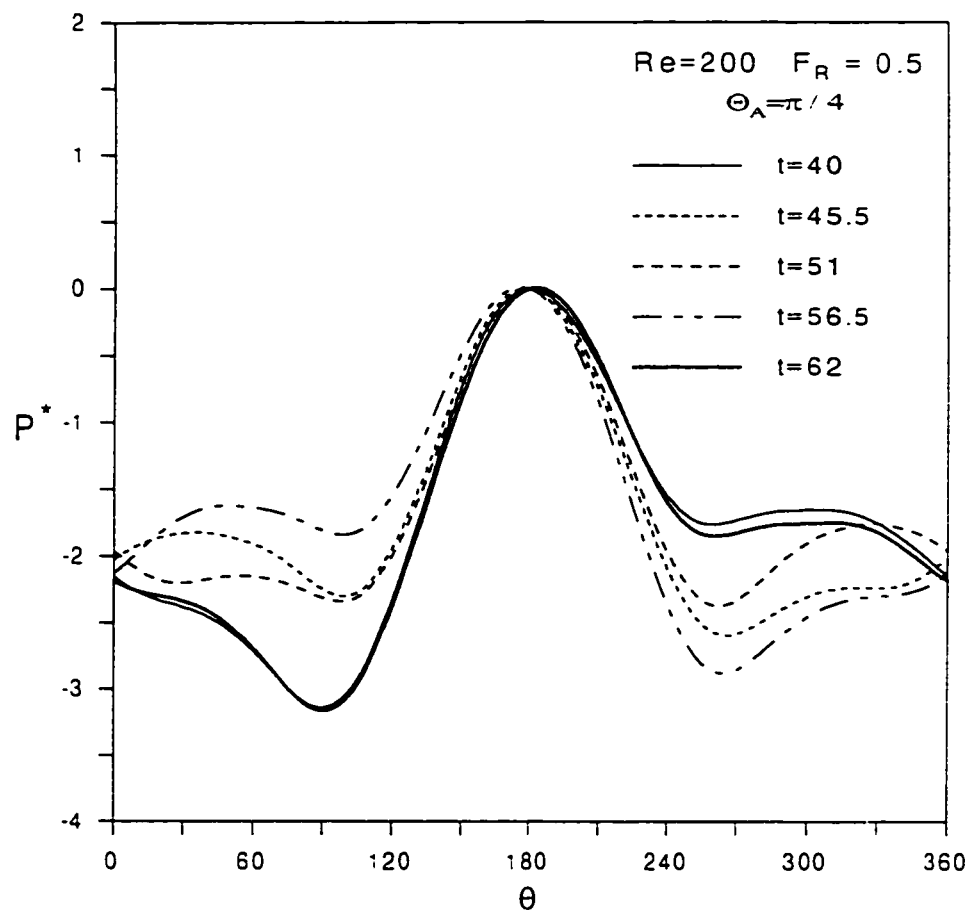
Figure 3.23 Surface pressure distribution in a complete cycle
of oscillation (unlock-on regime).
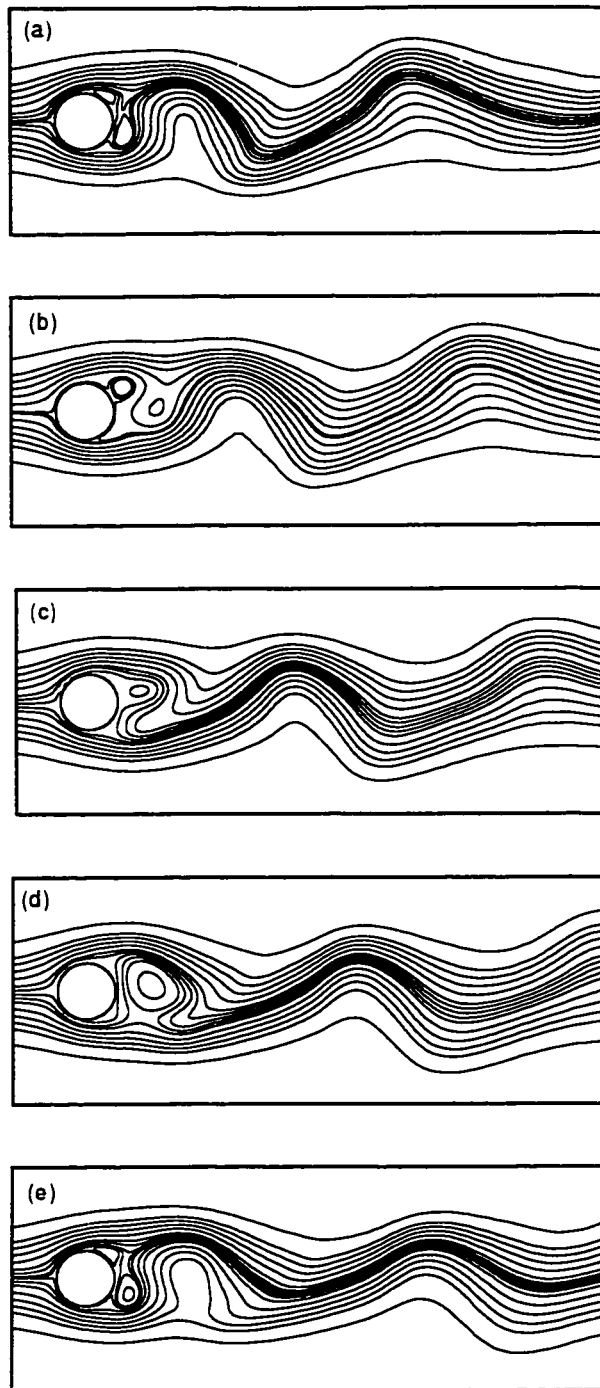
Figure 3.24 Streamlines patterns in two complete cycles of cylinder oscillation (Re=200, $\Theta_A = \pi / 8$ and $F_R=2$).
a) t=40, b) t=42.75, c) t=45.5, d) t=48.25, e) t=51
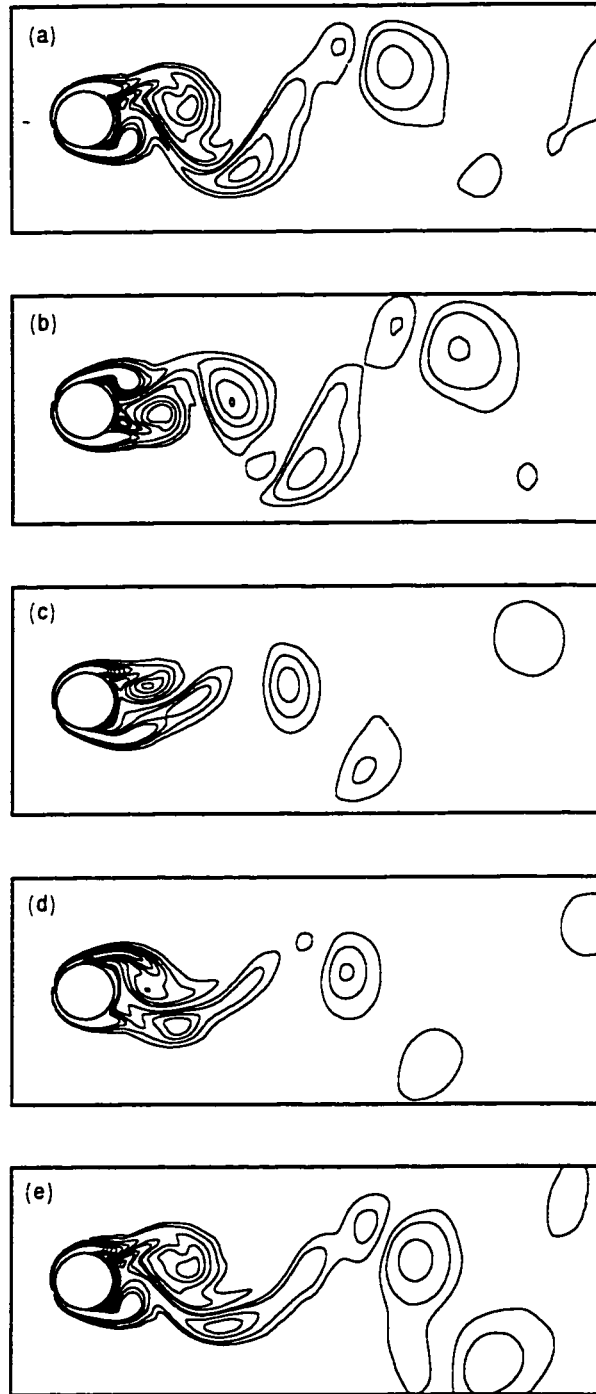
Figure 3.25 Equivorticity patterns in two complete cycles of
cylinder oscillation (Re=200, $\Theta_A = \pi / 8$ and $F_R=2$).
a) t=40, b) t=42.75, c) t=45.5, d) t=48.25, e) t=51
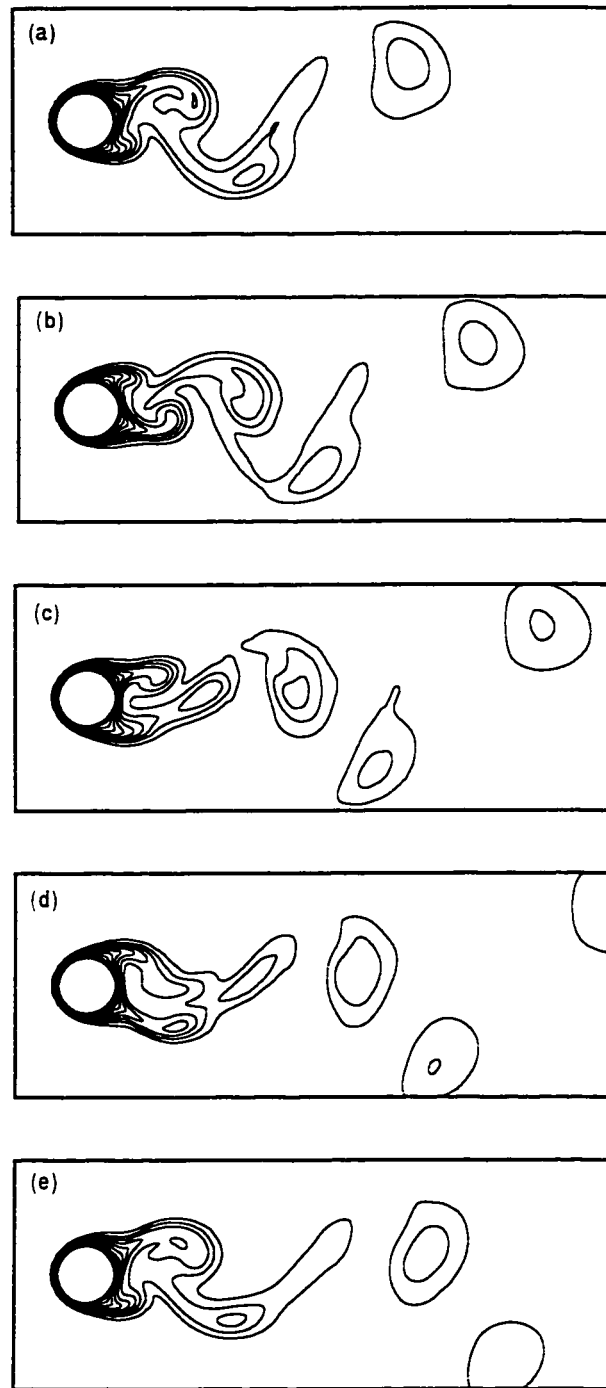
Figure 3.26 Isotherms patterns in two complete cycles of
cylinder oscillation (Re=200, $\Theta_A= \pi / 8$ and $F_R=2$).
a) t=40, b) t=42.75, c) t=45.5, d) t=48.25, e) t=51
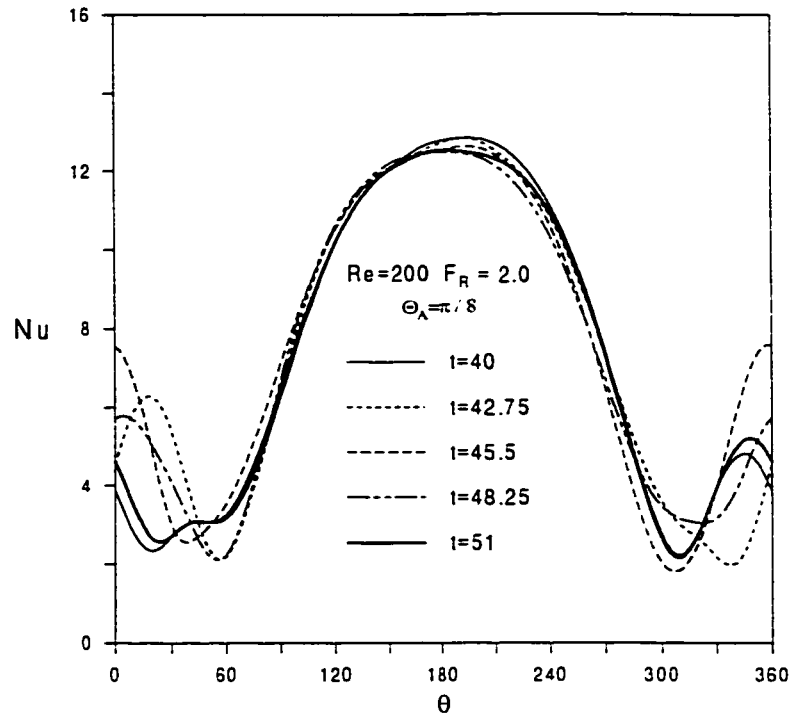
Figure 3.27 Local Nusselt Number distribution in two complete cycles of cylinder oscillation (unlock-on regime).
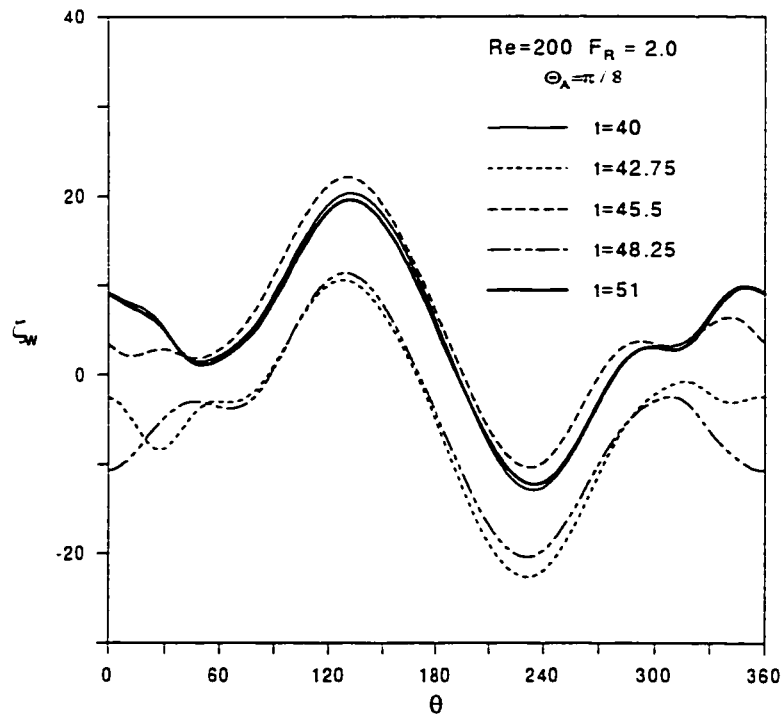
Figure 3.28 Surface vorticity distribution in two complete cycles of cylinder oscillation (unlock-on regime).
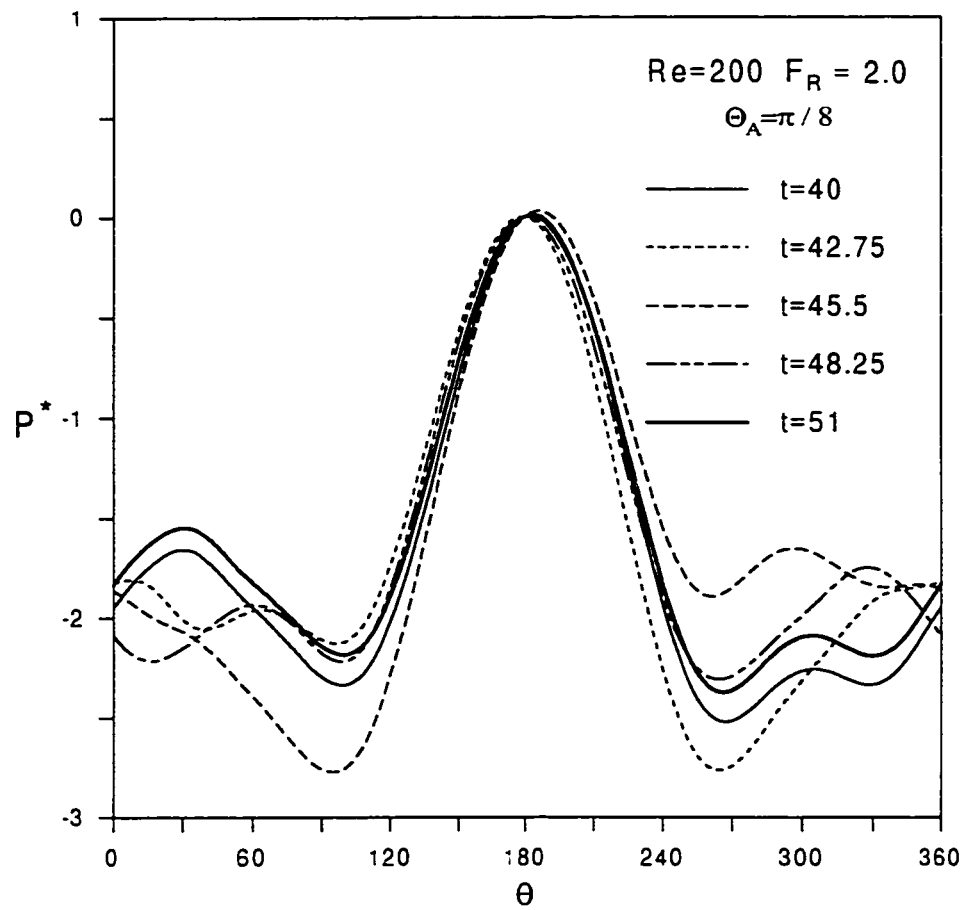
Figure 3.29 Surface pressure distribution in two complete cycles of cylinder oscillation (unlock-on regime).

3.9.2.2 The Lock-on Regime

As the forcing frequency, f, approaches the natural frequency, f_o, the interaction between the natural and forced patterns becomes stronger and the frequency of vortex shedding shifts to synchronize with the imposed oscillation frequency. The synchronization occurs over a span of frequency that brackets the natural frequency. Figure 3.28 shows a comparison between the lift records for non-synchronized and synchronized regimes at Re=100 and $\Theta_A = \pi / 4$. For the non-synchronized regimes shown in Figure 3.28a, the lift force is fluctuating in wave forms, composed of two effects; one induced by the natural and the other induced by the forced oscillation. In the synchronized regimes shown in Figure 3.28b, the lift force is fluctuating with only the imposed frequency and with nearly uniform amplitude [1].

Figure 3.29 shows the lift record for a synchronized regime at Re=40, α =0.2 and S=0.1. The numerical results presented by Okajima [22] are also given in the same figure for comparison. Both lift records are oscillating at the same frequency of cylinder velocity. The difference in amplitudes as well as the phase shift between the present results and that of Okajima [22] may be attributed to the different imposed initial conditions. However, the present average value for the lift coefficient amplitude ($\approx$ 0.51) compares well with the experimental value reported by the same authors ($\approx$ 0.47). Figures 3.30 show typical examples for records of the lift and drag forces at Re=200, $\Theta_A = \pi /2$ and at frequencies within the synchronization range, along with both the cylinder velocity and time traces of tangential velocity component in the far wake. It can be observed that the lift force oscillates at the same forced frequency whereas the fluctuating part of drag force oscillates at twice the cylinder frequency. Also, it can be seen that the tangential velocity component

in the far wake oscillates at the cylinder frequency. Fourier analysis of the near wake (Figure 3.33a) and far wake (Figure 3.33b) for the case of Re=200, $\Theta_A = \pi/2$ and F_R=0.83 (S=0.15) shows clearly the domination of forcing frequency.

Figures 3.34 and 3.35 respectively show the effect of frequency on the lift and drag forces respectively. The figures show that the amplitude of the lift force as well as the time-averaged drag force increase significantly in the range of synchronization, reaching a maximum near the middle of that range. The significant increase of both drag and lift forces within the lock-on frequency range has been reported in the references [1, 59, 61]. Shown in Figure 3.36 is the present results for the average amplitude of the lift coefficient for the case of Re = 80, α =0.2 and at different frequencies along with both experimental and numerical results reported in reference [22]. The figure shows that the present values for the lift coefficient amplitude reach its maximum around the natural Strouhal number and decreases further as the dimensionless frequency deviates from that number. It can be seen that the present data roughly fit to the experimental data of reference [22] with a frequency shift of about 0.02.

Shown in Figures 3.37 is the time variation of the average Nusselt number, $\overline{Nu}$, at different frequencies in the range of synchronization at Re=200 and $\Theta_A = \pi/2$. The figure shows that the obtained $\overline{Nu}$ fluctuates almost regularly with dominant frequency equal to twice the imposed frequency of the cylinder. In addition, there is an appreciable enhancement in heat transfer for high frequencies within the lock-on range. This may be explained on the basis that higher forced frequencies cause higher rate of vortex formation and shedding which enhances the rate of heat convection from the cylinder surface. On the other hand, at low

frequencies lock-on regimes, the $\overline{Nu}$ is even smaller than that for a fixed cylinder for the vortices in this case shed at a rate lower than the natural one.

The computed time-averaged Nusselt number for the cases considered are presented in Table 3.3. The table also contains the percentage increase/decrease in Nusselt number with respect to the one obtained for a fixed cylinder. The results show that a sensible enhancement in heat transfer is observed at Re=200. One can also observe that this enhancement occurs within the synchronization range of frequency. For example, at this Reynolds number, 15% enhancement in heat transfer occurs at amplitude of $\Theta_A = \pi / 2$ and at F_R=1. The same effect can be seen in Figure 3.38 which shows the variation of the time-averaged heat transfer with frequency at Re=200 and at two amplitudes namely, $\Theta_A=\pi/2$ and $\Theta_A = \pi$. In the both cases the percentage increase in Nusselt number takes its maximum value (15% and 11.5% respectively) in the synchronization range around F_R=1. Previously reported results for the case of in-line and transverse oscillation [48, 51, 52] have shown sensible heat transfer enhancement only in the lock-on range of frequencies at Re=200. At high frequencies outside the lock-on regime, a slight enhancement in heat transfer is found at low amplitudes. However, at higher amplitudes this enhancement tends to decrease as shown in Table 3.3. Namely, 8.7 % increase in heat transfer is found at Re=200, $\Theta_A = \pi / 8$ and F_R=2. This percentage decreases to 5.8, 3.15 and 2.3 as the amplitude increases to $\Theta_A = \pi / 4$, $\pi / 2$ and π respectively.

In the cases of in-line and transverse oscillations previous researchers [48, 51, 52] reported an increase of heat transfer as the amplitude of oscillation increases. However, in the case of low speed rotational motion, as the amplitude of rotation increases the heat transfer tends to

decrease (see Badr [16]). This is due to the fact that a fluid layer in such case encloses the cylinder and act as a buffer zone causing a decrease in the rate of heat convection. However, this is not exactly the case in this study as can be seen in the following discussion.

In general, the thermal field and accordingly the rate of heat transfer is highly influenced by the velocity field. Two effects here are of prime importance. The first is the effect of amplitude and frequency of oscillation on the flow field near the cylinder surface. Larger amplitudes give rise to a larger shear layer wrapping the cylinder (or a good part of it). The nearer the frequency from the natural frequency the more organized, intensive fluid motion in the vicinity of the cylinder surface [48]. The second effect is the process of vortex shedding in the wake region. This process has a direct effect on heat convection since every shedding vortex carries with it a certain amount of heat. The shedding frequency as well as the size of the vortices are both important factors influencing the heat convection process.

According to the obtained results, the amplitude of oscillation has an additional influence to the occurrence of the lock-on phenomenon. Larger amplitudes at frequencies near the natural frequency creates the lock-on phenomenon. Therefore the effect of the amplitude is twofold. The first is the creation of a larger shear layer and the second is the change of vortex shedding frequency. The two effects may have corroborating or contradicting effects on heat transfer depending on the frequency (whether greater than or less than the natural frequency). Within the lock-on range, lower frequency of vortex shedding results in less heat transfer. The effect of the rate of vortex shedding on heat transfer may be indicated in Figures 3.37. The figure shows that when $F_R > 1$ the heat transfer rate increases considerably in comparison with that of a fixed cylinder. This can be seen in the high

frequency lock-on cases (F_R=1.11 and 1.5), where heat transfer enhancement is found. On the other hand, a decrease in the heat rate occurs as the rate of vortex shedding decreases as observed in the case of low frequency lock-on regime (F_R=0.83). In unlock-on regimes, the rate of vortex shedding is constant and thus there is no significant effect on heat convection. On the other hand, the effect of resonance (synchronization) is quite clear in Table 3.3 and Figure 3.38 where the nearer the forcing frequency from the center of resonance state i.e at F_R=1, the higher the heat rate. The reason for this increase may be attributed to the intensive fluid motion in the vicinity of the cylinder which leads to increasing the heat convection.

The streamlines, equivorticity lines and isotherms are plotted for typical lock-on regimes at Re=200, $\Theta_A = \pi / 2$ and at two frequency ratio, namely F_R=0.83 < 1 and F_R=1.11> 1 are shown in Figures 3.39-3.41 and 3.42-3.44, respectively. In all these figures, the time period between plots is one quarter of a complete cycle. Figures 3.39 and 3.42 clearly show the higher rate of vortex shedding at higher frequency in the lock-on regime. The corresponding equivorticity lines shows higher number of shedding vortices within the same time span. Both figures show that the streamlines adjacent to the cylinder surface are wrapping a good part of it when the angular velocity is maximum (see plots 3.39 b and d and also 3.42 b and d). The longitudinal spacing of the wake wave length shown in streamlines contours for both cases confirms that the wake wave length varies inversely with the frequency ratio (i. e. the wake contracts for F_R > 1 and expands for F_R < 1). This result has been reported by Sarpkaya [72] as one of the established facts about the state of synchronization for the case of transverse oscillation. The isotherms patterns for the same two cases are shown in Figures 3.41 and 3.44. The shedding vortices represent lumps of heated fluid moving away

from the cylinder. The location of such vortices are exactly the same as in equivorticity and isotherm patterns confirming again the accuracy of the present mathematical model. Moreover, the mechanism of heat diffusion within each vortex as it moves downstream is clearly shown in Figures 3.41 and 3.44. For example, Figure 3.44 b shows that the fluid contained within each of the shedding vortices gets cooler as they move away from the cylinder (the number of isotherms indicate the temperature level). The same mechanism applies to the diffusion of angular momentum by viscous forces and is clearly shown in Figures 3.40 and 3.43. The number of equivorticity lines represent the strength of each vortex. The periodicity of the flow and thermal fields is clearly shown in the streamline and isotherm plots since the beginning of the cycle is very much the same as compared to the end of it.

Figures 3.45-3.47 show the distribution of local Nusselt number, surface vorticity and surface pressure within a complete cycle of oscillation for the case of Re=200, $\Theta_A = \pi / 2$ and F_R=1.11. The local Nusselt number distributions show that the maximum Nu values are almost the same. The locations of these maximum values oscillates with the same cylinder oscillation within a range of about $\pm15°$ around θ =180°. Also, the locations of minimum values of Nu oscillate with cylinder frequency, but their values differ. It can be also observed that the figure is symmetric around θ =180° which clearly shows the symmetric heat transfer process for every half cycle. This explains the average Nusselt number $\overline{Nu}$ oscillation at frequency equal to twice the cylinder frequency. The periodicity in the flow field is confirmed further in surface vorticity and pressure distributions shown in Figures 3.46 and 3.47.

Table 3.3 Effect of Reynolds number , amplitude and frequency on the time- averaged Nusselt number

Re	$\dfrac{\Theta_A}{\pi}$	S/S_0	$\overline{\overline{Nu}}$	$\overline{\overline{Nu}}\,(s=0)$	%increase
		0.50	5.3		0
		0.75	5.4		1.8
100	0.125	1.00	5.4	5.3	1.8
		1.50	5.29		-0.19
		2.00	5.1		-3.7
		0.50	5.3		0
		0.75	5.16		-2
100	0.25	1.00	5.49	5.3	5.4
		2.00	5.31		0.1
		4.00	5.3		0
		0.50	5.25		-0.1
		0.75	5.25		-0.1
100	0.5	1.00	5.67	5.3	6.95
		1.50	5.43		2
		2.00	5.32		0.3
		0.50	4.99		-5.8
		0.75	5.06		-4.5
100	1	1.00	4.95	5.3	-6
		1.50	5.1		-3.7
		2.00	4.99		-5.8
		0.50	7.28		4.1
		0.83	7.12		1.8
200	0.125	1.00	7.18	6.99	2.7
		1.50	7.34		5.0
		2.00	7.6		8.7
		0.50	7.35		5.1
		1.00	7.01		2.0
200	0.25	1.50	7.5	6.99	7.2
		2.00	7.4		5.8
		0.50	7.33		4.40
		1.00	8.04		15.00
200	0.5	1.11	8.03	6.99	14.9
		1.50	7.66		9.50
		2.00	7.21		3.15
		0.50	6.97		-0.28
		1	7.80		11.5
200	1	1.25	7.54	6.99	7.80
		1.5	7.42		6.10
		2	7.15		2.30
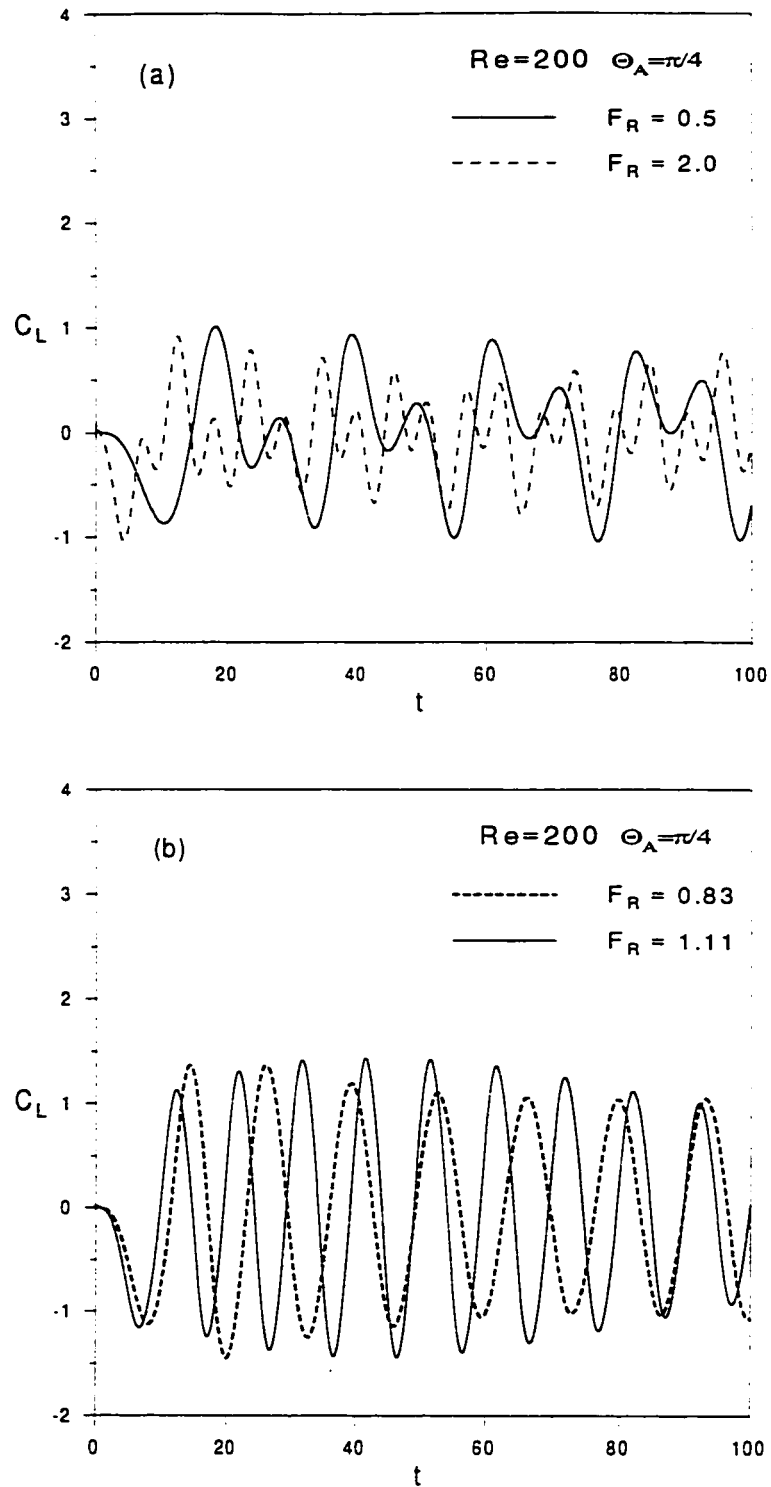
Figure 3.30 The time variation of lift coefficient at Re=200 and $\Theta_A = \pi/4$
a)unlock-on regimes b)lock-on regimes
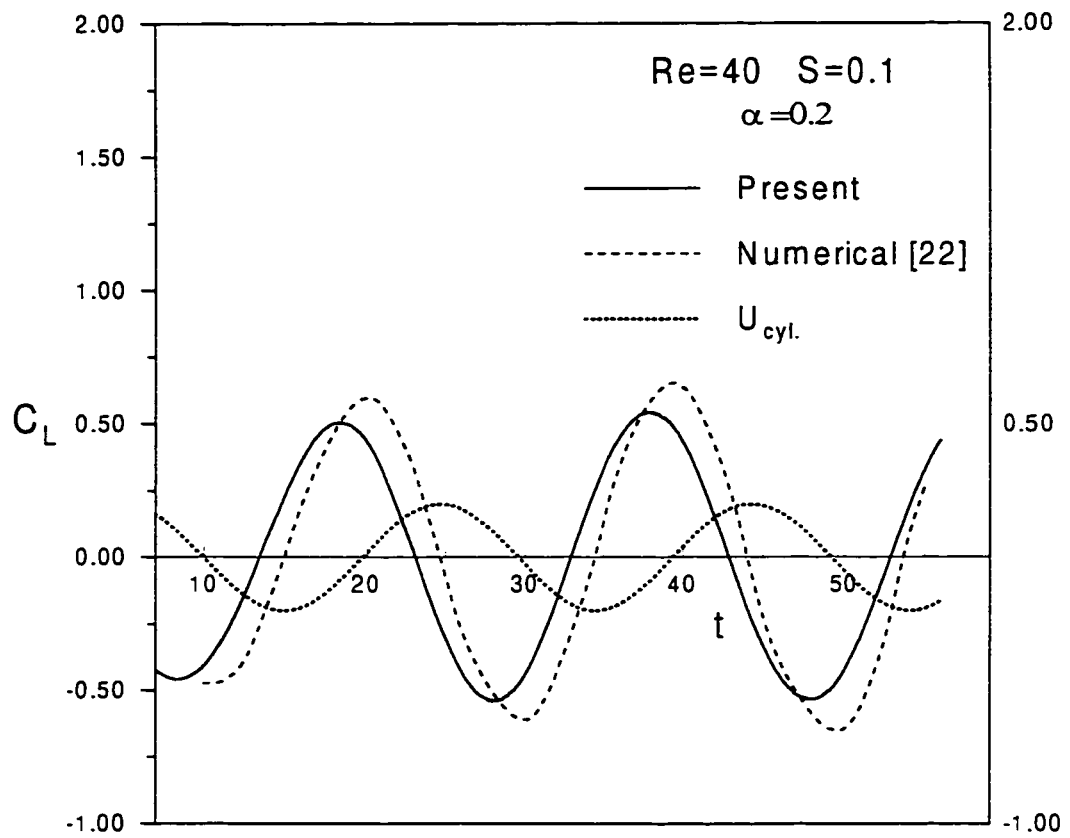
Figure 3.31 The time variation of lift coefficient at Re=40, S=1 and α = 0.2 ; comparison with numerical work of reference [22].
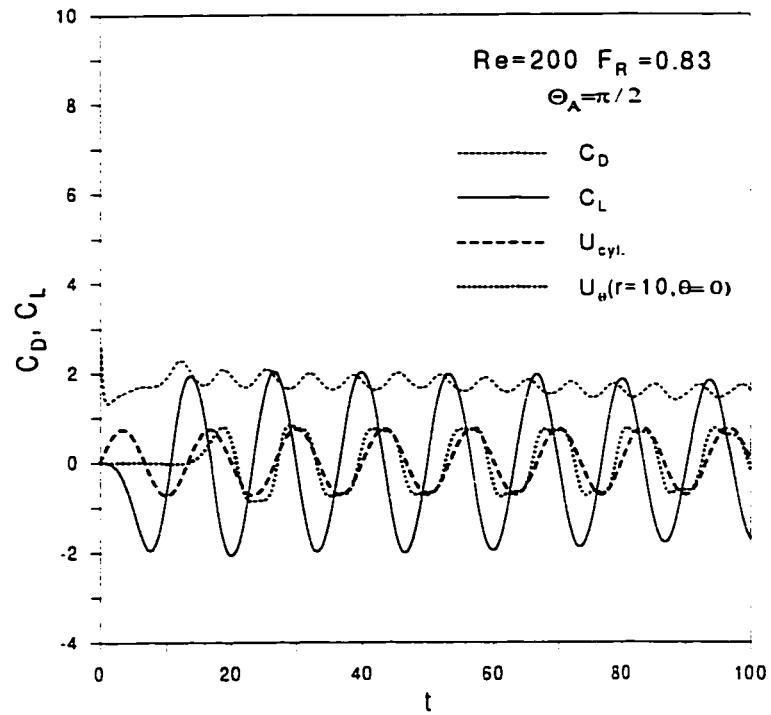
Figure 3.32 a
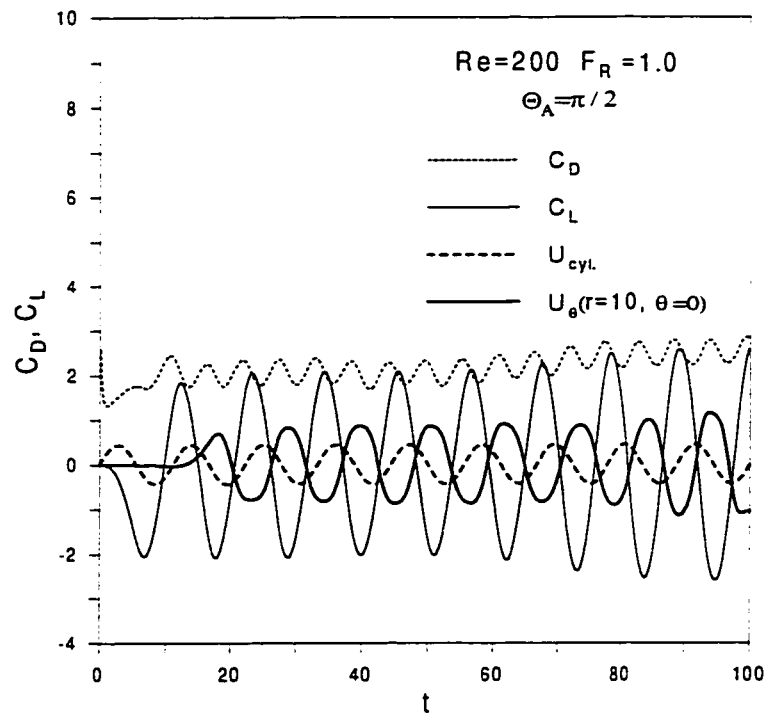
Figure 3.32 b

Figure 3.32 Time variation of drag coefficient, lift coefficient
and angular velocity in the far wake   a) F_R=0.83,   b)F_R=1
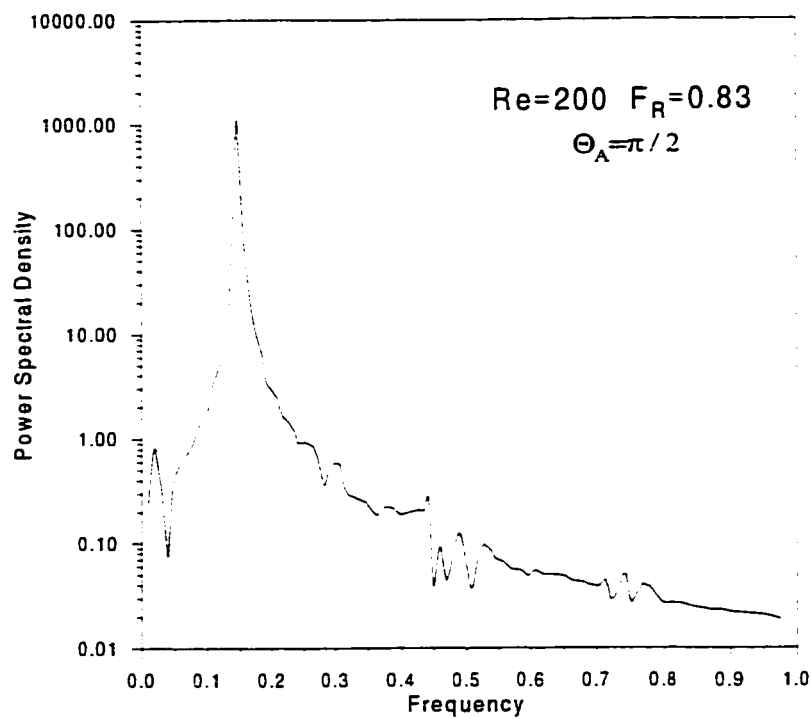
Figure 3.33 a
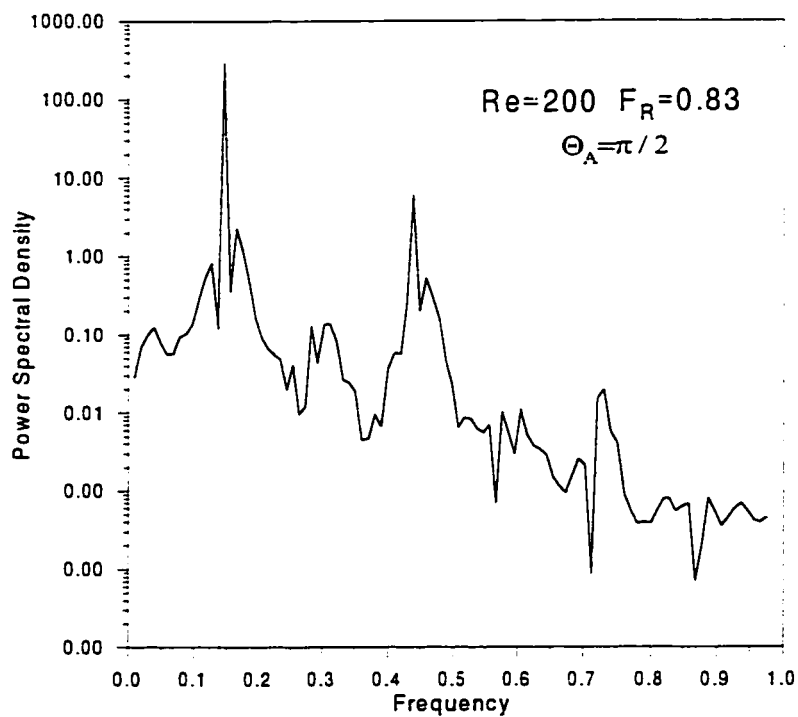
Figure 3.33 b

Figure 3.33 Fourier analysis for the case Re=200, Θ_A= $\pi/2$ and F_R=0.83
a) the near wake b)the far wake
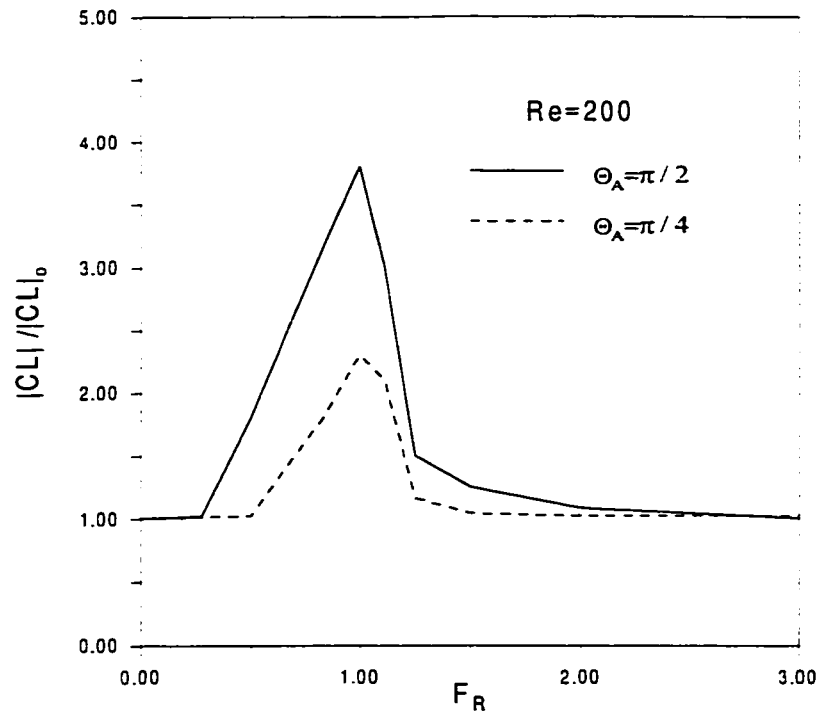
Figure 3.34 Effect of frequency ratio on lift coefficient amplitude.
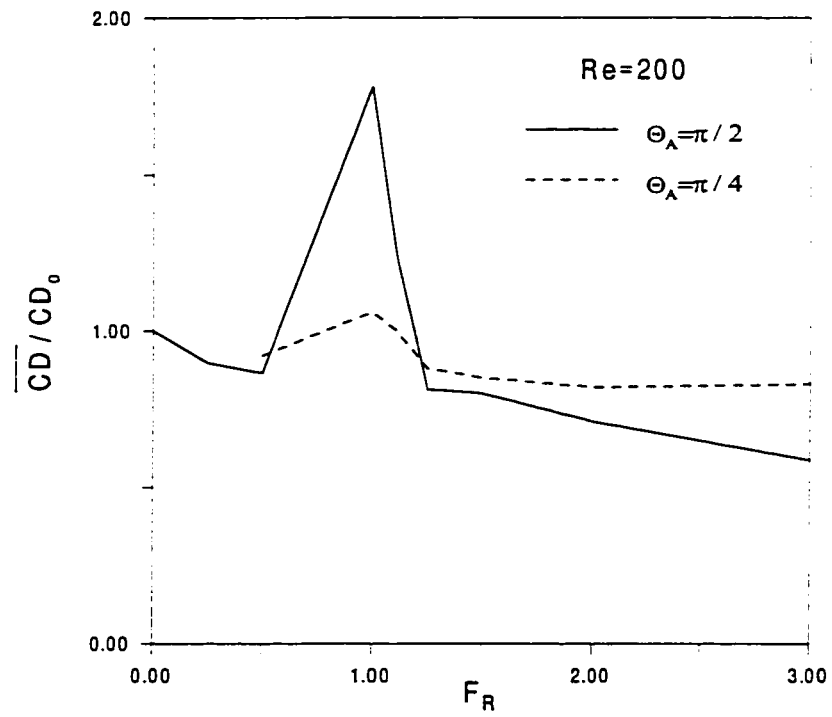
Figure 3.35 Effect of frequency ratio on time-averaged drag coefficient.
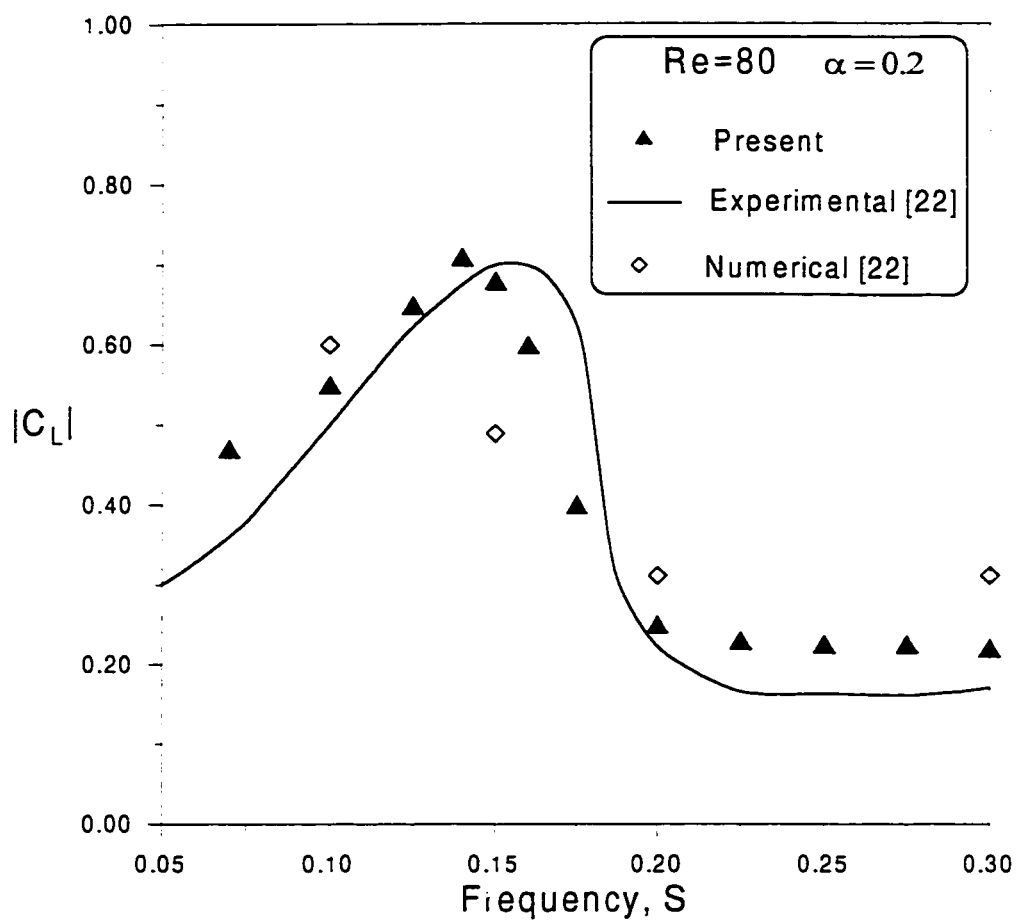
Figure 3.36 Effect of frequency on the average lift coefficient amplitude; comparison with experimental and numerical results of reference [22].
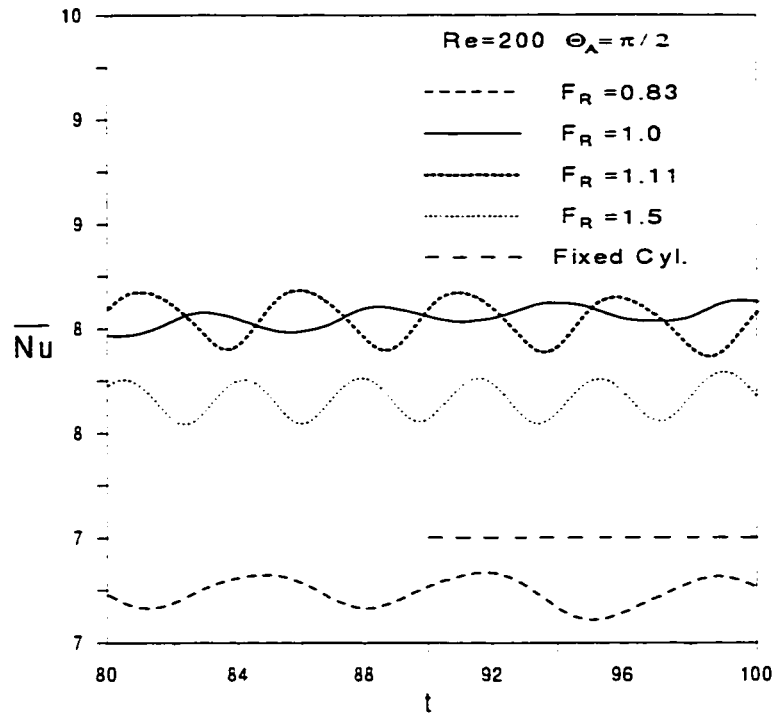
Figure 3.37 The time variation of average Nusselt within the lock-on range of frequencies at Re=200 and $\Theta_A = \pi / 2$.
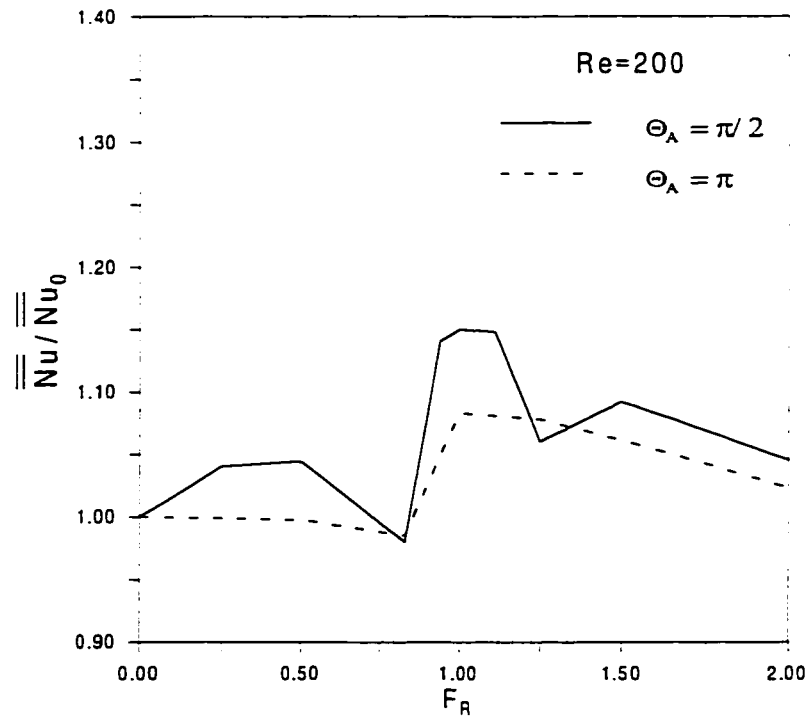
Figure 3.38 Effect of frequency ratio on the time-avereged Nusselt number
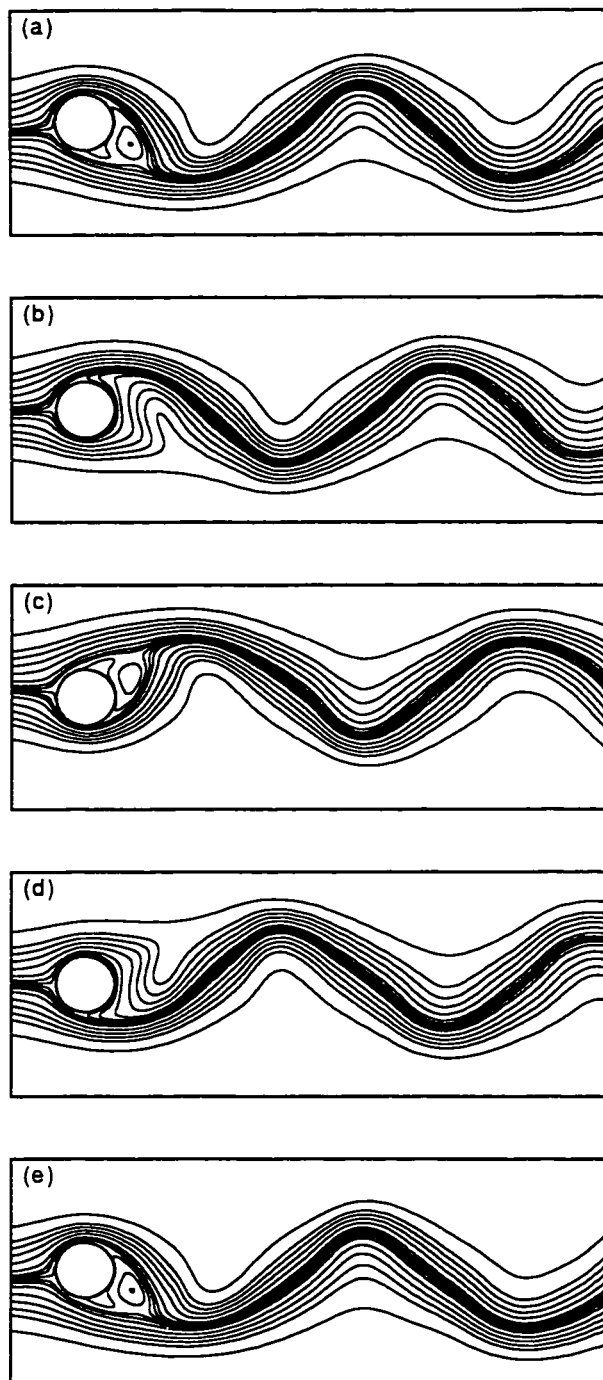
Figure 3.39 Streamline patterns in a complete cylinder cycle
for the case of Re=200, $\Theta_A = \pi / 2$ and F_R=0.83 .
a) t=t_o, b) t=t_o+1/4T_p c) t=t_o+1/2T_p (d) t=t_o+3/4T_p (e)t=t_o+T_p
where T_p is the time period of cylinder oscillation cycle
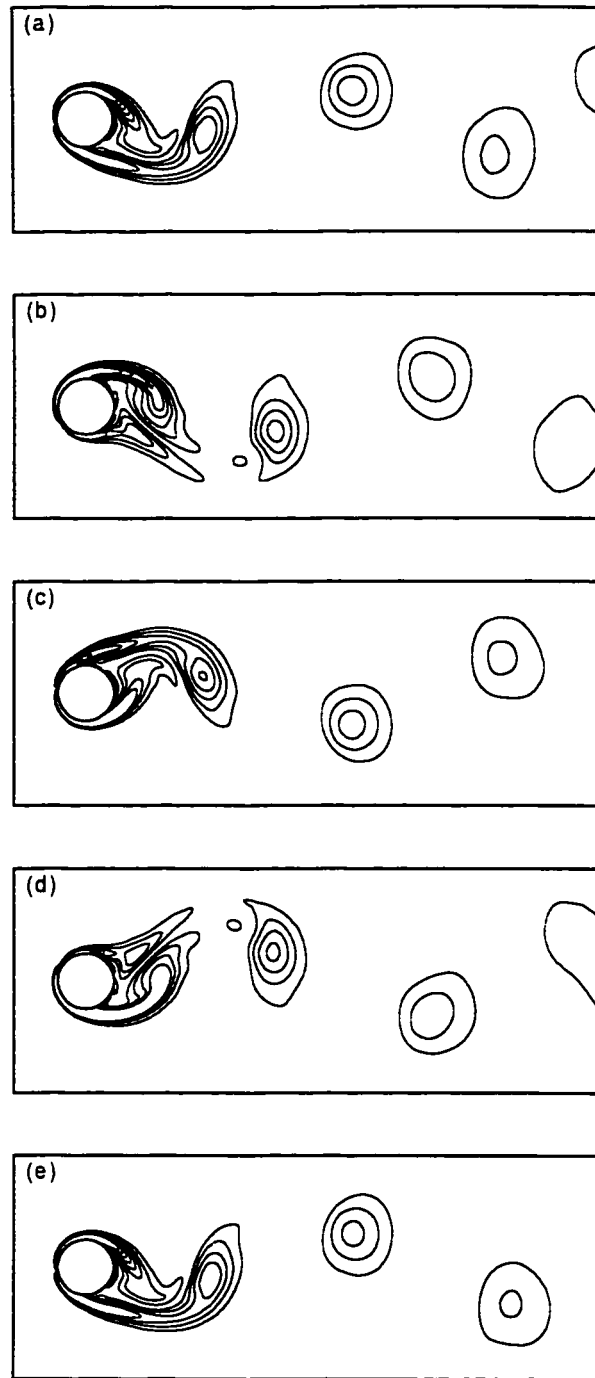
Figure 3.40 Vortex patterns in a complete cylinder cycle
for the case of Re=200, $\Theta_A = \pi / 2$ and F_R=0.83 .
a) $t=t_o$, b) $t=t_o+1/4T_p$ c) $t=t_o+1/2T_p$ (d) $t=t_o+3/4T_p$ (e)$t=t_o+T_p$,
where T_p is the time period of cylinder oscillation cycle
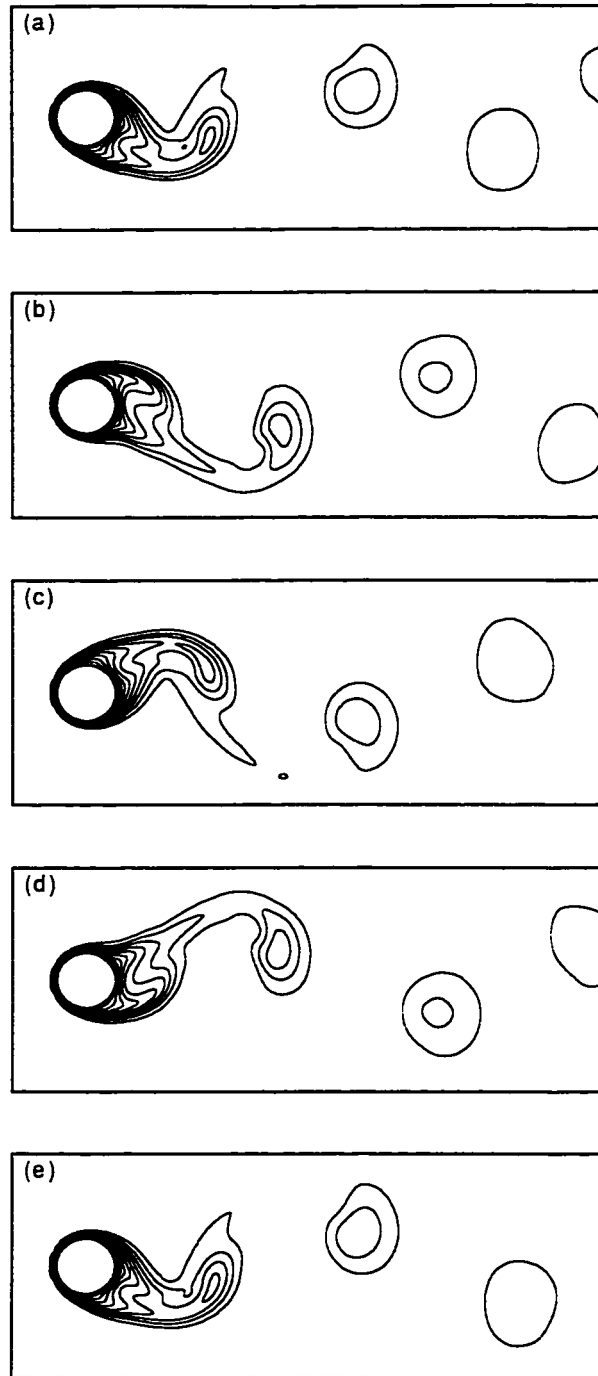
Figure 3.41 Isotherms patterns in a complete cylinder cycle
for the case of Re=200, $\Theta_A = \pi / 2$ and F_R=0.83)
a) t=t_o, b) t=t_o+1/4T_p c) t=t_o+1/2T_p (d) t=t_o+3/4T_p (e)t=t_o+T_p,
where T_p is the time period of cylinder oscillation cycle
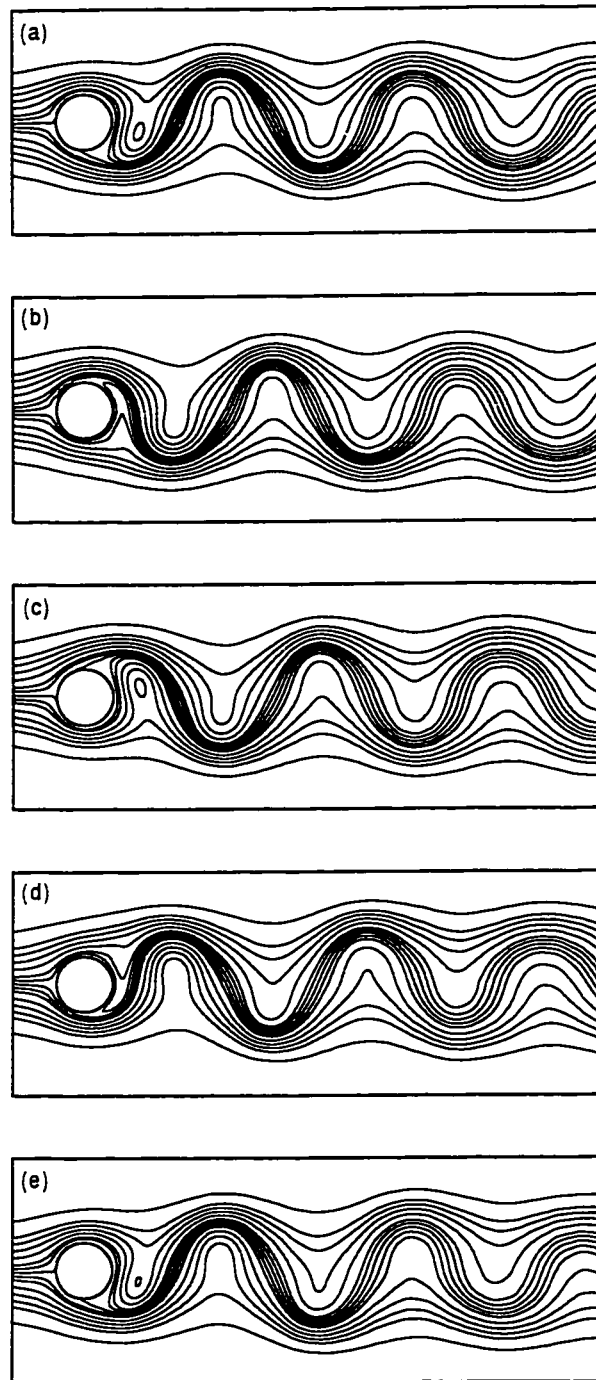
Figure 3.42 Streamlines patterns in a complete cylinder cycle
for the case of Re=200, $\Theta_A = \pi / 2$ and $F_R = 1.11$.
a) $t=t_o$, b) $t=t_o+1/4T_p$ c) $t=t_o+1/2T_p$ (d) $t=t_o+3/4T_p$ (e)$t=t_o+T_p$,
where T_p is the time period of cylinder oscillation cycle
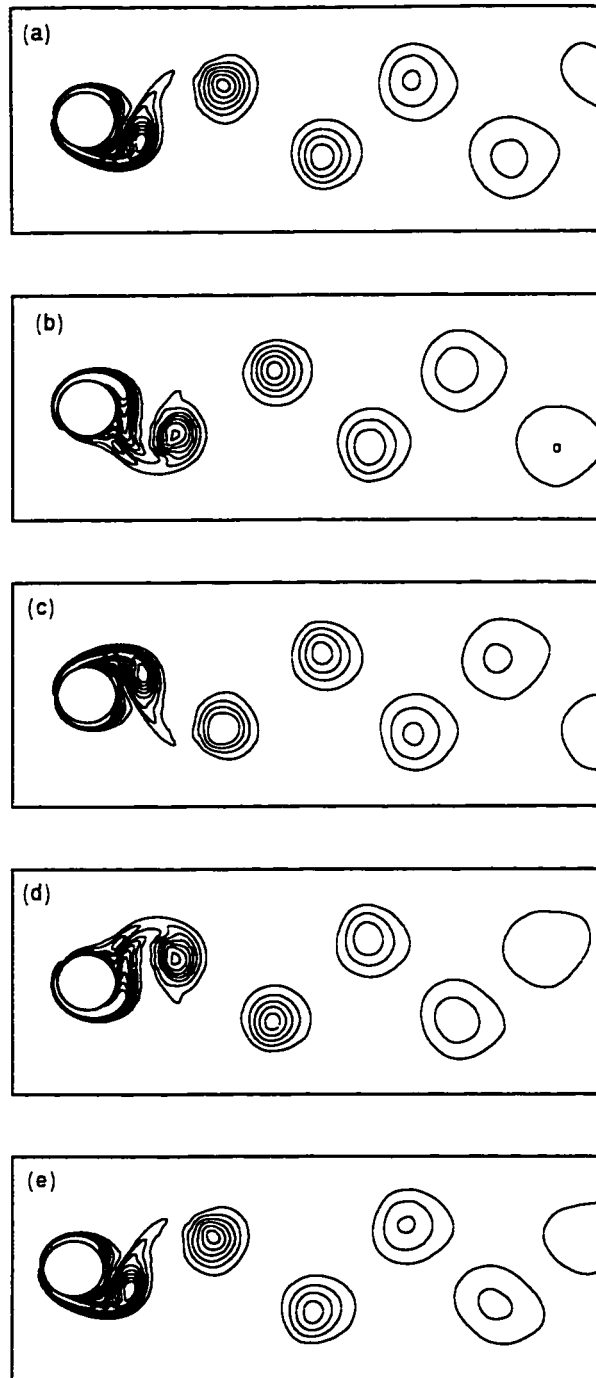
Figure 3.43 Vortex patterns in a complete cylinder cycle
for the case of Re=200, $\Theta_A = \pi / 2$ and $F_R = 1.11$.
a) $t=t_o$, b) $t=t_o+1/4T_p$ c) $t=t_o+1/2T_p$ (d) $t=t_o+3/4T_p$ (e)$t=t_o+T_p$,
where T_p is the time period of cylinder oscillation cycle
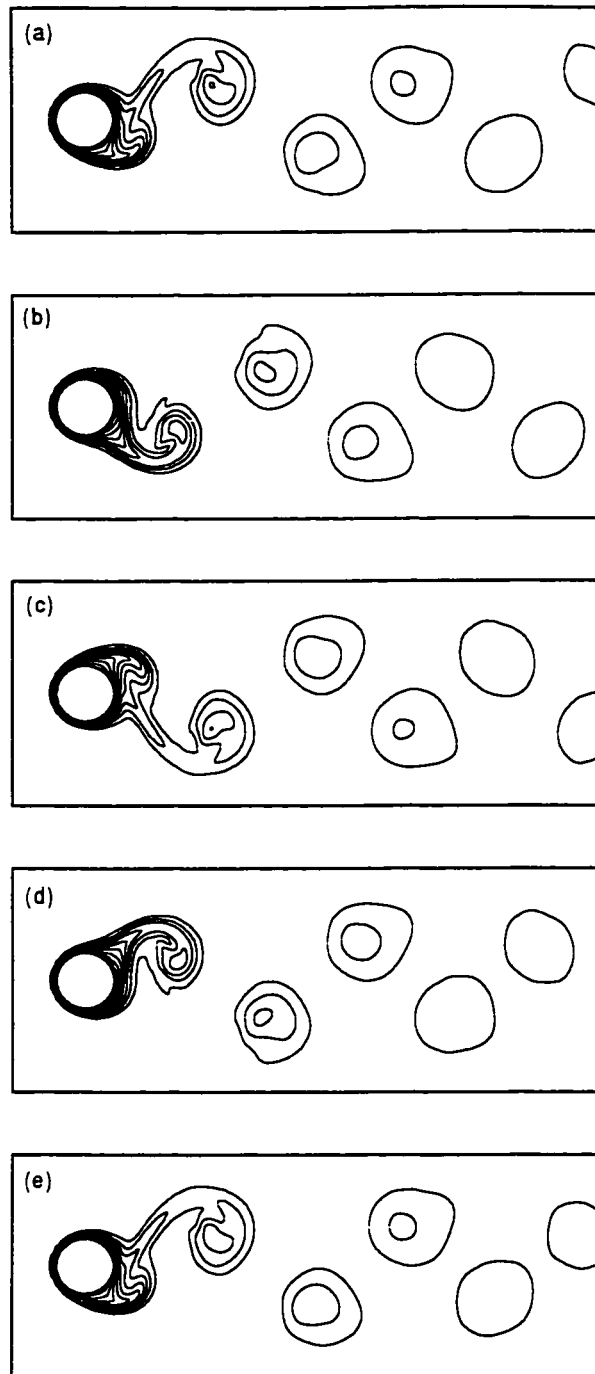
Figure 3.44 Isotherms patterns in a complete cylinder cycle
for the case of Re=200, $\Theta_A = \pi / 2$ and $F_R=1.11$.
a) $t=t_o$, b) $t=t_o+1/4T_p$ c) $t=t_o+1/2T_p$ (d) $t=t_o+3/4T_p$ (e)$t=t_o+T_p$,
where T_p is the time period of cylinder oscillation cycle
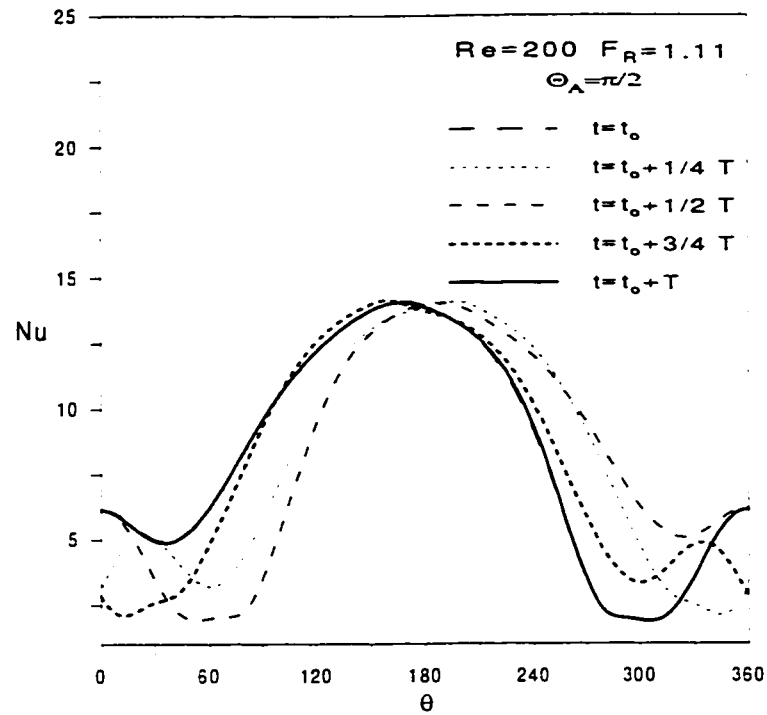
Figure 3.45 Local Nusselt number distribution in a complete cycle
at Re=200, $\Theta_A = \pi / 2$ and $F_R=1.11$.
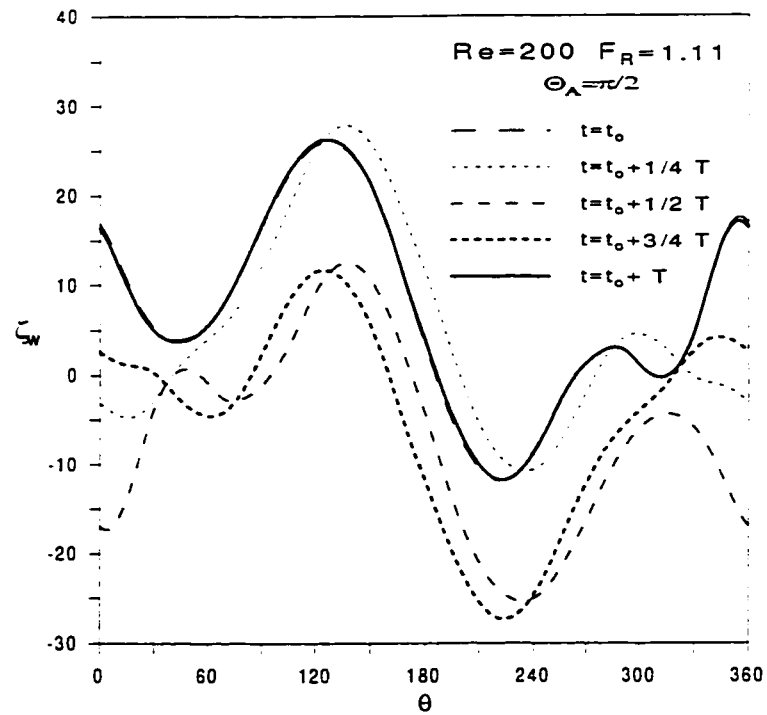
Figure 3.46 Surface vorticity distribution in a complete cycle
at Re=200, $\Theta_A = \pi / 2$ and $F_R=1.11$.
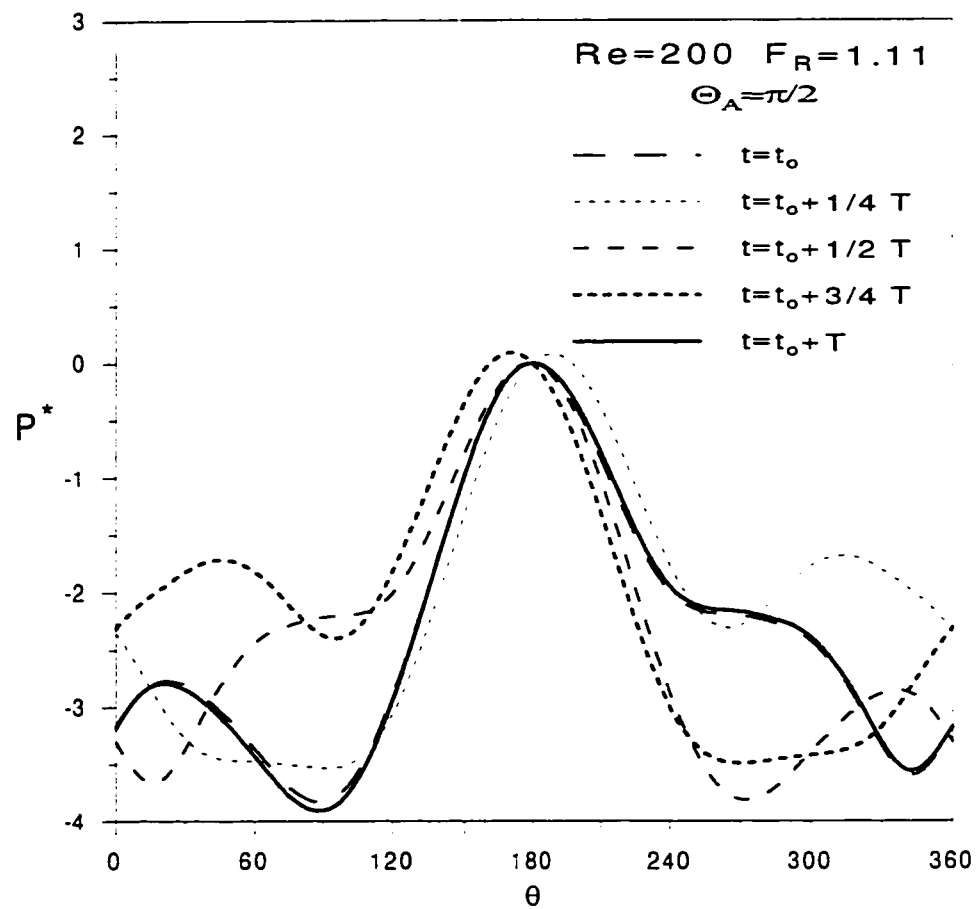
Figure 3.47 Surface pressure distribution in a complete cycle
at Re=200, $\Theta_A = \pi / 2$ and $F_R=1.11$.

From the results presented so far, it is expected that a transition regime between lock-on and unlock-on regimes should exist. This regime is characterized by an intermittent frequency switching between the natural frequency and the forcing one. Figure 3.48 shows the time variation of the lift coefficient as well as the corresponding Fourier analysis for a typical case representing the transition regime. Figure 3.48a shows a change of frequency approximately every two cycles. The larger amplitudes occurs at the forcing frequency and the smaller amplitudes at the natural frequency. The Fourier analysis of C_L (Figure3.48b) shows the equal existence of the two frequencies (S and S_o). Vortex shedding at alternating frequencies at the boundary in between lock on and unlock-on regimes has been observed experimentally by Stansby [60] and numerically by Karniadakis [62]. The far wake analysis of the same case is shown in Figure 3.49 where the variation of tangential velocity component U_θ with time is presented (Figure 3.49a) and the corresponding Fourier analysis (Figure 3.49b). The same two intermittent frequencies are clearly shown (S and S_o) as before.

The effect of oscillation amplitude on the lock-on frequency range has shown to be very significant. The larger the amplitude of oscillation the wider the lock-on frequency range. As the amplitude decreases, the lock-on frequency range becomes narrower until it reaches zero at a threshold amplitude Θ_{A1}. In this study, the numerical experiments has shown that for all amplitudes less than $\pi/40$, the vortices shed at the natural frequency regardless of the forcing frequency. However, the exact threshold value is not known. The conclusion that there is a threshold value above which the lock on regime is possible is in agreement with the findings of Koopman [70] for the case of transverse oscillation.

Increasing the lock-on frequency range with the amplitude means that at any fixed frequency there is a unique threshold amplitude above which the synchronized regime is possible. To clarify this fact, the lift record is examined at Re=200 and F_R=0.5 and for the four amplitudes $\Theta_A = \pi / 8, \pi / 4, \pi / 2$ and π. The two amplitudes $\Theta_A = \pi / 8$ and $\Theta_A = \pi / 4$ resulted in a non lock-on regime, with the lift coefficient fluctuating at almost the natural frequency in a beating wave form as shown in Figure 3.50. As the amplitude elevated to $\Theta_A = \pi / 2$, the regime is still a unlock-on (Fourier analysis revealed domination of natural frequency in the far wake) with clear signs for transition to lock-on regime, which does occur at $\Theta_A = \pi$. The threshold amplitude at this frequency ratio lies between $\Theta_A = \pi / 2$ and $\Theta_A = \pi$. No attempt, however, has been made to determine exactly the value of the amplitude at which the regime becomes completely synchronized with the cylinder oscillation.

At higher amplitudes $\Theta_A > \Theta_{A2}$ (where Θ_{A2} lies between $\pi / 4$ and $\pi / 2$), an interesting phenomenon is obtained. That is, at frequencies greater than the upper boundary for the periodic lock-on regime, the near wake synchronize with the cylinder oscillation (i.e vortices shed at the imposed frequency) while the far wake response approaches gradually the unlock-on regime as the imposed frequency increases. This gradual "breakup" in the far wake synchronized structure with the increase of forcing frequency was observed in the flow visualization made by Tokumaru [23]. To clarify this phenomenon, both the near and far wakes are examined at Re=200 , $\Theta_A = \pi / 2$ and for four different frequency ratios, namely F_R=1.11, F_R=1.5, 2 and F_R=3. The lift record for these cases are shown in Figures 3.51(a-d). Plotted in the same figures is the cylinder surface velocity and the traces of

tangential velocity component in the far wake. Figure 3.51a shows clearly that both the near wake (represented by lift coefficient) and far wake (represented by tangential velocity) oscillate at the imposed frequency (represented by cylinder velocity). This indicates that at this frequency a periodic lock-on regime is obtained. As the frequency increases to $F_R=1.5$ Figure 3.51b shows clearly that only the near wake is synchronized while the far wake structure is showing a transition between lock-on and unlock-on regimes. As the frequency increases further to $F_R=2$ and 3 (Figure 3.51c,d) the near wake response is still synchronized whereas, the far wake response switches to a non lock-on regime where the natural frequency dominates.

The flow and thermal fields for the case of Re=200, $\Theta_A=\pi/2$ and $F_R=2$ at equal time steps during a complete cycle are presented in Figures 3.52-3.54. The streamline plots for this case (Figure 4.52) show that the near wake structure shows vortices shedding alternately at the forcing frequency. These generated vortices, however, coalesce and evolve into a structure with a lower frequency in the far wake as shown in the same figure. The equivorticity pattern for the same case shows that the vortices in the far wake are separated by a larger distance than that in the near wake. The coalescence of vortices is clearly shown in Figures 3.53 b, c and d. The isotherm plots for the same case show the unsteady thermal wake. The shape of this thermal wake is similar to the shape of the vortex street. Moreover, the frequency of thermal field in the near wake as well as in the far wake is equal to the corresponding ones for the flow field.

Based on the obtained results in the range considered of parameters, one can sketch the frequency selection diagram in the frequency-amplitude plane, as shown in Figure 3.55. The

diagram gives only a qualitative summary of the response states in the wake. However, an exact quantitative diagram is prohibitively expensive, requiring a huge amount of computations. The features of the main regions in the diagram can be summarized as follows :

1. For amplitudes $\Theta_A < \Theta_{A1}$ the unlock-on regime is prevailing with vortices shedding at natural frequency regardless of the forcing frequencies.

2. For amplitudes between Θ_{A1} and Θ_{A2}, one can distinguish four limiting frequencies, namely, f_{b1} , f_{b2}, f_{b3}, and f_{b4} (see Figure 3.55). These frequencies mark the transition between different wake-flow regimes. The upper and lower boundaries of the lock-on region are given by f_{b3}, and f_{b2} respectively. On the other hand, the figure indicates two receptivity regions identified by f_{b2} to f_{b1} and f_{b3} to f_{b4}. The range of frequencies between f_{b2} and f_{b3} is a periodic lock-on region labeled L in the figure. At the outskirts of this region exist two regions (K and M) characterized by a transition regimes. In these regimes, the vortex shedding frequency switches back and forth between two limits; the first is the natural frequency and the second is the forcing frequency. Forcing frequencies less than f_{b1} or greater than f_{b4}, result in unlock-on regimes, regions (G and N).

3. At amplitudes greater than Θ_{A2} and forcing frequencies greater than upper boundaries of the lock-on region, the near wake is locked-on to the forcing frequency whereas, the far wake either has a transition regime, region (H) or a non-lock-on regimes, region (R) .
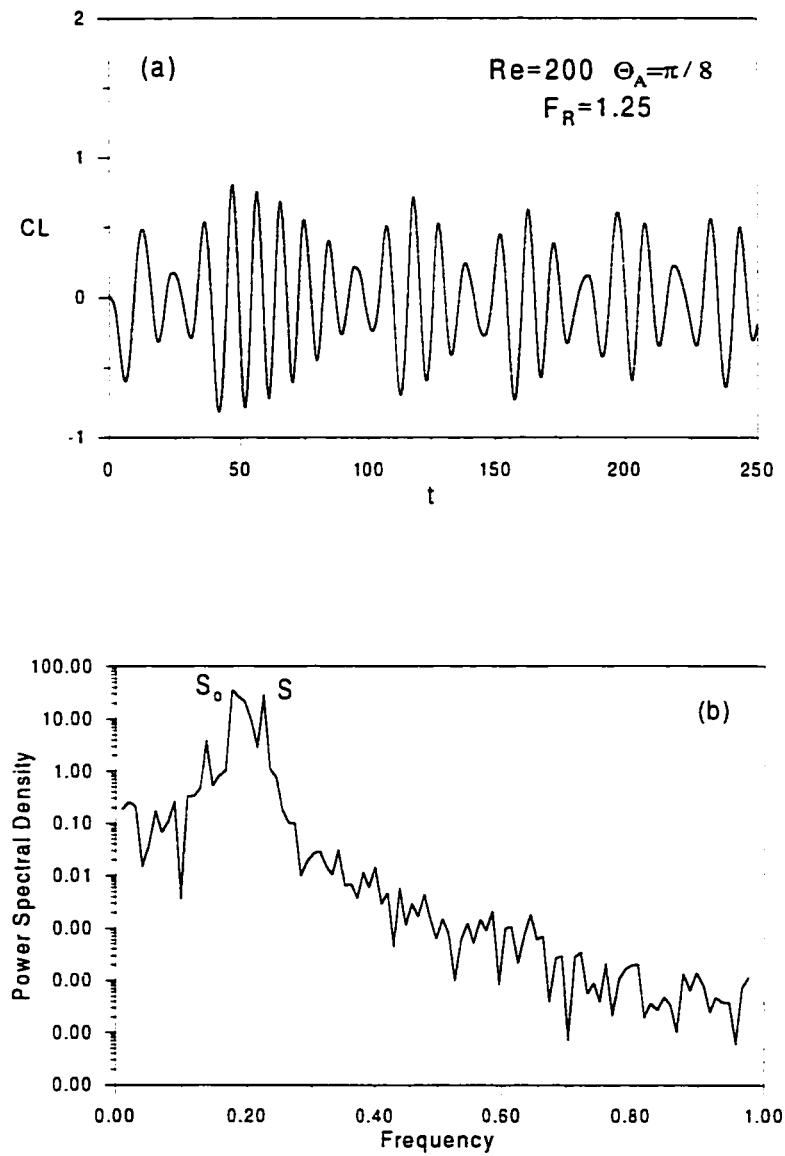
Figure 3.48 The time variation of lift coefficient and corresponding Fourier analysis : a) lift coefficient b) Fourier analysis.
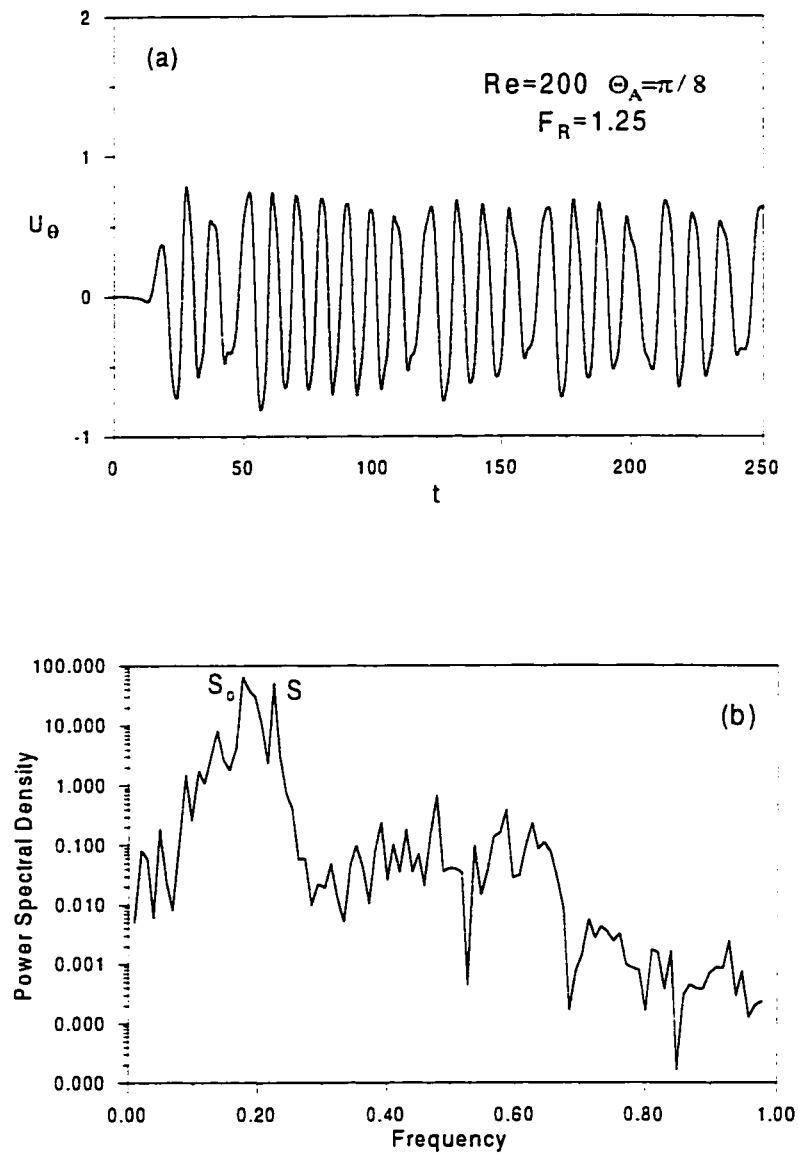
Figure 3.49 Time traces of angular velocity at point (r=10, θ = 0) and corresponding Fourier analysis : a) angular velocity b) Fourier analysis.
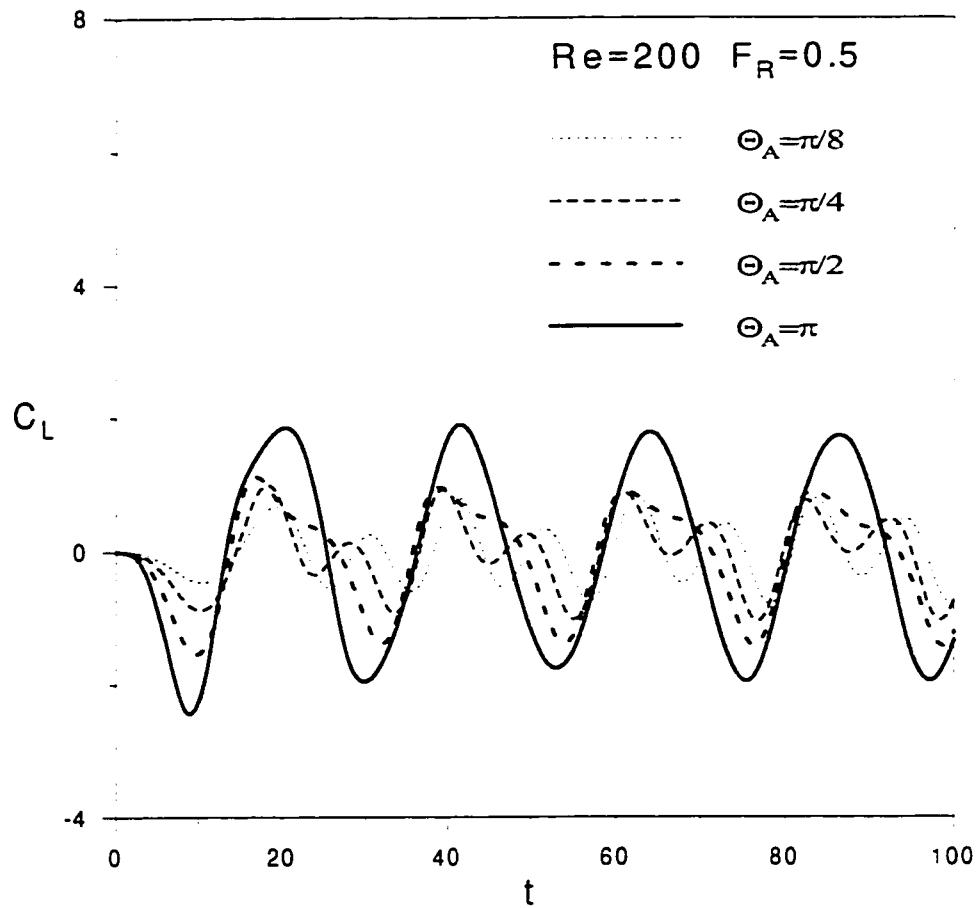
Figure 3.50 Effect of oscillation amplitude on the
time variation of lift coefficient
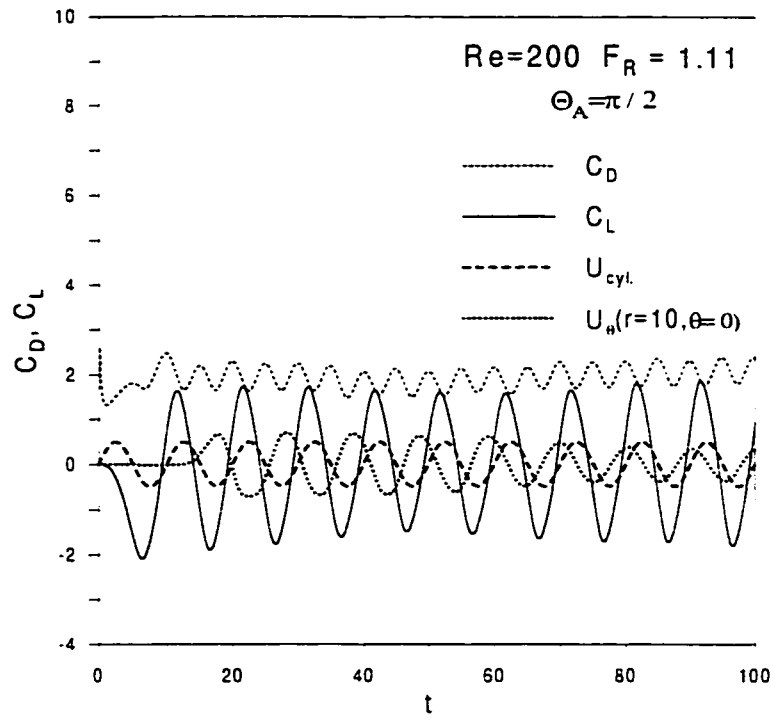
Figure 3.51 a
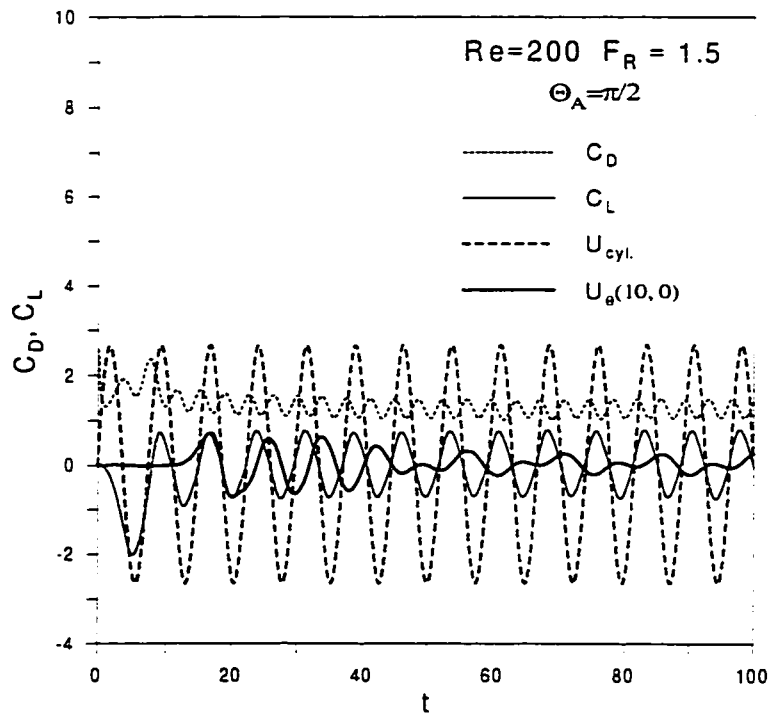
Figure 3.51 b
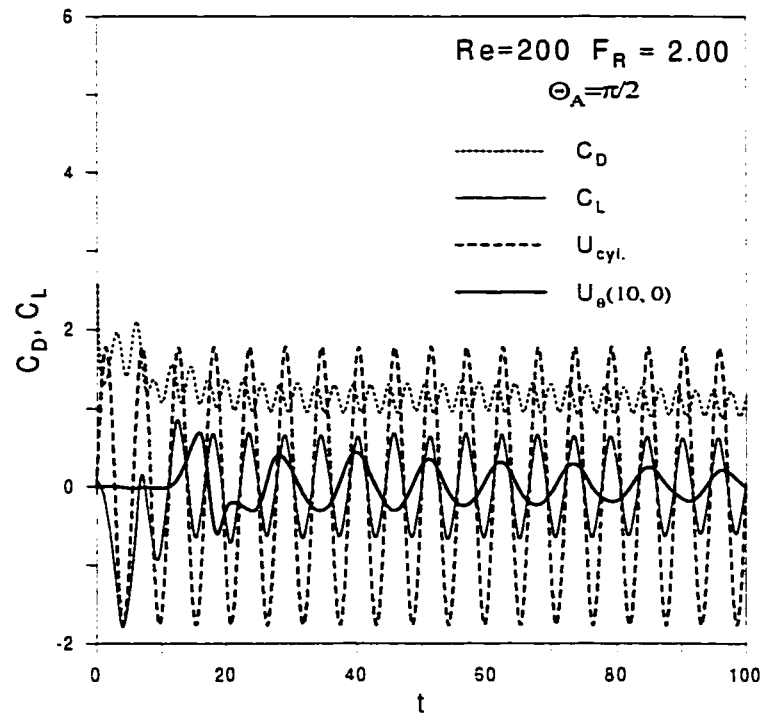
Figure 3.51 c
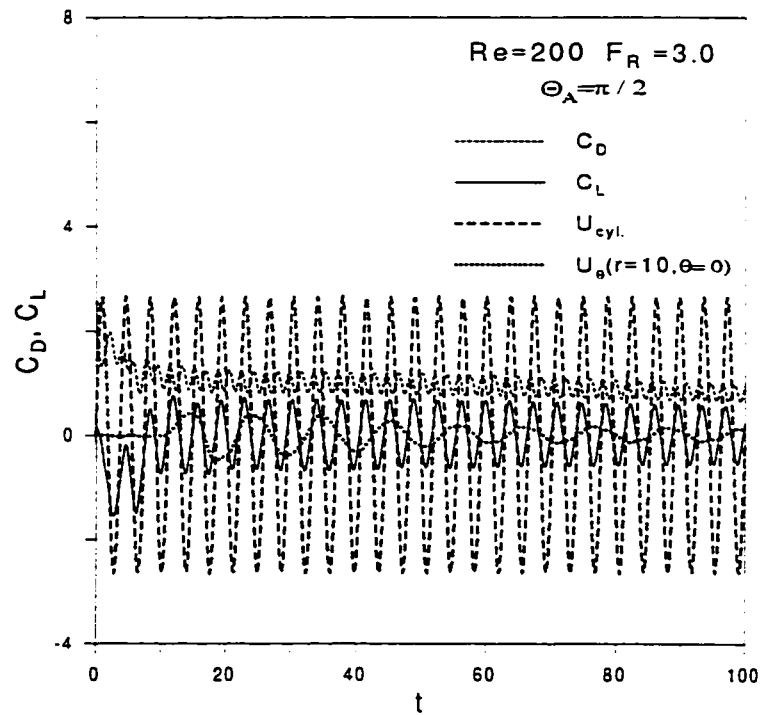
Figure 3.51 d

Figure 3.51 The time variation of drag and lift coefficients as well as time traces of angular velocity at point ($r = 10$, $\theta = 0$) at Re=200, $\Theta_A = \pi/2$
a) $F_R = 1.11$, b) $F_R = 1.5$, c) $F_R = 2$ and d) $F_R = 3$
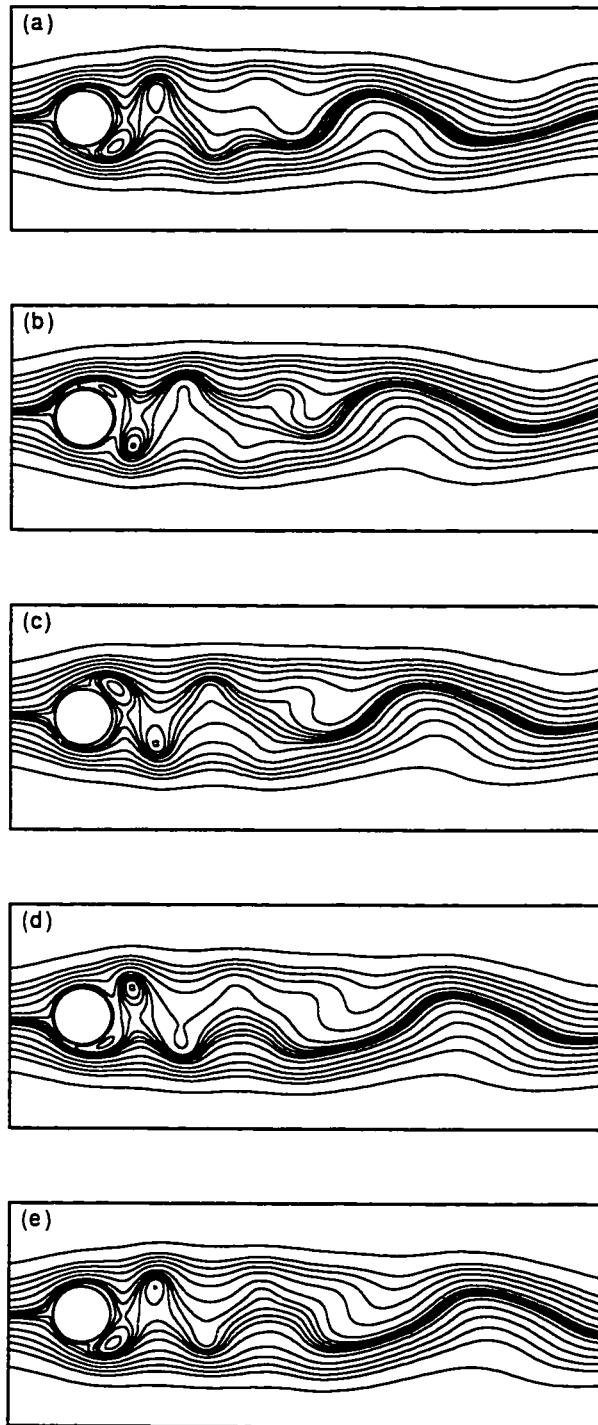
Figure 3.52 Streamlines patterns in a complete cylinder cycle
for the case of Re=200, $\Theta_A = \pi / 2$ and $F_R=2$.
a) $t=t_o$, b) $t=t_o+1/4T_p$ c) $t=t_o+1/2T_p$ (d) $t=t_o+3/4T_p$ (e)$t=t_o+T_p$,
where $T_p =5.55$ is the time period of cylinder oscillation cycle
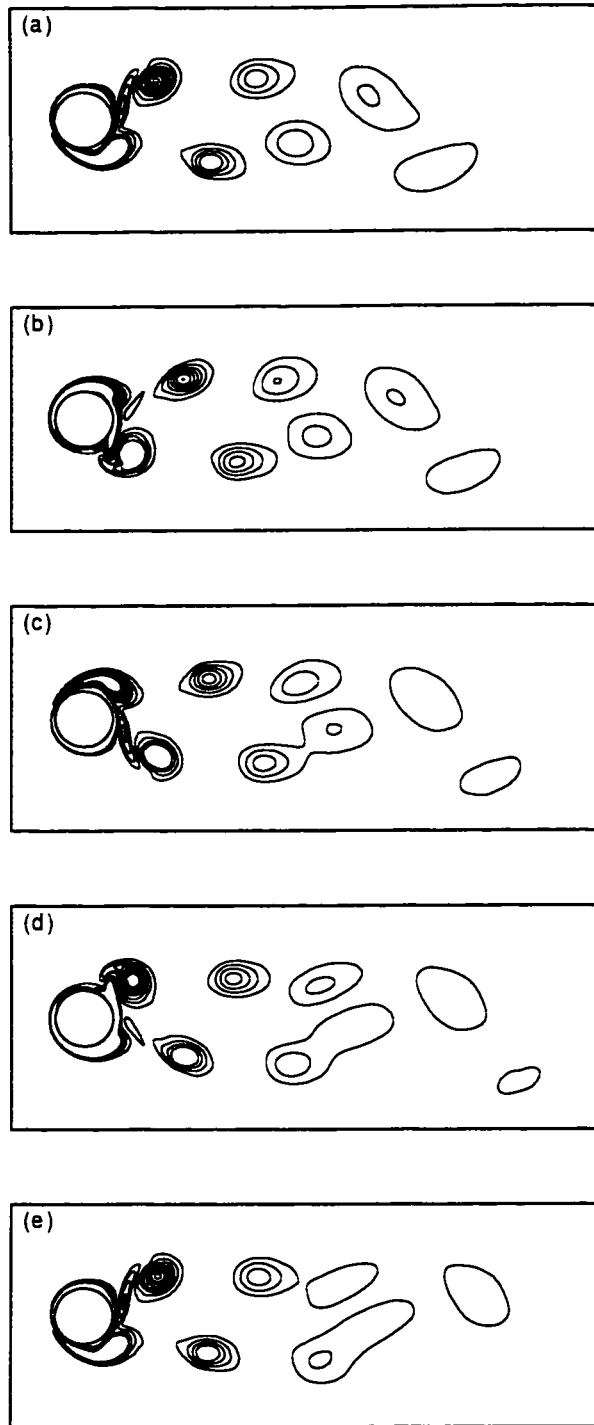
Figure 3.53 Vortex patterns in a complete cylinder cycle
for the case of Re=200, $\Theta_A = \pi / 2$ and $F_R=2$.
a) $t=t_o$, b) $t=t_o+1/4T_p$ c) $t=t_o+1/2T_p$ (d) $t=t_o+3/4T_p$ (e)$t=t_o+T_p$,
where $T_p =5.55$ is the time period of cylinder oscillation cycle
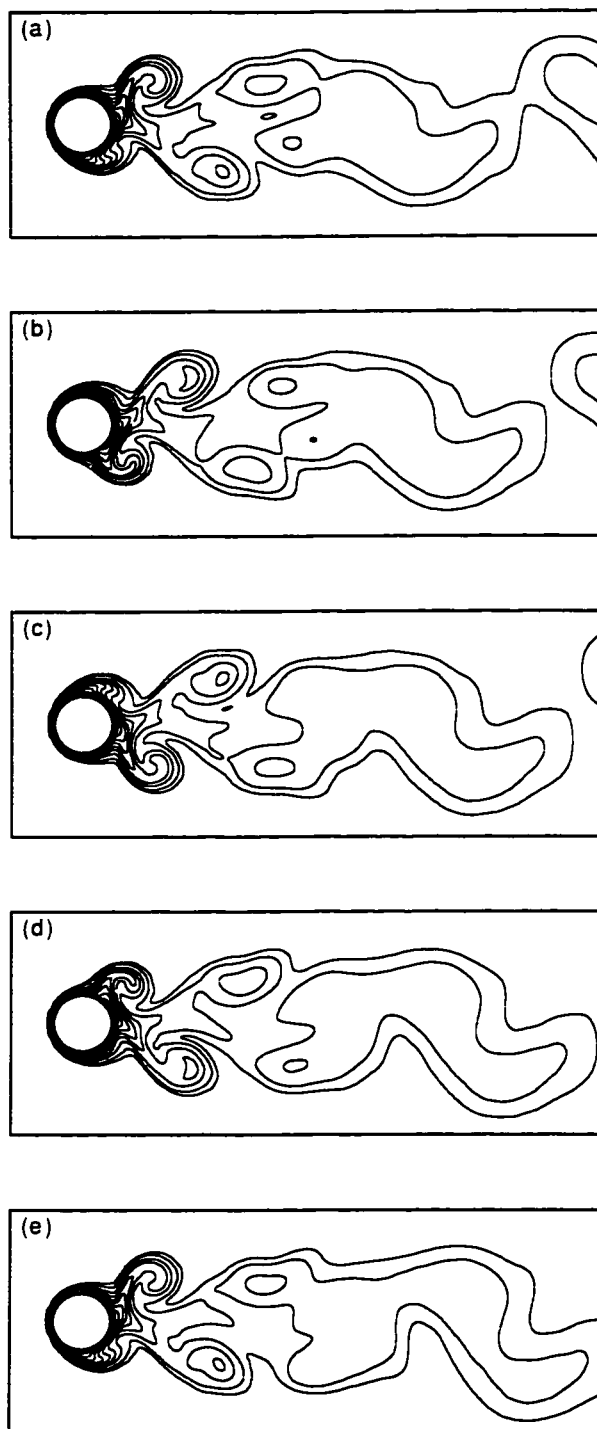
Figure 3.54 Isotherms patterns in a complete cylinder cycle
for the case of Re=200, $\Theta_A = \pi / 2$ and $F_R=2$)
a) t=t$_o$, b) t=t$_o$+1/4T$_p$ c) t=t$_o$+1/2T$_p$ (d) t=t$_o$+3/4T$_p$ (e)t=t$_o$+T$_p$,
where T$_p$ =5.55 is the time period of cylinder oscillation cycle

Figure 3.55 Laminar wake response state selection diagram

CHAPTER 4

HEAT CONVECTION FROM A CYLINDER PERFORMING STEADY OR OSCILLATORY ROTARY MOTION IN A QUIESCENT FLUID

The problem considered in this chapter is the heat convection from a horizontal cylinder performing steady or rotary motion in a quiescent fluid. The physical system to be considered is shown in Figure 4.1 consisting of an isothermal horizontal circular cylinder of infinite length and radius c placed in a quiescent fluid at temperature T_x. The cylinder rotates either steadily with constant angular speed or performs angular harmonic oscillations. The cylinder surface velocity may be written as

$$U'_w = \begin{cases} U'_{st} & \text{for steady rotation} \\ U'_{os} \sin(2\pi ft') & \text{for rotationl oscillaton} \end{cases} \tag{4.1}$$

where U'_{st} is steady surface velocity ($= \omega_{st}c$), U'_{os} is the amplitude of oscillating surface velocity ($= \omega_{os}c$), f is the oscillation frequency and t' is the time. The effect of temperature variation on the fluid properties are considered negligible except for the body force term in the momentum equation. The flow is assumed two dimensional and radiation and viscous dissipation effects are neglected. The fluid motion is mainly due to cylinder rotation as well as buoyancy forces.
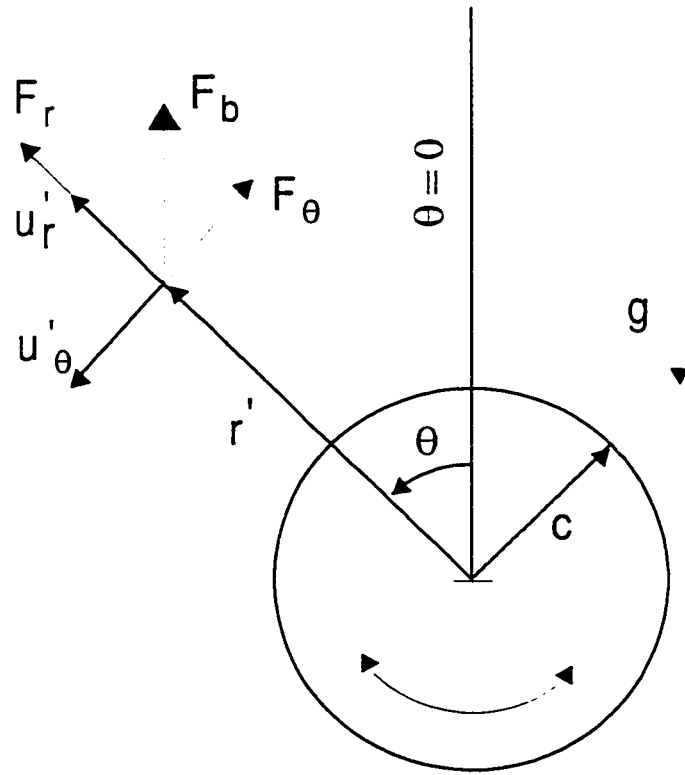
Figure 4.1 Coordinate System

4.1 The Governing Equations

The governing equations for the present problem are the same as that mentioned in chapter 3 with the addition of buoyancy effects to the momentum equations. In stream function-vorticity form the governing equations can read the following :

$$\frac{\partial \zeta'}{\partial t} + u'_r \frac{\partial \zeta'}{\partial r'} + \frac{u'_\theta}{r'} \frac{\partial \zeta'}{\partial \theta} = \nu \nabla^2 \zeta' + \frac{1}{\rho} \left(\frac{\partial F_\theta}{\partial r'} + \frac{F_\theta}{r'} - \frac{1}{r} \frac{\partial F_r}{\partial \theta} \right) \tag{4.2}$$

$$\zeta' = -\nabla^2 \psi' \tag{4.3}$$

$$\frac{\partial T}{\partial t} + u'_r \frac{\partial T}{\partial r'} + u'_\theta \frac{\partial T}{r' \partial \theta} = \frac{k}{\rho c_p} \nabla^2 T \tag{4.4}$$

F_r and F_θ represent the radial and angular components of the buoyancy force and are defined as

$$F_r = \rho g \beta (T - T_\infty) \cos(\theta)$$

$$F_\theta = -\rho g \beta (T - T_\infty) \sin(\theta)$$

Using the modified polar coordinates (ξ, θ) where $\xi = \ln r$ and θ is angular coordinate, the equations of motion and energy can be written in terms of the dimensionless vorticity, stream function and temperature as :

$$e^{2\xi} \frac{\partial \zeta}{\partial t} = \left(\frac{\partial^2 \zeta}{\partial \xi^2} + \frac{\partial^2 \zeta}{\partial \theta^2} \right) - \frac{\partial \psi}{\partial \theta} \frac{\partial \zeta}{\partial \xi} + \frac{\partial \psi}{\partial \xi} \frac{\partial \zeta}{\partial \theta}$$
$$+ \frac{1}{8} e^\xi Gr \left[\frac{\partial \phi}{\partial \xi} \sin \theta + \frac{\partial \phi}{\partial \theta} \cos \theta \right] \tag{4.5}$$

$$e^{2\xi} \zeta = \frac{\partial^2 \psi}{\partial \xi^2} + \frac{\partial^2 \psi}{\partial \theta^2} \tag{4.6}$$

$$e^{2\xi} \frac{\partial \phi}{\partial t} = \frac{1}{Pr} \left(\frac{\partial^2 \phi}{\partial \xi^2} + \frac{\partial^2 \phi}{\partial \theta^2} \right) - \frac{\partial \psi}{\partial \theta} \frac{\partial \phi}{\partial \xi} + \frac{\partial \psi}{\partial \xi} \frac{\partial \phi}{\partial \theta} \tag{4.7}$$

where Pr is prandtl number ($= \nu / \alpha$) and Gr is the Grashof number [$= 8g\beta(T_w - T_x)c^3 / \nu^2$].

The variables t, ψ, ζ and ϕ are the dimensionless time, stream function, vorticity and temperature and are defined as

$$t = t'c^2 / \nu, \quad \psi = \psi' / \nu, \quad \zeta = -\zeta'c^2 / \nu \text{ and } \phi = (T - T_x)/(T_w - T_x)$$

The dimenstionless radial and transverse velocity components u_r, u_θ are defined as

$$u_r = u_r'c / \nu = e^{-\xi}\partial\psi / \partial\theta, \qquad u_\theta = u_\theta'c / \nu = -e^{-\xi}\partial\psi / \partial\xi$$

where primes denote dimensional velocities. The dimensionless surface velocity is defined as:

$$U_w = U_w'(c) / \nu = \frac{1}{2} \begin{cases} Re_{st} & \text{for steady rotation} \\ Re_{os} \sin(\pi St) & \text{for rotational oscillation} \end{cases}$$

where Re_{st} ($=2cU_{st}/\nu$) and Re_{os} ($=2cU_{os}/\nu$) are the Reynolds numbers for the two cases based on steady and maximum amplitude surface velocities respectively, and $S = 2fc^2 / \nu$ is the dimensionless oscillation frequency.

The boundary conditions for ψ, ζ and ϕ are based on the no-slip, impermeability and isothermal conditions on the cylinder surface and the ambient conditions far away from it. These conditions can be expressed as

at $\xi = 0$, $\psi = 0$, $\partial\psi/\partial\theta = 0$,

$$-2\partial\psi/\partial\xi = \begin{cases} Re_{st} & \text{for steady rotation} \\ Re_{os} \sin(\pi St) & \text{for rotational oscillation} \end{cases} \text{ and } \phi = 1 \qquad (4.8a)$$

The ambient static conditions far away from the cylinder surface are given by

$$-e^{-\xi} \partial\psi/\partial\xi \to 0, \quad e^{-\xi}\partial\psi/\partial\theta \to 0, \quad \zeta \to 0 \text{ and } \phi \to 0, \qquad (4.8b)$$

4.2 The Method of Solution

The method of solution is similar to that used in chapter 3. The three sets of differential equations (similar to those deduced in chapter 3 Eqns. 3.17-3.19) can be written as :

$$\frac{\partial^2}{\partial \xi^2} \begin{pmatrix} F_o \\ F_n \\ f_n \end{pmatrix} - n^2 \begin{pmatrix} 0 \\ F_n \\ f_n \end{pmatrix} = e^{2\xi} \begin{pmatrix} G_o \\ G_n \\ g_n \end{pmatrix} \qquad (n = 1, , N) \qquad (4.9)$$

$$e^{2\xi} \frac{\partial}{\partial t} \begin{pmatrix} G_o \\ G_n \\ g_n \end{pmatrix} = \frac{\partial^2}{\partial \xi^2} \begin{pmatrix} G_o \\ G_n \\ g_n \end{pmatrix} - n^2 \begin{pmatrix} 0 \\ G_n \\ g_n \end{pmatrix} + \begin{pmatrix} S_o \\ S_{n1} \\ S_{n2} \end{pmatrix} \qquad (n = 1, , N) \qquad (4.10)$$

$$e^{2\xi} \frac{\partial}{\partial t} \begin{pmatrix} H_o \\ H_n \\ h_n \end{pmatrix} = \frac{1}{Pr} \frac{\partial^2}{\partial \xi^2} \begin{pmatrix} H_o \\ H_n \\ h_n \end{pmatrix} - \frac{n^2}{Pr} \begin{pmatrix} 0 \\ H_n \\ h_n \end{pmatrix} + \begin{pmatrix} R_o \\ R_{n1} \\ R_{n2} \end{pmatrix} \qquad (n = 1, , N) \qquad (4.11)$$

where S_o, S_{n1}, S_{n2}, R_o, R_{n1} and R_{n2} are all easily identifiable functions of ξ and t and are found in appendix A2. The boundary conditions for all functions present in equations (4.9)-(4.11) are obtained from equations (4.8) and can be expressed as

at $\xi = 0$

$$F_o = F_n = f_n = h_n = H_n = 0, \quad H_o = 2, \quad \frac{\partial F_n}{\partial \xi} = \frac{\partial f_n}{\partial \xi} = 0$$

$$\frac{\partial F_o}{\partial \xi} = \begin{cases} -Re_{st} & \text{for steady rotation} \\ -Re_{os} \sin(\pi St) & \text{for rotational oscillation} \end{cases} \qquad (4.12a)$$

and as $\xi \rightarrow \infty$

$$F_o, \ F_n, \ f_n, \ G_o, \ G_n, \ g_n, \ H_0, \ H_n, \ h_n \rightarrow 0$$

$$\text{and} \qquad e^{-\xi} \frac{\partial F_n}{\partial \xi} = e^{-\xi} \frac{\partial f_n}{\partial \xi} = 0 \qquad (4.12b)$$

Integrating both sides of equation (4.9) with respect to ξ from $\xi=0$ to $\xi=\infty$ and using the boundary conditions in equation (4.12) gives the following integral conditions:

$$\int_0^\infty e^{2\xi} G_o \, d\xi = \begin{cases} Re_{st} & \text{for steady rotation} \\ Re_{os} \sin(\pi St) & \text{for rotational oscillation} \end{cases} \qquad (4.13a)$$

$$\int_0^\infty e^{2\xi} G_n \, d\xi = 0 \qquad (4.13b)$$

$$\int_0^\infty e^{2\xi} g_n \, d\xi = 0 \qquad (4.13c)$$

The above integral conditions are used for calculating the values of the functions G_o, g_n and G_n on the cylinder surface (i.e. $\zeta_{\xi=0}$) not only to get a better accuracy but also to satisfy the periodicity of the pressure around the cylinder surface.

In order to advance the solution of ψ, ζ and ϕ in time, the initial condition at time t=0 must be known. In this problem, the cylinder is assumed to be impulsively rotated and instantaneously heated. The initial conditions which simulate the physical situation for ψ and ζ where no fluid motion is present can be written as:

at $\xi=0$,

$$F_o = F_n = f_n = 0, \qquad \frac{\partial F_o}{\partial \xi} = \begin{cases} -Re_{st} & \text{steady rotation} \\ 0 & \text{rotational oscillation} \end{cases}$$

$$F_o = F_n = f_n = G_o = G_n = g_n = 0 \qquad 0 < \xi < \infty \qquad (n = 1,2, \ ,N) \qquad (4.14)$$

The time-dependent solution starts when the cylinder surface is suddenly heated to a uniform temperature T_w. The instantaneous temperature rise at time t=0 results in $\phi=1$ on the cylinder surface and $\phi=0$ everywhere in the rest of the domain. The initial conditions are obtained as

$$H_o = 2, \quad H_n = h_n = 0 \quad \text{at} \quad \xi = 0$$
$$H_o, \ H_n, \ h_n \rightarrow 0 \qquad 0 < \xi < \infty \qquad (4.15)$$

4.3 Local and Average Nusselt Numbers

The local and average Nusselt numbers are defined as

$$Nu = 2ch/k, \qquad \overline{Nu} = 2c\overline{h} / k$$

where h, $\overline{h}$ are the local and average heat transfer coefficients defined as

$$h = \dot{q} / (T_s - T_\infty) , \qquad \dot{q} = -k(\partial T / \partial r')_{r'=c}$$

and ,

$$\overline{h} = \frac{1}{2\pi} \int_0^{2\pi} h \, d\theta$$

where $\dot{q}$ is the rate of heat transfer per unit area. From the above definitions one can

deduce the relation between Nu , $\overline{Nu}$ and the functions H_0 ,H_n , h_n which can be written

as:

$$Nu = -2 \left(\frac{\partial \phi}{\partial \xi} \right)_{\xi=0} = -\left[\frac{\partial H_0}{\partial \xi} + 2 \sum_{n=1}^{N} \left(\frac{\partial h_n}{\partial \xi} \sin n\theta + \frac{\partial H_n}{\partial \xi} \cos n\theta \right) \right]_{\xi=0} \qquad (4.16)$$

and

$$\overline{Nu} = -\left(\frac{\partial H_0}{\partial \xi} \right)_{\xi=0} \qquad (4.17)$$

the time-averaged Nusselt number can obtained as follows

$$\overline{\overline{Nu}} = \frac{1}{(t_2 - t_1)} \int_{t1}^{t2} \overline{Nu} \, dt \qquad (4.18)$$

where t_1 and t_2 are the time at the beginning and at the end of last two cycles of oscillation

respectively. Although the differential equations (4.8-4.10) and the boundary and integral

conditions 4.11 and 4.12 are different from those deduced in chapter 3, the numerical

procedure is almost the same and therefore will not be discussed again.

4.4 Results and Discussion

In order to ascertain the validity of the mathematical model as well as the numerical technique, the problem of natural convection from a fixed cylinder is first studied and the obtained results are compared with the numerical and experimental results available in the literature. Figure 4.2 shows a comparison between the present computations for the time variation of $\overline{Nu}$ with the numerical results of Wang et al. [12] at Ra=10. The time scale in the present calculations is modified to match the time scale considered in their work. It can be seen that the agreement is good specially when approaching steady state at large time. Figure 3a shows a comparison at low Rayleigh number (Ra=0.37) between present computations for local Nusselt number and the experimental and numerical results obtained by Fujii et al. [13]. In the same figure, the bench mark solution obtained by Saitoh et al. [14] is also plotted. The figure shows an excellent agreement with both references. Figure 3b shows another comparison at relatively high Rayleigh number (Ra=1000) between the present results and both numerical results of Saitoh et al. [14] and the results obtained by Kuehn and Goldstein [15]. The agreement is fairly good, however, there is a difference not exceeding 5% with reference[15] at angle $\theta = 180°$ (front stagnation point). This difference may be attributed to the questionable assumptions of inflow-outflow outer boundary conditions adopted in [15].
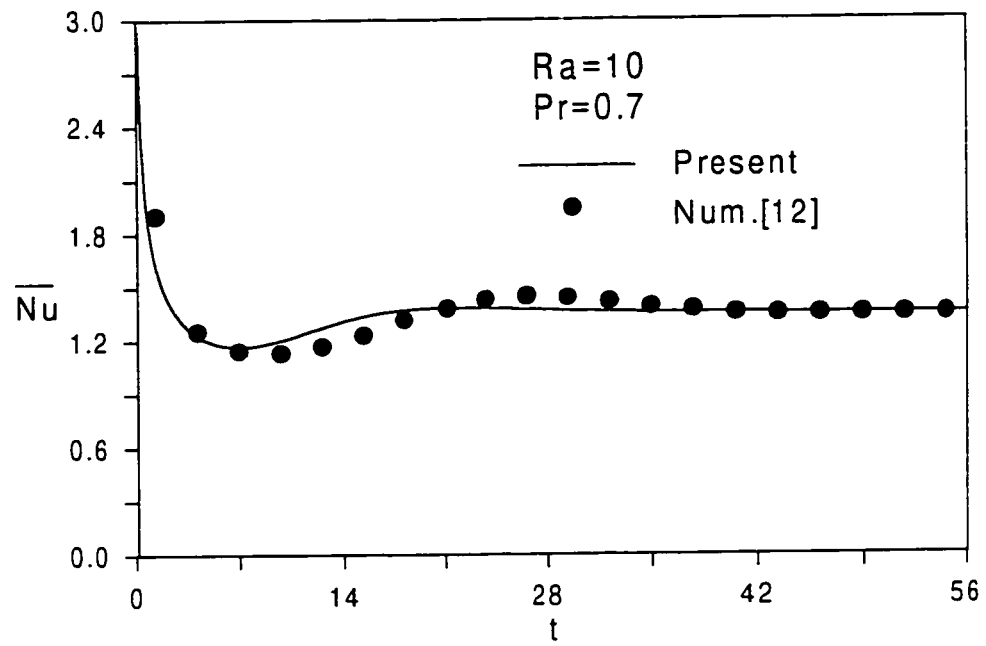
Figure 4.2 Comparison between present work and Numerical work of [12]
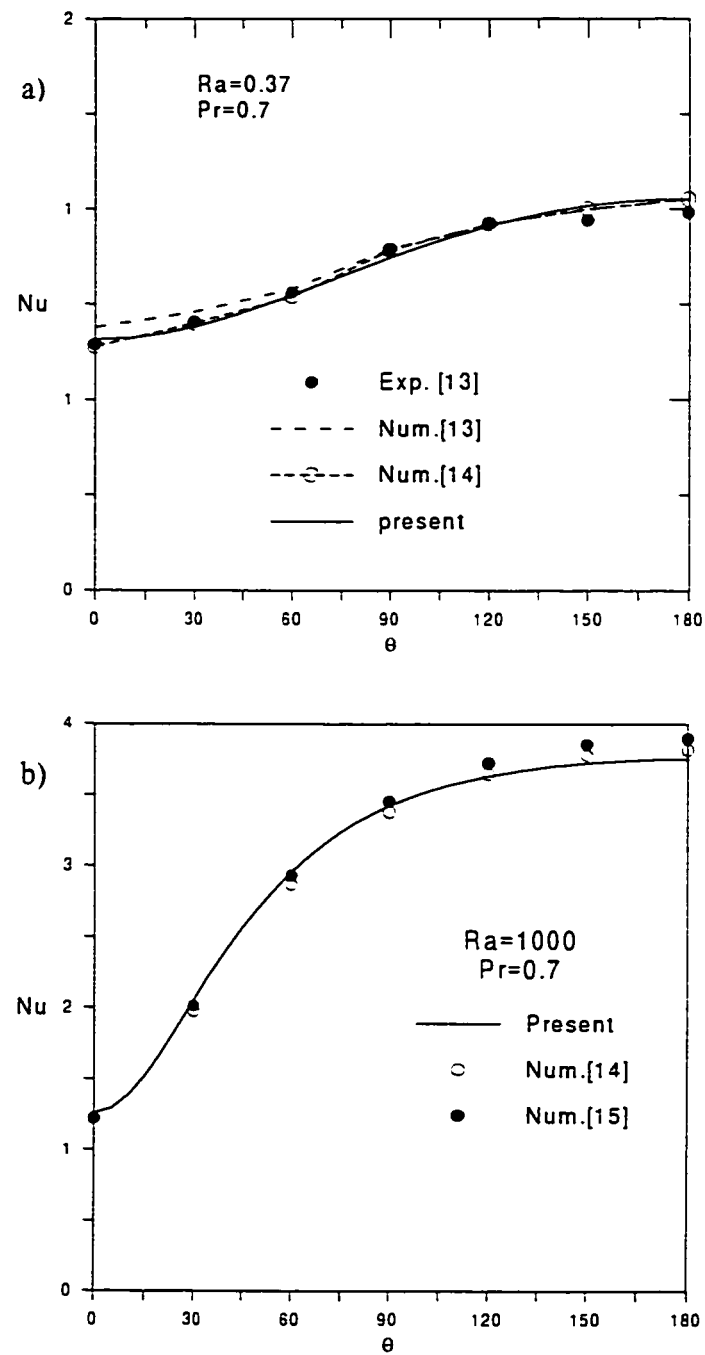
Figure 4.3 Comparison between present results for Nu with that of
a) references [13] and [14]   b) references [14] and [15]

4.4.1 Steady Rotating Cylinder

The effect of steady rotation on heat convection is studied for Ra up to 10^3 and Re_{st} up to 400. Figure 4.4 shows the time variation of $\overline{Nu}$ at $Re_{st}=100$ and for different values of Ra. Immediately after the cylinder temperature is increased, the heat transfer coefficient is initially high due to high temperature gradient near the surface. In this early time stages, the conductive mode of heat transfer dominates with isotherm contours are almost concentric circles. Furthermore, following the sudden rotation and due to the no-slip condition the fluid layer adjacent to the cylinder wraps it and rotates with almost the same angular velocity. The heat transfer through that layer is only due to conduction. A quick decrease in heat transfer rate occurs during this early stage until it reaches a minimum at a certain critical time. Beyond this critical time, the buoyancy force start developing, causing the fluid to set in motion and hence transition to the convective mode. The transition from conduction to convection for this case is in the form of overshoot. At later times, the buoyancy force effect dominates and the heat transfer rate gradually approaches its final steady value. The time needed to reach steady state at a certain value of Re_{st} depends on Ra. The higher the Ra, the faster and stronger the effect of convection and hence the smaller the time needed to reach steady state.

Figures 4.5a and 4.5b show the effect of Ra on $\overline{Nu}$ at constant Re_{st} together with a comparison with the experimental results obtained by Etemad [4]. Using logarithmic coordinates for both Ra and $\overline{Nu}$ results in a straight line variation for $\overline{Nu}$ as shown in the figures. The figures also show small differences at low Rayleigh numbers, however, these differences increase with increasing Rayleigh number until reaching a maximum of about
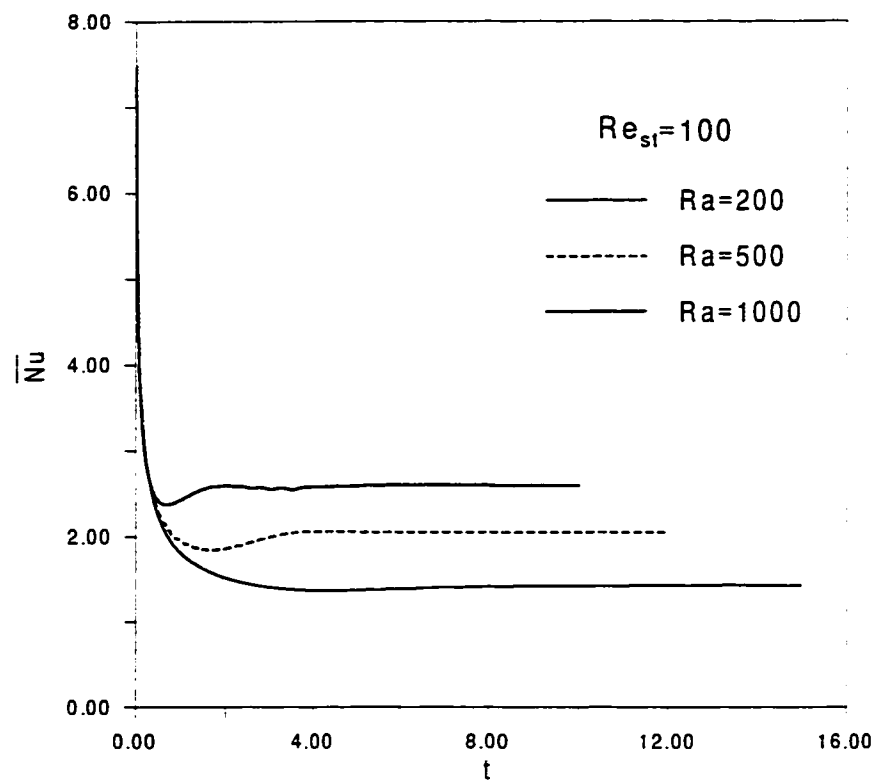
Figure 4.4 Effect of Rayleigh number Ra on the time variation of the average Nusselt number for steady rotating cylinder at $Re_{st}=100$.
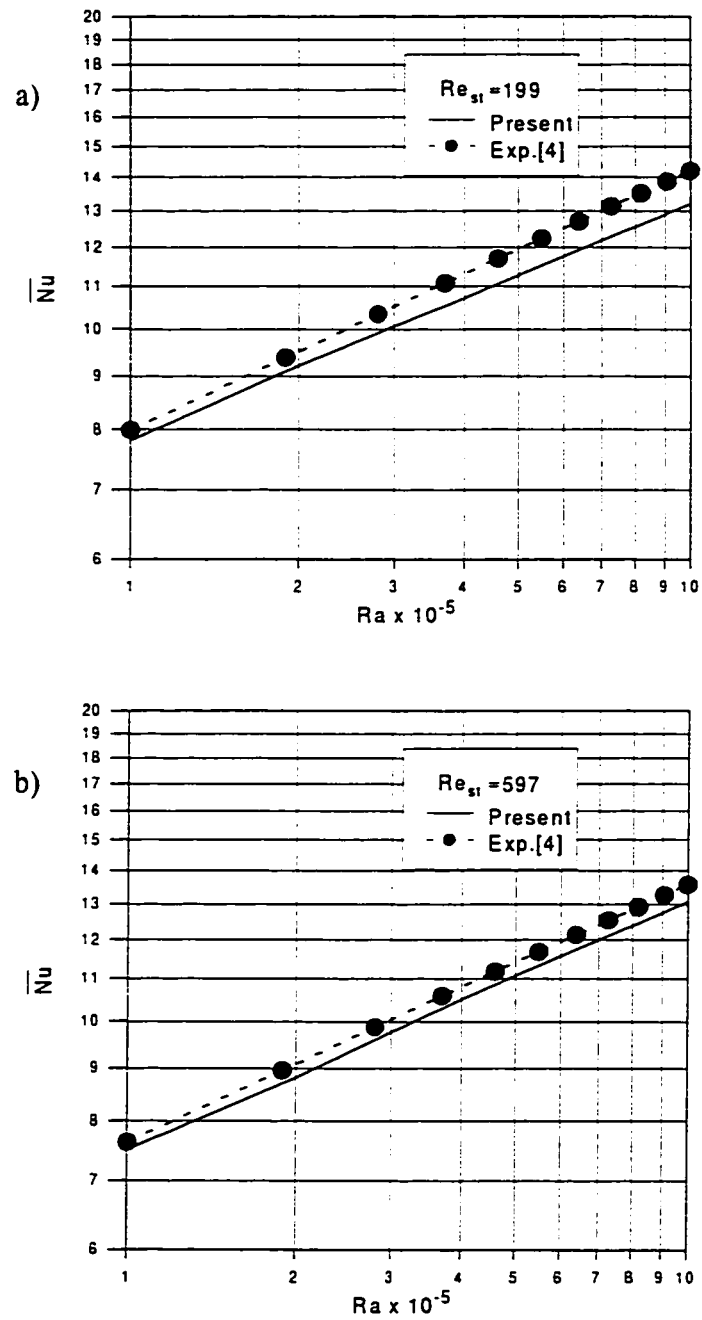
Figure 4.5 Comparison between present work and the
experimental work of [4] at a) Re_{st}=199, b)Re_{st}=497

8% at Re_{st} =199 and Ra = 10^6. This comparison provides a further check for the present computational scheme and confirms consistency with the findings of Etemad [4].

Figure 4.6 shows the time variation of $\overline{Nu}$ at Ra=500 and different values of Rotation. At early time stages, and due to domination of conduction mode, the effect of Re_{st} on heat transfer is insignificant. As time goes, the effect of convection starts with observable effect of Re_{st} on the heat rate. At later times, the steady state heat rate is reached. The time needed to reach this steady state value increases as Re_{st} increases. In a previous study, Badr and Ahmed [8] found that for $Ra/PrRe^2$ less than 0.3, the steady state condition was not reached in the range of time considered in their work. However, the time scale used in the present study allows to advance the solution enough in time to reach steady state for all $Ra/PrRe^2$ considered. The value of steady Nusselt number, as shown in Figure 4.6 decreases as Re_{st} increases namely, increasing Re_{st} from 100 to 400 decreases the $\overline{Nu}$ from 2.05 to 1.07 (i.e about 49%) in the case of Ra=500 . This trend is consistent with the experimental results of Etemad [4].

The details of the steady flow and thermal fields are presented in Figures 4.7-4.10 (for the cases of Ra=10^3 and Re_{st}=0, 20, 100 and 200 respectively) in the form of streamlines and constant temperature contours. The streamlines of the symmetrical case of Re_{st}=0 (Figure 4.7a) show two large counter-rotating vortices in the downstream side of the cylinder while the constant temperature contours (Figure 4.7b) show a mushroom-type isotherm pattern. The local Nusselt number distribution for this case is shown in Figure 4.11 where Nu is maximum at θ = 180° (the front stagnation point) and is minimum at θ = 0 . At a small speed of rotation (Re_{st}=20), the streamlines are slightly shifted counter-clockwise and the

same occurs for the isotherms (Figures 4.8a and 4.8b) resulting in a non-symmetrical local Nusselt number distribution as shown in Figure 4.11. Increasing the rotational speed further to Re_{st}=100 makes both velocity and thermal fields more dominated by cylinder rotation as shown in Figure 4.9a and 4.9b. The points of maximum and minimum local Nusselt number shift to $\theta = 320°$ and $135°$ respectively. Figure 4.9a shows also a small rotating fluid layer adjacent to the cylinder surface. Such a layer acts as a buffer isolating the cylinder from the main stream and causing a decrease in the overall heat transfer rate. One of the interesting features of the velocity field in this case is the higher velocity on the right side of the cylinder and the lower velocity on the left side. This is mainly because the shear layer driven by the cylinder assists the buoyancy driven flow on the right side and resists it on the left side. This leads to higher heat transfer rates on the right side ($\theta = 180° \rightarrow 360°$) as shown in Figure 4.11. Further increase of the rotational speed to Re_{st}=200 creates a thick rotating layer (buffer layer) around the cylinder (Figure 4.10a) and causing the rate of heat transfer to drop sharply as shown in Figure 4.11. The local Nusselt number distribution becomes more dominated by the cylinder rotation with less effect of the natural convection.

Figure 4.12 shows the distribution of vorticity on the cylinder surface at Ra=1000 and at different Re_{st}. The figure shows that with increasing speed of rotation the overshoot in absolute wall vorticity increases. Moreover, due to the effect of rotation, the point of maximum vorticity (positive) and the point of maximum vorticity (negative) are no longer at positions θ =90 and 270, as for fixed cylinder, but rather move in the direction of rotation to be at angles greater than 90 and 270 respectively.
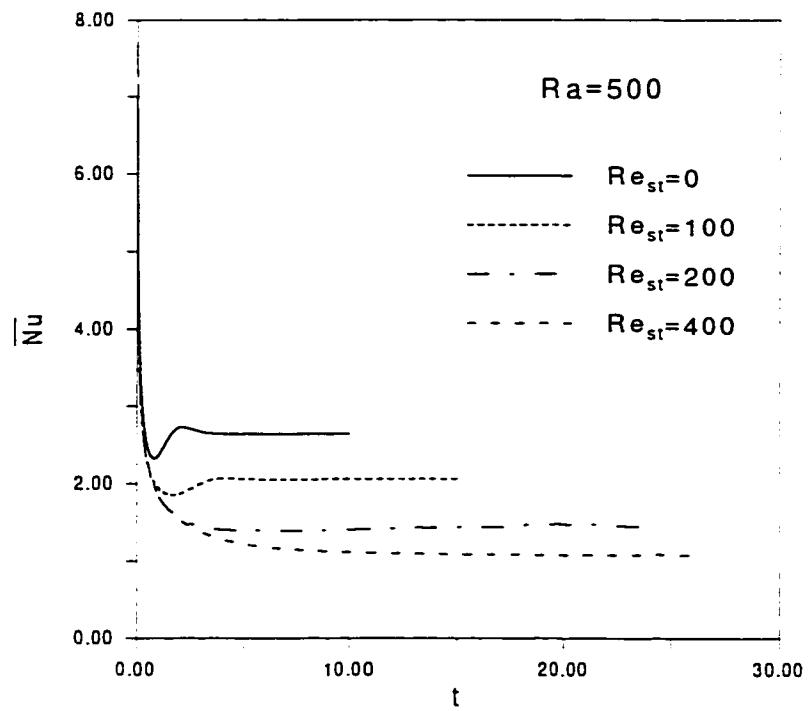
Figure 4.6 The time variation of average Nusselt number
at different values of Re_{st}
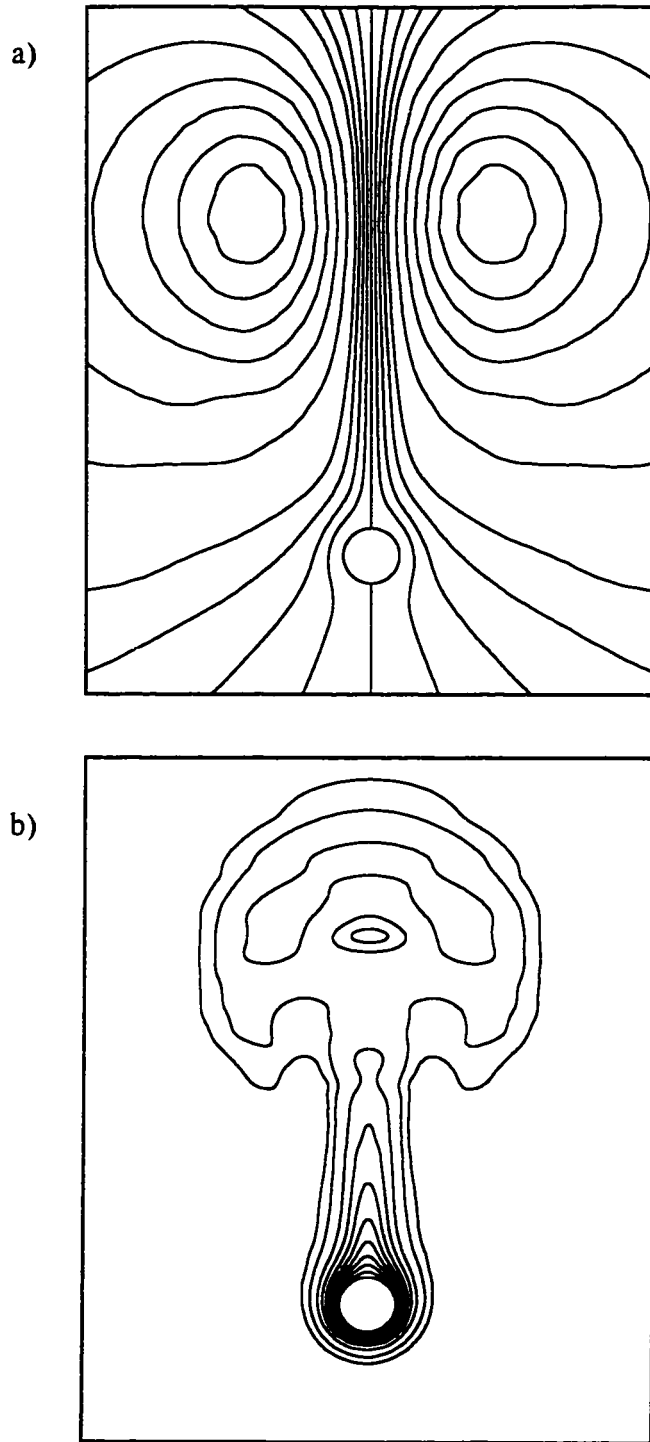
Figure 4.7 Steady streamline patterns and the corresponding
isotherms at Ra=1000 and Re_{st}=0
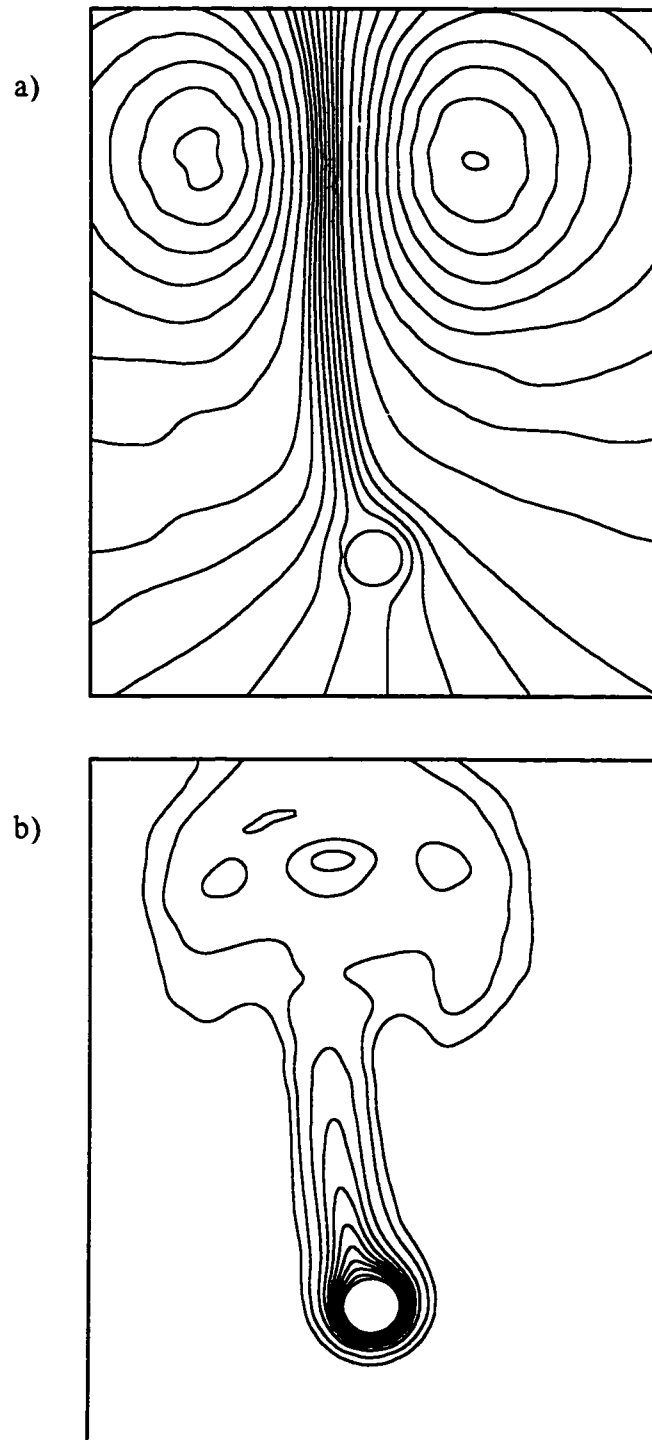
Figure 4.8 Steady streamline patterns and the corresponding isotherms at Ra=1000 and Re_{st}=20
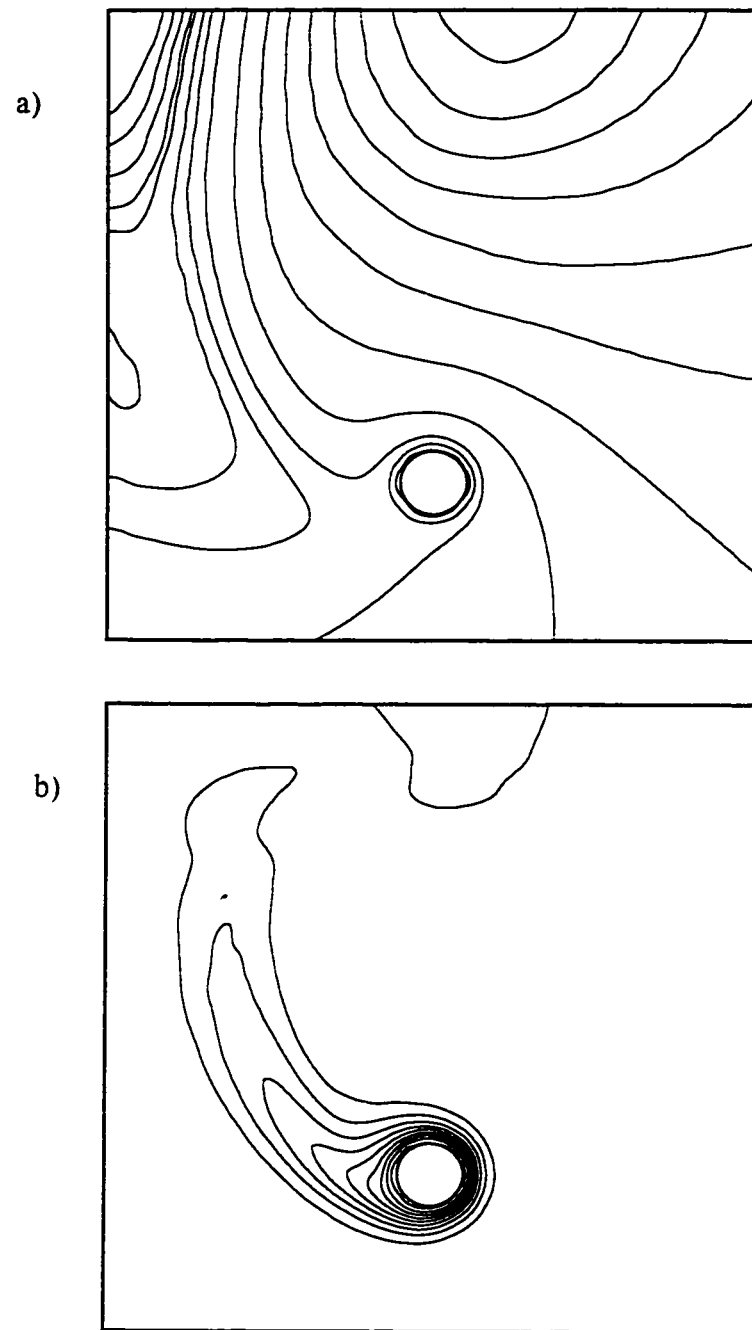
Figure 4.9 Steady streamline patterns and the corresponding
isotherms at Ra=1000 and Re$_{st}$=100
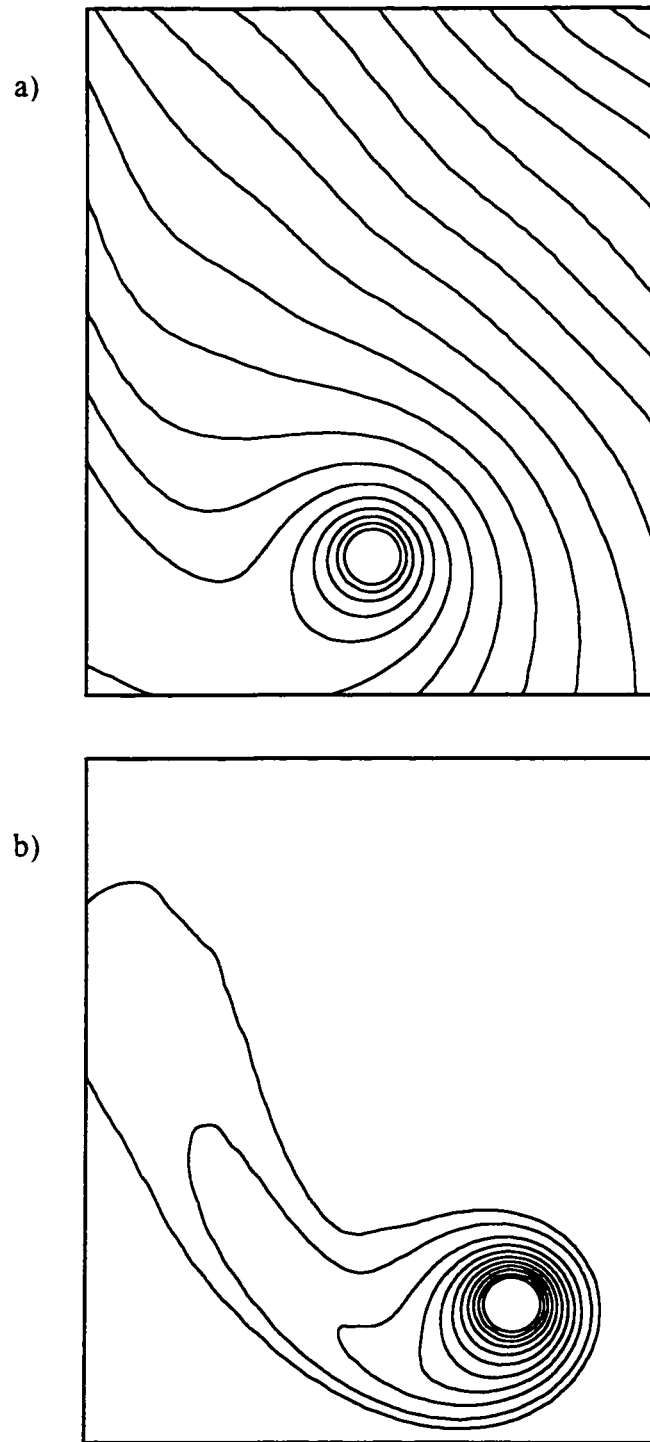
Figure 4.10 Steady streamline patterns and the corresponding
isotherms at Ra=1000 and Re$_{st}$=200
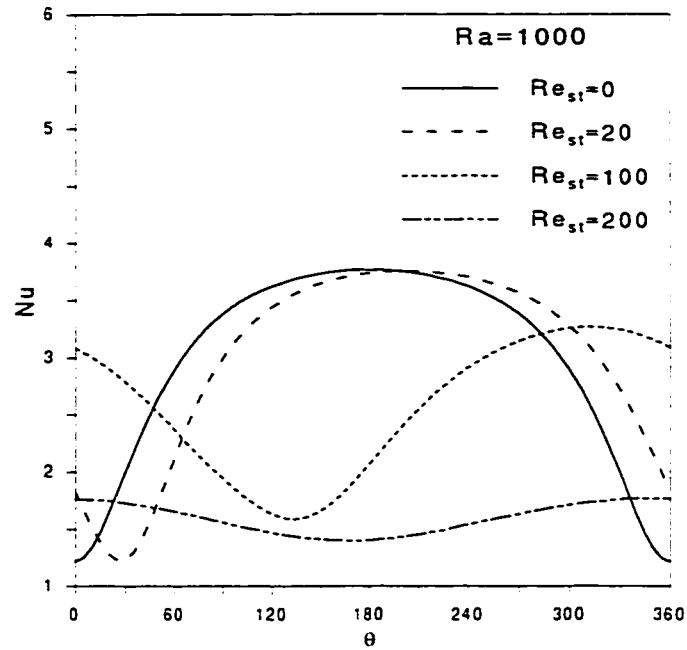
Figure 4.11 Local Nusselt number distribution for steady rotating cylinder at Ra=1000 and at different values of Re_{st}
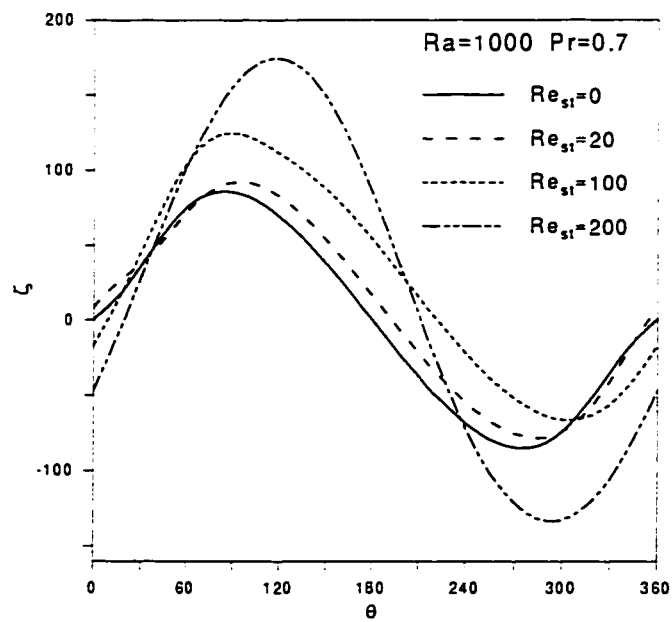
Figure 4.12 Surface vorticity distribution for steady rotating cylinder at Ra=1000 and at different values of Re_{st}

4.4.2 Rotationally Oscillating Cylinder

The effect of rotational oscillations on heat convection is investigated for Rayleigh numbers, Ra, up to 1000, Reynolds numbers, Re_{os}, up to 400 and dimensionless frequencies, S, up to 0.8. At small times following the sudden temperature rise, the variation of $\overline{Nu}$ with time is very much the same as in the case of fixed or steady rotating cylinders. This is quite expected since the thermal field is dominated by conduction at small times. Figure 4.13 shows this phenomenon for the three cases of fixed cylinder ($Re_{st}=0$), a rotating cylinder ($Re_{st}=100$) and an oscillating cylinder ($Re_{os}=500$, S=0.4) where Ra=500 for all cases. As the time increases, the buoyancy-driven flow develops causing transition to the convective mode. Once this is reached, the effect of cylinder oscillation becomes more pronounced resulting in a periodic variation of $\overline{Nu}$. It can be seen that the frequency of $\overline{Nu}$ is twice that of the cylinder motion which can be attributed to the similar heat convection process every half cycle of the cylinder oscillation.

Table 4.1 displays the results of the average Nusselt number for all the cases considered knowing that $\overline{Nu}$ represents the average Nusselt number over the cylinder surface and $\overline{\overline{Nu}}$ represents the time-average of $\overline{Nu}$ over a complete cycle of oscillation. The table shows that for the same Ra and Re_{os}, $\overline{\overline{Nu}}$ is found to be in between two limiting cases. The first case corresponds to steady natural convection from a fixed cylinder while the second corresponds to steady heat convection from a cylinder steadily rotating at a velocity equal to the maximum velocity of oscillation. The table also shows that the effect of oscillation frequency on $\overline{\overline{Nu}}$ at the same Ra and Re_{os} is small (not exceeding 4%) for the frequencies

considered. However, the higher the frequency the smaller the amplitude of $\overline{Nu}$ as shown in Figure 4.14. The figure also shows that the frequency of oscillation does not have profound effects on $\overline{Nu}$.

The effect of oscillation Reynolds number, Re_{os}, on the average rate of heat convection can be seen in Table 4.2. For the same frequency, increasing Re_{os} tends to decrease $\overline{\overline{Nu}}$. Higher Re_{os} in this case indicates larger amplitude of oscillation. This trend is consistent in the entire range of Ra. Figure 4.15 shows the time variation of $\overline{Nu}$ for the cases of Ra=500, S=0.4 and Re_{os}=20, 100, 200 together with a comparison with the case of a fixed cylinder. It is clear from the figure that the smaller the Reynolds number the smaller the amplitude of $\overline{Nu}$ and the closer the mean of $\overline{Nu}$ to the value due to natural convection from a fixed cylinder at the same Ra. On the other hand, the higher the values of Re_{os} the larger the amplitude of $\overline{Nu}$ and the smaller the time-averaged value of $\overline{Nu}$.

Figure 4.16 Shows the development of flow and thermal fields during one complete cycle of oscillation, namely the third cycle, at Ra=500, Re_{os}=100 and S=0.4. At zero instantaneous velocity of the cylinder at positions A (beginning of cycle), C (middle of cycle) and E (end of cycle), the streamline plots show that the stagnation points are no longer at vertical positions, but rather shifted due to the effect of fluid rotation in the vicinity of the cylinder. The isotherms plots at these positions also show that the thermal plume breakaway points (the downstream stagnation point) are shifted from $\theta = 0°$. The streamlines and isotherms at position A are similar to those at position E which reflects the approximate periodic behavior of flow and thermal fields especially in the neighborhood of the cylinder. On the

other side, at positions B (quarter of cycle) and D (three quarters of cycle) where the cylinder assumes its maximum velocity, the thickness of the fluid layer rotating with the cylinder at these positions is significant.

Figure 4.17 shows the development of local Nusselt number distribution in the aforementioned cycle of cylinder oscillation. The distributions at the beginning of the cycle, positions A, and at the end of the cycle, position E, are very close which confirms the approximate periodic behavior of flow and thermal fields in the neighborhood of the cylinder. At positions B and D, the Nu distribution becomes more uniform with a reduction in the average Nusselt number in comparison with those at positions A, C and E. This reduction, is attributed to the thick fluid layer rotating with the cylinder at these high velocity periods. The figure also shows that the thermal plume breakaway angle, corresponding to minimum Nusselt number, for positions B and D is located at about $120°$, $240°$ respectively, which means that the positions of thermal breakaway angle in the first half of the cycle is about a mirror image of that in the second half of the cycle. These similar distributions of the thermal field and local Nusselt number every half cycle explain why $\overline{Nu}$ is being oscillating at twice the frequency of the cylinder oscillation.
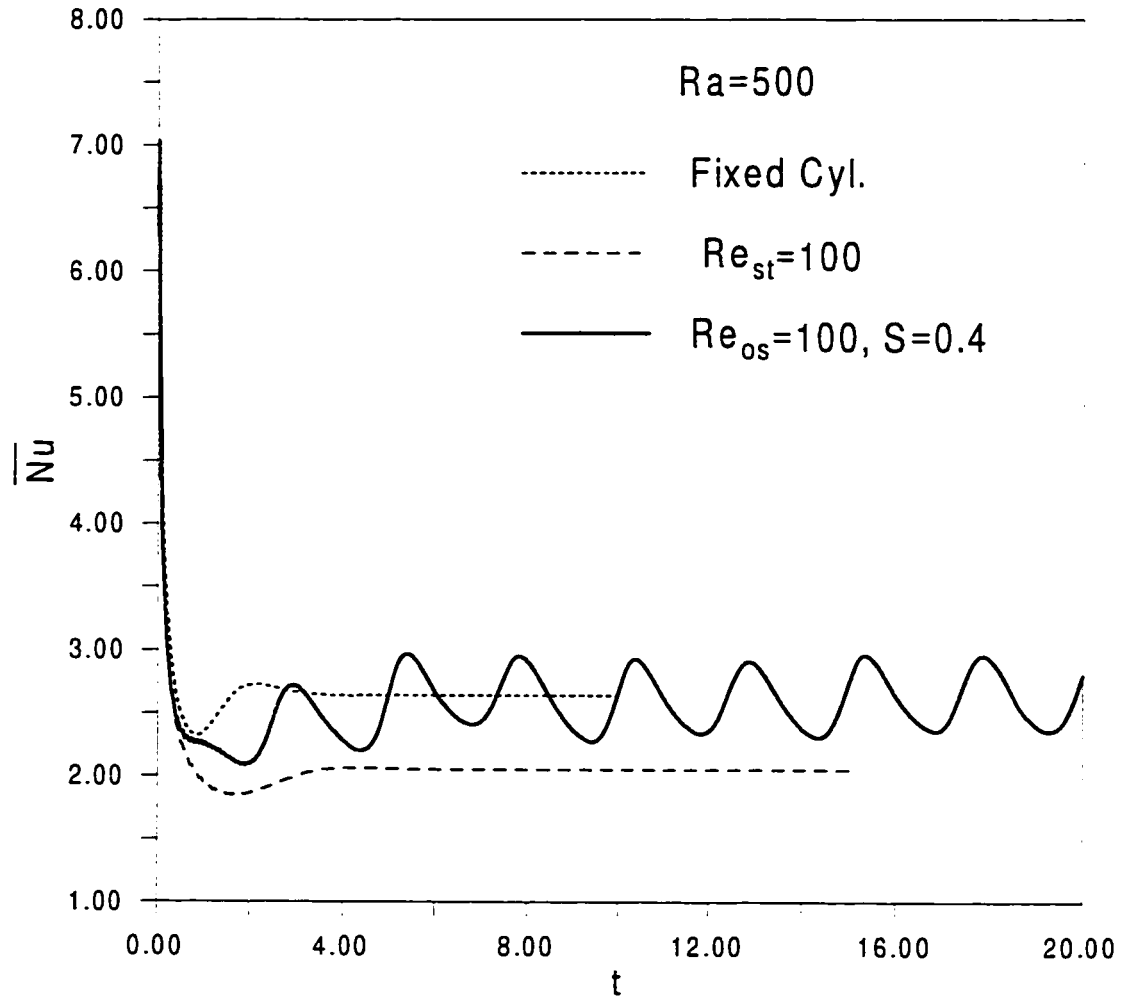
Figure 4.13 Time variation of average Nusselt number at Ra=500
for the cases of a) Oscillating cylinder at Re_{os}=100 and S=0.4,
b) Fixed cylinder and c) Steady rotating cylinder at Re_{st}=100

Table 4.1 Effect of frequency S on heat convection from an oscillating cylinder

	Fixed Cyl.	Steady Rotation		Oscillating Cylinder		
Ra	$\overline{Nu}_f$	Re_{st}	$\overline{Nu}_{st}$	Re_{os}	S	$\overline{\overline{Nu}}$
					0.1	1.66
100	2.01	100	1.174	100	0.2	1.72
					0.4	1.65
					0.1	1.39
100	2.01	200	0.925	200	0.2	1.32
					0.8	1.35
					0.1	2.6
500	2.65	100	2.05	100	0.4	2.61
					0.8	2.61
					0.2	2.05
500	2.65	200	1.25	200	0.4	2.08
					0.8	2.00
					0.2	2.49
1000	3.09	200	1.54	200	0.4	2.57
					0.8	2.58

Table 4.2 Effect of Re_{os} on the heat convection from oscillating cylinder

Ra	S	Re_{os}	$\overline{\overline{Nu}}$
		20	2.01
100	0.4	100	1.65
		200	1.32
		20	2.7
500	0.4	100	2.61
		200	2.07
1000	0.4	100	3.08
		200	2.57

$\overline{Nu}_f$ is the average Nu due to natural convection from a fixed cylinder

$\overline{Nu}_{st}$ is the average Nu due to heat convection from a steady rotating cylinder

$\overline{\overline{Nu}}$ is the time-averaged $\overline{Nu}$ due to heat convection from an oscillating cylinder
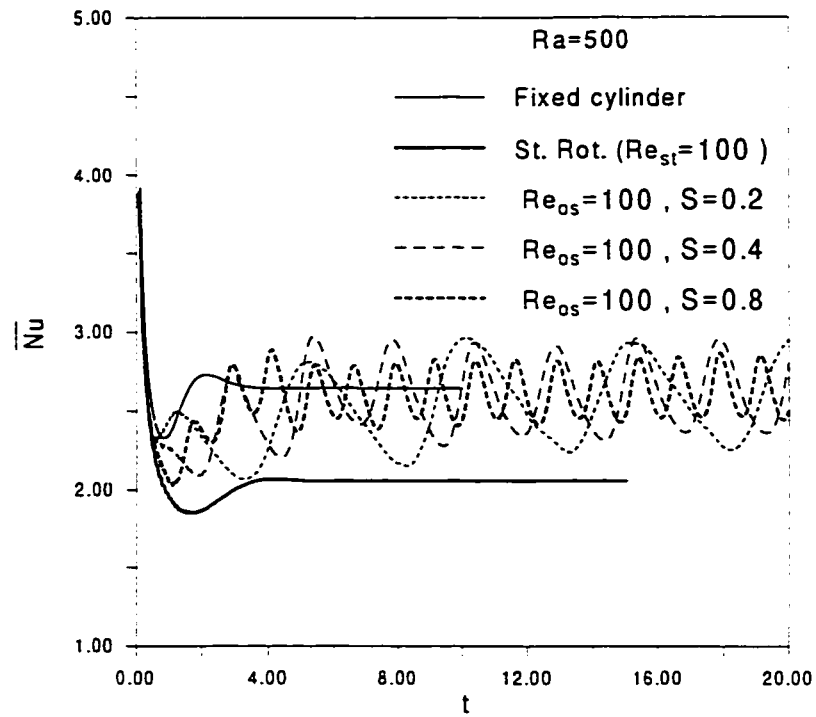
Figure 4.14 The time variation of average Nusselt number at
Ra=500, Re_{os}=100 and at different values of frequency S
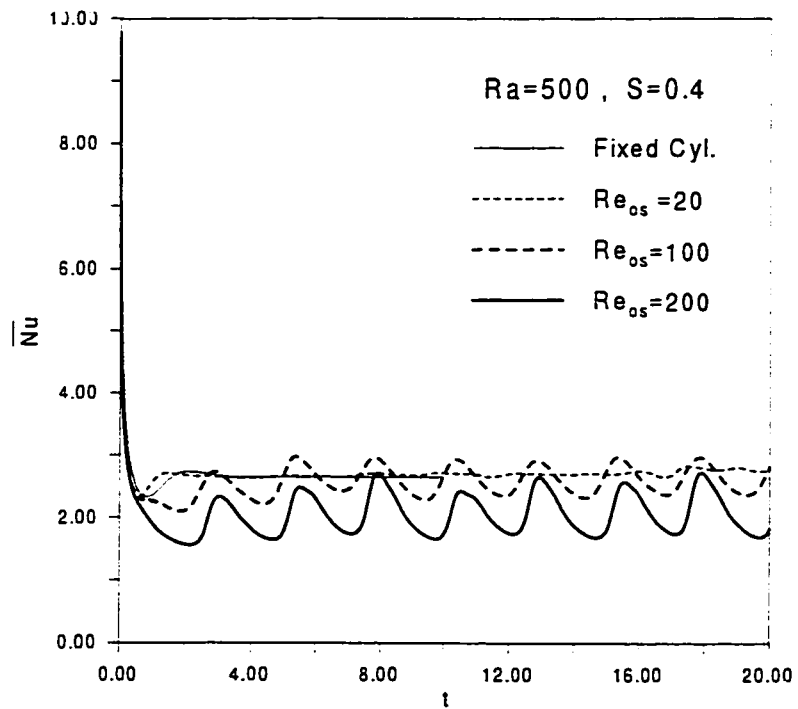
Figure 4.15 Effect of Reynolds number of oscillation on the
time variation of Nusselt number at Ra=500, S=0.4

a)
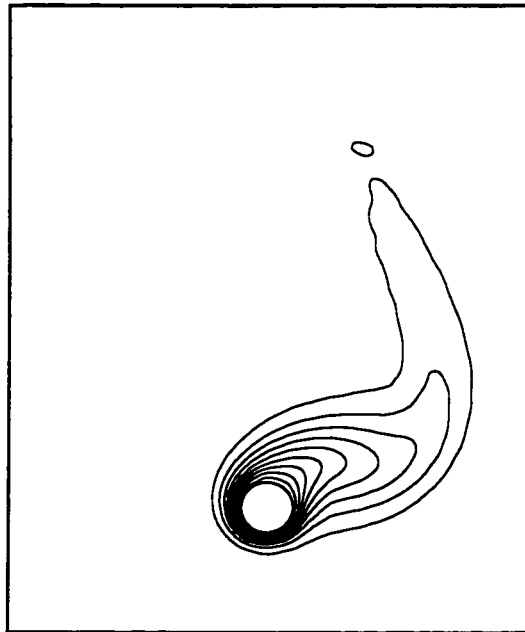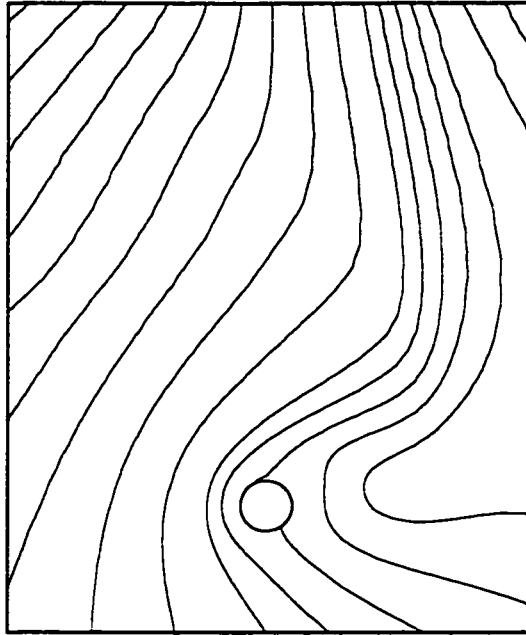
Figure 4.16a Position A

b)
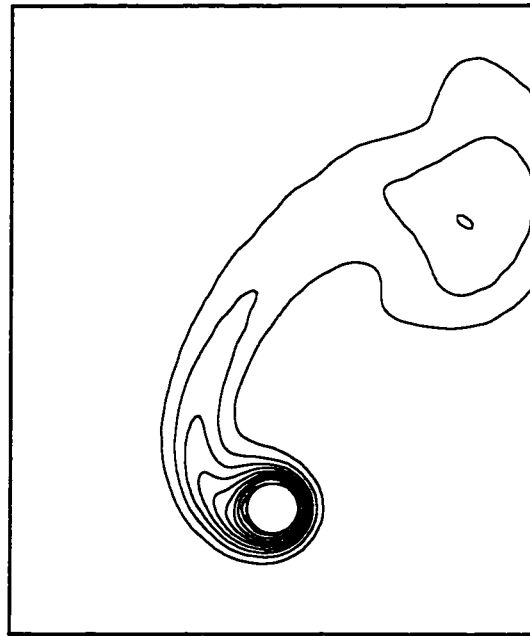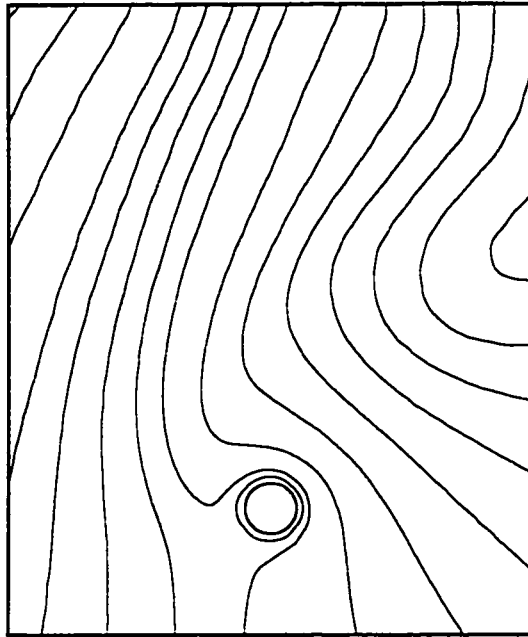
Figure 4.16b Position B

c)
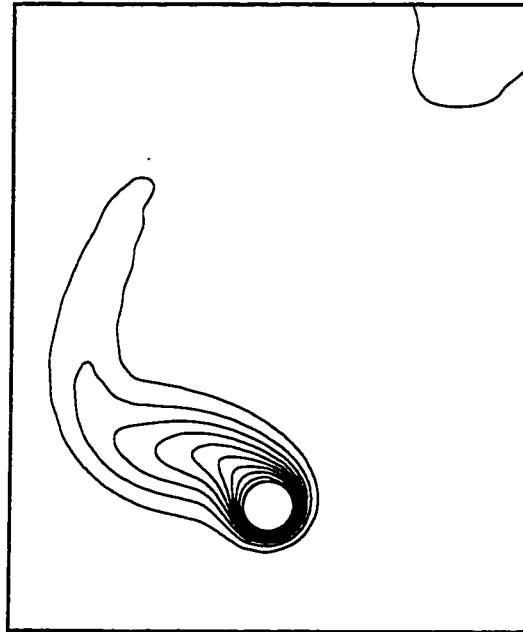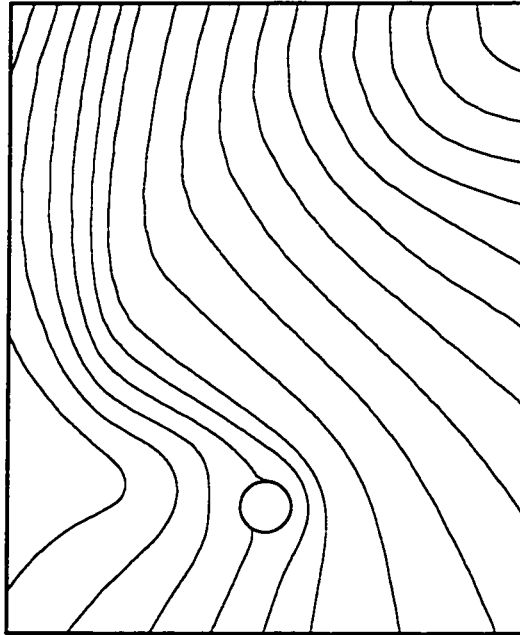
Figure 4.16c Position C

d)
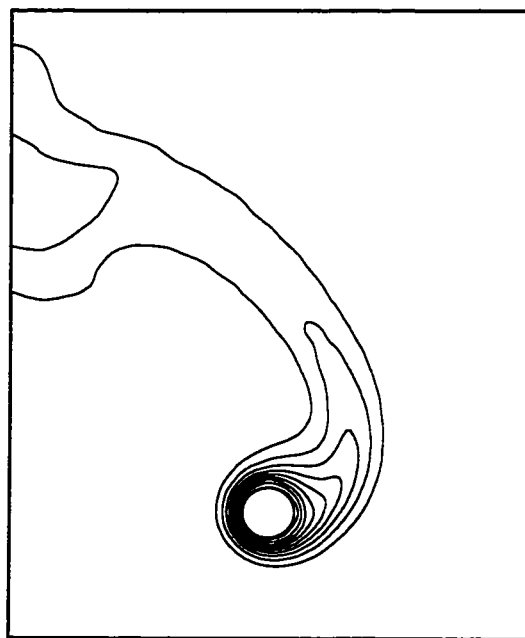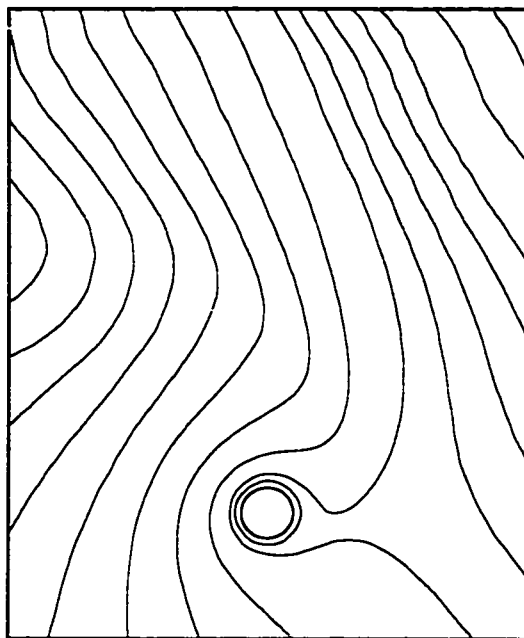
Figure 4.16d Position D

e)
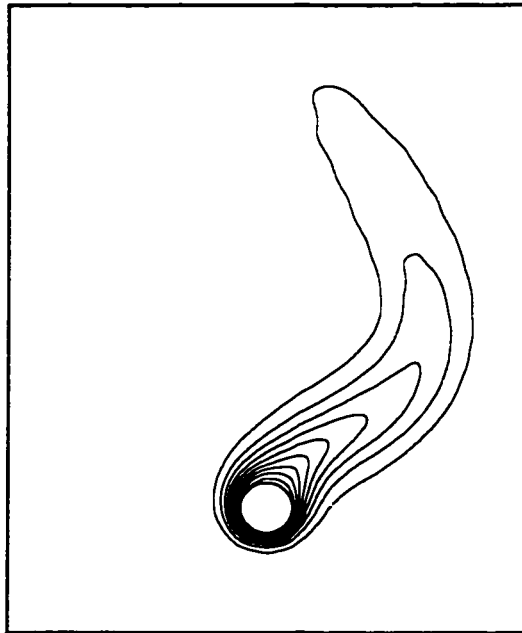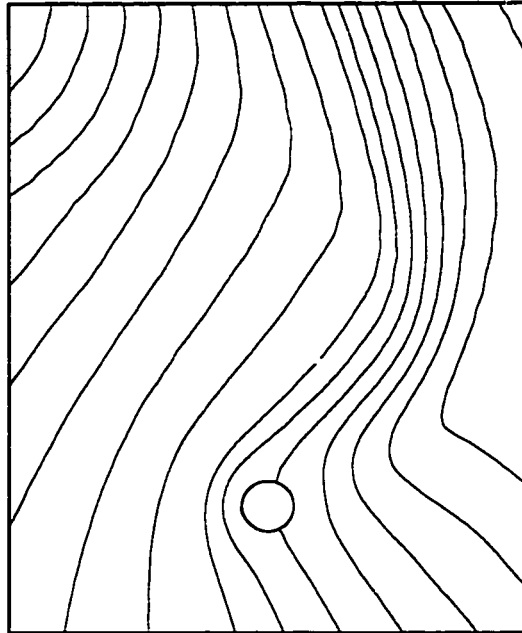
Figure 4.16e Position E

Figure 4.16 Streamline plots and corresponding isotherms plots in
one complete oscillation cycle at Ra=500, Re_{os}=100 and S=0.4
A) start of cycle,   B) 1/4 T,   C)1/2 T,   D)3/4 T,   E) end of cycle
where T is the time period of one cycle of oscillation
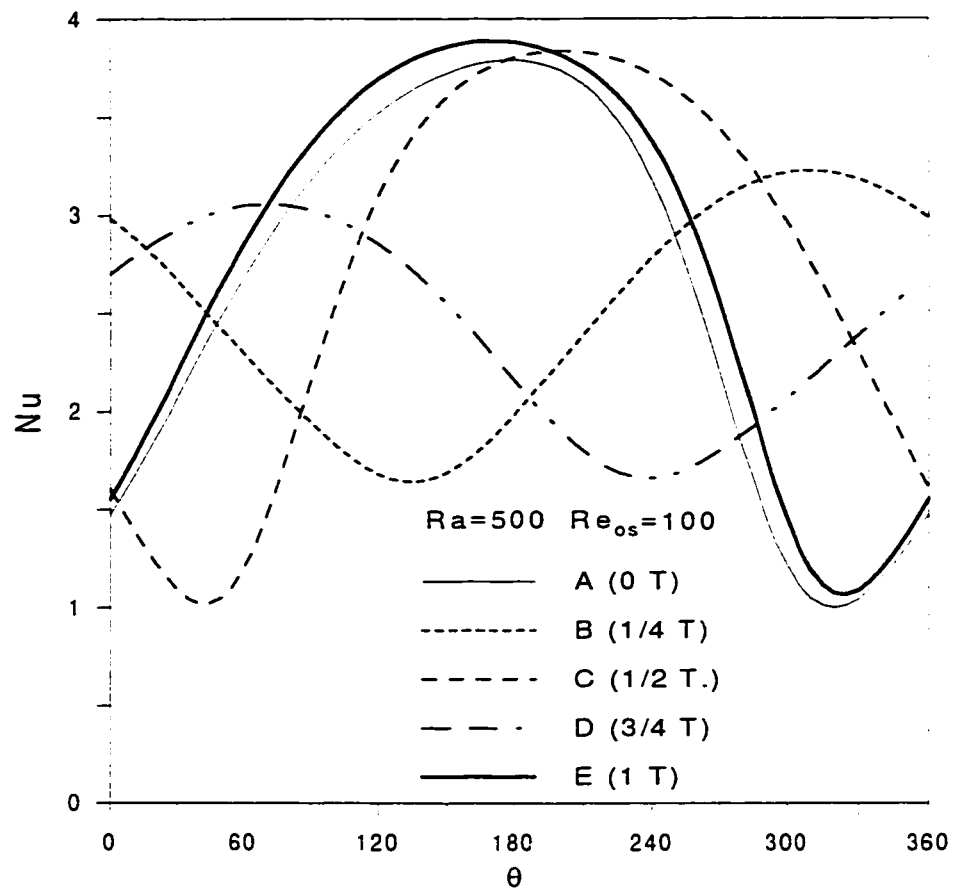
Figure 4.17 Local Nusselt number distribution in one complete
cycle of oscillation at Ra=500, Re$_{os}$=100 and S=0.4

CHAPTER 5

HEAT CONVECTION FROM A VERTICALLY OSCILLATING CYLINDER IN A QUIESCENT FLUID

In this chapter, the problem of heat convection from a vertically oscillating cylinder in a quiescent fluid is considered. The physical system is shown in Figure 5.1, consisting of an isothermal horizontal circular cylinder of infinite length and radius c placed in a quiescent fluid at temperature T_∞. At time t=0, the cylinder is simultaneously heated to a temperature T_w and subject to vertical oscillatory motion of the form:

$$Y = A_m \cos(2 \pi f \tau), \tag{5.1}$$

where A_m and f are the amplitude and frequency of oscillation. The effect of temperature variation on fluid properties are considered negligible except for the body force term in the momentum equation. The induced flow due to cylinder motion and buoyancy forces is assumed two dimensional and radiation and viscous dissipation effects are neglected.

5.1 The Governing Equations

The finite-differences schemes, which are normally Eulerian in their frame of reference, require the discretization of the entire flow domain into a computational mesh. This discrete Eulerian grid system does not readily accommodate the continuous motion of the
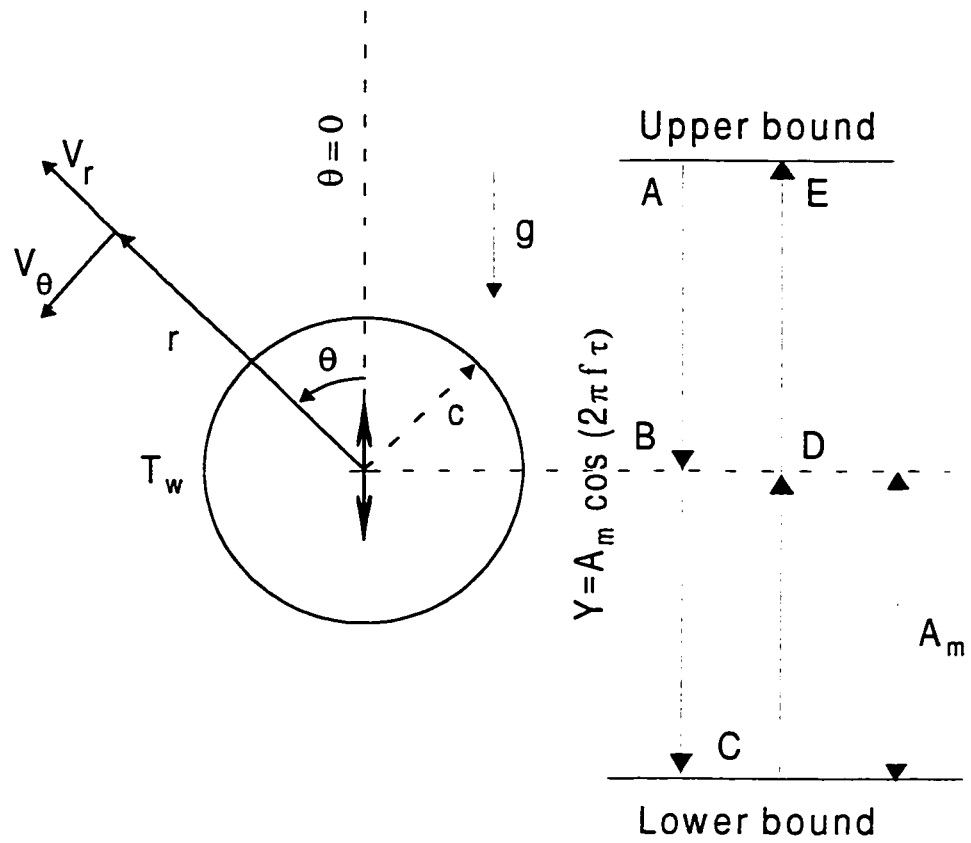
Figure 5.1 Coordinate system and cylinder positions during one cycle of oscillation

solid boundary. In order to simplify the analysis, the computational grid is assumed to move with the cylinder in a frame of reference with the origin being at the center of the cylinder. To solve the equations for fluid motion in this accelerating reference grid system, the momentum equations must be transformed from their inherent inertial reference to a non-inertial reference frame. For a fluid particle the equation of motion may be written in a vector form :

$$\rho \frac{d\vec{v}}{dt} = \vec{F} \tag{5.2}$$

where $\vec{V}$ is velocity vector and $\vec{F}$ is the total force vector acting on the particle, where $\frac{d\vec{V}}{dt}$ is the absolute acceleration. For a particle in the moving coordinates system Eq. (5.2) becomes

$$\rho \frac{d(\vec{V}_r + \vec{V}_{fr})}{dt} = \vec{F} \tag{5.3}$$

where $\vec{V}_{fr}$ is the velocity vector of the non-inertial coordinate system relative to an inertial reference and $\vec{V}_r$ is the Eulerian velocity vector in the non-inertial coordinate system. The velocity $\vec{V}_r$ is function in space and time while $\vec{V}_{fr}$ is only function of time and so Eq. (5.3) becomes as

$$\rho \frac{d\vec{V}_r}{dt} + \rho \frac{d\vec{V}_{fr}}{dt} = \vec{F} \tag{5.4}$$

where $\frac{d\vec{V}_{fr}}{dt}$ is simply the acceleration of the cylinder with respect to the inertial coordinate system. The result of attaching the computational grid system to the oscillating cylinder is the addition of a simple acceleration term which is constant over the computational field at

each incremental time step of the finite difference solution. Using cylindrical coordinates, the final form of the governing equations in the non-inertial frame of reference can be written as:

Continuity equation:

$$\frac{\partial u_r'}{\partial r'} + \frac{u_r'}{r'} + \frac{1}{r'}\frac{\partial u_\theta'}{\partial \theta} = 0 \tag{5.4}$$

Radial momentum equation:

$$\frac{\partial u_r'}{\partial \tau} + u_r'\frac{\partial u_r'}{\partial r'} + \frac{u_\theta'}{r'}\frac{\partial u_r'}{\partial \theta} - \frac{u_\theta'^2}{r'} = -\frac{\partial p}{\rho \partial r'} + v(\nabla^2 u_r' - \frac{u_r'}{r'^2} - \frac{2}{r'^2}\frac{\partial^2 u_\theta'}{\partial \theta^2}) + F_r - \frac{\partial u_{rc}'}{\partial \tau} \tag{5.5}$$

Angular momentum equation:

$$\frac{\partial u_\theta'}{\partial \tau} + u_r'\frac{\partial u_\theta'}{\partial r'} + \frac{u_\theta'}{r'}\frac{\partial u_\theta'}{\partial \theta} - \frac{u_\theta' u_r'}{r'} = -\frac{1}{\rho r'}\frac{\partial p}{\partial \theta} + v(\nabla^2 u_\theta' - \frac{u_\theta'}{r'^2} + \frac{2}{r'^2}\frac{\partial^2 u_r'}{\partial \theta^2}) + F_\theta - \frac{\partial u_{\theta c}'}{\partial \tau} \tag{5.6}$$

Energy equation:

$$\frac{\partial T}{\partial \tau} + u_r'\frac{\partial T}{\partial r'} + \frac{u_\theta'}{r'}\frac{\partial T}{\partial \theta} = \frac{k}{\rho c_p}\nabla^2 T \tag{5.7}$$

where, r' and θ are the radial and angular displacements in the non-inertial frame. u_r' and u_θ' are radial and angular velocities. u_{rc}' and $u_{\theta c}'$ are radial and angular velocities of non-inertial frame relative to the inertial frame. F_r and F_θ are the radial and angular component of body force defined as

$$F_r = \rho g\beta(T - T_\infty)\cos(\theta), \qquad F_\theta = -\rho g\beta(T - T_\infty)\sin(\theta) \tag{5.8}$$

Now, let us introduce the stream function ψ' and vorticity ζ' defined as

$$u_r' = \frac{\partial \psi'}{r'\partial \theta}, \quad u_\theta' = -\frac{\partial \psi'}{\partial r'} \tag{5.9}$$

$$\zeta' = (\frac{\partial u'_\theta}{\partial r'} + \frac{u'_\theta}{r'} - \frac{1}{r'}\frac{\partial u'_r}{\partial \theta}) \qquad (5.10)$$

Using equation (5.9) along with continuity and momentum equations (5.4-5.7) we get

vorticity transport equation.

$$\frac{\partial \zeta'}{\partial \tau} + u'_r \frac{\partial \zeta'}{\partial r'} + \frac{u'_\theta}{r'}\frac{\partial \zeta'}{\partial \theta} = \nu \nabla^2 \zeta' + \frac{1}{\rho}(\frac{\partial F_\theta}{\partial r'} + \frac{F_\theta}{r'} - \frac{1}{r}\frac{\partial F_r}{\partial \theta}) \qquad (5.11)$$

Using equation (5.9) in (5.10) we get

$$\zeta' = -\nabla^2 \psi' \qquad (5.12)$$

$$\frac{\partial T}{\partial \tau} + u'_r \frac{\partial T}{\partial r'} + u'_\theta \frac{\partial T}{r'\partial \theta} = \frac{k}{\rho c_p}\nabla^2 T \qquad (5.13)$$

The above equations are the same as those known for inertial frame of references. The boundary conditions at the cylinder surface for ψ', ζ' and ϕ are taken the same as before (the no-slip, impermeability and isothermal conditions). However, the condition far away are now the relative oscillatory motion with respect to the new moving frame. These conditions can be expressed as

$$\psi' = \frac{\partial \psi'}{\partial \theta} = 0 \ , \ \frac{\partial \psi'}{\partial r'} = 0 \ , \ \text{and} \ T=T_w \quad \text{at} \quad r' = c \qquad (5.14a)$$

$$\frac{\partial \psi'}{\partial \theta} = r'U \sin(2\pi f\tau)\cos(\theta), \ \frac{\partial \psi'}{\partial r'} = U \sin(2\pi f\tau)\sin(\theta) \ , \ \zeta' \to 0$$

$$\text{and} \ T = T_\infty \ \text{as} \ r' \to \infty \qquad (5.14b)$$

The governing equations (5.11-5.13) and boundary conditions (5.14) are transformed to their dimensionless form by introducing the following dimensionless quantities.

$$r = \frac{r'}{c}, \ u_r = \frac{u'_r}{U}, \ u_\theta = \frac{u'_\theta}{U}, \ t = \tau\frac{U}{c}, \ \psi = \frac{\psi'}{cU}, \ \beta = f\frac{d^2}{\nu}$$

$$\zeta = -\zeta'\frac{c}{U}, \ \text{and} \ \phi = (T - T_\infty)/(T_w - T_\infty)$$

where U is the amplitude of the cylinder velocity and β is the frequency parameter.

Using the above quantities, equations (5.11-5.13) can now be written as

$$\frac{\partial \zeta}{\partial t} + u_r \frac{\partial \zeta}{\partial r} + \frac{u_\theta}{r} \frac{\partial \zeta}{\partial \theta} = \frac{2}{Re^2} \nabla^2 \zeta \tag{5.15}$$

$$\zeta = \nabla^2 \psi \tag{5.16}$$

$$\frac{\partial \phi}{\partial t} + u_r \frac{\partial \phi}{\partial r} + u_\theta \frac{\partial \phi}{r\partial \theta} = \frac{2}{Re\,Pr} \nabla^2 \phi \tag{5.17}$$

where $u_r = \dfrac{\partial \psi}{r\partial \theta}$, $u_\theta = -\dfrac{\partial \psi}{\partial r}$, $Re = \dfrac{2cU}{v}$, is Reynolds number and $Pr = \dfrac{\mu c_p}{k}$ is the Prandtl

number. The cylinder surface dimensionless velocity can be then expressed as :

$$U_c = -\sin(\pi t/KC)$$

where KC (=U/fd) is the Keulegan-Carpenter number which represents an apparent

frequency on the dimensionless time scale t. In terms of Re and β, the KC can be expressed

as KC=Re/β. On the other hand, the amplitude to diameter ratio can be expressed in terms

of KC as $A_m/d = KC/2\pi$.

Similar to the formulation given in chapter 3, the polar coordinates (ξ, θ) are introduced,

where $\xi = \ln r$. In these coordinates the equations can be written as:

$$e^{2\xi} \frac{\partial \zeta}{\partial t} = \frac{2}{Re}\left(\frac{\partial^2 \zeta}{\partial \xi^2} + \frac{\partial^2 \zeta}{\partial \theta^2}\right) - \frac{\partial \psi}{\partial \theta}\frac{\partial \zeta}{\partial \xi} + \frac{\partial \psi}{\partial \xi}\frac{\partial \zeta}{\partial \theta} \tag{5.18}$$

$$e^{2\xi}\zeta = \frac{\partial^2 \psi}{\partial \xi^2} + \frac{\partial^2 \psi}{\partial \theta^2} \tag{5.19}$$

$$e^{2\xi}\frac{\partial\phi}{\partial t} = \frac{2}{\text{Re}\,\text{Pr}}\left(\frac{\partial^2\phi}{\partial\xi^2}+\frac{\partial^2\phi}{\partial\theta^2}\right) - \frac{\partial\psi}{\partial\theta}\frac{\partial\phi}{\partial\xi}+\frac{\partial\psi}{\partial\xi}\frac{\partial\phi}{\partial\theta} \qquad (5.20)$$

the boundary conditions are then written as:

$$\psi = \frac{\partial\psi}{\partial\theta} = 0 \,, \quad \frac{\partial\psi}{\partial\xi} = 0 \,, \quad \text{and} \quad \phi = 1 \quad \text{at} \quad \xi = 0 \qquad (5.21a)$$

$$\frac{\partial\psi}{\partial\theta} \rightarrow e^{-\xi}\cos\theta\sin(\pi t / KC), \quad \frac{\partial\psi}{\partial\xi} \rightarrow e^{-\xi}\sin\theta\sin(\pi t / KC)\,, \quad \zeta \rightarrow 0$$

$$\text{and} \quad \phi \rightarrow 0 \quad \text{as} \quad \xi \rightarrow \infty \qquad (5.21b)$$

5.2 The Method of Solution

The method of solution is similar to that used in chapter 3. The three sets of differential

equations obtained (similar to Eqs. 3.17-3.19) can be written as :

$$\frac{\partial^2 f_n}{\partial\xi^2} - n^2 f_n = e^{2\xi}g_n \qquad (n = 1,\,, N) \qquad (5.22)$$

$$e^{2\xi}\frac{\partial g_n}{\partial t} = 2(\frac{\partial^2 g_n}{\partial\xi^2} - n^2 g_n)/\text{Re}^2 + S_n \qquad (n = 1,\,, N) \qquad (5.23)$$

$$e^{2\xi}\frac{\partial}{\partial t}\begin{pmatrix}H_o\\H_n\end{pmatrix} = \frac{2}{\text{Pe}}\frac{\partial^2}{\partial\xi^2}\begin{pmatrix}H_o\\H_n\end{pmatrix} - \frac{n^2}{\text{Pe}}\begin{pmatrix}0\\H_n\end{pmatrix} + \begin{pmatrix}R_o\\R_n\end{pmatrix} \qquad (n = 1,\,, N) \qquad (5.24)$$

where S_n , R_o and R_n are all easily identifiable functions of ξ and t and are shown in

appendix A3. The boundary conditions for all the functions presented in equations (5.13)

are obtained from equations (5.8) and can be expressed as

$$f_n = H_n = 0, \quad H_o = 2, \quad \frac{\partial f_n}{\partial\xi} = 0 \quad \text{when} \quad \xi = 0$$

whereas, as $\xi \rightarrow \infty$ $f_n, g_n, H_0, H_n, h_n \rightarrow 0$

$$\text{and} \quad e^{-\xi}\frac{\partial f_n}{\partial \xi} \rightarrow \delta_{n,1}\sin(\pi t / KC) \tag{5.25}$$

Integrating both sides of equation (5.9) with respect to ξ from $\xi=0$ to $\xi=\infty$ and using the boundary conditions in equation (5.25) gives the following integral conditions:

$$\int_0^\infty e^{(2-n)\xi}g_n d\xi = 2\delta_{n1}\sin(\pi t/KC) \tag{5.26}$$

The above integral conditions are used for calculating the values of the function g_n on the cylinder surface not only to get better accuracy but also to satisfy the periodicity of the pressure around the surface.

In order to advance the solution of ψ, ζ and ϕ in time, the initial condition at time $t=0$ must be known. In this problem, the cylinder is assumed to start its motion from the upper end at the same time instantaneously heated to temperature T_w. Using the boundary-layer coordinates and treating the initial conditions in the same way used in chapter 3. The initial solution (at $t = 0$) can be written as:

$$\psi^*(z,\theta,0) = 0, \quad \zeta^*(z,\theta,0) = 0$$

$$\text{and} \quad \phi(z,0) = -\text{erf}(z\sqrt{Pr}) + 1 \tag{5.27}$$

Although the differential equations (5.22-5.24) and the boundary and integral conditions 5.25 and 5.26 are different from those deduced in chapter 3, the numerical procedure is almost the same and therefore will not be discussed again.

5.3 Local and average Nusselt numbers

The local and average Nusselt numbers are defined as

$$Nu=2ch/k, \qquad \overline{Nu} = 2c\overline{h} / k \tag{5.28}$$

where h, $\bar{h}$ are the local and overall heat transfer coefficients defined as

$$h = \dot{q}/(T_w - T_\infty),$$

$$\dot{q} = -k(\partial T/\partial r')_{r'=c}$$

and ,

$$\bar{h} = \frac{1}{2\pi}\int_0^{2\pi} h \, d\theta \qquad (5.29)$$

where $\dot{q}$ is the rate of heat transfer per unit area. From the above definitions one can deduce the relation between the Nu , $\overline{Nu}$ and the functions H_0 ,H_n , h_n which can be written as:

$$Nu = -2\left(\frac{\partial \phi}{\partial \xi}\right)_{\xi=0} = -\left[\frac{\partial H_0}{\partial \xi} + 2\sum_{n=1}^{N}\left(\frac{\partial h_n}{\partial \xi}\sin n\theta + \frac{\partial H_n}{\partial \xi}\cos n\theta\right)\right]_{\xi=0} \qquad (5.30)$$

and

$$\overline{Nu} = -\left(\frac{\partial H_0}{\partial \xi}\right)_{\xi=0} \qquad (5.31)$$

the time averaged Nusselt number can obtained as follows

$$\overline{\overline{Nu}} = \frac{1}{t_2 - t_1}\int_{t1}^{t2}\overline{Nu} \, dt \qquad (5.32)$$

where the time period between t_1 and t_2 covers the last two cycles of oscillation.

5.4 Results and Discussion

In order to investigate the effect of cylinder oscillation on heat convection, a series of simulations was run for a range of Grashof number, Gr, up to 10^5, Keulegan-Carpenter number, KC, up to 10 and frequency parameter, β, up to 40. To check further the reliability

of the present Navier-Stokes code, a run was made at KC = 4 and β = 250 where, at these values both experimental and theoretical results of Justesen [36] are available for comparison. This comparison is shown in Figure 5.2, where the present prediction of flow field development in a half cycle of oscillation, is compared with both numerical and flow visualization made by the same author. The present results show a good agreement especially with the flow visualization.

Table 5.1 displays the effect of oscillation parameters KC and β on the time-averaged Nusselt number $\overline{\overline{Nu}}$, when the buoyancy effect is negligible. The table shows clearly that at any fixed value of the frequency parameter β, $\overline{\overline{Nu}}$ increases as KC increases. This increase, however, becomes more significant as β increases. Namely, as KC increases from 2 to 10 at β=10, 269% increase in $\overline{\overline{Nu}}$ is found. This percentage increases to 410%, 471% and 547% at the values of β=20, 25 and 40 respectively.

Figure 5.3 Shows the development of both flow and thermal fields in a complete cycle of oscillation at Gr=0, KC=4 and β =25. These streamline and isotherm patterns are plotted at five positions. The positions A, B, C, D and E shown in Figure 5.1 indicate the position of the cylinder in Figures 5.3a, b, c, d and e respectively. The figures show that both the flow and thermal fields resume their initial distributions as the cylinder undergoes a complete cycle of oscillation. When the cylinder begins to move from one end of the oscillation, (positions A, C and E shown in Figures 5.3a, c, and e,) the flow field is dominated by two counter-rotating vortices which were formed during the previous course of motion while another two counter-rotating vortices away from the cylinder are induced. However, at

positions B and D these vortices disappear with only very small ones originating in the separated flow region in the rear side of the cylinder. In general, the isotherms shown in the figure have lobe-shaped contours with almost equal extent on both lower and upper sides of the cylinder. In spite of the fact that the thermal field upstream differs from that downstream near the cylinder surface at the middle of the stroke (positions B and D), the far fields in both directions (ϕ =0.1) are almost symmetric. Figures 5.4 and 5.5 show the local Nusselt number and surface vorticity distributions during one complete cycle for the same case. The figures show that Nu and ζ_ω distributions are exactly the same at positions A and E reflecting the periodicity of both flow and thermal fields. Also, it can be seen that the minimum value of Nu is almost the same for all positions. The maximum values of Nu at positions B and D are exactly the same and occur at $\theta = 180°$ and $\theta =0°$. The two curves are mirror images from each other. Further, Figure 5.5 shows that the maximum vorticity on the surface during the cycle occurs at maximum velocities positions B and D.

Shown in Figure 5.6 is the development of both flow and thermal fields in a complete cycle of oscillation at the same value of β (β = 25) but at a higher value of KC (KC=10). These distributions are plotted at the same aforementioned positions. At this value of KC the amplitude-diameter ratio becomes higher than that at KC=4, causing significant changes in the flow and thermal fields. The figure also shows that the flow field possesses extensive vortex motion during the entire cycle. This is unlike the case of KC=4 where vortex motion is pronounced only in the decelerated parts of the cycle, namely near the top and bottom ends of cylinder motion. The isotherms for the same case are no longer lobe-shaped contours but rather change to form two large mushroom-shaped heated areas located near

the upper end and lower end of the stroke. These two heated areas are connected together by a vertical thin thermal layer web. Figures 5.7 and 5.8 respectively show the local Nusselt number and surface vorticity distributions during the same cycle. The figures show that the flow and thermal fields are nearly periodic since the distributions at the beginning and end of the cycle are almost the same. It is of interest to point out that at this KC value, regions of high surface vorticity are approximately the same at all time during a complete cycle . This appears clearly in Figure 5.8 where the values of maximum surface vorticity at all cylinder positions are almost the same but occur at different angular locations. The same applied to the local Nusselt number distribution as can be seen in Figure 5.7.

Figure 5.9a, b and c show the time variation of $\overline{Nu}$ during a complete cycle when Gr=0, KC=10 and at different values of β. The figures show that $\overline{Nu}$ is fluctuating at a frequency equal to twice that of the cylinder oscillation. Also, it can be seen that as β increases $\overline{\overline{Nu}}$ increases. The amplitude of $\overline{Nu}$ as well as the relative position of maximum $\overline{Nu}$ within the cycle however, do not change much as β increases. On the other hand, Figures 5.10a, b and c show the variation of $\overline{Nu}$ with time for the case of Gr=0 and β =25 and for three values of KC, namely, KC=2, 4 and 10 during a complete cycle. It can be observed that $\overline{Nu}$ is fluctuating at a frequency equal to twice that of the cylinder oscillation as in the previous case. Also, as KC increases not only the time-averaged Nusselt number $\overline{\overline{Nu}}$ increases but also the amplitude of $\overline{Nu}$ increases. It is noteworthy that the relative position of $\overline{Nu}$ maximum within a cycle differs as KC varies. In the case of KC=2 (Figure 5.10a) the heat transfer enhancement mostly happen near positions A, C and E where the cylinder is at both

ends of the stroke. At KC=4 (Figure 5.10b) the maximum value of $\overline{Nu}$ occurs near the middle of the decelerated parts of the cycle (i.e. between B and C and between D and E), whereas at KC=10, Figure 5.10c, the $\overline{Nu}$ maximum shifts near the maximum velocity positions B and D.

It seems that the heat transfer process depends on two factors, the first and the more effective, is the strength of vortex motion in the vicinity of the cylinder and the second is the velocity of the cylinder. The first factor is responsible for convection of heat enhanced by vortical motion near the surface. Such vortical motion drives also a low temperature fluid close to the surface. The second factor is responsible for generating high velocity gradient near of the cylinder which leads to enhancing heat transfer. Accordingly, high heat rate is expected at the positions characterized by domination of vortex motion as well as high cylinder velocity. At low values of KC (KC=2) the cylinder velocity is small and weak vortices only form at the end positions of the motion leading to the higher values of $\overline{Nu}$ near the positions A, C and E. At KC=4, the vortex motion dominates only in the decelerated parts of motion (see Figure 5.3) but due to the relative increase in the cylinder velocity, $\overline{Nu}$ peaks in the middle of the decelerated parts. As the KC increases further to KC=10 the extensive vortex motion dominates at all positions and the maximum value of $\overline{Nu}$ can be only decided by cylinder velocity, which does occur near the maximum velocity positions B and D.

Table 5.2 shows the effect of oscillation parameters, KC and β, on $\overline{\overline{Nu}}$ considering the effect of buoyancy forces. The table also shows the percentage increase in $\overline{\overline{Nu}}$ in

comparison with that of a fixed cylinder at the same Gr. The effect of oscillation is only significant at high values of KC and low values of Gr . This effect, however, dwindles as KC decreases. The table also shows that when KC is small (KC=2), the increase of β tends to decrease $\overline{\overline{Nu}}$ slightly until it becomes even smaller than that for a fixed cylinder. On the other hand, a quick comparison between Tables 5.1 and 5.2 shows that the buoyancy effect plays a minor role in enhancing heat convection at high values of KC and β. Namely, at KC=10 and β=40, $\overline{\overline{Nu}}$ = 9.31 when Gr=0 (Table 5.1), whereas at Gr=10^3, 10^4 and 10^5 $\overline{\overline{Nu}}$ = 9.31, 9.03 and 9.34 respectively.

To show the effect of Grashof number on the flow and thermal fields, Figure 5.11 is plotted at equal intervals in one complete cycle for the case KC=10, β = 25 and Gr =10^5. The figure shows that the flow field at such high Gr is mainly driven by buoyancy forces. The upward buoyancy driven flow interacts with the forced flow driven by the cylinder motion resulting in extensive vortex formation in the neighborhood of the cylinder. The thickness of the thermal boundary layer and its geometrical shape varies significantly during one complete cycle. This is mainly because in part of the motion the buoyancy driven flow assists the shear flow driven by the cylinder motion while in the other part both motions oppose each other. The figure also shows that the thermal field is characterized in general by a very thin thermal layer in the lower side of the cylinder and a thicker one on the upper side. Figure 5.12 and Figure 5.13 respectively show the local Nusselt number and surface vorticity distributions in the same cycle. The figures show that Nu and ζ_w distributions are nearly periodic, showing the periodicity of flow and thermal fields in the neighborhood of the cylinder.

Figure 5.14 shows the time variation of the average Nusselt number, $\overline{Nu}$, for the case of KC=4 and β =25 at different Grashof numbers. It can be observed that the frequency of $\overline{Nu}$ is shifted from twice the cylinder oscillation frequency, when Gr=0 to the cylinder frequency when Gr = 10^4. In the case of Gr=0 thermal field is similar every half cycle as shown in Figure 5.3. This leads to have two equal peaks for $\overline{Nu}$, one during the downward motion and the other during the upward motion. As Gr increases, the buoyancy driven flow not only causes dissimilar thermal field every half cycle of oscillation but also increases $\overline{Nu}$ at all positions. Accordingly, as Gr increases the two peaks of $\overline{Nu}$ are getting higher but their rate of increase differs. The one getting higher rate is obtained during the course of downward cylinder motion whereas the other with a relative lower rate is obtained during the course of upward motion.

Table 5.1 Effect of β and KC on the time-averaged Nusselt number for the case of Gr=0.

β	KC	$\overline{\overline{Nu}}$
10	2	1.01
	4	1.31
	10	3.73
20	2	1.25
	4	1.68
	10	6.37
25	2	1.33
	4	2.2
	10	7.25
40	2	1.44
	4	3.37
	10	9.31

Table 5.2 Effect of KC and β on the time-averaged Nusselt number
considering buoyancy effects.

KC	Gr	β	$\overline{\overline{Nu}}$	Nu_o	% increase
10	10^3	10	3.31		19
		20	6.34	2.78	128
		40	9.31		235
	10^4	10	4.79		8
		20	5.71	4.4	30
		40	9.03		105
	10^5	10	8.12		11
		20	8.32	7.29	14
		40	9.34		28
4	10^3	10	2.79		0.4
		20	2.93	2.78	5.3
		40	2.94		5.4
	10^4	10	4.5		2.2
		20	4.51	4.4	2.5
		40	4.98		13.1
2	10^3	10	2.79		0.4
		20	2.76	2.78	-0.7
		40	2.73		-1
	10^4	10	4.51		2.5
		20	4.50	4.4	2.3
		40	4.36		-0.9

Nu_o is the Nusselt number for the case of fixed cylinder at the same Gr
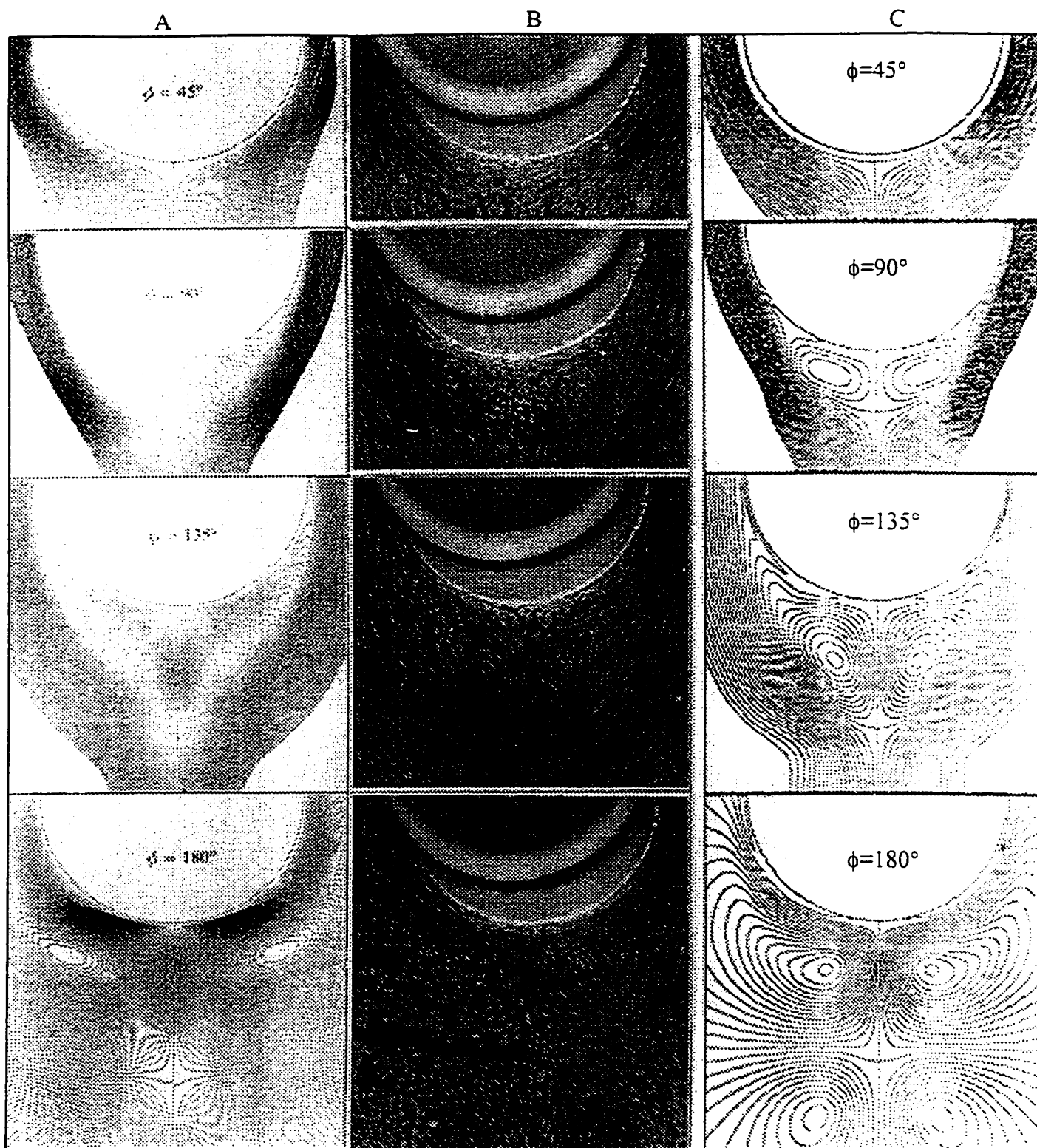
Figure 5.2 Flow development in half cycle of oscillation and comparison with reference [37]
A) Numerical [37]   B) Experimental [37]   C) Present study
$\phi=45°$ (T/8), $\phi=90°$ (T/4), $\phi=135°$ (3T/8) and $\phi=180°$ (T/2)
where T is the time period of one complete cycle

158

Figure 5.3 Streamline pattern and corresponding isotherms in a
complete cycle of oscillation at Gr=0 , KC=4 and β = 25
a) Topmost position   b)Maximum downward velocity position
c) lowest position   d)Minimum upward velocity position
e) Topmost position

Figure 5.4 Local Nusselt number distribution in a complete cycle of oscillation at Gr=0, KC=4 and β = 25.

Figure 5.5 Surface vorticity distribution in a complete cycle of oscillation at Gr=0, KC=40 and β = 25.

Figure 5.6 Streamline pattern and corresponding isotherms in a
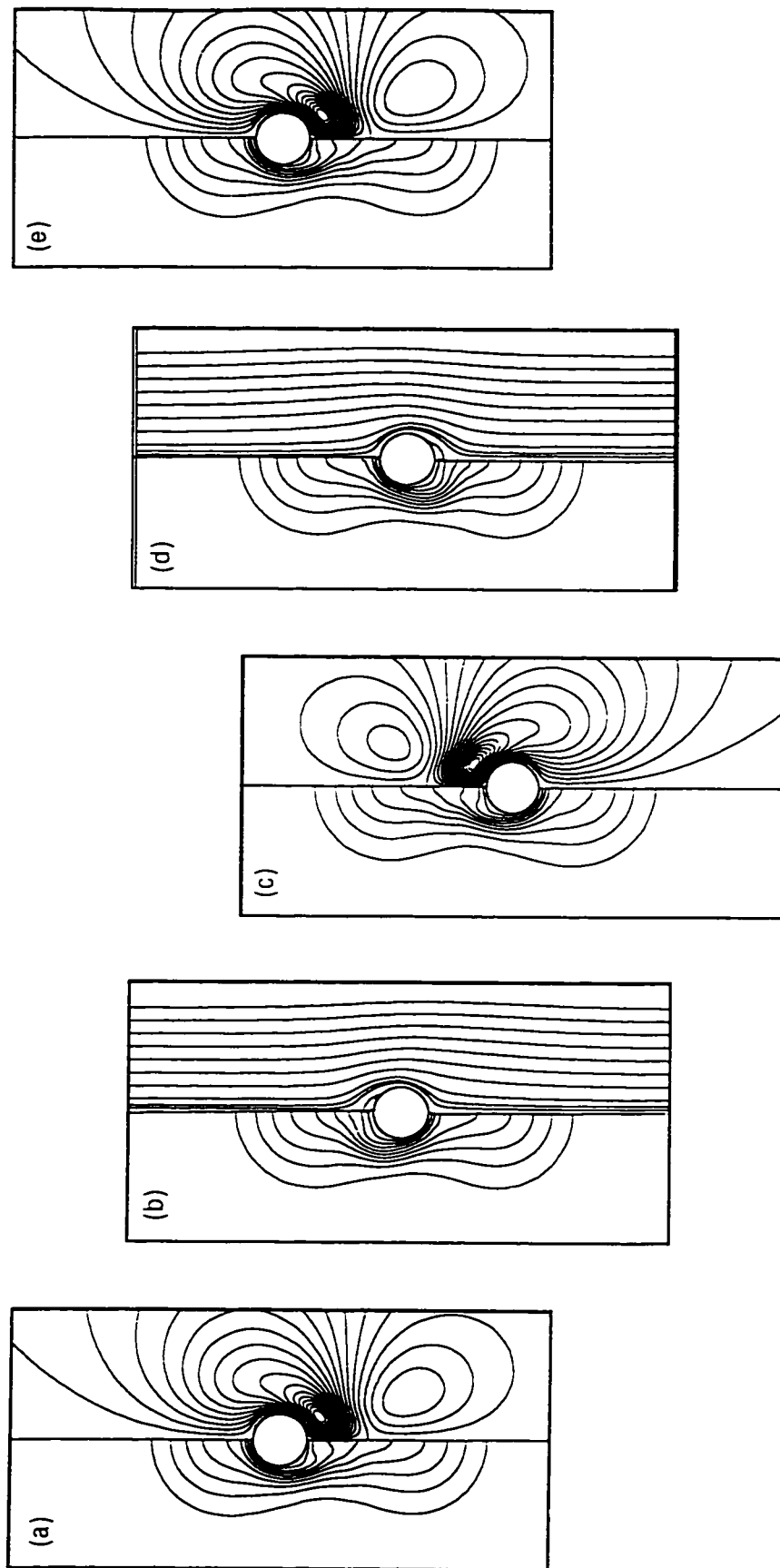complete cycle of oscillation at Gr=0, KC=10 and $\beta = 25$
a) Topmost position   b)Maximum downward velocity position
c) lowest position   d)Minimum upward velocity position
e) Topmost position

Figure 5.7 Local Nusselt number distribution in a complete cycle of oscillation at Gr=0, KC=10 and β = 25.

Figure 5.8 Surface vorticity distribution in a complete cycle of oscillation at Gr=0, KC=10 and β = 25.
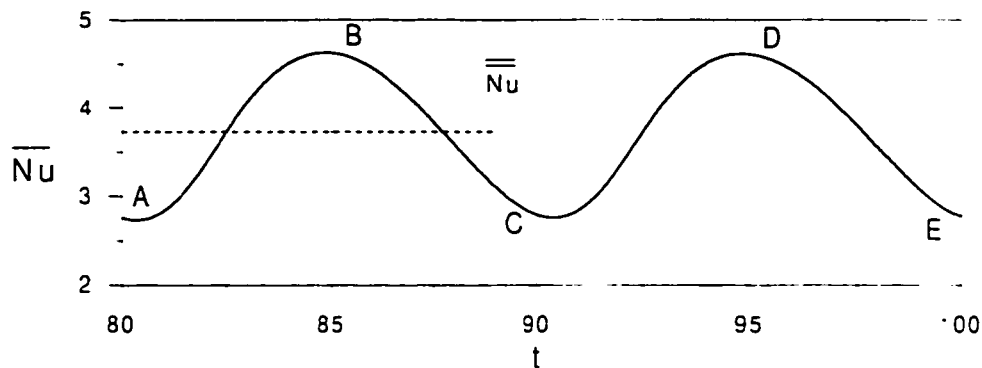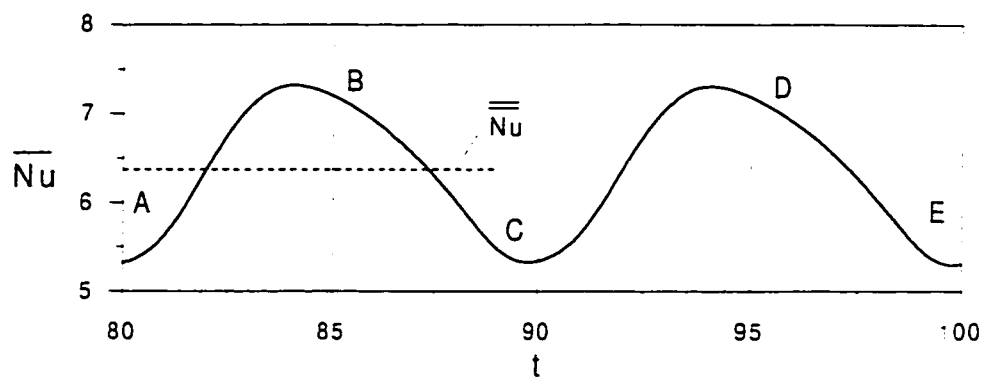
Figure 5.9a

Figure 5.9b
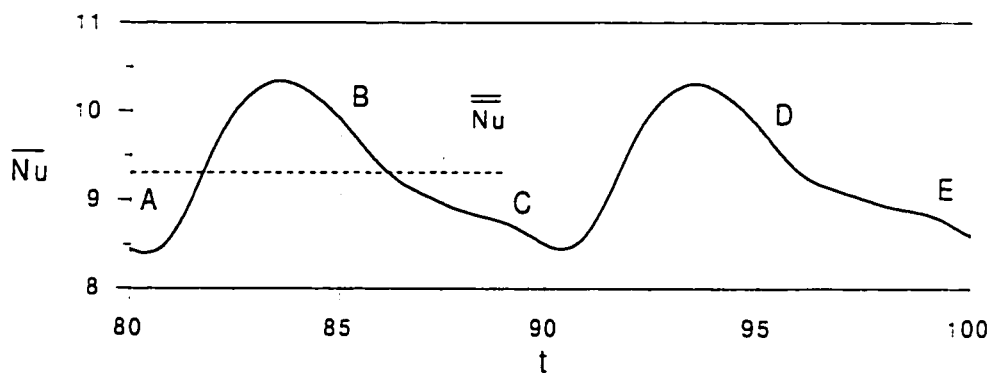
Figure 5.9c

Figure 5.9 The average Nusselt number distribution in a complete cycle of oscillation at Gr=0 and KC=10 a) β = 10, b) β = 20 and c) β = 40.
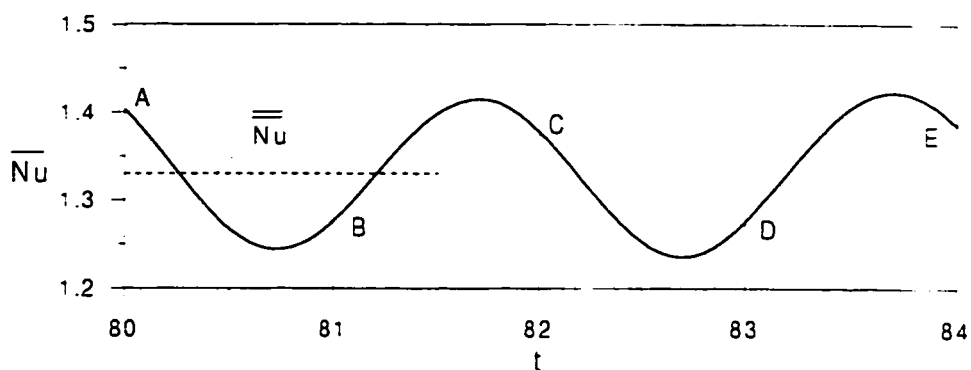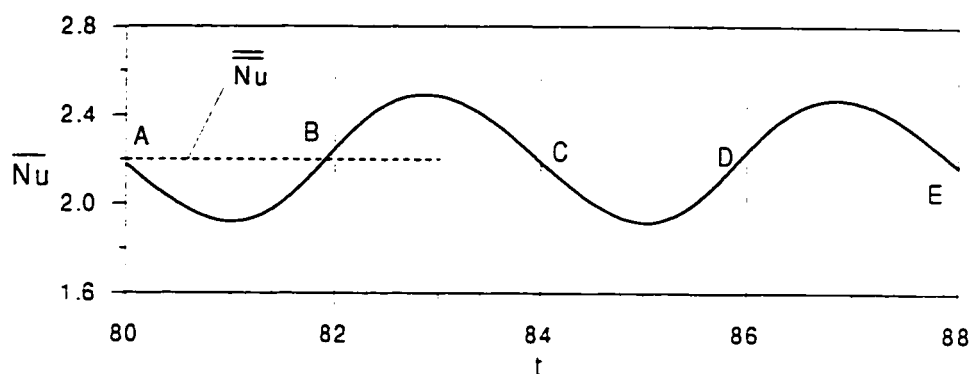
Figure 5.10a

Figure 5.10b
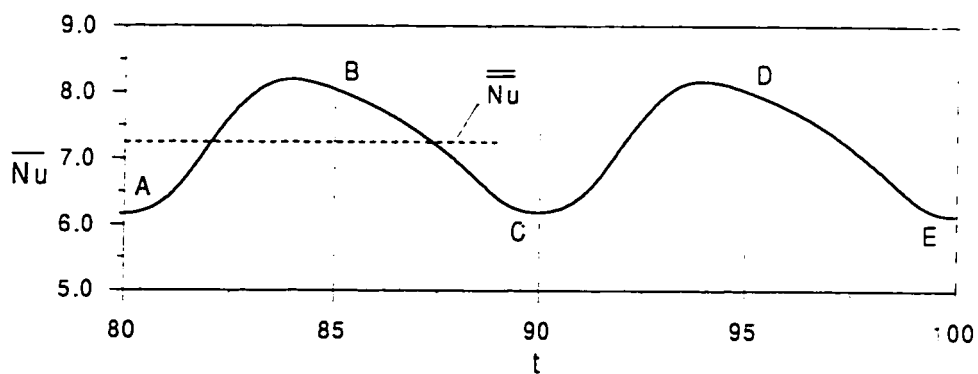
Figure 5.10c

Figure 5.10 The average Nusselt number distribution in a complete cycle of oscillation at Gr=0 and β = 25 a) KC=2, b)KC=4 and c)KC=10.
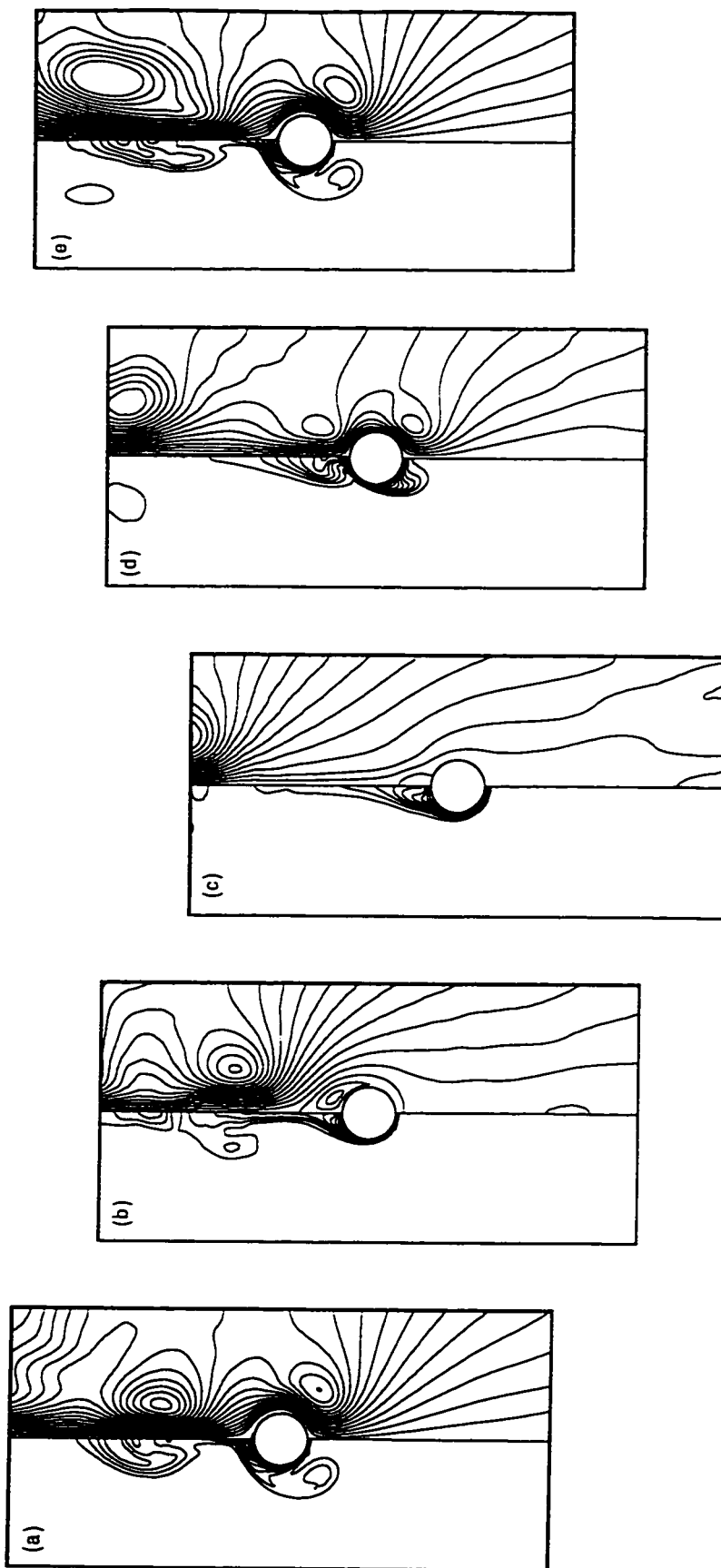
Figure 5.11 Streamline pattern and corresponding isotherms in
a complete cycle of oscillation at $Gr=10^5$, $KC=10$ and $\beta = 25$
a) Topmost position   b)Maximum downward velocity position
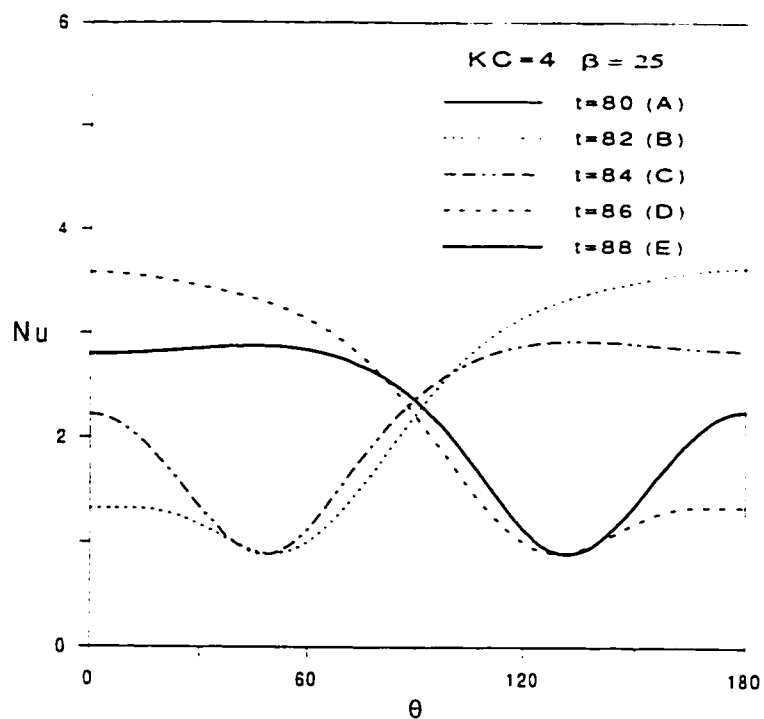c) lowest position   d)Minimum upward velocity position
c) Topmost position
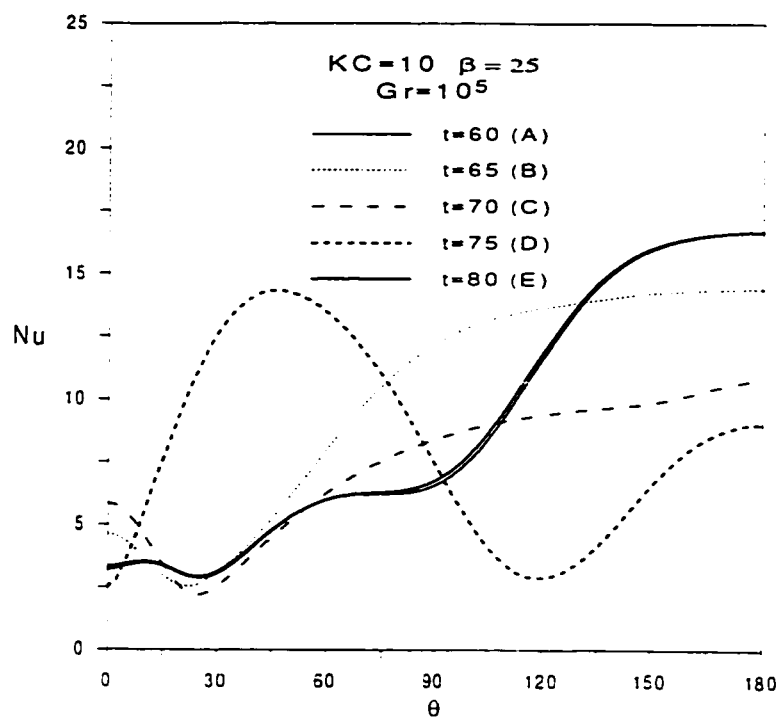
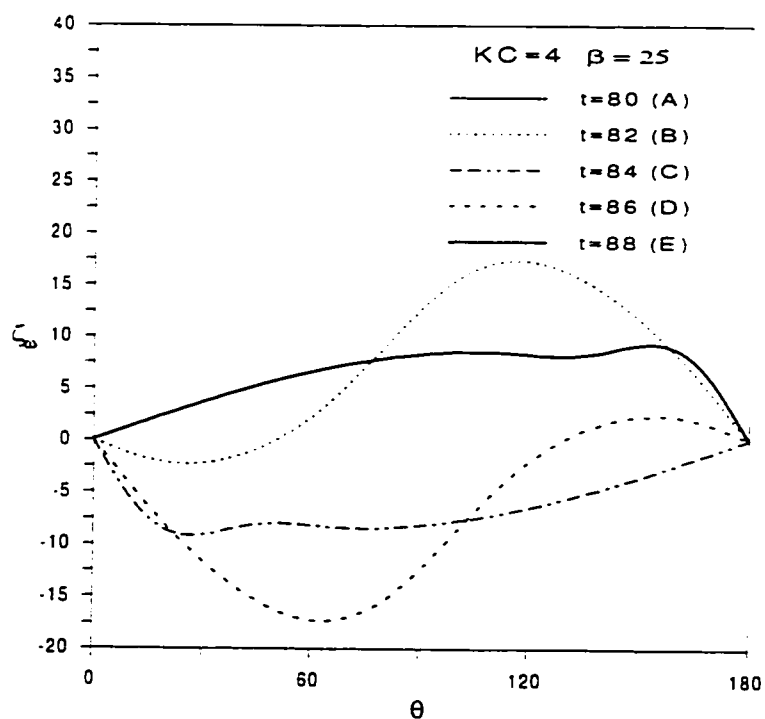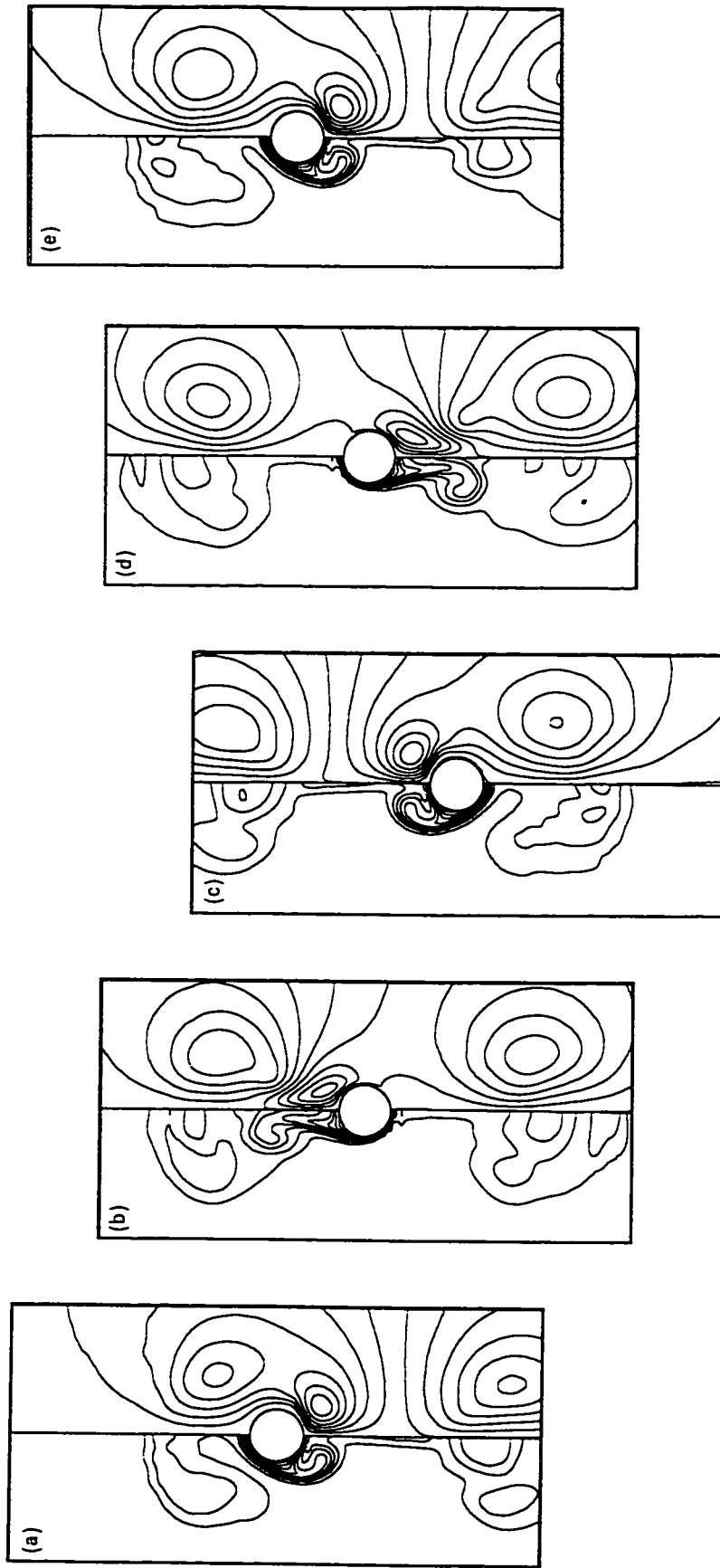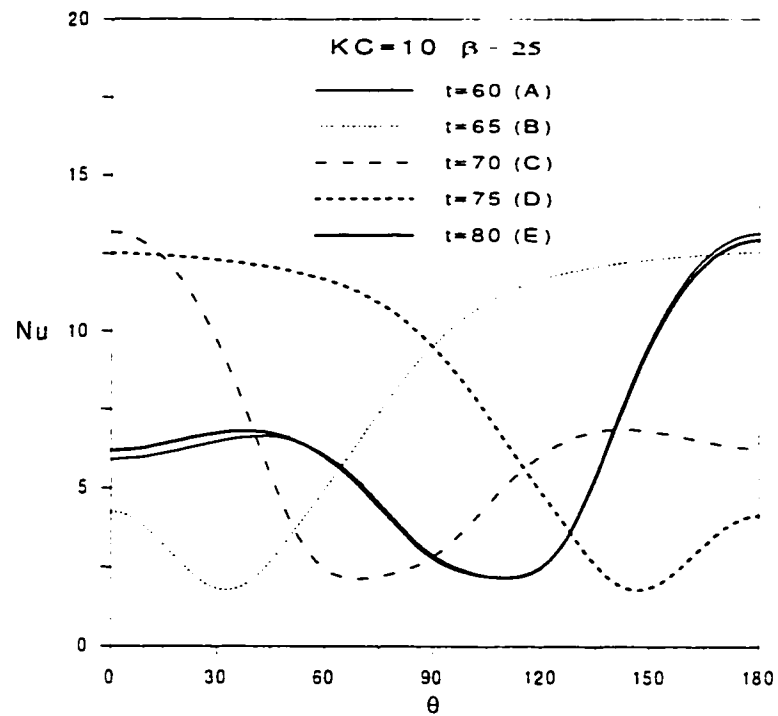Figure 5.12 Local Nusselt number distribution in a complete cycle of oscillation at Gr=10^5, KC=10 and β = 25.
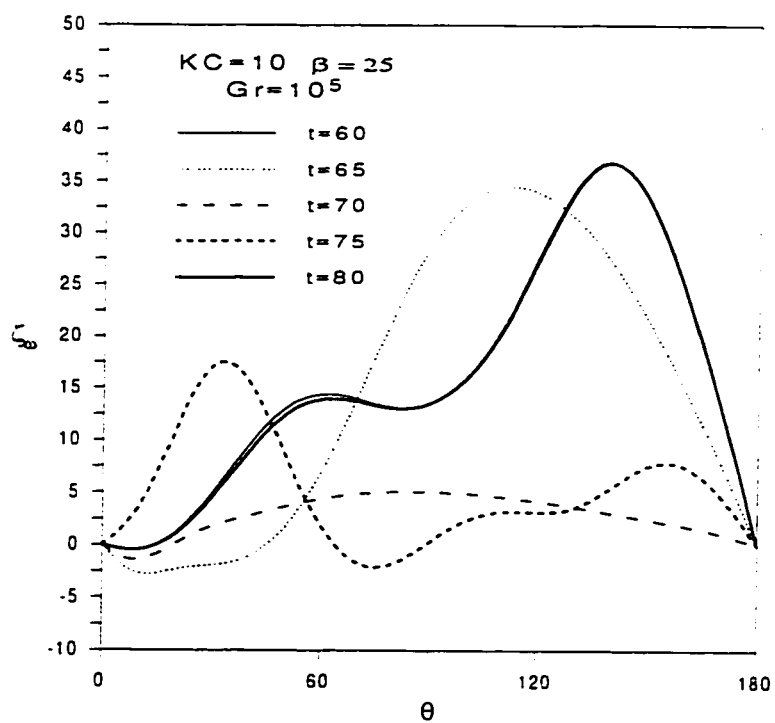
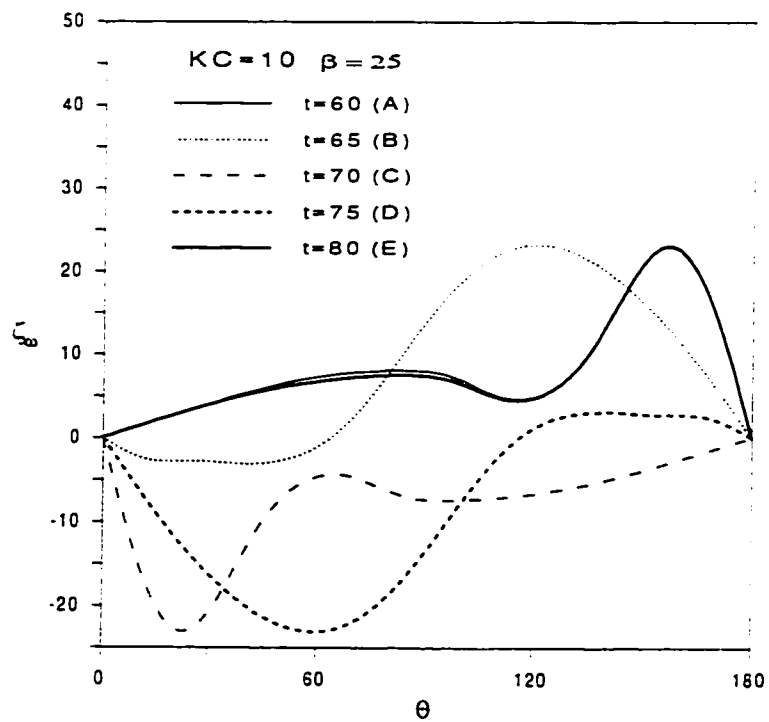Figure 5.13 Surface vorticity distribution in a complete cycle of oscillation at Gr=10^5, KC=10 and β = 25.
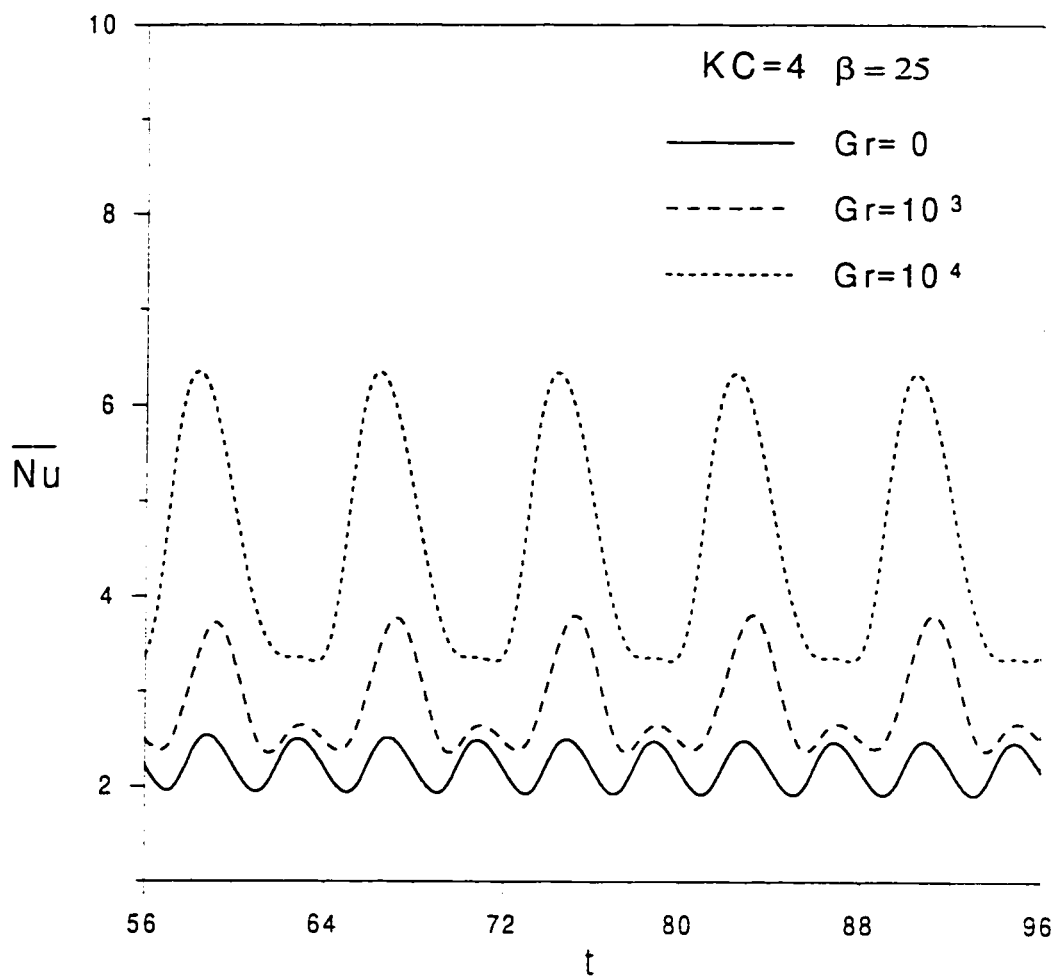
Figure 5.14 Time variation of $\overline{Nu}$ at KC=4 and β =25
and at different Grashof numbers.

CHAPTER 6

CONCLUSIONS

In this study, the problems of heat convection from a cylinder performing either rotational or rectilinear oscillations are considered. In the following, the main conclusions drawn for each of the cases considered are presented.

1) Forced convection from rotationally oscillating cylinder in a cross stream

The unsteady flow and heat convection characteristics for a heated cylinder performing rotational oscillation about its own axis and placed in a uniform stream is investigated. The governing equations of motion and energy are solved numerically to determine the flow field characteristics and the heat transfer coefficients for various Reynolds numbers, amplitude of oscillation and the frequency ratio. The lock-on phenomenon has been predicted and its effect on the flow and thermal fields has been determined. The results show that the lock-on phenomenon occurs within a band of frequency near the natural frequency. This band, however, becomes wider as the amplitude of oscillation increases. The heat transfer coefficient as well as lift and drag coefficients show an increase within the lock-on frequency range. This increase however, becomes more significant in the middle of lock-on range near the natural frequency.

2) Mixed convection from a cylinder performing steady or oscillating rotary motions in a quiescent fluid

The problem of laminar, two dimensional heat convection from a circular cylinder performing steady or oscillating rotary motions is investigated. The cylinder is placed with its axis horizontal in a quiescent fluid of infinite extent. Because of viscous dissipation, the flow process is confined to the region adjacent to the cylinder and is mainly driven by shear and buoyancy forces. For a steady rotating cylinder, the study covers Rayleigh numbers, Ra, up to 1000 and Reynolds numbers, Re_{st} , (based on surface velocity) up to 400. The study revealed that , for the same Ra, the rate of heat transfer tend to decrease with increasing the speed of rotation in the range of Re_{st} considered. In the case of rotational oscillation, the heat transfer process is governed by Ra , Re_{os} (Reynolds number based on maximum surface velocity) and the dimensionless frequency of oscillation, S_f. The study covers Ra up to 1000, Re_{os} up to 400 and S_f up to 0.8. The results revealed that, for the same Ra, the heat transfer rate fluctuates around an average that lies in between two limiting values. The first, is the steady heat rate due to natural convection from a fixed cylinder and the second is the steady heat rate from a cylinder rotating steadily at a speed equal to the maximum speed of rotational oscillation. The smaller the value of Re_{os} the nearer the time-averaged Nusselt number to that of fixed cylinder at the same Ra and the higher Re_{os} the lower the average Nusselt number. The effect of frequency is only limited to changing the amplitude of the fluctuating Nusselt number.

3- Heat convection from a cylinder performing rectilinear oscillation in a quiescent fluid

The problem of heat convection from a vertically oscillating cylinder in a quiescent fluid is investigated in the range of Grashof number, Gr, up to 10^5, Keulegan-Carpenter number, KC, up to 10 and frequency parameter, β, up to 40. The study has shown that in the absence of buoyancy effects (Gr=0), as KC increases the flow field becomes characterized by extensive vortex motion at all cylinder positions. The results has shown also a significant increase in heat convection as either KC or β increases. However, as Gr increases, the effect of oscillation parameters on heat convection has shown to be insignificant in comparison with the natural convection from a fixed cylinder at the same Gr.

Appendix A1

The functions S_0, S_{n1} and S_{n2} used in Equations (3.18a-c) are defined as:

$$S_0 = \sum_{n=1}^{N} n\left(\frac{\partial}{\partial\xi}(g_n F_n) - \frac{\partial}{\partial\xi}(f_n G_n) \right) \tag{A1.1}$$

$$S_{n1} = \sum_{m=1}^{N} \left\{ \frac{\partial g_m}{\partial\xi}(Kf_K - Jf_J) + \frac{\partial G_m}{\partial\xi}[KF_K - (m-n)F_J] + mG_m\left(\frac{\partial F_K}{\partial\xi} - \frac{\partial F_J}{\partial\xi}\right) \right.$$
$$\left. + mg_m\left[\frac{\partial f_K}{\partial\xi} - \text{sgn}(m-n)\frac{\partial f_J}{\partial\xi}\right] \right\} \tag{A1.2}$$

$$S_{n2} = \sum_{m=1}^{N} \left\{ \frac{\partial g_m}{\partial\xi}[KF_K + (m-n)F_J] - mG_m\left[\frac{\partial f_K}{\partial\xi} + \text{sgn}(m-n)\frac{\partial f_J}{\partial\xi}\right] \right.$$
$$\left. + mg_m\left(\frac{\partial F_K}{\partial\xi} + \frac{\partial F_J}{\partial\xi}\right) - \frac{\partial G_m}{\partial\xi}(Kf_K + Jf_J) \right\} \tag{A1.3}$$

Where, $K = m+n$, $J = |m-n|$, $\delta_n = \begin{cases} 1 \text{ when } n = 1 \\ 0 \text{ when } n \neq 1 \end{cases}$

and sgn(m-n) means the sign of the term (m-n).

The functions Z_0, Z_{n1} and Z_{n2} used in Equations (3.19a-c) are defined as:

$$Z_0 = \sum_{n=1}^{N} n\left(\frac{\partial}{\partial\xi}(h_n F_n) - \frac{\partial}{\partial\xi}(f_n H_n) \right) \tag{A1.4}$$

$$Z_{n1} = \sum_{m=1}^{N} \left\{ \frac{\partial H_m}{\partial\xi}[KF_K - (m-n)F_J] - mh_m\left[\frac{\partial f_K}{\partial\xi} - \text{sgn}(m-n)\frac{\partial f_J}{\partial\xi}\right] \right.$$
$$\left. + mH_m\left(\frac{\partial F_K}{\partial\xi} - \frac{\partial F_J}{\partial\xi}\right) + \frac{\partial h_m}{\partial\xi}(Kf_K - Jf_J) \right\} \tag{A1.5}$$

$$Z_{n2} = \sum_{m=1}^{N} \left\{ \frac{\partial h_m}{\partial\xi}[KF_K + (m-n)F_J] - mH_m\left[\frac{\partial f_K}{\partial\xi} + \text{sgn}(m-n)\frac{\partial f_J}{\partial\xi}\right] \right.$$
$$\left. + mh_m\left(\frac{\partial F_K}{\partial\xi} + \frac{\partial F_J}{\partial\xi}\right) - \frac{\partial H_m}{\partial\xi}(Kf_K + Jf_J) \right\} \tag{A1.6}$$

The function $E_n(\xi, t)$ used in Equation (3.28) is defined as:

$$E_n(\xi, t) = \frac{1}{2}\left(nf_n \frac{\partial G_0}{\partial\xi} - ng_n \frac{\partial F_0}{\partial\xi} + S_{n2} \right)$$

Appendix A2

The functions S_0, S_{n1} and S_{n2} used in equations 4.10 and 4.11 are defined as:

$$S_0(\xi, t) = e^\xi \frac{Gr}{8}\left(\frac{\partial h_1}{\partial \xi} + h_1\right) + \sum_{n=1}^{N} n\left(\frac{\partial}{\partial \xi}(g_n F_n) - \frac{\partial}{\partial \xi}(f_n G_n)\right) \tag{A2.1}$$

$$S_{n1} = e^\xi \frac{Gr}{16}\left(\frac{\partial h_{n-1}}{\partial \xi} - \frac{\partial h_{n-1}}{\partial \xi} + (n-1)h_{n-1} + (n+1)h_{n-1}\right)$$

$$+ \frac{1}{2}\sum_{m=1}^{N}\left\{\frac{\partial g_m}{\partial \xi}[KF_K + (m-n)F_J] - mG_m\left[\frac{\partial f_K}{\partial \xi} + sgn(m-n)\frac{\partial f_J}{\partial \xi}\right]\right.$$

$$\left. + mg_m(\frac{\partial F_K}{\partial \xi} + \frac{\partial F_J}{\partial \xi}) - \frac{\partial G_m}{\partial \xi}(Kf_K + Jf_J)\right\} - \frac{n}{2}[f_n \frac{\partial G_o}{\partial \xi} - g_n \frac{\partial F_o}{\partial \xi}] \tag{A2.2}$$

$$S_{n2} = e^\xi \frac{Gr}{16}\left(\delta_{n1}\frac{\partial H_0}{\partial \xi} + \frac{\partial H_{n-1}}{\partial \xi} - \frac{\partial H_{n-1}}{\partial \xi} - (n-1)H_{n-1} - (n+1)H_{n-1}\right)$$

$$+ \frac{1}{2}\sum_{m=1}^{N}\left\{\frac{\partial g_m}{\partial \xi}(Kf_K - Jf_J) + \frac{\partial G_m}{\partial \xi}[KF_K - (m-n)F_J] + mG_m(\frac{\partial F_K}{\partial \xi} - \frac{\partial F_J}{\partial \xi})\right.$$

$$\left. + mg_m\left[\frac{\partial f_K}{\partial \xi} - sgn(m-n)\frac{\partial f_J}{\partial \xi}\right]\right\} + \frac{n}{2}[F_n \frac{\partial G_o}{\partial \xi} - G_n \frac{\partial F_o}{\partial \xi}] \tag{A2.3}$$

Where, $K=m+n$, $J=|m-n|$, $\delta_{n1} = \begin{cases} 1 \text{ when } n = 1 \\ 0 \text{ when } n \neq 1 \end{cases}$

and $sgn(m-n)$ means the sign of the term $(m-n)$.

The functions R_0, R_{n1} and R_{n2} used in equation are defined as:

$$R_0 = \sum_{n=1}^{N} n\left(\frac{\partial}{\partial \xi}(h_n F_n) - \frac{\partial}{\partial \xi}(f_n H_n)\right) \tag{A2.4}$$

$$R_{n1} = \frac{1}{2}\sum_{m=1}^{N}\left\{\frac{\partial h_m}{\partial \xi}[KF_K + (m-n)F_J] - mH_m\left[\frac{\partial f_K}{\partial \xi} + sgn(m-n)\frac{\partial f_J}{\partial \xi}\right]\right.$$

$$\left. + mh_m(\frac{\partial F_K}{\partial \xi} + \frac{\partial F_J}{\partial \xi}) - \frac{\partial H_m}{\partial \xi}(Kf_K + Jf_J)\right\} \tag{A2.5}$$

$$R_{n2} = \frac{1}{2}\sum_{m=1}^{N}\left\{\frac{\partial H_m}{\partial \xi}[KF_K - (m-n)F_J] - mh_m\left[\frac{\partial f_K}{\partial \xi} - sgn(m-n)\frac{\partial F_J}{\partial \xi}\right]\right.$$

$$\left. + mH_m(\frac{\partial F_K}{\partial \xi} - \frac{\partial F_J}{\partial \xi}) + \frac{\partial h_m}{\partial \xi}(Kf_K - Jf_J)\right\} \tag{A2.6}$$

Appendix A3

The functions S_{n1} used in equations are defined as:

$$S_n = e^{\xi} \frac{Gr}{2 Re^2} \left(\delta_{n1} \frac{\partial H_0}{\partial \xi} + \frac{\partial H_{n-1}}{\partial \xi} - \frac{\partial H_{n-1}}{\partial \xi} - (n-1)H_{n-1} - (n+1)H_{n-1} \right.$$

$$\left. + \frac{1}{2} \sum_{m=1}^{N} \frac{\partial g_m}{\partial \xi} (Kf_K - Jf_J) + mg_m \left[\frac{\partial f_K}{\partial \xi} - \text{sgn}(m-n) \frac{\partial f_J}{\partial \xi} \right] \right\} \qquad (A3.1)$$

Where, $\quad K=m+n, \quad J=|m-n|, \quad \delta_{n1} = \begin{cases} 1 \text{ when } n = 1 \\ 0 \text{ when } n \neq 1 \end{cases}$

and sgn(m-n) means the sign of the term (m-n).

The functions R_0, R_{n1} and R_{n2} used in equation are defined as:

$$R_0 = -\sum_{n=1}^{N} n \left(\frac{\partial}{\partial \xi} (f_n H_n) \right) \qquad (A3.2)$$

$$R_{n1} = -\frac{1}{2} \sum_{m=1}^{N} mH_m \left[\frac{\partial f_K}{\partial \xi} + \text{sgn}(m-n) \frac{\partial f_J}{\partial \xi} \right] + \frac{\partial H_m}{\partial \xi} (Kf_K + Jf_J) \qquad (A3.3)$$

Nomenclature

A_m	amplitude of vertical oscillation
c	cylinder radius
d	cylinder diameter
f	forcing frequency
f_n , F_n	Fourier coefficients
f_o	natural frequency
F_R	frequency ratio (= f/f_o or =S/S_o)
g	gravitational acceleration
g_n, G_n	Fourier coefficients
Gr	Grashof number ($g\beta(T_s - T_\infty)(d)^3 / v^2$
h, $\bar{h}$	local and average heat transfer coefficients
h_n , H_n	Fourier coefficients
k	thermal conductivity
KC	Kuelegan-Karpenter number
Nu, $\overline{Nu}$	local and average Nusselt numbers
$\overline{\overline{Nu}}$	time averged Nusselt number
P, P^*	pressure and dimensionless pressure
Pr	Prandtl number (v/α)
Pe	peclet number (RePr)
r	dimensionless radial coordinate (r'/c)
Ra	Rayleigh number (Gr Pr)
Re	Reynolds number
Re_{st}	Reynolds number ($2\omega_{st}c^2/v$)
Re_{os}	oscillation Reynolds number ($2\omega_{os}c^2/v$)
S	dimensionless forcing frequency
S_o	natural Strouhal number

173

t	dimensionless time
t'	time
T	temperature
U	maximum velocity of vertical oscillation
u_r', u_θ'	radial and tangential components of velocity
u_r	dimensionless radial velocity
u_θ	dimensionless tangential velocity
V	free stream velocity

Greek symbols

α	velocity amplitude
β	frequency parameter
ϕ	dimensionless temperature $(T - T_\infty)/(T_s - T_\infty)$
ξ	dimensionless logarithmic coordinates (ln r)
μ	dynamic viscosity.
ν	kinematics viscosity
ω_{st}	steady angular speed
ω_{os}	oscillatory angular speed
ρ	density
τ	time
θ	angular coordinates
ψ	stream function
ζ	vorticity

Subscripts

s, w,	cylinder surface
∞	at infinite distance from the surface

BIBLIOGRAPHY

1. Tanida, Y., Okajima, A. and Watanabe, Y., Stability of the circular cylinder oscillating in uniform flow or in a wake, J. Fluid Mechanics, 61(4), p769, 1973.

2. Tokumaru, P.T. and Dimotakis, P.E., Rotary oscillation control of cylinder wake, J. Fluid Mechanics 224, p77, 1991.

3. Anderson, I. T. and Saunders, O. A., Convection from an isolated heated horizontal cylinder rotating about its axis, Proc. Roy. Soc. A, 217, p555, 1953.

4. Etemad, G. A., Free convective heat transfer from a rotating cylinder to ambient air, with interferometric study of flow, Trans. ASME 77, p1283, 1955

5. Dropkin, D. and Carmi, A., Natural convection heat transfer from a horizontal cylinder rotating in air, Heat transfer and Fluid Mechanics Institute, Stanford University, 1956.

6. Kays, W.M. and Bjorklund, I.S., Heat transfer from a rotating cylinder with and without crossflow, Trans. Am. Soc. Mech. Engrs. 80, p70, 1958.

7. Seban, R. A. and Johnson, H. A., Heat transfer from a horizontal cylinder rotating in oil, NASA Memo 4-22-59 W April, 1959.

8. Becker, K.M., Measurement of convective heat transfer from a horizontal cylinder rotating in a tank of water, Int. J. Heat and Mass Transfer, 6, p1053, 1963.

9. Badr, H. M. and Ahmed, S.M., Heat convection from a horizontal cylinder rotating in a quiescent fluid, Trans. of CSME 10 (3), p141, 1986.

10. Farouk ,B. and Ball, S., Convective flows around a rotating isothermal cylinder, Int. J. Heat and Mass Transfer. 28(10), p1921, 1985.

11. Wu-Shung, F., Chao-Sheng, C. and Wen-Jiann, S., Enhancement of natural convection heat transfer of an enclosure by a rotating circular cylinder, Int. J. Heat Mass Transfer, 37(13), p885, 1994.

12. Wang, P., Kahawita, R. and Nguyen, D. L., Transient laminar natural convection from horizontal cylinders, Int. J heat and Mass Transfer, 34 (6), p1429, 1991.

13. Fujii, T., Fujii, M. and Honda, T., Theoretical and experimental study on free convection around a horizontal wire, J. Soc. Mech. Engrs. 48(431), p1312, 1982.

14. Saitoh, T., Sajiki, T. and Maruhaara, K., Bench mark solutions to natural convection heat transfer problem around a horizontal circular cylinder, Int. J. Heat and Mass Transfer, 36(5), p1251, 1993.

15. Kuehn, T.H. and Goldstein, R. J., Numerical solution to the Navier-Stokes equations for laminar natural convection about a horizontal isothermal circular cylinder, Int. J. Heat and Mass Transfer, 23, p971, 1980.

16. Badr, H. M. and Dennis, S. C. R., Laminar forced convection from a rotating cylinder, Int. J. Heat and Mass Transfer, 28(1), p253, 1985.

17. Ryohatchi, S. and Tomoaki, O. heat transfer from a rotating cylinder with and without cross flow, Trans. JSME, 57 (533b), p210, 1991.

18. Chio, C.C. and Lee, S. L., Forced convection on a rotating cylinder with an incident air jet, Int. J. Heat and Mass Transfer, 36(15), p3841, 1993.

19. Ali, M.S., Mixed convection from a horizontal cylinder rotating in a cooling cross stream, M.Sc. king Fahd University of Petroleum and Mineral, June 1994.

20. Nguyen, Hoa D., paik, S. and Douglass, R.W., Unsteady mixed convection about a rotating circular cylinder with small fluctuations in the free stream velocity, Int. J. Heat and Mass Transfer 39(3), p511, 1996.

21. Hori, Ei-ichi, Boundary layer on a circular cylinder in rotational oscillation, Bulletin of JSME, 5(17), 1962.

22. Okajima, A., Takata H. and Asanuma, T., Viscous flow around a rotationally oscillating circular cylinder, Inst. Space and Aero. Sci. Rep. 532. University of Tokyo, 1975.

23. Tanida, S., Visual Observation of the flow past a circular cylinder performing a rotary oscillation, J. of the Physical Society of Japan, 45(3), 1978.

24. Wu, J.M., Mo, J.D. and Vakili, A.D., On the wake of a circular cylinder with rotational oscillations, AIAA-89-1024, 1989.

25. Roberts, F.A. and Roshko, A., Effects of periodic forcing on mixing in turbulent shear layers and wakes, AIAA Shear Flow Conf. Paper 85-0570, 1985.

26. Williams, D. R. and Amato, C.W., Unsteady pulsing of cylinder wakes. In Proc. First Natl Fluid Dynamics Congr. (AIAA-88-3532-cp), p731, 1988.

27. Tokumaru, P.T. and Dimotakis, P. E., The lift of a cylinder executing rotary motions in a uniform flow, J. Fluid Mechanics, 255, p1, 1993.

28. Childs, E. P. and Mayle, R.E., Heat transfer on a rotationally oscillating cylinder in cross-flow, Int. J. Heat and Mass Transfer 27(1), p85, 1984.

29. Blasius, H., The boundary layers in fluids with little friction, NACA TM 1256.

30. Howrarth, L., On the calculation of steady flow in the boundary layer near the surface of a cylinder in a stream, ARCR&M1632, 1935.

31. Lighthill, M. J., The response of laminar skin friction and heat transfer to fluctuation in the stream velocity, Proc. R. Soc. A224, p1, 1954.

32. Williamson, C. H. K., Sinusoidal flow relative to circular cylinder, J. Fluid Mechanics, 155, p141, 1985.

33. Obasaju, E. D., Bearman, P. W. and Graham, J. M. R., A study of forces, circulation and vortex patterns around a circular cylinder in oscillating flow, J. Fluid Mechanics, 196, p467, 1988.

34. Tatsuno, M. and Bearman, P. W., A visual study of the flow around an oscillating circular cylinder at low Keulegan-Carpenter numbers and at low Stokes numbers, J. Fluid Mechanics, 211, p157, 1990.

35. Bearman, P. W., Downie, M. J., Graham, J. M. R. and Obasaju, E. D., Forces on cylinders in viscous oscillatory flow at low Keulegan-Carpenter numbers, J. Fluid Mechanics, 154, p337, 1985.

36. Sarpkaya, T., Forces on a circular cylinder in viscous oscillatory flow at low Keulegan-Carpenter numbers, J. Fluid Mechanics, 165, p61, 1986.

37. Justesen, P., A numerical study of oscillating flow around a circular cylinder, J. Fluid Mechanics, 222, p157, 1991.

38. Badr, H. M., Dennis, S. C. R., Kocabiyik, S. and Nguyen, P., Viscous oscillatory flow about a circular cylinder at small to moderate Strouhal number, J. Fluid Mechanics, 303, p215, 1995.

39. Zhang, H. and Zhang, X., Flow structure analysis around an oscillating circular cylinder at low KC number : A numerical study, Computers & Fluids, 26(1), p83, 1997.

40. Lemlich, R. and Anandha-Roa, M., The effect of transverse vibration on free convection from a horizontal cylinder. Int. J. Heat and Mass Transfer, 8, p27, 1965.

41. Martinelli, R. C. and Boelter, L. M. K., The effect of vibration on heat transfer by free convection from a horizontal cylinder, proc. 5th Int. J. Heat and Mass Transfer. Cong. Appl. Mech. P578, 1938.

42. Boelter, L. M. K and Mason, W. E., Vibration-its effect on heat transfer, power plant Engng, 44, p43, 1940.

43. Deaver, F. K., Penney, W.R. and Jefferson, T. B., Heat transfer from an oscillating horizontal wire to water, trans. ASME, series C, J. Heat transfer, 84, p251, 1962.

44. Lemlich, R., Effect of vibration on natural convective heat transfer, industr. Engng Chem., 47, p1175, 1955.

45. Fand, R. M. and Kaye, J., the influence of vertical vibration on heat transfer by free convection from a horizontal cylinder, International Development in Heat Transfer, 490-498 ASME, 1961.

46. Teleki, C. and Levy, M. R., Influence of vertical vibrations on the rate of heat transfer from a horizontal cylinder in air, wright Air Development Command, TN 59-357, 1960.

47. Saxena, U.C. and Laird, A. D. K., Heat transfer from a cylinder oscillating in a cross-flow, Trans. ASME, J. Heat transfer, 100, p684, 1978.

48. Sreenivasan, K. and Ramachandran, A., Effect of vibration on heat transfer from a horizontal cylinder to a normal air stream. Int. J. Heat and Mass Transfer, 3, p60, 1961.

49. Kimoto, H., Kadotsuji, A. and Hirosc, T., Effect of vibration on the natural convection heat transfer of a horizontal cylinder, Bull. JSME, 26(217), p1154, 1983.

50. Momose, K., Asami, T. and Hosokawa, Y., Local characteristics of heat transfer from a vibrating cylinder, Heat Transfer-Japanese Research, 22 (5), p462, 1993.

51. Karanth, D., Rankin, G. W. and Sridhar, K., A finite difference calculation of forced convective heat transfer from an oscillating cylinder, Int. J. Heat and Mass Transfer, 37(11), p1619, 1994.

52. Chin-Hsiang, C., Jing-Lia, H. and Win, A., Numerical prediction of lock-on effect on convective heat transfer from a transversely oscillating circular cylinder, Int. J. Heat and Mass Transfer, 40(8), p1825, 1997.

53. Badr, H. M., Effect of free-stream fluctuations on laminar forced convection from straight tube, Int. J. Heat Mass Transfer, 40(15), p3653, 1997.

54. Collins, W. M. and Dennis, S. C. R., Flow past an impulsively started circular cylinder, J. Fluid Mechanics, 60, p105, 1973.

55. Badr, H. M. and Dennis, S. C. R., Time-dependent viscous flow past an impulsively started rotating and translating circular cylinder, J. Fluid Mechanics, 158, p447, 1985.

56. Ta Phuoc loc and Bouard, R., Numerical solution of the early stage of the unsteady viscous flow around a circular cylinder: a comparison with experimental visualization and measurements, J. Fluid Mechanics, 180, p93, 1985.

57. Ta Phuoc Loc, Numerical analysis of unsteady secondary vortices generated by an impulsively started circular cylinder, J. Fluid Mechanics, 100, part 1, p111, 1980.

58. Coutanceau, M. and Menard, C., Influence of rotation on the near-wake development behind an impulsively started circular cylinder, J. Fluid Mechanics, 158, p399, 1985.

59. Bishop, R. E. D. and Hassan, A. Y., The lift and drag forces on a circular cylinder oscillating in a flowing fluid, Proceedings of the Royal Society, Series A, 227, 1964.

60. Stansby, P. K., The locking-on vortex shedding due to cross-stream vibration of circular cylinder in uniform and shear flows, J. Fluid Mechanics, 74, p641, 1976.

61. Hurlbut, S. E., Spaulding, M. L. and White, F. M., Numerical Solution for laminar two dimensional flow about a cylinder oscillating in a uniform stream, ASME, J. Fluid Engineering, 104, p214, 1982.

62. Karniadakis, G. and Triantayllou, S. G., Frequency selection and asymptotic states in laminar wakes, J. Fluid Mechanics, 199, p441, 1989.

63. Eckert, E. R. G. and Soehngen, E., Distribution of heat transfer coefficients around circular cylinders in cross-flow at Reynolds numbers from 20 to 500, Trans. ASME, 74(3), p343, 1952.

64. Kramers, H. A., Heat transfer from sphere to flowing media, Physics, 12, p61, 1946.

65. Richardson, P. D., Heat and mass transfer in turbulent separated flows, Chem. Eng. Sci., 18, p149, 1963.

66. Morgan, V. T., The overall convective heat transfer from smooth circular cylinder, in Advances in heat transfer, vol. 11 (J. P. Hartnett and T. F. Irvine, Jr., eds.), 199-264, Academic press, New York, 1975.

67. Jain, P. C., and Goel, B. S., A numerical study of unsteady laminar forced convection from a circular cylinder, J. Heat Transfer, 98(2), ser. C, p303, 1976.

68. Rashid, A. A., Steady-state numerical solution of the Navier-Stokes and energy equations around a Horizontal cylinder at moderate Reynolds numbers from 100 to 500, Heat Transfer Engineering, 17(1), 1996.

69. Relf, E. F., and Simmons, L. F., G., Aero. Res. Counc. R. & M. No. 917, 1924.

70. Roshko, A., On the development of turbulent wakes from vortex streets, NACA Rep., 1191, 1954.

71. Koopman, G. H., The vortex wakes of vibrating cylinders at low Reynolds numbers, J. Fluid Mechanics, 28, p501, 1967.

72. Sarpkaya, T., Vortex-induced oscillations, A Selective Review, J. of Applied Mech., 46, p241, 1979.

73. Patankar, S.V., Numerical heat transfer and fluid flow, Hemisphere Washinton, D. C., 1980.

Vita

- Fathi Mohamed Abd El-Azim Mahfouz was born June 16, 1962 in Egypt.

- He received his B. Sc. degree in Mechanical Engineering from Faculty of Engineering Menoufia University, Egypt in May, 1985.

- He received his M. Sc. degree in Mechanical Engineering from Faculty of Engineering Menoufia University, Egypt in December, 1990.

- He joined the King Fahd University of Petroleum and Minerals in 1993.

- He finished all the requirements of his Ph.D. degree in Mechanical Engineering from King Fahd University of Petroleum and Minerals Dhahran, Saudi Arabia in May, 1998.

IMAGE EVALUATION
TEST TARGET (QA-3)

1.0
1.1
1.25
1.4
1.6
1.8
2.0
2.2
2.5
2.8
3.2
3.6
4.0
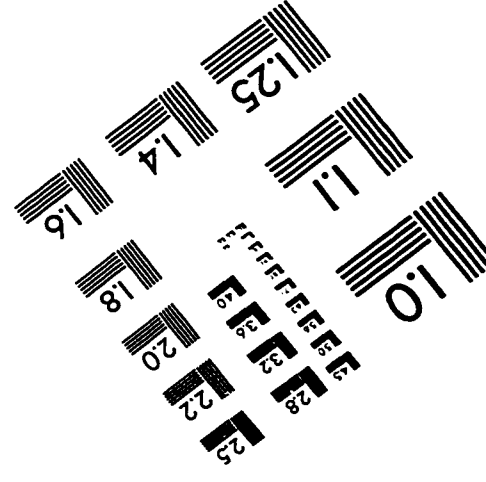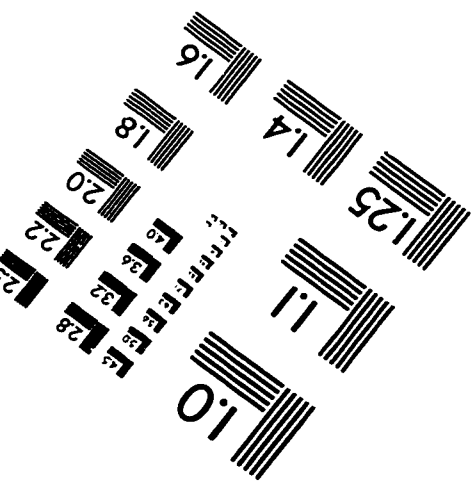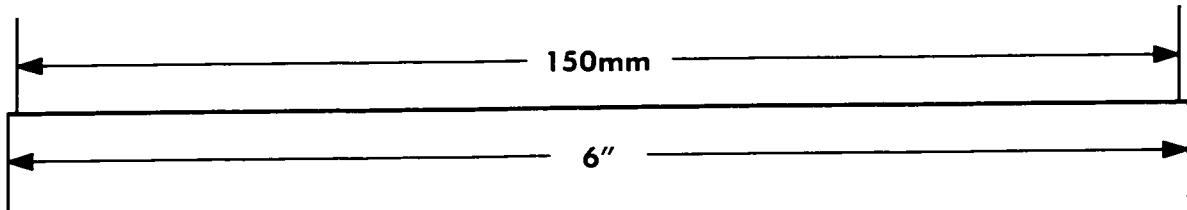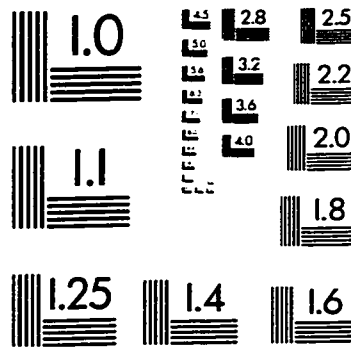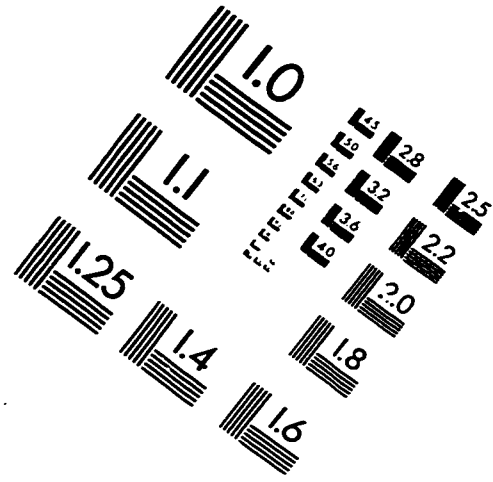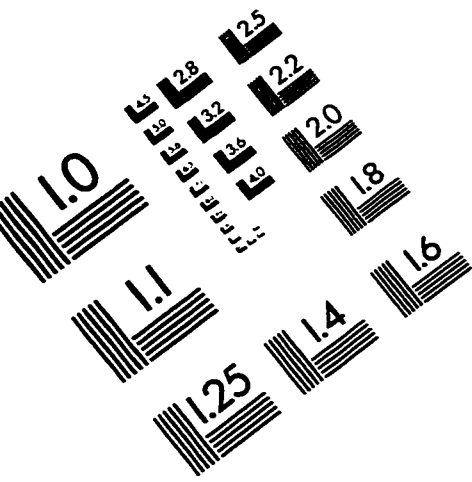
APPLIED IMAGE . Inc

1653 East Main Street
Rochester, NY 14609 USA
Phone: 716/482-0300
Fax: 716/288-5989

150mm

6"